

## MECHANISMS OF CURRENT TRANSITION IN HIGH COMPENSATED SILICON SAMPLES WITH ZINC NANOCLUSTERS<sup>†</sup>

 Eshkuvat U. Arzikulov\*, M. Radzhabova, Sh.J. Quvondiqov, G. Gulyamov

*Samarkand State University named after Sharaf Rashidov*

*140104, University Boulevard 15, Samarkand, Republic of Uzbekistan*

*\*Corresponding Author e-mail: eshkuvata@gmail.com*

Received July 20, 2023; revised July 31, 2023; accepted August 2, 2023

This article presents experimental results on the study of the current-voltage characteristics of strongly compensated n- and p-type silicon samples diffusion-doped with zinc at a temperature of 80 K. The current-voltage characteristics of the studied samples contain both sublinear and superlinear sections. Several (up to eight) characteristic areas were found, the number of which depends on the degree of illumination, temperature, and electrical resistivity of the sample. Under certain conditions, there is an alternation of sections of the current-voltage characteristic with negative differential conductivity of the N- and S-type, behind which current instabilities with an infra-low frequency are observed. The appearance of sections of the current-voltage characteristic with a quadratic dependence is explained by the presence of fast and slow recombination centers associated with zinc nanoclusters, and sublinear sections are explained in terms of the theory of the "injection depletion effect". The formation of nanoclusters with the participation of zinc ions was confirmed by atomic force microscopy studies.

**Keywords:** *Compensated silicon; Current-voltage characteristic; Current flow; Zinc; Nanocluster; Negative differential conductivity; Sublinearity; Superlinearity*

**PACS:** 72.8.-r, 72.80.Cw

### 1. INTRODUCTION

It is known that the shape of the current-voltage characteristic (CVC) of semiconductors containing deep levels (DL) can have three or more characteristic regions [1]. It has been experimentally established [2] that on many semiconductor materials, usually in the first section of the CVC, a linear dependence of the current on the applied voltage is observed, i.e., Ohm's law is satisfied. In the second section, there is a power-law relationship between current and voltage, i.e., dependence of type  $I = U^n$ , where  $n > 1$ . In the third section of the  $I(U)$  dependence, starting from certain voltage values, a sharp increase in current is observed. Further, with an increase in the electric field strength, a decrease in current is observed, i.e., there is a region with negative differential conductivity (NDC). Usually the NDC is N- or S-type. Combinations of S- and N-type NDCs are also possible [3]. Under certain conditions, they can replace each other, and it is also possible to transform the S-shaped I-V characteristic into an N-shaped one over time. The statistical characteristic can also have a more complex form. The observation of the CVC in the NDC region is associated with current instabilities, i.e., current or voltage fluctuations with different frequencies and shapes can be observed depending on the experimental conditions [4, 5].

This article presents the experimental results of the dependence of the current density  $j$  on the electric field strength  $E$  of strongly compensated silicon samples diffusion-doped with zinc with nanoclusters. A study of the surface morphology before and after the diffusion process of samples using AFM atomic force microscopy (Figure 1 and 2) showed that nano-sized periodic structures and pyramid-shaped objects are formed on the surface and near-surface region of diffusion-doped samples, which mainly consist of atoms zinc.

### 2. EXPERIMENTAL METHODS, RESULTS AND IT'S DISCUSSION

Studies of the I-V characteristics in n-Si<P, Zn> samples were carried out under various background illuminations of integrated light at a temperature of  $T=80$  K measured [15]. The influence of the internal resistance of a constant voltage source on the form of the I-V characteristic has not been investigated by us. However, in all experiments, the operating point was located on a given section of the CVC.

The type of CVC of the studied samples strongly depends on the degree of illumination of the samples. At relatively low illumination ( $0.05 \div 0.01$  Lx), the CVC of the samples consists of several clearly defined sections (Fig. 3, curve 1): the first section is when the applied electric field in the sample is less than  $12.6$  V/cm, a dependence of the form  $I = U^{0.22}$  is observed, the second section - when  $E$  is in the range of values  $12.6$  V/cm  $\leq E \leq 18.9$  V/cm, a dependence of the form  $I = U^{0.77}$  is observed, the third section - when  $E$  lies in in the range of  $19$  V/cm  $\leq E \leq 62.9$  V/cm, an almost quadratic dependence is observed, i.e.  $I = U^{1.91}$ , the fourth section - when  $E$  is in the range of values  $62.9$  V/cm  $\leq E \leq 94.3$  V/cm, again a dependence close to the second section is observed, i.e. dependence of the form  $I = U^{0.71}$ . A further increase in  $E$  in the range of  $94.3$  V/cm  $\leq E \leq 471.1$  V/cm leads to a sharp increase in current. In this case, the dependence  $I(U)$  has the following form:  $I = U^{4.26}$ . When the value of  $E$  lies in the range  $471.1$  V/cm  $\leq E \leq 816.1$  V/cm, a dependence

<sup>†</sup> **Cite as:** E.U. Arzikulov, M. Radzhabova, Sh.J. Quvondiqov, G. Gulyamov, East Eur. J. Phys. 3, 400 (2023), <https://doi.org/10.26565/2312-4334-2023-3-43>

© E.U. Arzikulov, M. Radzhabova, Sh.J. Quvondiqov, G. Gulyamov, 2023

of the form  $I = U^{1.65}$  is observed. A further increase in  $E$  does not lead to noticeable changes in the current values, i.e., there is a weak sublinear dependence of the form  $I = U^{0.52}$ .

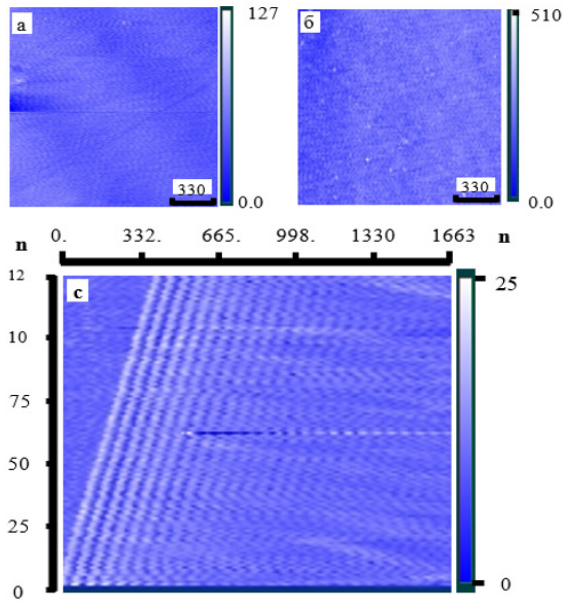


**Figure 1.** AFM images of the surface of a single-crystal silicon sample (a) - before diffusion zinc atom, (b) - after diffusion at  $T = 1145^\circ\text{C}$ , (c) - after diffusion at  $T = 1150^\circ\text{C}$

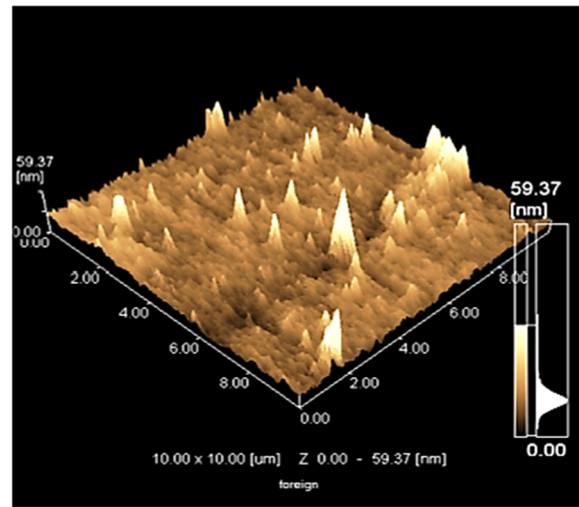


**Figure 2.** Surface morphology images of n-Si<P,Zn> samples obtained in an atomic microscope (AFM)

An increase in the illumination intensity of the integrated light leads to a noticeable change in both the nature of the  $I(U)$  dependence and the region of existence of one or another dependence in electric field strength. So, for example, an increase in the intensity of integral illumination from 0.012 Lx to values of 0.048 Lx leads to a decrease in the number of characteristic sections from 8 to 6, in addition, sections with NDP of both N - and S - types are added to the  $I(U)$  dependence, alternating with instabilities current (current self-oscillations). At relatively high intensities of the integral light, one dependence of the form  $I = U^{0.77}$  is observed in the  $I(U)$  dependence in the range  $25.2 \text{ V/cm} \leq E \leq 42.1 \text{ V/cm}$  (Fig. 4).

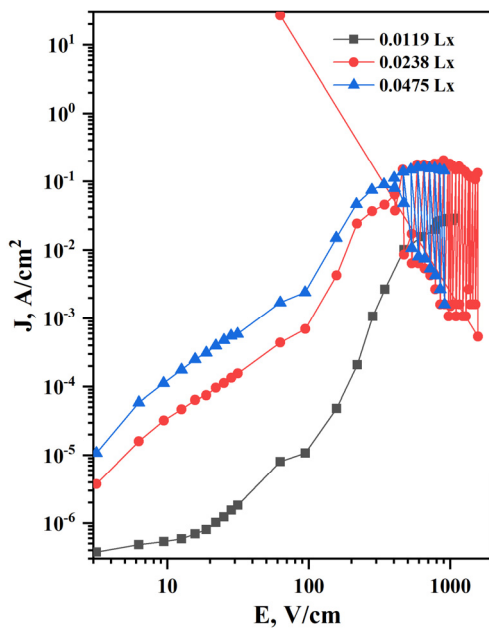


**Figure 3.** CVC of an n-Si<P, Zn> sample with  $\rho = 6.91 \cdot 10^4 \Omega \cdot \text{cm}$  under various background illuminations of integrated light.  $T=80 \text{ K}$

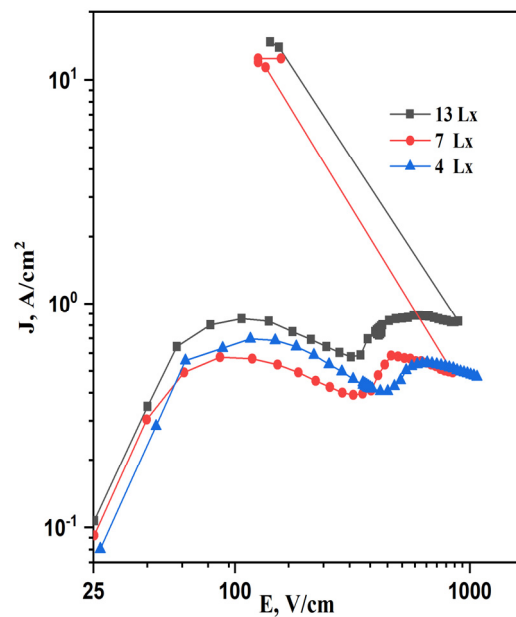


**Figure 4.** CVC of an n-Si<P, Zn> sample with  $\rho = 7.64 \cdot 10^4 \Omega \cdot \text{cm}$  at relatively high background integral illumination intensities.  $T=80 \text{ K}$

A further increase in  $E$  leads to a decrease in the current growth rate, which, passing through a maximum, begins to decrease, i.e., the NDC region is observed. A further increase in  $E$  leads to the second section with NDC. Two consecutive N-shaped sections are in the range of  $42.1 \text{ V/cm} \leq E_1 \leq 319 \text{ V/cm}$  and  $320 \text{ V/cm} \leq E_2 \leq 751 \text{ V/cm}$ , respectively.

At the same time, in the first section with NDC, in a certain range of E values, infra-low-frequency current oscillations with deep modulation ~ 99.98 % are observed, which disappears when a certain value of E is reached. In the second section with NDC, also when a certain value of E is reached, quasi-harmonic current oscillations begin, which come from single-cycle spike-shaped to push-pull with modulation coefficients of ~99.98 %, 90.5 %, respectively, with an increase in E. A further increase in E leads to a sharp increase in current at a certain critical value of E, i.e., an S-shaped section of the CVC is observed.

A further increase in E after the end of the second N-shaped section leads to a sharp increase in current. At a certain critical value of  $E_c$ , an S-shaped section is observed in the  $I(U)$  dependence curve.

The results obtained can be interpreted as how zinc atoms in silicon, under strong compensation, form not only deep levels, but also quantum dots with large charge carrier capture cross sections.

On Figure 4 shows a typical  $I-V$  characteristic for one of the  $n-Si<P, Zn>$  samples with a specific resistance at room temperature of  $\sim 7.64 \cdot 10^4 \Omega \cdot cm$ . As can be seen from the figure, the  $I-V$  characteristics of the sample under study partially contain characteristic sections of the  $I-V$  characteristics corresponding to semiconductors with deep levels, i.e., it contains segments of linear, quadratic, and sharp dependences of the photocurrent density on the applied electric field. In addition, in the studied samples, there are two regions of the N-type NDC and one region of the S-type NDC.

The nonlinearity of the CVC is found not only in many semiconductor devices, in which the main working element is p-n - junctions, but also in many semiconductor materials in which there are no p-n - junctions at all [3]. In semiconductor materials, if we exclude the influence of contacts, it is most often due to the effects of strong fields. It is known that in strong electric fields the dependence of the mobility on the field strength is observed up to velocity saturation, NDP, impact ionization, and breakdown. However, in weak electric fields, the manifestation of the nonlinearity of the CVC is also possible [6].

Studies of the processes of current passage of silicon samples doped with zinc unambiguously showed that the transport of electrons at low electric field strengths (E) obeys Ohm's law, and not too small E is described by the space charge-limited current theory (SCCT) and the capture of electrons to levels located in the band gap of the sample [5].

As is known [4], the reasons for the nonlinear behavior of the CVC in semiconductors have not been unequivocally established. A possible reason for the nonlinearity of the current-voltage characteristics in silicon samples doped with zinc can be the mechanisms known as space charge-limited current and ionization of centers in strong electric fields [6,8]. According to [6] when a voltage is applied to a high-resistance sample, a current arises in the circuit due to the injection of charge carriers from a metal electrode, which is described by a power law in the form  $I \sim E^2$ . The nonlinear section of the CVC in high-resistance crystals containing shallow and deep traps was associated with the implementation of monopolar or double injection [8].

The presence in the  $Si<P, Zn>$  HC samples of r - (slow) and s - (fast) recombination centers associated with the centers of zinc atom ions, as well as the t attachment level, suggests that in fields where there is a quadratic dependence of the current strength on the strength electric field ( $I \sim E^2$ ) in the  $I-V$  characteristics, the trap character of conductivity is realized. The data obtained in the quadratic region of the  $I-V$  characteristics show that in the samples of p- and n-type  $Si<P, Zn>$ , the transfer of charge carriers in electric fields ( $E < 10^2 V/cm$ ) is mainly due to monopolar injection and is consistent with the Lampert theory [8].

The sublinear segments of the  $I-V$  characteristics of the studied samples of the p- and n-type  $Si<P, Zn>$  can be satisfactorily explained in terms of the theory of the "injection depletion effect" [8]. Theoretically, the appearance of such a current-voltage characteristic is possible only with opposite directions of ambipolar diffusion of nonequilibrium current carriers and their ambipolar drift, which in our case is mainly determined by injection modulation of the charge of deep levels [10]. Due to the difference in diffusion coefficients, electrons run far ahead, and holes move slowly, as a result of which they are separated in space and an electric field arises between them, which slows down their movement. Reducing their speed causes a decrease in current, i.e., a sublinear portion of the CVC is observed.

An analysis of the obtained experimental data in relatively high fields (at  $E > 10^2 V/cm$ ) shows that the increase in conductivity with an increase in the electric field strength is associated with an increase in the concentration of excess current carriers. This allows us to assume that the presence of a section of a sharper increase in current in the  $I-V$  characteristic, where  $n > 3$ , can be explained by the fact that in samples of p - and n - type  $Si<B, Zn>$  at electric fields  $E > 10^2 V/cm$ , field devastation (or ionization) of traps.

The phenomenon of thermal quenching of photoconductivity [11] can lead to the appearance of a part of the  $I-V$  characteristic with the NDC of the illuminated sample. With an increase in the electric field strength and current density through the sample, the Joule power released in it increases. This also increases the temperature of the sample. An increase in temperature can lead to a sharp decrease in the photoelectron concentration due to the quenching of the phase transition and, due to the following condition (1), also to a change in the sign of the differential conductivity.

$$\sigma = en\mu \left( 1 + \frac{dln\mu}{dlnE} + \frac{dlnn}{dlnE} \right) \quad (1)$$

where  $e$  - is where the value of the charge of the mobile carrier,  $n$ - and  $\mu$ - are the concentration of charge carriers and their mobility,  $E$  - electric field strength.

Thus, the differential conductivity becomes negative if either the mobility of charge carriers or the concentration (or both) sharply enough depends on the field strength, decreasing with its increase. It is characteristic of which of these factors plays the main role, we can talk about drift ( $\mu = \mu(E)$ ) or concentration ( $n = n(E)$ ) nonlinearity.

Another mechanism that leads to a strong change in the concentration of charge carriers may be due to a sharp increase in the degree of ionization of shallow donors or acceptors during heating of free carriers. This increase can be associated both with an increase in the impact ionization rate during heating of charge carriers, and with the field dependence of the probability of their capture by like-charged traps. Indeed, the latter probability decreases with increasing carrier energy [3]. Both of these factors lead to the fact that when a certain critical value of the field strength  $E_c$  is reached (on the order of several V/cm in germanium and silicon at helium temperatures), a low-temperature breakdown of small impurities occurs. In fields on the order of  $10^2 \text{ V/cm}$ , almost complete release of charge carriers from traps occurs, which leads to a sharp superlinearity of the CVC. In compensated samples, in this case, S - shaped sections are observed in the CVC. At present, however, there is still no complete clarity regarding the specific mechanism of the origin of the region corresponding to the NDC [3].

The mechanism of the occurrence of S-shaped I–V characteristics in heavily doped and simultaneously supercritical semiconductors was investigated in [6]. At low temperatures and at relatively high K ( $K \geq 0.75$ , where K is the degree of compensation of the sample), the electrons are in potential wells formed around the NC and the electrical conductivity of such a material is very low. With an increase in E, the “heating” of the electronic subsystem begins and, as a result, the population of states with high electron or hole mobility increases sharply. This, in turn, leads to the appearance of an NDR. If  $K < 0.75$ , the CVC will not have an S-shaped form, since the activation energy arises only at high degrees of compensation [10,12]. It should also be added that in this case the critical electric field increases with increasing degree of compensation.

Based on the above, it is possible to explain the presence of N - and S - shaped sections of the CVC in samples of p - and n - type Si<P, Zn> at low temperatures and in the presence of integral illumination. An increase in temperature, of course, in the middle part of the crystal, as a result of Joule heating, causes the effect of thermal quenching of photoconductivity. If the intensity of this process is sufficiently high, then a region of a strong electric field arises near the sample. Then the I–V characteristic of such a sample has a section with NDC [8]. The presence of two sections with NDC can be explained by the presence of two BCs responsible for thermal quenching in the studied samples, the first of which manifests itself at relatively low electric field strengths, and the second at relatively high E.

On the other hand, in order to explain the obtained experimental data, it is also necessary to use the model of a semiconductor with quantum dots (QDs) [13,14]. The presence in the band gap of various traps for charge carriers associated with impurity atoms significantly affects the I–V characteristics of semiconductors. This is especially evident in high-resistance, i.e., compensated semiconductor materials. In this case, instead of the usual Ohm's law, an S- or N-shaped section with a negative resistance appears on the I–V characteristic [15].

Under certain conditions for the time of flight of electrons and holes through the base  $\tau_n$  and  $\tau_p$  (where  $\tau_n$  and  $\tau_p$  are the time of flight of electrons and holes, respectively), the CVC of the samples consists of several sections - linear (at low electric fields), quadratic, and as well as areas of a sharp increase in the current of an almost vertical nature at  $U \approx U_{LFT}$  (where  $U \approx U_{LFT}$  is the minimum voltage that leads to complete filling of traps in the material).

Samples of Si<P, Zn> with NCs with a maximum charge state, obtained by the method of high-temperature diffusion, have a sufficiently high electrical resistivity ( $\rho \approx 10^3 \div 10^5 \Omega \cdot \text{cm}$ ). These NCs act as deep traps for electrons and holes. Unlike conventional traps, where electrons are at a fixed energy level, electrons in NCs are not only bound, but can also be at different quantized energy levels with different density of states and capture cross sections. The distribution of electrons over levels depends on the degree of injection; in addition, the process of tunneling between nanocrystals is possible. Therefore, it can be expected that the I–V characteristics in such materials should have their own features, which was experimentally discovered by the samples of Si<P, Zn> studied by us with NCs.

In p-type samples with NC and with  $\rho_1 \sim 1.5 \cdot 10^2$ ;  $\rho_2 \sim 1.0 \cdot 10^3$ ;  $\rho_3 \sim 1.0 \cdot 10^4 \Omega \cdot \text{cm}$ , uncompensated holes should remain (respectively  $p_1 = 1.8 \cdot 10^{14}$ ;  $p_2 = 1.25 \cdot 10^{13}$  and  $p_3 = 8 \cdot 10^{12} \text{ cm}^{-3}$ ), which should ensure the appropriate conductivity of the material in the area under study temperatures, taking into account the change in the mobility of holes with a change in temperature. However, at a temperature  $T = 80 \text{ K}$ , the resistivity of the samples increases from 3 to 6 orders of magnitude, which means that the hole concentration decreases by the same factor. This conduction behavior can be associated either with the capture of holes and electrons to energy levels lying below the Fermi level at  $T = 300 \text{ K}$ , or with the entry of holes into deep potential wells, limiting their participation in conduction. The absence of any energy levels associated with the zinc atom in the lower half of the bandgap in the range  $E_V < E \leq E_V + 0.3 \text{ eV}$  suggests that both options are not realized [17-19].

Therefore, we assume that holes in the valence band are accumulated between the nearest multiply positively charged NCs of zinc atoms. The depth of potential wells is determined, on the one hand, by the charge multiplicity and the concentration of clusters, and, on the other hand, by the concentration of holes in these wells.

Multicharged clusters act as powerful traps for holes with anomalously large capture cross sections. In the region of low electric fields, the dependence of the current is described as  $I = U^n$ , and the value of n, depending on the resistivity of the samples, varies in the range  $n \sim 0.65 - 1.5$ , i.e., with a decrease in the resistivity of the samples, the I–V characteristic changes from a sublinear character to a superlinear (quadratic) character. A further increase in the electric field leads to a rather strong ‘change in the current, while the value of n increases with a decrease in the resistivity of the samples and changes in the range  $n = 2.2 - 3.2$  i.e., current increases faster than quadratic. At higher electric fields, a sharp increase in

current is observed, almost vertical, i.e., current increases by several orders of magnitude. This type of current-voltage characteristic allows us to assume that currents limited by the space charge (CLSC) with deep traps take place in the samples under study [20,21].

The values of  $U_{LFT}$ , measured in the experiments, increase significantly with the increase in the resistivity of the samples and amount to 15 V, 185 V, and 500 V, respectively. It should also be noted that with a decrease in the resistivity of the samples, the value of  $n$  in the vertical section of the CVC also decreases. Knowing the concentrations of charge carriers at a given temperature, we calculated the positions of the Fermi level in these samples at  $T=80$  K, which are  $F_1=0.15$  eV,  $F_2=0.199$  eV and  $F_3=0.254$  eV, respectively. Therefore, it can be assumed that traps with different concentrations and ionization energies operate in these samples, and they are higher than the Fermi level. If we take into account that the samples under study have p-type conductivity, then it should be assumed that the existing traps are located near the top of the valence band [22,23].

Therefore, it can be assumed that the traps responsible for the effect of limiting trap filling in the samples under study are associated with the energy levels of clusters of zinc atoms, and apparently create a whole spectrum of deep energy levels with ionization energies in the range  $E=(E_V+0.31) \div (E_V+0.55$  eV) [6,16].

An analysis of these results shows that the active traps in the samples under study have different ionization energies and concentrations. If we take into account that the samples under study contain only NCs with different charge multiplicities, then it can be assumed that the detected energy levels correspond to their different charge states.

### 3. CONCLUSIONS

Based on the study of the surface morphology using AFM, as well as the photoelectric properties of the synthesized silicon samples diffusion-doped with zinc, the formation of nanosized multiply charged clusters was established, which significantly changes the structure of the energy states of the zinc atom in silicon. As a result, instead of the well-known, two acceptor energy levels corresponding to atomic zinc, a whole spectrum of deep donor energy levels of zinc nanoclusters appears, lying in the range  $E=E_V+(0.16 \div 0.55)$  eV.

It has been established that the I–V characteristics of the studied samples contain sections characteristic of semiconductors, doped with impurities with deep levels.

For the first time, a CVC type containing two N-shaped sections and one S-shaped section in one sample was discovered.

### ORCID

✉ Eshkuvat U. Arzikulov, <https://orcid.org/0000-0001-9179-3402>

### REFERENCES

- [1] M.K. Bakhadirkanov, N.F. Zikrillayev, and S.B. Isamov, Photoelectric phenomena in silicon with multiply charged nanoclusters (Lambert Academic Publishing, 2019). <https://www.morebooks.shop/shop-ui/shop/product/978-620-0-48701-8> (in Russian)
- [2] M. K. Bakhadyrkanov, and S.B. Isamov, “Energy level spectra of multiply charged nanoclusters of manganese atoms in silicon,” *Elektronnaya obrabotka materialov*, **47**(6), 8-11 (2011). <https://eom.ifa.md/ru/journal/shortview/497> (in Russian)
- [3] V.L. Bonch-Bruevich, I.P. Zvyagin, and A.G. Mironov, in: *Domain electric instability in semiconductors*, (Nauka, Moscow 1972). pp. 36-45. (in Russian)
- [4] M.K. Bachadyrchanov, S.B. Isamov, N.F. Zikrillayev, and E.U. Arzikulov, “Infrared quenching of photoconduction in silicon with multicharge manganese clusters,” *Surf. Engin. Appl. Electrochem.* **49**, 308–311 (2013). <https://doi.org/10.3103/S1068375513040029>
- [5] M.K. Bachadyrchanov, S.B. Isamov, N.F. Zikrillayev, and E.U. Arzikulov, “Effect of Elasticity of Diffusant Vapors on Concentration of Electroactive Atoms and Degree of Compensation of Si (Zn) Models,” *Technical Physics Letters*, **17**(12), 1-4 (1991). <https://journals.ioffe.ru/articles/viewPDF/25973> (in Russian)
- [6] S. Weiss, R. Beckmann, and R. Kassing, “The electrical properties of zinc in silicon,” *Applied Physics A Solids and Surfaces*, **50**(2), 151-156 (1990), <https://doi.org/10.1007/bf00343410>
- [7] A.N. Akimov, V.G. Erkov, E.L. Molodtsova, S.P. Suprun, and V.N. Shumskii, “Injection currents in a narrow-gap dielectric  $Pb_{1-x}Sn_xTe<In>$ ,” *FTP*, **39**(5), 563-568 (2005). <https://journals.ioffe.ru/articles/viewPDF/5796> (in Russian)
- [8] M.A. Lamper,t and R.B. Schilling, “Chapter 1 Current Injection in Solids: The Regional Approximation Method,” *Semiconductors and Semimetals*, **6**, 1-96 (1970), [https://doi.org/10.1016/s0080-8784\(08\)62630-7](https://doi.org/10.1016/s0080-8784(08)62630-7)
- [9] V.E. Lashkarev, A.V. Lyubchenko, and M.K. Sheinkman, *Nonequilibrium Processes in Photoconductors*, (Naukova Dumka, Kyiv, 1981). (in Russian)
- [10] B.I. Shklovsky, and A.L. Efros, in: *Electronic properties of doped semiconductors*, (Science, Moscow, 1979). pp. 123-128. (in Russian)
- [11] A. Rose, in: *Fundamentals of the theory of photoconductivity*, (Foreign Literature, Moscow, 1962). pp. 78-81, pp. 100-113. (in Russian)
- [12] M.K. Sheinkman, and A.Ya. Shik, “Long-term relaxations and residual conductivity in semiconductors,” *Soviet Physics Semiconductors and Devices*, **10**(2), (1976). (in Russian)
- [13] J. Zhang, and B.I. Shklovskii, “Density of States and Conductivity of Granular Metal or Array of Quantum Dots,” *Phys. Rev. B*, **70**, 115317 (2004). <https://doi.org/10.1103/PhysRevB.70.115317>
- [14] N.N. Gerasimenko, and Yu. N. Parkhomenko, in: *Silicon as a material for nanoelectronics*, (Technosfera, Moscow, 2007), pp. 43-45). (in Russian)

- [15] M.K. Bakhadyrkhanov, G.Kh. Mavlonov, S.B. Isamov, Kh.M. Iliev, K.S. Ayupov, Z.M. Saparniyazova, and S.A. Tachilin, "Electrophysical properties of silicon doped with manganese by low-temperature diffusion," *Inorg. Mater.* **47**(5), 479-483 (2011). <https://doi.org/10.1134/S0020168511050062>
- [16] M.K. Bakhadyrkhanov, N.F. Zikrillaev, S.B. Isamov, and K. Khaidarov, "Nanoscale graded-gap structure in silicon with multiply charged nanoclusters," *Microelectronics*, **42**(6), 444 (2013). (in Russian)
- [17] M.A. Rafiq, "Carrier transport mechanisms in semiconductor nanostructures and devices," *Journal of Semiconductors*, **39**(6), 061002 (2018), <https://doi.org/10.1088/1674-4926/39/6/061002>
- [18] V.G. Baskakov, and N.A. Mishustin. Quantomechanical calculation metal-semiconductor contact, in: *IV International scientific-technical forum STSO-2021, Proceedings*, 2, pp.62-65. (in Russian)
- [19] A.S. Chernobrovkina, V.G. Litvinov, V.V. Tregulov, and A.V. Ermachikhin, "Study of current transport mechanisms in por-Si/p-Si semiconductor structures with thick por-Si layer, in: *IV International scientific-technical forum STSO-2021, Proceedings*, pp.74-83. (in Russian)
- [20] S. Boughdachi, Y. Badali, Y. Azizian-Kalandaragh, and Ş. Altındal, "Current-Transport Mechanisms of the Al/(Bi<sub>2</sub>S<sub>3</sub>-PVA Nanocomposite)/p-Si Schottky Diodes in the Temperature Range Between 220 K and 380 K," *J. Electron. Mater.* **47**, 6945-6953 (2018). <https://doi.org/10.1007/s11664-018-6593-y>
- [21] M. Labed, J. Y. Min, A. B. Slim, N. Sengouga, C.V. Prasad, S. Kyoung, and Y.S. Rim, "Tunneling via surface dislocation in W/ $\beta$ -Ga<sub>2</sub>O<sub>3</sub> Schottky barrier diodes," *J. Semicond.* **44**(7), 072801 (2023), <http://dx.doi.org/10.1088/1674-4926/44/7/072801>
- [22] T. Abdulmecit, "On current-voltage and capacitance-voltage characteristics of metalsemiconductor contacts," *Turkish Journal of Physics*, **44**(4), 302-347 (2020). <https://doi.org/10.3906/fiz-2007-11>
- [23] D. Degler, U. Weimar, and N. Barsan, "Current understanding of the fundamental mechanisms of doped and loaded semiconducting metal oxide-based gas sensing materials," *ACS Sens.* **4**(9), 2228-2249 (2019). <https://doi.org/10.1021/acssensors.9b00975>

#### МЕХАНІЗМИ ПЕРЕХІДНОГО СТРУМУ В ВИСОКОКОМПЕНСОВАНИХ ЗРАЗКАХ КРЕМНІЮ З НАНОКЛАСТЕРАМИ ЦИНКУ

Ешқуват У. Арзікулов, М. Раджабова, Ш.Й. Кувондиков, Г. Гулямов

Самаркандський державний університет імені Шарафа Рашидова,

140104, Університетський бульвар, 15, Самарканд, Республіка Узбекистан

У статті наведено експериментальні результати дослідження вольт-амперних характеристик сильнокомпенсованих зразків кремнію n- та р-типу, легованих цинком при температурі 80 К. Вольт-амперні характеристики досліджуваних зразків містять як сублінійні, так і надлінійні ділянки. Виявлено декілька (до восьми) характерних ділянок, кількість яких залежить від освітленості, температури та питомого електроопору зразка. За певних умов відбувається чергування ділянок вольт-амперної характеристики з негативною диференціальною провідністю N- і S-типу, за якими спостерігаються нестабільності струму з інфранизькою частотою. Поява ділянок вольт-амперної характеристики з квадратичною залежністю пояснюється наявністю швидких і повільних центрів рекомбінації, пов'язаних з нанокластерами цинку, а сублінійних ділянок пояснюється в рамках теорії «ефекту інжекційного виснаження». Утворення нанокластерів за участю іонів цинку підтверджено дослідженнями атомно-силової мікроскопії.

**Ключові слова:** компенсований кремній; вольт-амперна характеристика; протікання струму; цинк; нанокластер; негативна диференціальна провідність; сублінійність; надлінійність

## PERMITTIVITY MODEL SELECTION BASED ON SIZE AND QUANTUM-SIZE EFFECTS IN GOLD FILMS<sup>†</sup>

 Iuliia Riabenko<sup>a,b,\*</sup>,  Sergey Shulga<sup>a</sup>, Nikolai A. Makarovskii<sup>c</sup>,  Konstantin Beloshenko<sup>a</sup>

<sup>a</sup>V.N. Karazin Kharkiv National University, School of radiophysics, biomedical electronics and computer systems, Kharkiv, Ukraine

<sup>b</sup>Institute of Quantum Optics, Leibniz University Hannover, Hannover, Germany

<sup>c</sup>V.N. Karazin Kharkiv National University, School of Physics, Kharkiv, Ukraine

\*Corresponding Author: [jriabenko@karazin.ua](mailto:jriabenko@karazin.ua), [riabenko@iqo.uni-hannover.de](mailto:riabenko@iqo.uni-hannover.de)

Received July 9, 2023; revised July 27, 2023; in final form August 2, 2023; accepted August 3, 2023

The article is focused on optical properties of nanostructures containing spherical gold nanoparticles of various radii. We explore correlation between the particle radius and the choice of permittivity model applied to describe optical absorption spectra of gold granules. The experiments show splitting of the absorption band of granular gold films to form a second absorption peak. The first peak is associated with the phenomenon of plasmon resonance, while the second one reflects quantum hybridization of energy levels in gold. Quantum effects are shown to prevail over size effects at a granule diameter of about 5-6 nm. The Mie theory gives a rigorous solution for the scattered electromagnetic field on a sphere taking into account optical properties of the latter, however, it does not specify the criteria for selecting a model to calculate dielectric permittivity. Both calculations and experiments confirm the limiting diameter of gold nanoparticles where the Hampe-Shklyarevsky model is applied. Meanwhile, this model is still unable to predict the splitting of the plasma absorption band. The data presented in the article can be used for a predetermined local field enhancement in composite media consisting of a biolayer and metal nanoparticles. The conducted research provides a deeper understanding of the influence of a terahertz high-intensity electromagnetic field localized in the space on quantum dots.

**Keywords:** *Permittivity; Mie theory; Hampe-Shklyarevsky model; Absorption spectra; Plasma absorption band; Gold granules*

**PACS:** 78.67.\_n, 78.67.Bf, 73.22.\_f, 77.22.Ch, 78.40.Kc, 61.46.Df, 81.07.\_b, 81.07.Ta

### INTRODUCTION

The Mie theory [1] is based on Maxwell equations which describe the fields where a plane monochromatic wave interacts with a spherical surface while physical properties of the latter differ significantly from those of the environment. The main difference lies in dielectric permittivity [2] which depends on the extinction coefficient [3, 4], a parameter measured experimentally.

$$A = A_{abs} + A_{sct} = q\sigma_{ext} = q(\sigma_{abs} + \sigma_{sct}) \quad (1)$$

where  $A$  consists of the absorption coefficient ( $A_{abs}$ ) and the scattering coefficient ( $A_{sct}$ ). It can also be presented as a product of  $q$  and  $\sigma_{ext}$  where  $q$  denotes the particle filling factor (specific volume occupied by particles) and  $\sigma_{ext}$  is the effective cross-section of one particle extinction. The latter is obtained by adding the effective cross-section of absorption by one particle ( $\sigma_{abs}$ ) and the effective cross-section of scattering by one particle ( $\sigma_{sct}$ ).

The choice of the permittivity model for particles which scatter or absorb light determines the effective extinction cross-section. However, it is more challenging to delineate the limits of applicability for a certain model describing permittivity of particles. When the particle radius is much smaller than the irradiation wavelength ( $a \ll \lambda$ ), the formulas for the effective cross section of absorption and scattering are as follows [5]:

$$\sigma_{abs} = 4\pi \frac{\omega}{c} n_0 a^3 \text{Im} \frac{\varepsilon - \varepsilon_0}{\varepsilon + 2\varepsilon_0} \quad (2)$$

$$\sigma_{sct} = \frac{8\pi}{3} \left(\frac{\omega}{c} n_0\right)^4 a^6 \left| \frac{\varepsilon - \varepsilon_0}{\varepsilon + 2\varepsilon_0} \right|^2 \quad (3)$$

Where  $\omega$  is the frequency of the electromagnetic radiation incident on the particle while  $n_0$  refers to the refractive index of the medium surrounding the particle with the radius of  $a$ .

Thus, the effective extinction cross section determines the limits of a particular permittivity model for particles which either absorb or scatter light. For a continuous metal film, the Drude theory [6 - 8] is applied since it describes the reflection spectra well. This theory [6] describes permittivity as follows:

$$\varepsilon = 1 + \frac{\omega_p^2}{-\omega^2 + i\nu\omega} \quad (4)$$

where  $\omega_p = \sqrt{\frac{4\pi n e^2}{m}}$  denotes the plasma frequency of free electrons.

<sup>†</sup> **Cite as:** I. Riabenko, S. Shulga, N.A. Makarovskii, K. Beloshenko, East Eur. J. Phys. 3, 406 (2023). <https://doi.org/10.26565/2312-4334-2023-3-44>  
© I. Riabenko, S. Shulga, N.A. Makarovskii, K. Beloshenko, 2023

This formula is based on the assumption that permittivity only relies on plasma of the free electron gas in the metal rather than size effects. One of the first attempts to record size effects was made by Maxwell Garnet [9] who suggested that metal spherical granules isolated from each other represent dipoles located on a non-absorbing dielectric substrate with  $\varepsilon_0$  permittivity. In this case [10], the effective permittivity of the colloid  $\varepsilon_{ep}$  is described by the following equation:

$$\varepsilon = (n - ik)^2 = 1 + \frac{3q \frac{n_m^2 - 1}{n_m + 2}}{1 - q \frac{n_m^2 - 1}{n_m + 2}} \quad (5)$$

where  $n$  and  $k$  refer to effective optical constants of the colloid while  $n_m$  is the complex refractive index of the substance the granule consists of (assumed to be the same as that of metal).

The Drude theory is applicable to describe the reflection spectra of a continuous metal film [6, 8], where only the free electron gas in the metal contributes to permittivity while size effects are not taken into account. The Maxwell Garnet model [9, 11] used the Lorentz-Lorentz relation [12] to describe the effective permittivity of a colloid, which gives a result inapplicable in the case of a two-dimensional colloid of a granular film. On the other hand, the effective value of the complex dielectric constant of the film depends on the concentration of granules [13, 14], not on their size. Attempting to resolve the contradictions, Hampe [15] experimented with deposition of fine gold particles on fused quartz substrates. After annealing the prepared samples, Hampe used a spectrophotometer and an electron microscope for measurements to show that, despite the fact that annealing does not change the filling factor, the absorption maximum was increasing with a sharper peak as gold particle size was growing, and its position in the spectrum changed. Hampe also suggested that an anomalous absorption band is associated with oscillations of free electrons inside the granules. However, Hampe did not take into account the dipole-dipole interaction between the granules. All of the above ideas were combined in the Hampe-Shklyarevskii theory [16] where the values of the real and imaginary parts of the effective permittivity of a granular film were found to agree with the experiment [17]. This theory describes eigenfrequency as follows:

$$\omega_s^2 = \frac{\omega_p^2}{\varepsilon_m + 2\varepsilon_0} - \frac{\omega_p^2}{3(\varepsilon_m q + (1-q)\varepsilon_0)} \left(\frac{a}{b}\right)^3 S \quad (6)$$

The granule radius ( $a$ ) and the distance between the granules ( $b$ ) and  $S$  as the sum that specifies the coordinates of each dipole granule relative to the origin were taken into account. However, the values obtained did not account for interzone transitions.

Thus, the hypothesis of a hybrid or combined nature of plasma resonance was put forward. Thus, we divided  $\varepsilon_1(\omega)$  [18] into two components, one of which corresponds to free electrons, and the other is related to interband absorption. The paper suggests that gold has zero values of  $\varepsilon_1(\omega)$  at  $\omega \sim 3.2$  eV. Thus, hybrid resonance can be associated with changes in motion of both d- and s-electrons. The presence of such a resonance must depend, in particular, on the oscillator strength and the frequencies of transitions under consideration. Thus, in [19], permittivity formulas were obtained for a colloid containing small metal spheres and optical properties of a colloid containing small silver particles were analyzed.

Based on the classical theory of dispersion, the complex dielectric constant can be represented as:

$$\varepsilon^l(\omega) = 1 + \sum_{i=1}^n \frac{\omega_{pi}^2}{\omega_{0i}^2 - \omega^2 + i\gamma_{0i}\omega} \quad (7)$$

where  $\omega_{0i}$  – natural frequencies of the  $i$ -transition,  $\gamma_{0i}$  – relaxation frequency,  $\omega_{pi}^2 = \frac{4\pi n_i e^2}{m}$  – plasma frequency of the  $i$ -transition with the participation of  $n_i$  electrons ( $n_i = f_i n$  where  $f_i$  – oscillator strength for the  $i$ -transition,  $n$  – total concentration of electrons).

The dielectric constant of the considered environment can be found by adding up the optical properties of the spheres and their environment using the following expression [19]:

$$\varepsilon(\omega) = \varepsilon_0(1 - q) + q \frac{\sum_i (\omega_{si}^2 \Pi_{i \neq j} r_j)}{\prod_i r_i + \sum_i \omega_{si}^2 \Pi_{i \neq j} r_j} \quad (8)$$

where  $r_i = \omega_{0i}^2 - \omega^2 + i\gamma_{0i}\omega$  is the denominator in the  $i$ -term in (7) and  $\omega_{si}^2 = \omega_{pi}^2(1 + 2\varepsilon_0)^{-1}$ . The products and the sum in (8) correspond to the number of oscillators. Based on this formula, the optical properties of a colloids can be calculated if the characteristics of individual oscillators  $\omega_{0i}$ ,  $\omega_{pi}$ ,  $\gamma_{0i}$  are known.

## MATERIAL AND METHODS

Samples were prepared for research according to the method described in detail in [20] with some improvements described below.

The Au film was sprayed onto a SiO<sub>2</sub> substrate in a 10<sup>-7</sup> Torr vacuum by means of evaporation from a boat. The substrate was preliminarily cleaned in potassium dichromate and then treated with ion discharge under low vacuum



conditions (approximately  $10^{-2}$  Torr). The initial film thickness reached 100 nm. For the first time, a specifically modified laser implantation technology was used for thermal treatment of a gold film and partial implantation of gold nanoparticles into the near-surface layer of fused quartz in the most active band from a thermal point of view.

The gold film was exposed to thermal treatment using two lasers which were located on the same optical axis and were heating the sample with the film from both sides. A 10 W Holmium doped yttrium aluminum laser (Ho:YAG) with a wavelength of 2.1  $\mu\text{m}$  irradiated the gold film. The opposite side of the substrate was heated by a 25 W CO<sub>2</sub> laser with a wavelength of 10.6  $\mu\text{m}$ . The temperature gradient in SiO<sub>2</sub> was controlled by a Fluke Ti400 infrared camera with a wavelength range of 8 – 15  $\mu\text{m}$ . The Ho:YAG laser was chosen due to the fact that the emissivity of gold at a wavelength of 2.1  $\mu\text{m}$  is  $\sim 0.4$  [21]. In other words, 40% of the laser radiation is absorbed by the gold film, while 60% is reflected. On the other hand, fused quartz absorbs light at a wavelength of 10.2 – 10.6  $\mu\text{m}$ , which leads to e-fold attenuation of the laser radiation at the depth of about 1– 2 mm. Since the substrates used in the experiment are 5 mm thick, the substrate is heated by the CO<sub>2</sub> laser beam at half the depth. Laser beams are at the same optical axis perpendicular to the substrate which gives an opportunity to heat the sample on both sides creating a local non-equilibrium state necessary to structure the gold film (Fig. 1).

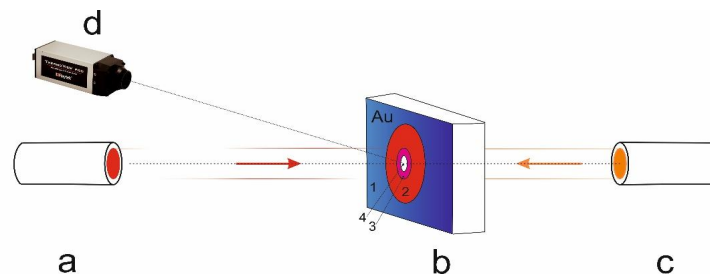


**Figure 1.** Experimental setup to form a nanoparticles cluster structure. a) neodymium-doped yttrium aluminum laser; b) substrate with a film (numbers indicate bands on the sample); c) CO<sub>2</sub> laser; d) Fluke Ti400 infrared camera

The temperature gradient was 384°C per mm. After the exposure time of 15 minutes, pronounced color bands emerged on the surface of the sample in the transmission light. In band 1, the original film before irradiation was of a blue color. In bands 2, 3, 4, we observed a purple color under the temperature of 568°C, a pink color under 974°C, a dark gray under 1214°C, respectively. A Shimadzu UV2600 double-beam spectrophotometer was used to take spectrophotometric measurements for all the four bands. All quartz substrates, both reference samples and samples with applied films, were taken from the same batch, and the relief of the band surface was measured with an 801NER Pro AFM microscope.

### RESULTS AND DISCUSSION

After the exposure of the sample to laser radiation, we detected 4 bands of markedly different colors. The optical properties and dimensions of the film in the bands are shown in Table 1. We carried out spectrophotometry for all the bands (Fig. 2). The surface morphology of each band was examined with an AFM microscope (Fig. 3). The color of the bands depends on the filling factor  $q$  and the size of the cluster structure. It is also determined by whether gold was implanted into the near-surface layer of fused quartz. Gold particles were implanted only in the central band which was confirmed by its chemical and mechanical resistance and stability of the optical properties after the chemical or mechanical impact.

**Table 1.** The optical and dimensional properties of the film in the bands.

Bands	Cluster size	Nanoparticle size	$\omega_s^{exp}$	$\omega_s^{theor}$
Blue	500 nm	10-25 nm	$3.316 \times 10^{15} \text{ s}^{-1}$ 568 nm	$3.25 \times 10^{15} \text{ s}^{-1}$ a~20 nm b~150 nm q=0.1
Purple	300 nm	8-15 nm	$3.443 \times 10^{15} \text{ s}^{-1}$ 547 nm	$3.4 \times 10^{15} \text{ s}^{-1}$ a~10 nm b~30 nm q=0.07
Pink	-	2-6 nm	$3.664 \times 10^{15} \text{ s}^{-1}$ 514 nm	$3.7 \times 10^{15} \text{ s}^{-1}$ a~3 nm b~30 nm q=0.008
Implantation band	500 nm	10-25 nm	$3.316 \times 10^{15} \text{ s}^{-1}$ 568 nm $4.956 \times 10^{15} \text{ s}^{-1}$ 380 nm	$3.25 \times 10^{15} \text{ s}^{-1}$ a~20 nm b~150 nm q=0.1

The initial thickness of the film was calculated to be  $100\text{ nm}$ , which corresponded to a continuous gold film. This fact was confirmed by photometric measurements: curve 1 in Fig. 2 is typical for a gold film. The model used to describe the permittivity is based on the Drude theory. When exposed to laser beams, the films undergo morphological changes which result in plasma resonance bands (curves 2, 3, 4 in Fig. 2).

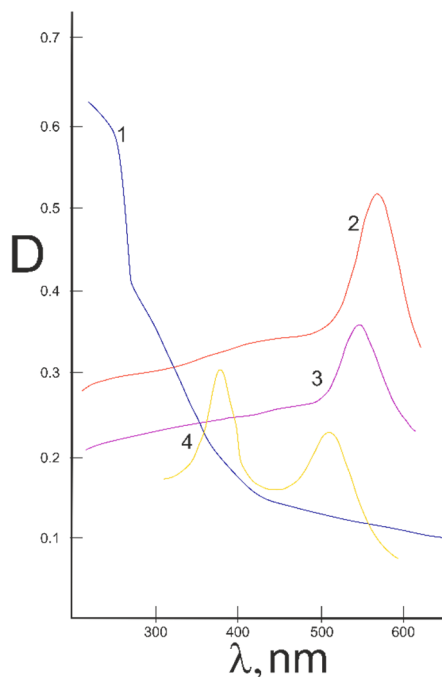


**Figure 2.** Optical density spectrum. 1 – continuous film; 2, 3 – irradiation band; 4 – implantation band

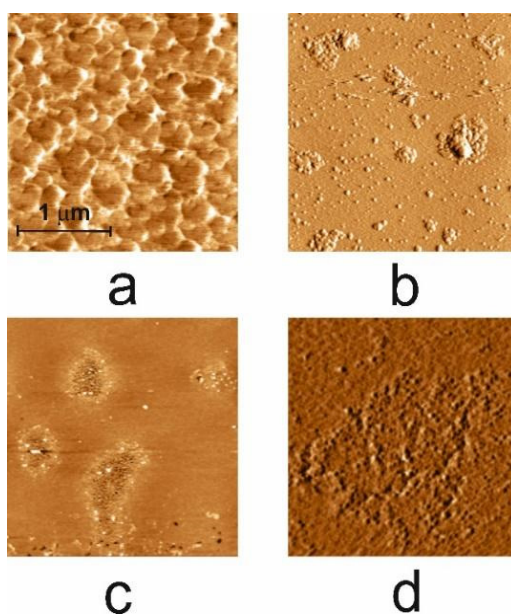


**Figure 3.** AFM micrograph of the sample. a) blue band (polycrystalline gold film); b) purple band (cluster structure with large granules located separately); c) pink band (cluster structure with an increased distance between granules); d) implantation band (“crater” structure with granules implanted in the surface layer)

The AFM micrographs show the structural changes that the film undergoes in different thermodynamic bands. Plasma resonance bands and their positions indicate that a colloid is formed on the substrate surface while gold partially evaporates. The radius of the implanted nanoparticles is shown in Fig. 4 and is about  $3\text{ nm}$ . Importantly, structural changes in the film lead to a shift in the plasma resonance band to an area with a short wavelength, which is well explained by the Hampe-Shklyarevskii theory. However, an additional absorption peak, not associated with plasma resonance, is detected in the central impact band. Instead, it is connected with interband transitions in gold granules. In this case the Hampe-Shklyarevskii theory cannot be applied to describe permittivity of metal granules. Quantum mechanics needs to be involved to describe this phenomenon.

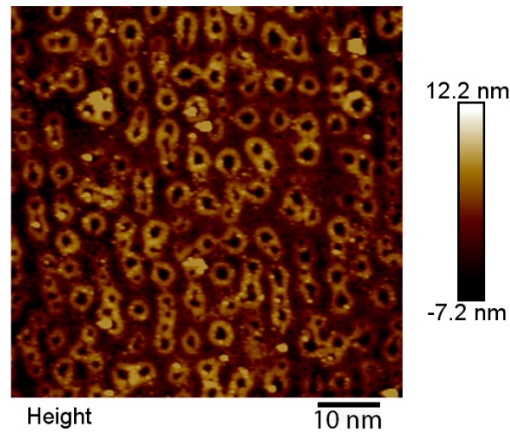


**Figure 4.** AFM micrograph of the optical films implanted in the surface layer.

The experimental technique allowed us to simulate a case when islands with a diameter of about 150 nm exposed to CO<sub>2</sub> radiation transformed into clusters with islands of a 30 nm diameter and with a distance between them equal to their diameter. Further irradiation led to the formation of colloids with a size of about 7 nm and a distance between clusters of approximately 150 nm. It gave an opportunity to study absorption spectra and surface morphology on the same substrate, which resulted in controllability and repeatability of the given parameters, such as the filling factor, the size of nanoparticles, and the distance between them. Plasma resonance frequencies for various parameters of the colloids are given in Table 1. Theoretical calculations were based on formula (6) used to determine the Frohlich frequency taking into account the dipole-dipole interaction between the granules. The permittivity of quartz  $\epsilon_0 = 2.15$  [13] and the permittivity of gold associated with interband transitions  $\epsilon_m = 2.13$  are referred to in [13]. The position of the second maximum cannot be described proceeding from the Hampe-Shklyarevskii model, however, its properties can be based on the energies of the energy levels in the metal granule described in the quantum theory of Sommerfeld [22, 23].

The main objective of the research was to determine applicability of the Hampe-Shklyarevskii theory to describe permittivity of a granular colloid based on the size of granules. The fundamental assumption was the following: the Drude model is applicable if the nanoparticle size is approximately equal to the wavelength; in case of an isotropic colloid, when the distance between granules is much greater than the particle radius, it is the Maxwell Garnett model that can be applied; in case of clusters when this distance is approximately equal to the particle radius, the Hampe-Shklyarevskii model is appropriate. However, the limits of applicability of the latter depend on an increase in interband transitions.

In order to determine the size of nanoparticles on the basis of the permittivity model associated with inter-zone transitions, it can be assumed that the difference in the energies of the levels within the metal granule described in the Sommerfeld theory [22, 24] should be approximately equal to the kinetic energy of the electron on the Fermi surface [25].

The eigenfrequencies of plasmons excited in small spheres can be determined with the following vector equation [19]:

$$Re\{Det[r_i \delta_{ij} \mp \omega_{sj}^2]\} = 0 \quad (9)$$

In the presence of off-diagonal elements in (9), the eigenfrequencies of plasmons differ from  $(\omega_{0i}^2 - \omega_{si}^2)^{1/2}$ , which causes a hybrid resonance whose properties depend on the characteristics of all oscillators determining the optical changes in the environment. The understanding of such changes involves an approach based on quantum mechanics as well as the study of the electron energies in the metal. In this case, possible optical transitions on positive ions that form the core of a metal crystal are taken into account as well as the ionic component of the susceptibility  $\chi_{ion}$  [2]. Thus, the impact of ionic susceptibility on optical transitions in gold can be explained as follows. Au has the  $4f^{14}5d^{10}6s^1$  valence electron configuration [26]. When atoms condense to form a metal, electrons located in  $6s^1$  orbitals turn into free electrons. In crystals, the outer  $4f^{14}5d^{10}$  electrons form energy bands, and optical transitions from the  $5d$  band to the  $5s$  band partially filled with free electrons lead to an additional absorption band with a certain minimum threshold frequency  $\omega_b$  [27]. For gold,  $\omega_b$  lies in the visible area and, if  $\omega_b > \omega$ , the ionic susceptibility is a real value ( $\chi_{ion} > 0$ ). So, the eigenvalue of an electron in metal is determined by the following expression [28]:

$$E = \frac{2\pi^2 \hbar^2}{L^2 m} (l_1^2 + l_2^2 + l_3^2) \quad (10)$$

where  $l_1, l_2, l_3$  – quantum numbers,  $m$  – electron mass,  $L$  – length of the side of a cell, and  $L > a$  – sides of an elementary cell in metal. The abovementioned mathematical equation can be written as follows:

$$\Delta E \sim m v_F^2 \quad (11)$$

where  $v_F = 1.8 \times 10^8$  cm/s – the Fermi velocity (for gold [28])

By substituting (10) into (11) and performing the necessary calculations, we obtain

$$L = 2a \sim \sqrt{2} \frac{\pi \hbar}{mv_F} l \approx 5 \text{ nm} \quad (12)$$

These results agree with the values obtained with the AFM microscope, which showed that an increase in the absorption band associated with interband transitions is observed with a nanoparticle radius of about 3 nm.

### CONCLUSIONS

This paper covers the conditions which allow for applicability of different permittivity models used to describe optical spectra of composites containing gold nanoparticles. The applicability of different models was found to depend on the particle radius. We performed calculations and conducted an experiment to confirm the limiting diameter of gold nanoparticles where the Hampe-Shklyarevsky model is applicable. The article presents a methodology for determining the effects dielectric permittivity of metal nanoparticles is based on. Electrodynamic effects localized in space have generally been considered as dependent on the effects of plasmon-polariton interaction which accounts for the high-frequency peak of the absorption band, the latter being fully explained and well-studied [14, 29]. On the other hand, the effect associated with the interband absorption led to a shift of the plasma absorption band to the low-frequency region [30]. However, a separate absorption band in the low-frequency region, which would be clearly defined, has not been detected in previous studies.

The presented experiment revealed two spectrally separated bands. The high-frequency band shows plasmon-polariton interaction with the incident electromagnetic field, while the low-frequency band illustrates interband transitions in gold. Meanwhile, the experimental technique made it possible to create, on the one hand, films with a high-volume filling factor for the granule material which is important for preserving the amount of absorbed energy by maintaining concentration of the substance; on the other hand, there are spatial regions in the system where quantum mechanical effects prevail. The Hampe-Shklyarevsky model does not predict for such effects. Thus, the implanted granule represents a pair of coupled oscillators [31]. One oscillator is a quantum dot whose resonant frequency coincides with the low-frequency peak, the other is a polariton whose resonant frequency corresponds to the high-frequency peak. The experimental data reveal how the near field affects the quantum mechanics system. Near field measurement techniques are well known in the microwave range [32, 33] but poorly developed in the optical range. The methodology presented in this article is intended to fill the existing gap. The study carried out allows a deeper understanding of the effect of a terahertz high-intensity electromagnetic field localized in space on quantum dots. This technique is relevant for the study of surface-enhanced Raman scattering on a monomolecular biolayer. It is well known that the enhancement of Raman scattering is associated with high-intensity electromagnetic fields localized in the near field where the biolayer is located. No development of biosensors with predetermined metrological properties is impossible without a theoretical calculation of the electromagnetic field localization and experimental verification of the calculated data.

**Competing interests.** The authors did not receive support from any organization for the submitted work.

### ORCID

✉ Iuliia Riabenko, <https://orcid.org/0000-0001-8682-8009>; ✉ Sergey Shulga, <https://orcid.org/0000-0002-9392-9366>  
✉ Konstantin Beloshenko, <https://orcid.org/0000-0002-9387-3147>

### REFERENCES

- [1] M. Born, and E. Wolf, *Principles of optics: electromagnetic theory of propagation, interference and diffraction of light*. (Elsevier, 2013).
- [2] D. Landau, and E.M. Lifshitz, *Electrodynamics of continuous media*, vol. 8. (Elsevier, 2013).
- [3] M. Nic, et al., *IUPAC Compendium of chemical terminology: the gold book*. (International Union of Pure and Applied Chemistry, 2005).
- [4] Saidi, A., SAIJA, R., IATÌ, M. A., & CRUPI, V. Analytical and Numerical Approaches for Light Scattering by Nanostructured Materials (2023). [https://iris.unime.it/retrieve/a22741dc-0562-4982-a0d6-9e10c68db133/Tesi\\_dottorato\\_Saidi.pdf](https://iris.unime.it/retrieve/a22741dc-0562-4982-a0d6-9e10c68db133/Tesi_dottorato_Saidi.pdf)
- [5] H.C. Hulst, and H.C. van de Hulst, *Light scattering by small particles*. (Courier Corporation, 1981).
- [6] R. Gross, and A. Marx, *Solid State Physics*. (Oldenbourg Wissenschaftsverlag Verlag, 2012).
- [7] Snoke, D. W. *Solid state physics: Essential concepts*. (Cambridge University Press 2020).
- [8] Tao, L., Deng, S., Gao, H., Lv, H., Wen, X., & Li, M. Experimental investigation of the dielectric constants of thin noble metallic films using a surface plasmon resonance sensor. *Sensors*, **20**(5), 1505 (2020). <https://doi.org/10.3390/s20051505>
- [9] J.Cl. Maxwell-Garnett, "XII. Colours in metal glasses and in metallic films," *Philosophical Transactions of the Royal Society of London. Series A, Containing Papers of a Mathematical or Physical Character*, **203**, 385-420 (1904).
- [10] R. Ruppin, "Evaluation of extended Maxwell-Garnett theories," *Optics communications*, **182**(4-6), 273-279 (2000). [https://doi.org/10.1016/S0030-4018\(00\)00825-7](https://doi.org/10.1016/S0030-4018(00)00825-7)
- [11] Liu, N., & Jin, Y. Q. A discussion on the effective permittivity of multi-component medium derived by Maxwell-Garnett, strong fluctuation and quasicrystalline-CP modeling. *Waves in Random and Complex Media*, **31**(6), 1921-1930 (2021). <https://doi.org/10.1080/17455030.2020.1711991>
- [12] E. Dobierzewska-Mozrzyms, "Optical Anomalies of Metallic Island Films," *Opt. Appl.* **15**(2), 187-200 (1985).
- [13] Krasavin, A. V. A brief review on optical properties of planar metallic interfaces and films: from classical view to quantum description. *Journal of Physics: Photonics*, **3**(4), 042006 (2021). <https://doi.org/10.1088/2515-7647/ac2569>
- [14] U. Kreibig, and M. Vollmer, *Optical properties of metal clusters*, Vol. 25. (Springer Science & Business Media, 2013).

- [15] W. Hampe, "Beitrag zur Deutung der anomalen optischen Eigenschaften feinstteiliger Metallkolloide in großer Konzentration," *Z. Physik*, **152**, 476–494 (1958). <https://doi.org/10.1007/BF01327751>
- [16] I.N. Shklyarevskii, and T.I. Korneeva, "Optical Constants of Silver Thin Films," *Optics and Spectroscopy*, **31**, 144 (1971).
- [17] I.N. Shklyarevskii, Y.Y. Bondarenko, and N.A. Makarovskii, Plasma resonance in granular gallium films deposited on rough NaCl and KCl single-crystal surfaces. *Opt. Spectrosc.* **88**, 547-550 (2000). <https://doi.org/10.1134/1.626836>
- [18] H.R.P.H. Ehrenreich, and H.R. Philipp, "Optical properties of Ag and Cu," *Physical Review*, **128**(4), 1622 (1962). <https://doi.org/10.1103/PhysRev.128.1622>
- [19] I.N. Shklyarevskii, V.K. Miloslavskiy, and O.N. Yarovaya, "Effect of interband transitions on low-frequency plasma resonance in small metal spheres," *Optica i Spectroscopiya*, **46**(2), 303-309 (1979). (in Russian)
- [20] Zheng, Yu, et al. "Optical properties of colloidal gold nanoparticles implemented into a subsurface layer of fused silica," *Ukr. J. Phys. Opt* **18**(2), 102-108 (2017). <https://doi.org/10.3116/16091833/18/2/102/2017>
- [21] S. Adachi, *Handbook on Optical Constants of Metals, The: In Tables and Figures*, (World Scientific, 2012).
- [22] N.W. Ashcroft, and N.D. Mermin, *Solid state physics*, (Holt, Rinehart and Winston, 1976).
- [23] Galsin, J. S. *Solid state physics: An introduction to theory*, (Academic Press, 2019).
- [24] Schiller, R., & Horváth, Á. Specific heat of metals and standard electrode potentials. *AIP Advances*, **12**(5) (2022). <https://doi.org/10.1063/5.0082443>
- [25] J.M. Ziman, "Electrons in metals: A short guide to the fermi surface," *Contemporary Physics*, **4**(2), 81-99 (1962). <https://doi.org/10.1080/00107516208201722>
- [26] A. Cirri, *Surface Chemical Control over the Valence Electronic Structure of Gold Nanoparticles*. (The Pennsylvania State University, 2016).
- [27] K. Kolwas, and A. Derkachova, "Impact of the interband transitions in gold and silver on the dynamics of propagating and localized surface plasmons," *Nanomaterials*, **10**(7), 1411 (2020). <https://doi.org/10.3390/nano10071411>
- [28] N.W. Ashcroft, and N.D. Mermin, *Solid state physics*, (Cengage Learning, 2022).
- [29] Wang, L., Hasanzadeh Kafshgari, M., & Meunier, M. Optical properties and applications of plasmonic-metal nanoparticles. *Advanced Functional Materials*, **30**(51), 2005400 (2020). <https://doi.org/10.1002/adfm.202005400>
- [30] I.N. Shklyarevskii, N.A. Makarovskii, and A.P. Silka, "Nature of the high-frequency plasma resonance band of granular silver films deposited onto a zinc sulfide sublayer," *Optics and Spectroscopy*, **68**(4), 531-533 (1990). (in Russian)
- [31] J. Wan, K.S. Beloshenko, M. Makarovskiy, I. Riabenko, S. Shulga and S. Prokhorenko, "Resonance light absorption of granular aluminum and silver films placed on a rough sublayer of multilayered ZnS," *Ukr. J. Phys. Opt.* **20**(1), 11 (2019). [http://ifo.lviv.ua/journal/UJPO\\_PDF/2019\\_1/0201\\_2019.pdf](http://ifo.lviv.ua/journal/UJPO_PDF/2019_1/0201_2019.pdf)
- [32] A.S. Kupriianov, V.V. Khardikov, K. Domina, S.L. Prosvirmin, W. Han, and V.R. Tuz, "Experimental observation of diffractive retroreflection from a dielectric metasurface," *Journal of Applied Physics*, **133**(16), 163101 (2023). <https://doi.org/10.1063/5.0145338>
- [33] A. Sayanskiy, A.S. Kupriianov, S. Xu, P. Kapitanova, V. Dmitriev, V.V. Khardikov, and V.R. Tuz, "Controlling high-Q trapped modes in polarization-insensitive all-dielectric metasurfaces," *Phys. Rev. B*, **99**(8), 085306 (2019). <https://doi.org/10.1103/PhysRevB.99.085306>

#### ВИБІР МОДЕЛІ ДИЛЕКТРОНІЧНОСТІ НА ОСНОВІ РОЗМІРНОГО ТА КВАНТОВО-РОЗМІРНОГО ЕФЕКТУ В ПЛІВКАХ ЗОЛОТА

Юлія Рябенко<sup>a,b</sup>, Сергій Шульга<sup>a</sup>, Микола Макаровський<sup>c</sup>, Костянтин Білошенко<sup>a</sup>

<sup>a</sup>Харківський національний університет імені В.Н. Каразіна, Факультет радіофізики, біомедичної електроніки та комп'ютерних систем, Харків, Україна

<sup>b</sup>Інститут квантової оптики Ганноверського університету Лейбніца, Ганновер, Німеччина

<sup>c</sup>Харківський національний університет імені Н. Каразіна, фізичний факультет, Харків, Україна

У статті досліджено оптичні властивості наноструктур, що містять наночастинки золота різного радіусу. Ми досліджуємо радіус частинки як критерій для вибору моделі діелектричної проникності, спрямованої на опис спектрів оптичного поглинання гранул золота. Експерименти показали розщеплення смуги поглинання гранульованих плівок золота з утворенням другого піку поглинання. Перший пік пов'язаний з явищем плазмонного резонансу, а другий відображає квантову гібридизацію енергетичних рівнів у золоті. Було показано, що квантові ефекти переважають над розмірними при діаметрі гранул приблизно 5-6 нм. Теорія Мі дає строгий розв'язок для розсіяного електромагнітного поля на сфері з урахуванням оптичних властивостей останньої, однак не визначає критеріїв вибору моделі для розрахунку діелектричної проникності. І розрахунки, і експерименти підтвердили граничний діаметр наночастинок золота, де застосована модель Хампе-Шкляревського. Тим часом ця модель все ще не могла передбачити розщеплення смуги поглинання. Наведені в статті дані можуть бути використані для заданого локального підсилення поля в композитних середовищах, що складаються з біошару та металевих наночастинок. Проведені дослідження дозволяють глибше зрозуміти вплив локалізованого в просторі електромагнітного поля високої інтенсивності терагерцового діапазону на квантові точки.

**Ключові слова:** діелектрична проникність; теорія Мі; модель Хампе-Шкляревського; спектри поглинання; плазмова смуга поглинання; гранули золота

## AB-INITIO STUDY OF STRUCTURAL, ELECTRONIC AND OPTICAL PROPERTIES OF ZnX (X = Te, S and O): APPLICATION TO PHOTOVOLTAIC SOLAR CELLS<sup>†</sup>

**Faiza Benlakhdar<sup>a,\*</sup>, Idris Bouchama<sup>b,c</sup>, Tayeb Chihi<sup>c,d</sup>, Ibrahim Ghebouli<sup>c,d</sup>, Mohamed Amine Ghebouli<sup>e</sup>, Zohra Zerrougui<sup>e</sup>, Khettab Khatir<sup>f</sup>, Mohamed Alam Saeed<sup>g</sup>**

<sup>a</sup>Electronics Department, Faculty of Technology, University of Setif 1, 19000, Algeria

<sup>b</sup>Electronics Department, Faculty of Technology, University of Msila, Msila, 28000, Algeria

<sup>c</sup>Research Unit on Emerging Materials (RUEM), University Ferhat Abbas of Setif 1, Setif, 19000, Algeria

<sup>d</sup>Laboratory for Elaboration of New Materials and Characterization (LENMC), University of Ferhat Abbas, Setif 19000, Algeria

<sup>e</sup>Laboratory of Surfaces and Interfaces Studies Solid Materials (LESIMS), Department of Technology, Ferhat ABBAS Setif1 University, Setif, Algeria

<sup>f</sup>Department of Electrical Department, Faculty of Technology, University of Msila, Msila, 28000, Algeria

<sup>g</sup>Department of Physics, Division of Science & Technology, University of Education, Lahore, Pakistan

\*Corresponding author e-mail: [benlakhdar228@gmail.com](mailto:benlakhdar228@gmail.com)

Received April 25, 2023; revised June 6, 2023 accepted June 7, 2023

The purpose of this research is to investigate the structural, electronic, and optical properties of ZnX compounds, particularly those with X = Te, S, and O, which have direct bandgaps that make them optically active. To gain a better understanding of these compounds and their related properties, we conducted detailed calculations using density functional theory (DFT) and the CASTEP program, which uses the generalized gradient approximation (GGA) to estimate the cross-correlation function. Our results for lattice modulus, energy bandgap, and optical parameters are consistent with both experimental data and theoretical predictions. The energy bandgap for all compounds is relatively large due to an increase in s-states in the valence band. Our findings suggest that the optical transition between (O - S - Te) - p states in the highest valence band and (Zn - S - O) - s states in the lowest conduction band is shifted to the lower energy band. Therefore, ZnX compounds (X = Te, S and O) are a promising option for optoelectronic device applications, such as solar cell materials.

**Keywords:** ZnTe; ZnS; ZnO; CASTEP; DFT; Density of state; Optical properties

**PACS:** 36.40.Cg, 87.15.Pc, 87.19.rf, 91.60.Pn, 14.60.Cd, 84.60.Jt, 82.47.Jk

### I. INTRODUCTION

Zinc monochalcogenides (ZnX: X = O, S, Se and Te) are considered the prototype of II-VI semiconductors and can crystallize in either the zinc-blende (z) or wurtzite (w) type structures. The ZnX-z phases are optically isotropic, while the ZnX-w phases are anisotropic, with c serving as the polar axis [1]. Due to their optical properties, ZnX phases are considered prime candidates for use in optical devices, such as visual displays, high-density optical memories, transparent conductors, solid-state laser devices, photodetectors, and solar cells [1]. Thus, understanding the optical properties of these materials is crucial in designing and analyzing ZnX-based optoelectronic devices [1]. ZnO, with a wide direct band-gap of approximately 3.37 eV at room temperature, is a typical semiconductor used for optoelectronic applications. It also possesses transparent properties in visible light and is non-toxic since zinc is abundant in the earth [2].

ZnS, ZnSe, and ZnTe are part of a family of IIB-VIA compounds that crystallize in the cubic zinc-blende structure at ambient pressure and have direct energy band-gaps [3]. These wide band-gap semiconductors are of significant interest since they are capable of emitting light even at room temperature [4]. Zinc Telluride (ZnTe) is of particular interest due to its low cost, high optical absorption coefficient, and suitability for use in PV applications [5]. It has also made extensive contributions to the field of microelectronics and optoelectronics applications [6]. Researchers have conducted various studies to investigate the electronic, structural, and dynamic properties of zinc-based semiconductors, such as Agrawal *et al.*, who used ab-initio to calculate these properties [7]. D. Bahri *et al.* investigated the structural, electronic, and optical properties of ZnTe cubic zinc-blende phase with the space group F-43m [8]. J. Serrano *et al.* used ab-initio to study the network dynamics of ZnO [9]. P. Walter *et al.* calculated the electronic energy band structures of ZnTe and ZnSe using the experimental pseudo-voltage method, which included spin-orbit coupling [10].

The focus of current research is on investigating the structural, electronic, and optical properties of ZnX (X = Te, S, and O) for potential photovoltaic applications, using the Density Functional Theory and GGA/PBE gradient approximation.

### II. COMPUTATIONAL DETAILS

In this research, we utilized the CASTEP software [11] to analyze the structural, electronic, and optical characteristics of ZnX compounds, where X denotes Te, S, and O. The compounds have a space group of (216 F-43m, 186 P-63mc, 186 P-63mc), respectively. Through our assessments, we determined that (8×8×8) BZ k-point cell densities and planar wave discontinuities of 750 eV for ZnTe, 850 eV for ZnS, and 800 eV for ZnO were adequate. In general, the

<sup>†</sup> Cite as: F. Benlakhdar, I. Bouchama, T. Chihi, I. Ghebouli, M.A. Ghebouli, Z. Zerrougui, K. Khatir, M.A. Saeed, East Eur. J. Phys. 3, 413 (2023), <https://doi.org/10.26565/2312-4334-2023-3-45>

© F. Benlakhdar, I. Bouchama, T. Chihi, I. Ghebouli, M.A. Ghebouli, Z. Zerrougui, K. Khatir, M.A. Saeed, 2023

GGA approach is preferred over LDA because LDA tends to underestimate the lattice parameters and cell volume, whereas GGA overestimates them. To approximate the GGA method, we used the Perdew-Burke-Ernzerhof [12] approach to estimate the band gap. We conducted geometric optimization with a precision of  $1 \times 10^{-5}$  eV/atom and we used the Broyden-Fletcher-Goldfarb-Shanno (BFGS) algorithm to relax at the lowest energy levels, with force, pressure, and displacement values set at 0.001 eV/Å, 0.05 GPa, and  $5.0 \times 10^{-4}$  Å, respectively. We examined the electronic structures and other optical properties using total and partial densities of states, such as TDOS and PDOS, to achieve a more refined geometry.

### III. RESULTS AND DISCUSSIONS

#### a. Structural Properties

In the first stage of our study, we performed calculations to determine the equilibrium structural parameters of ZnX (X = Te, S, and O), including the lattice constant  $a_0$ , size modulus  $B_0$ , and its first derivative  $B_0'$ . The crystal structure of ZnX (X = Te, S, and O) is shown in Fig. 1. We focused on investigating the structural properties of ZnX and optimizing the lattice constants, and the results are presented in Table 1. The accuracy and validity of our research are confirmed by comparing our findings with existing theoretical and experimental data (as shown in Table 1). Our calculations show that the lattice constant  $a_0$  is 6.28 Å for ZnTe, 5.62 Å for ZnS, and 3.25 Å for ZnO. These values are slightly larger than the experimentally recorded values of 6.1 Å [13], 5.41 Å [13], and  $a = 3.249$  Å,  $c = 5.204$  Å [9], respectively. However, this discrepancy can be attributed to the difference in the atomic radii of ZnTe, ZnS, and ZnO, as well as the larger total energies, lattice relaxation constants, volume coefficients, and ground state energy of each material.

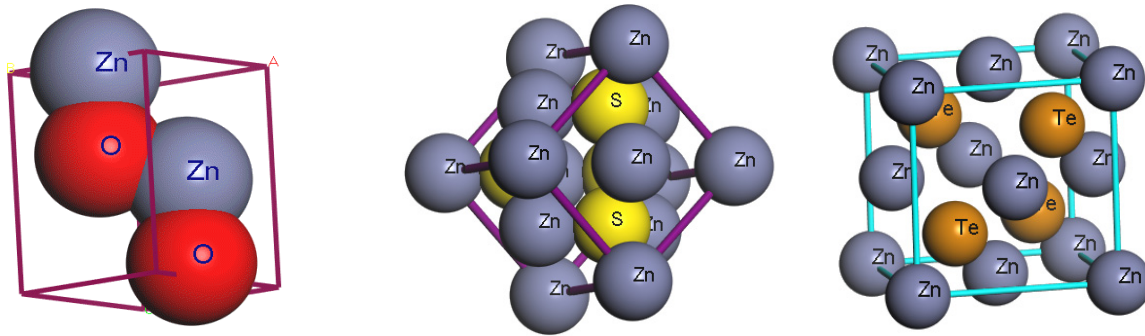


**Figure 1.** Crystal structures of: (a) ZnTe, (b) ZnS and (c) ZnO compounds.

We have optimized the structures of ZnTe, ZnS and ZnO at different pressure by fitting the Murnaghan equation of state [14], which gives the variation of the total energy as a function of the volume and given by:

$$E(V) = E_0 + \left[ \frac{B_0 V}{B'(B'-1)} \right] \cdot \left[ B' \left( 1 - \frac{V_0}{V} \right) + \left( \frac{V_0}{V} \right)^{B'} - 1 \right] \quad (1)$$

where  $V_0$ ,  $B$  and  $B'$  are the volume at equilibrium, the bulk modulus and its derivative. The modulus of compressibility and its pressure derivative  $B_0'$  written as follows:

$$B_0' = \frac{\partial B}{\partial P} \quad (2)$$

The fits of our data regarding the relative lattice constant  $a_0$  (Å), bulk modulus  $B_0$  (GPa) and the volume are given in Table 1.

**Table 1.** Calculated lattice constant  $a_0$  (Å), bulk modulus  $B_0$  (GPa) for ZnX (X = Te, S and O) compound compared with already published data.

Compound	$a_0(\text{Å})$	$V(\text{Å}^3)$	$B_0(\text{GPa})$	$B_0'$
ZnTe	6.28 <sup>n</sup>	61.986 <sup>n</sup>	41.30 <sup>n</sup>	4.266 <sup>n</sup>
	6.187 <sup>d</sup>	52.66 <sup>b</sup>	49.70 <sup>b</sup>	4.45 <sup>b</sup>
	6.103 <sup>i</sup>	52.96 <sup>c</sup>	51.40 <sup>c</sup>	4.50 <sup>c</sup>
	6.16 <sup>e</sup>	56.73 <sup>j</sup>	55.21 <sup>h</sup>	4.60 <sup>h</sup>
	6.00 <sup>h</sup>	58.73 <sup>b</sup>	45.20 <sup>j</sup>	4.63 <sup>j</sup>
	6.17 <sup>b</sup>	56.82 <sup>b</sup> Exp.	45.25 <sup>b</sup>	4.26 <sup>b</sup>
	6.1 <sup>e</sup> Exp		50.9 <sup>h</sup> Exp.	5.04 <sup>h</sup> Exp.
ZnS	5.62 <sup>n</sup>	44.60 <sup>n</sup>	62.043 <sup>n</sup>	4.094 <sup>n</sup>
	5.451 <sup>d</sup>		75.6 <sup>e</sup>	4.44 <sup>h</sup>
	5.44 <sup>e</sup>		89.67 <sup>h</sup>	4.00 <sup>h</sup> Exp.
	5.342 <sup>h</sup>		75 <sup>h</sup> Exp.	
	5.41 <sup>e</sup> Exp			

Compound	$a_0(\text{\AA})$	$V(\text{\AA}^3)$	$B_0(\text{GPa})$	$B'_0$
ZnO	$3.250^n$	$55.126^n$	$115.923^n$	$4.486^n$
	$a = 3.244^d$	$45.82^d$	$159.5^g$	$4.5^g$
	$c = 5.027^d$	$47.719^f$	$128.72^i$	$4.38^i$
	$a = 3.249^f$	$49.461^k$	$183^g \text{ Exp.}$	$4^g \text{ Exp.}$
	$c = 5.216^f$	$48.335^k \text{ Exp.}$		
	$a = 3.198^g$			
	$c = 5.167^g$			
	$a = 3.2496^g \text{ Exp.}$			
	$c = 5.2042^g \text{ Exp.}$			

<sup>a</sup>Ref [15], <sup>b</sup>Ref [16], <sup>c</sup>Ref [17], <sup>d</sup>Ref [1], <sup>e</sup>Ref [13], <sup>f</sup>Ref [18], <sup>g</sup>Ref [9], <sup>h</sup>Ref [3], <sup>i</sup>Ref [19], <sup>j</sup>Ref [17], <sup>k</sup>Ref [20], <sup>l</sup>Ref [2]

<sup>n</sup> Present calculations.

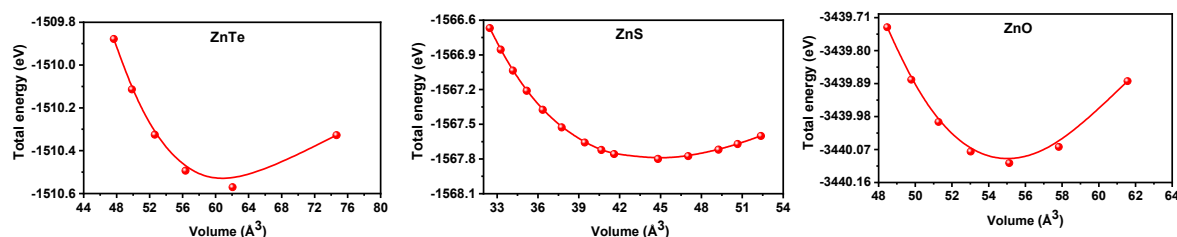


Figure 2. Total energy versus volume for ZnX (X = Te, S and O) compounds.

### b. Electronic properties

The band structure and the total density of states (TDOS) and partial density of states (PDOS) calculated with optimized values were utilized to examine the electronic properties of ZnX (X = Te, S and O). The band-gap energy, particularly, provided insights into the bonding nature. The PBE-GGA approximation was used in the calculations. The computed band-gap of the three compounds revealed that all were semiconducting in nature, as illustrated in Fig. 3. In addition, the direct band-gap values for ZnX (X = Te, S and O) were 2.436, 2.698, and 1.721 eV, respectively. The conduction and valence bands were situated above and below the Fermi level. Both the bottom of the conduction band and the top of the valence band were located at the same point k (G - G), confirming that ZnX (X = Te, S and O) is a direct band-gap. All the calculated band-gap values for ZnX (X = Te, S and O) at 0 GPa are presented in Table 2. All values shown in Table 2 are consistent with theoretical and experimental data reported in other references that employ the PBE-GGA approximation. It is worth noting that the calculated band-gaps were lower than experimental values, which is attributed to the known Kohn-Sham DFT calculation error. The relatively higher band-gap energy of ZnTe, ZnS and ZnO compounds suggests that these compounds could potentially exhibit enhanced optical properties.

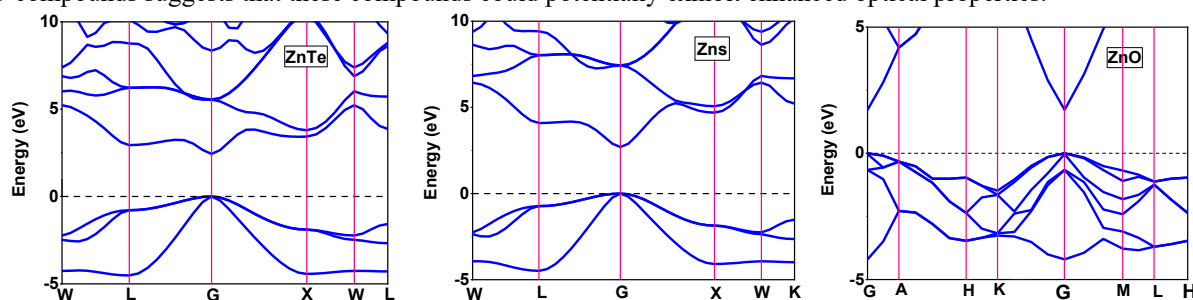


Figure 3. Calculated band structure of ZnX (X = Te, S and O) compounds using PBE-GGA approximation.

Table 2. Calculated band-gap value of ZnX at 0 GPa.

Compound	This work	Other theoretical calculations	Experiments
ZnTe	$2.436^n$	$1.711^d$	$2.39^f$
		$1.804^f$	
ZnS	$2.698^n$	$2.07^e$	$3.68^h$
		$2.11^g$	
		$1.317^h$	
ZnO	$1.721^n$	$0.8^a$	
		$3.38^c$	
		$0.73^k$	
		$3.37^l$	

<sup>a</sup>Ref [21], <sup>c</sup>Ref [18], <sup>d</sup>Ref [22], <sup>e</sup>Ref [23], <sup>j</sup>Ref [24], <sup>k</sup>Ref [25], <sup>g</sup>Ref [26], <sup>h</sup>Ref [27], <sup>l</sup>Ref [28], <sup>n</sup> Present calculations.



### c. Density of States

To better understand the band and optical properties of ZnX (X = Te, S and O), it is important to investigate the electronic density of states (DOS) [29] and its relationship with the band structure. In this study, the DOS was determined and its connection with the band structure was examined. The chemical bonding of ZnX was illustrated by counting single atoms using partial DOS (PDOS) and all atoms using total DOS (TDOS). The electronic DOS is a crucial electronic property as it provides a deeper understanding of the band structure. Fig. 4 shows the TDOS and PDOS obtained using the GGA-PBE approximation, with the Fermi level taken as the energy origin. The electron configuration of Zn, Te, S, and O were 3d<sup>10</sup>4s<sup>2</sup>, 3s<sup>2</sup>3p<sup>6</sup>, 4s<sup>2</sup>4p<sup>6</sup>5s<sup>2</sup>, and 2s<sup>2</sup>2p<sup>4</sup>, respectively. There are two regions, BV and BC, on both sides of the Fermi level: the BV region, dominated by Te-p, S-p, and O-p states, is centered between -5 eV and 0 eV for all three compounds. The second region, BC, centered between 0 eV and 5 eV, is dominated by Zn-s-p, Te-s-p, and S-s-p states. These results are consistent with previous reports.

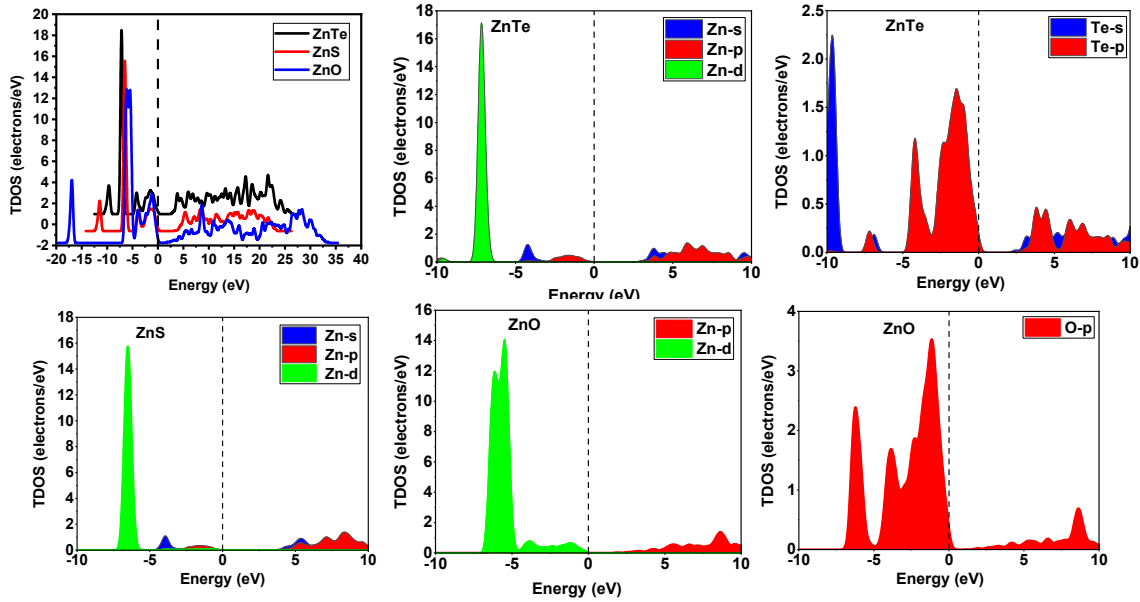


Figure 4. TDOS and PDOS spectra calculated using GGA-PBE approximation of ZnX (X = Te, S and O) compounds.

### d. Optical Properties

The investigation of photonic properties is crucial for the studied compounds, as they have potential applications in photovoltaic devices and the semiconductor industry. To describe the optical properties of these materials, the transverse dielectric function  $\epsilon(\omega)$  [30] is used. The frequency-dependent dielectric constants have been calculated using the following formula:

$$\epsilon(\omega) = \epsilon_1(\omega) + i.\epsilon_2(\omega) \quad (3)$$

The dielectric function is characterized by the real and imaginary parts,  $\epsilon_1(\omega)$  and  $\epsilon_2(\omega)$ , respectively [31]. The real part of  $\epsilon_1(\omega)$  corresponds to the dispersion of incident photons by the material, while the imaginary part of  $\epsilon_2(\omega)$  represents the energy absorbed by the material. The complex dielectric function  $\epsilon(\omega)$  is made up of two contributions: intraband and interband transitions [31]. The contribution from intraband transitions is significant only for metals. The interband transitions can be further divided into direct and indirect transitions. In this study, the indirect interband transitions, which involve phonon scattering and contribute minimally to  $\epsilon(\omega)$ , were neglected.

The complex dielectric function components were utilized to determine other optical parameters, including reflectivity R, refractive index n, optical conductivity  $\sigma$ , and absorption  $\alpha$  [32]. The equations used to calculate these parameters are as follows:

$$R(\omega) = \frac{(n-1)^2 + k^2}{(n+1)^2 + k^2} \quad (4)$$

$$n(\omega) = \frac{\sqrt{\epsilon_1^2(\omega) + \epsilon_2^2(\omega)} + \epsilon_1(\omega)}{\sqrt{2}} \quad (5)$$

$$Re[\sigma(\omega)] = \frac{\omega}{4\pi} \epsilon_2(\omega) \quad (6)$$

$$\alpha(\omega) = \sqrt{2}(\omega) \left[ \sqrt{\epsilon_1^2(\omega) + \epsilon_2^2(\omega)} - \epsilon_1(\omega) \right]^{\frac{1}{2}} \quad (7)$$

Fig. 5 through 9 depict various optical properties of ZnX (X = Te, S and O), including reflection spectra, absorption spectra, imaginary and real parts of the dielectric function, and photoconductivity.

### 1. Reflectivity R

The reflectivity  $R$  of a compound  $ZnX$  (where  $X = Te, S, \text{ or } O$ ) can be accurately predicted using computational tools such as the CASTEP program. For example, CASTEP simulations have shown that  $ZnTe$  exhibits a high reflectivity of approximately 96% in the infrared region, which makes it a promising material for infrared detectors and solar cells. Similarly,  $ZnS$  and  $ZnO$  have been found to exhibit high reflectivity in the visible and ultraviolet regions, respectively, with values reaching up to 87% and 96%. By tuning the composition and morphology of  $ZnX$  compounds, researchers can manipulate their reflectivity to suit specific applications. For instance, by growing  $ZnO$  thin films with a specific orientation, researchers can achieve high reflectivity of visible light while maintaining transparency.

Our analysis, as presented in Fig. 5, reveals that the reflectivity peaks of  $ZnTe$ ,  $ZnS$ , and  $ZnO$  compounds increase at low energy (up to 7 eV), and decrease significantly at high energy (below 20 eV), as the forbidden bandwidth reduces.

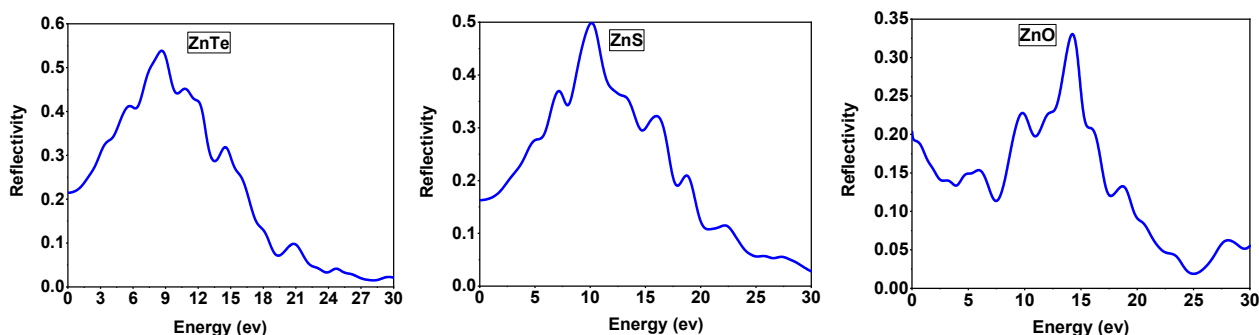


Figure 5. Reflectivity  $R$  as a function of energy of  $ZnTe$ ,  $ZnS$  and  $ZnO$  compounds calculated using GGA-PBE approximation.

### 2. Absorption A

The absorption, denoted by  $A$ , is an important optical property of materials that describes the amount of light absorbed by the material. The absorption of  $ZnX$  compounds, where  $X$  can be  $Te, S, \text{ or } O$ , can be accurately predicted using computational tools such as the CASTEP program. The results have shown that  $ZnTe$  has a high absorption coefficient of approximately  $25 \times 10^4 \text{ cm}^{-1}$  in the mid-infrared region, making it a promising material for mid-infrared detectors and emitters. Similarly,  $ZnS$  and  $ZnO$  have been found to exhibit high absorption in the ultraviolet and visible regions, respectively, with values reaching up to  $3 \times 10^5 \text{ cm}^{-1}$ . By understanding the absorption properties of  $ZnX$  compounds, researchers can design materials with specific absorption properties for various optoelectronic applications.

According to our study, when more electrons can be easily excited from the valence band to the conduction band, less energy is required, resulting in a redshift at the absorption edge. In this scenario, the probability of valence band electron guide transitioning to the excited state increases, leading to an obvious increase in the number of absorption peaks. Our findings, presented in Fig. 6, indicate that the maximum transmittance for  $ZnX$  ( $X = Te, S, \text{ and } O$ ) occurs in the energy regions between 0 eV and 5 eV, which are located in the infrared region.

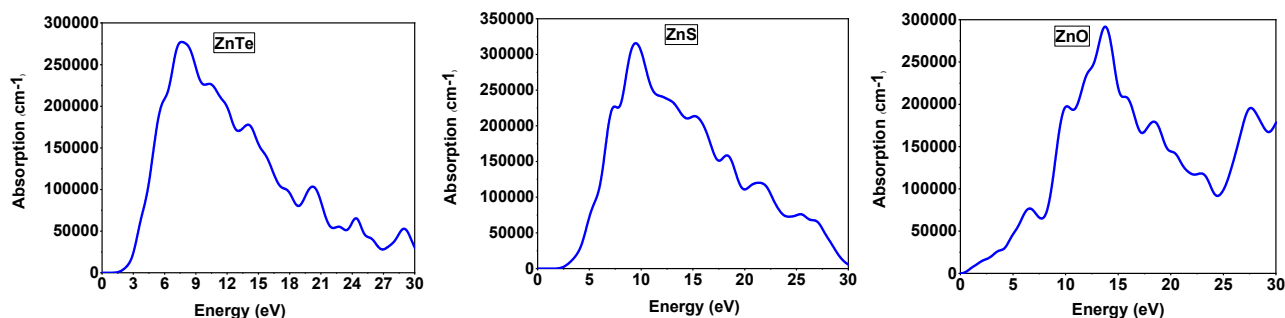


Figure 6. Absorption  $A$  as a function of energy of  $ZnTe$ ,  $ZnS$  and  $ZnO$  compounds calculated using GGA-PBE approximation

### 3. Refractive index

The refractive index, denoted by  $n$ , is an important optical property that characterizes how light propagates through a material. The refractive index of  $ZnX$  compounds, where  $X$  can be  $Te, S, \text{ or } O$ , can be accurately predicted using computational tools such as the CASTEP program. We have shown that the refractive index of  $ZnTe$  is approximately 2.5 in the mid-infrared region, making it a promising material for applications such as infrared lenses and waveguides. Similarly,  $ZnS$  and  $ZnO$  have been found to exhibit high refractive indices in the ultraviolet and visible regions, respectively, with values reaching up to 2 and 1.9. By understanding the refractive index of  $ZnX$  compounds, researchers can design materials with specific optical properties for various optoelectronic applications.

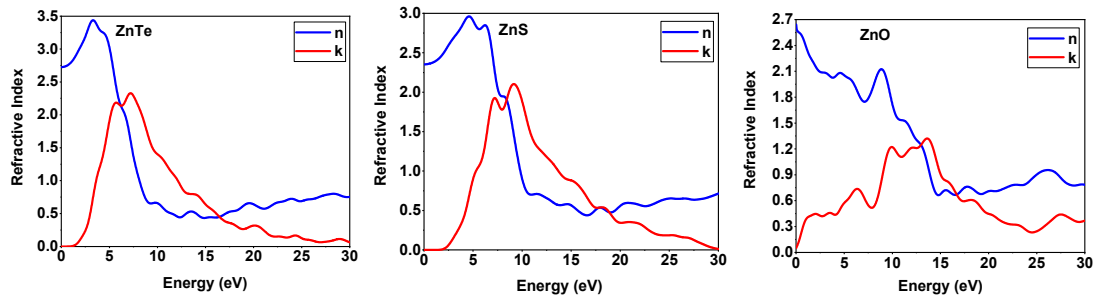


Figure 7. Refractive index as a function of energy of ZnTe, ZnS and ZnO compounds calculated using GGA-PBE approximation.

#### 4. Dielectric function

The dielectric function, denoted by  $\epsilon$ , is an important optical property that characterizes the response of a material to an external electric field. The simulation results using CASTEP have shown that the dielectric function of ZnTe is approximately 12 in the mid-infrared region, making it a promising material for applications such as infrared detectors and emitters. Similarly, ZnS and ZnO have been found to exhibit high dielectric functions in the ultraviolet and visible regions, respectively, with values reaching up to 9 and 5. By understanding the dielectric function of ZnX compounds, researchers can design materials with specific optical properties for various optoelectronic applications.

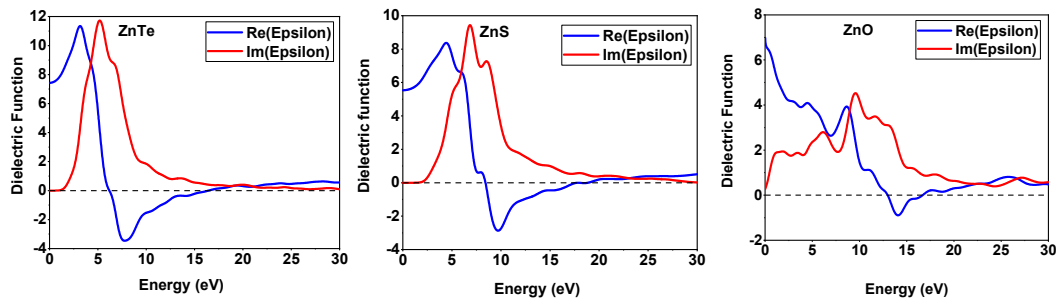


Figure 8. Dielectric function as a function of energy of ZnTe, ZnS and ZnO compounds calculated using GGA-PBE approximation.

#### 5. Conductivity

The conductivity, denoted by  $\sigma$ , is an important electronic property that characterizes the ability of a material to conduct electric current. The conductivity of ZnX can be accurately predicted using computational tools such as the CASTEP program. The simulation results have shown that ZnTe has a high electrical conductivity of approximately 7 S/m at room temperature, making it a promising material for applications such as solar cells and thermoelectric devices. ZnS and ZnO materials exhibit moderate to high electrical conductivity, respectively, with values reaching up to 9 and 5 S/m.

Finally, based on the current findings, it can be inferred that the ZnX ( $X = \text{Te, S and O}$ ) materials show promising potential as suitable options for optical and photovoltaic devices.

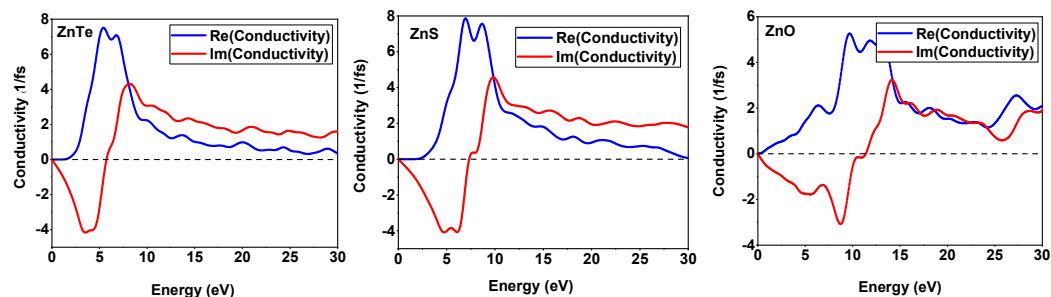


Figure 9. Conductivity as a function of energy of ZnTe, ZnS and ZnO compounds calculated using GGA-PBE approximation.

#### IV. Application to the substrate Cu(In,Ga)Se<sub>2</sub> solar cells

The conventional method of fabricating Cu(In,Ga)Se<sub>2</sub> (CIGS) thin-film solar cells involves the use of a substrate configuration that incorporates a CdS buffer layer and a doped ZnO or ITO window layer. This configuration has demonstrated conversion efficiencies exceeding 22% [29]. The exceptional optoelectronic properties of ZnX ( $X = \text{Te, Se, S ... etc}$ ) buffer layers have led to increased attention as a potential alternative to CdS buffer layers in recent years [33]. It is widely believed that the buffer layers play a critical role in preventing shunting through the TCO/CIGS interface, and they should possess suitable properties that help to minimize carrier recombination at the buffer/CIGS interface [34]. For

example, the efficiency of CIGS solar cells decreases significantly due to severe shunting when a conventional ZnO/TCO is directly deposited onto the CIGS layer [35]. According to some studies, the buffer layer demonstrated a higher level of electrical resistance compared to the top contact layer, which is highly conductive [30]. In this study, the use of ZnTe and ZnS as buffer layers in the substrate CIGS solar cell, along with the incorporation of the ZnO layer as a window layer, were investigated.

**IV.1. Device settings and simulation process**

Fig. 10 shows schematic of the substrate n<sup>++</sup>-ZnO/n-ZnS/p-Cu(In,Ga)Se<sub>2</sub> and n<sup>++</sup>-ZnO/n-ZnTe/p-Cu(In,Ga)Se<sub>2</sub> solar cell hetero-structures. To study the transport physics of these structures, the SCAPS-1D software solution solves the dipolar issues of the device using the Poisson equation and continuity equations for both electrons and holes. The SCAPS-1D simulator provides a software environment that can accurately replicate the behavior of a real solar cell [32,36]. Typically, the simulation process for a solar cell would require following the steps outlined in Fig. 11 through a series of screen-shots. The initial screenshot, labeled (a), displays the standard information input panel of the SCAPS-1D graphical user interface. This panel provides access to input buttons that enable the user to specify the simulation model and view the device's operating conditions, structure, and material parameters. The device simulation utilizes DOS mode. One particular layer's structure and material parameters, along with optical properties and defects, are displayed in screenshot (b). The results of light J-V characteristics in the form of a curve and axes are shown in screenshot (c). The simulation uses AM1.5 illumination spectrum with an incident power of 100 mW/cm<sup>2</sup>. Table 3 summarizes the input parameters of each layer, including thickness, permittivity constant, band gap, electron affinity, electron/hole mobility, effective density of states in conduction/valence band, donor/acceptor concentration, defect concentration, and absorption coefficient within a range of 320 - 1100 nm wavelength. The thermal velocity recombination for holes/electrons at front and back contacts is 1.0 × 10<sup>7</sup> cm/s.

All data that have been previously calculated using CASTEP are being considered in the simulation.

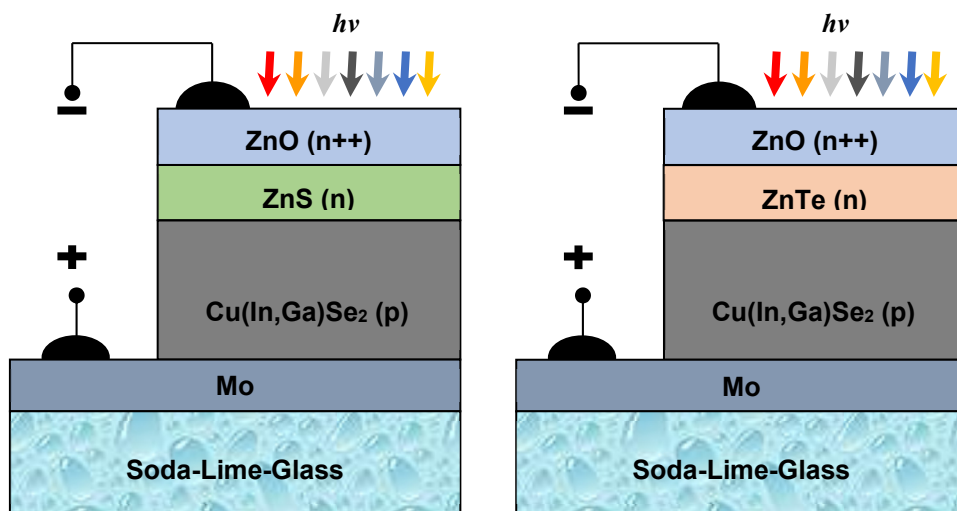
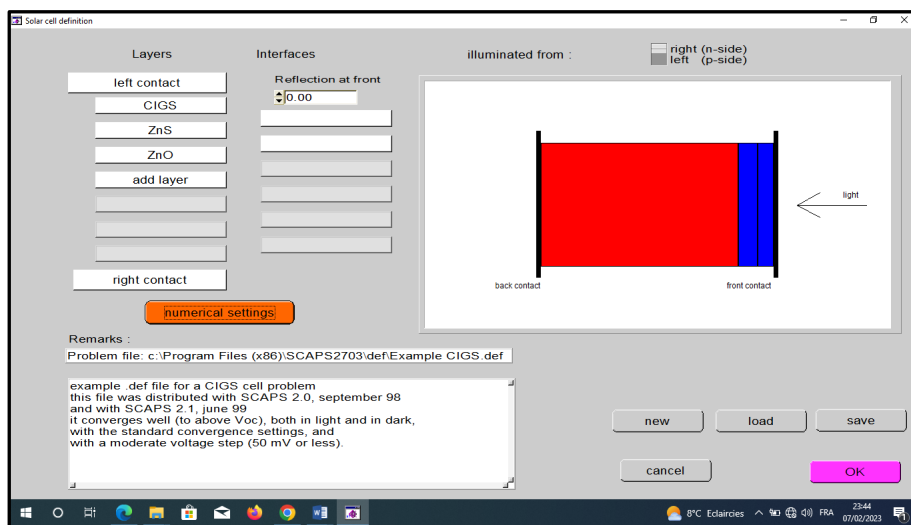
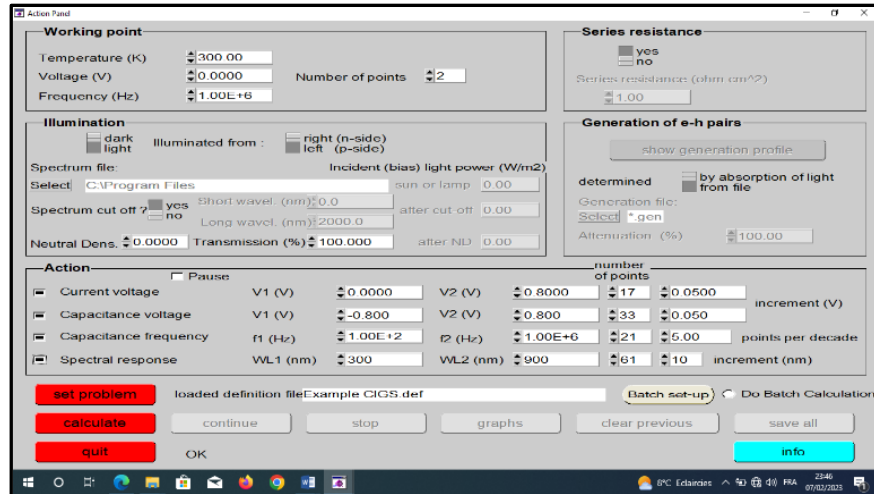


Figure 10. Schematic of the n<sup>++</sup>-ZnO/n-ZnS/Cu(In,Ga)Se<sub>2</sub> and n<sup>++</sup>-ZnO/n-ZnTe/Cu(In,Ga)Se<sub>2</sub> solar cell structures

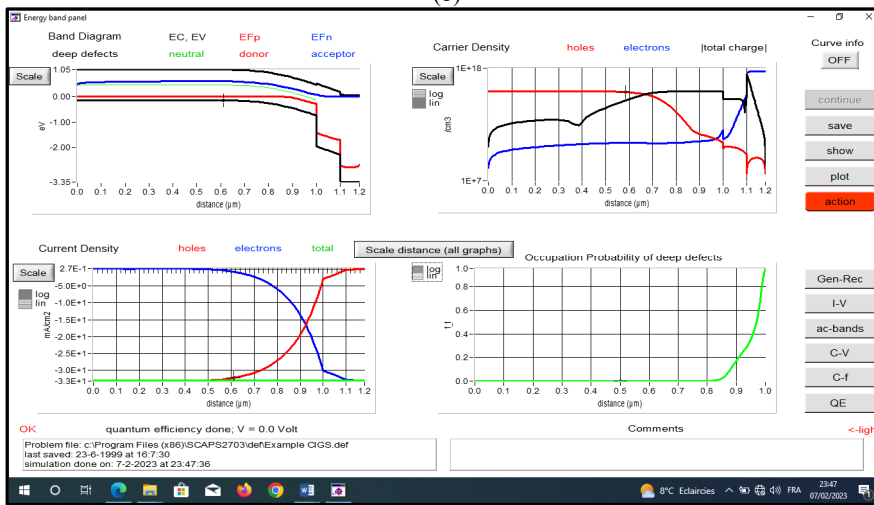


(a)

Figure 11. Typical data input panels of the SCAPS-1D graphical user interface, allowing to configure the solar cell device and its corresponding settings (continued on the next page)



(b)



(c)

Figure 11. Typical data input panels of the SCAPS-1D graphical user interface, allowing to configure the solar cell device and its corresponding settings (continued)

Table 3. Settings for ZnO, ZnTe, ZnS and Cu(In,Ga)Se<sub>2</sub> layers used in the simulation.

Parameters	Cu(In,Ga)Se <sub>2</sub> Absorber	ZnTe buffer	ZnS buffer	ZnO window
Thickness (nm)	3000	100	100	200
Band gap $E_g$ (eV)	1.12	2.43	2.69	3.3
Electron affinity $\chi_e$ (eV)	4.1	4.07	4.09	4.09
Relative permittivity $\epsilon_r$ (-)	13.6	10	10	9
Electron mobility $\mu_n$ (cm <sup>2</sup> /V s)	100	100	100	100
Electron mobility $\mu_p$ (cm <sup>2</sup> /V s)	25	25	25	25
Conduction band effective density of states $N_c$ (cm <sup>-3</sup> )	$2.0 \times 10^0$	$2.0 \times 10^0$	$2.0 \times 10^0$	$4.0 \times 10^0$
Conduction band effective density of states $N_v$ (cm <sup>-3</sup> )	$2.0 \times 10^0$	$1.5 \times 10^0$	$1.5 \times 10^0$	$9.0 \times 10^0$
shallow donor density (1/cm <sup>3</sup> )	0	$1.0 \times 10^0$	$1.0 \times 10^0$	$1.0 \times 10^0$
shallow acceptor density (1/cm <sup>3</sup> )	$5.5 \times 10^0$	0	0	0

<sup>o</sup> Ref [37], <sup>p</sup> Ref [31], <sup>q</sup> Ref [38], <sup>r</sup> Ref [39].

## IV.2. Effect of CIGS absorber thickness on solar cell performance

In an attempt to determine the most favorable thickness for a high-performance substrate CIGS solar cell that employs ZnTe and ZnS buffer layers, the thickness of the CIGS absorber was modified.

### 1. Case of ZnO/n-ZnS/p-CIGS/Mo solar cell structure

It is desirable to reduce the thickness of the absorber layer,  $d(\text{CIGS})$ , in order to lower costs while still maintaining high performance. ZnTe and ZnS buffer layers can help achieve this goal due to the abundance of these materials. In the

calculations, the thickness of the buffer layers is fixed at 100 nm. As shown in Fig. 12, the short-circuit current density ( $J_{sc}$ ), open circuit voltage ( $V_{oc}$ ), Fill Factor ( $FF$ ), and power conversion efficiency ( $\eta$ ) are all affected by the thickness of the CIGS absorber layer. For absorber thicknesses up to 4  $\mu\text{m}$ ,  $J_{sc}$  remains around 32.1  $\text{mA}/\text{cm}^2$  and  $V_{oc}$  is above 0.61 Volt. However, for the thinnest CIGS absorber layer, there is a slight reduction in  $V_{oc}$  which may be due to an increased influence of recombination at the Mo back contact layer, resulting in a smaller effective minority carrier lifetime. The fill factor slightly increases but remains above 79% for all absorber thicknesses greater than 4  $\mu\text{m}$ . The short-circuit current density and open circuit voltage show a strong dependence on the absorber thickness,  $J_{sc}$  increases from 29.12  $\text{mA}/\text{cm}^2$  to 32.08  $\text{mA}/\text{cm}^2$  as the CIGS absorber thickness varies from 1 to 4  $\mu\text{m}$ . For devices thinner than 1  $\mu\text{m}$ , current loss may be due to optical and/or electrical losses. The losses in  $J_{sc}$  and  $V_{oc}$  mainly contribute to the conversion efficiency losses. The optimum thickness for the CIGS absorber layer is greater than 4  $\mu\text{m}$ , which results in a maximum conversion efficiency of 15.6% with  $FF = 78.5\%$ ,  $V_{oc} = 0.61$  Volt and  $J_{sc} = 32.1$   $\text{mA}/\text{cm}^2$ .

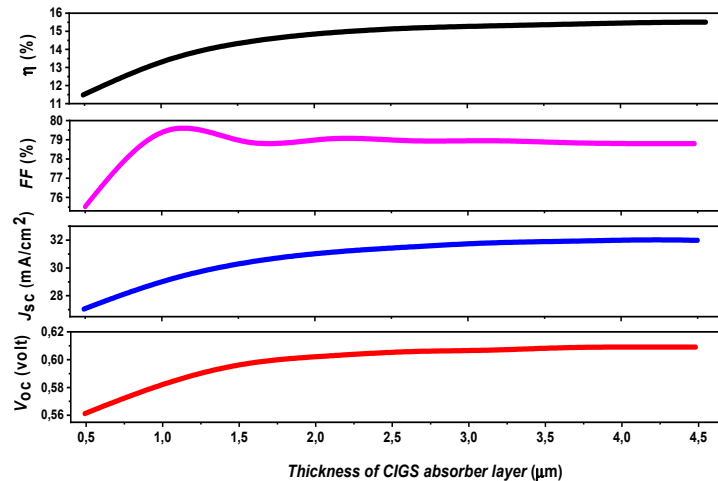


Figure 12. Solar cell performance using ZnS buffer layer as a function of the p-CIGS thickness.

## 2. Case of ZnO/n-ZnTe/p-CIGS/Mo solar cell structure

Fig. 13 presents the performance of ZnO/ZnTe/CIGS/Mo solar cell as a function of CIGS absorber thickness. It shows that the recorded efficiency is 14.66% and 16.58% at the CIGS thickness of 1  $\mu\text{m}$  and 4  $\mu\text{m}$ , respectively.

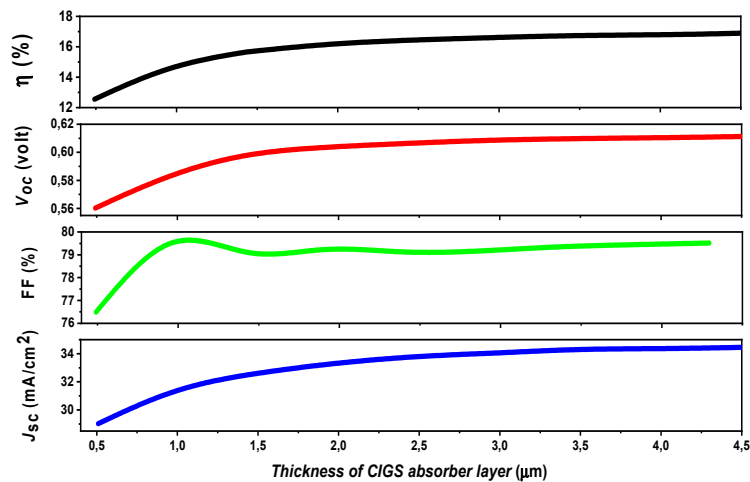


Figure 13. Solar cell performance using ZnTe buffer layer as a function of p-CIGS thickness.

A comparison of these results with the 16.12% efficiency at 2  $\mu\text{m}$  reveals that decreasing the absorber thickness by 1  $\mu\text{m}$  leads to an 11.58% drop in efficiency, whereas increasing it by 1  $\mu\text{m}$  results in only a 3.8% increase in efficiency. This trend continues to hold for absorber thicknesses more than 2  $\mu\text{m}$ . These findings support the theoretical assumption that a thickness of around 2  $\mu\text{m}$  is sufficient to absorb most of the incident light. However, reducing the absorber layer thickness below this value would bring the back contact too close to the depletion region, which would facilitate electron capture by the back contact during the recombination process. The open circuit voltage ( $V_{oc}$ ) and short circuit current density ( $J_{sc}$ ) increase with the thickness of the absorber layer, primarily due to the longer wavelengths' absorption, which contributes to electron-hole pair generation. When  $d(\text{CIGS})$  is greater than 4  $\mu\text{m}$ , the maximum Fill Factor of 79.5% is obtained. The highest efficiency of approximately 16.58%, with  $FF = 79.5\%$ ,  $V_{oc} = 0.61$  Volt, and  $J_{sc} = 34.05$   $\text{mA}/\text{cm}^2$  can be achieved when  $d(\text{CIGS})$  is approximately 4  $\mu\text{m}$ .

### III. CONCLUSIONS

The use of computational tools like CASTEP provides a powerful tool for the design and optimization of such materials, enabling the development of advanced optoelectronic devices. In this paper, the electronic structure and optical properties of ZnX systems were studied using the first principles of the ultra-smooth pseudovoltage method of density functional theory and the generalized gradient approximation method using the CASTEP tool. The search showed the following results: The network parameters took different values; Therefore, it is possible to deposit them on different substrates. The binary alloy is interesting, because it has a wide bandgap (2.436 eV, 2.698 eV, 1.721 eV) for ZnTe, ZnS and ZnO, respectively. From the results obtained, the structural, physical and optical properties are in close agreement with the available theoretical and experimental data which indicate the accuracy of the proposed calculation scheme. The properties of pure ZnX (X = Te, S, O) materials indicate that these materials have great potential for use in solar cells. The outcomes of the calculation reveal that although the efficiency grew alongside the absorber thickness,  $d(\text{CIGS})$ , the pace of this increase was much less beyond 2  $\mu\text{m}$ . The result concludes that the CIGS absorber layer's ideal thickness is likely to exceed 4  $\mu\text{m}$ .

### ORCID

● Faiza Benlakhdar, <https://orcid.org/0009-0003-1131-6289>

### Acknowledgments

The authors show recognition to the scientists, at the Department of Electronics and Information Systems (ELIS) of the University of Gent, Belgium, that developed the freely SCAPS-1D simulator.

### REFERENCES

- [1] B.G. Svensson, "Electronic structure and optical properties of Zn X (X=O, S, Se, Te)," pp. 1–14, 2018.
- [2] M. Lee, Y. Peng, and H. Wu, "Effects of intrinsic defects on electronic structure and optical properties of Ga-doped ZnO," *J. Alloys Compd.* **616**, 122-127 (2014) <https://doi.org/10.1016/j.jallcom.2014.07.098>
- [3] R. Khenata, "Elastic, electronic and optical properties of ZnS, ZnSe and ZnTe under pressure," *Computational Materials Science*, **38**, 29-38 (2006). <https://doi.org/10.1016/j.commatsci.2006.01.013>
- [4] Y. Yu, J. Zhou, H. Han, and C. Zhang, "Ab initio study of structural, dielectric, and dynamical properties of zinc-blende ZnX (X = O, S, Se, Te)," *Journal of Alloys and Compounds*, **471**, 492-497 (2009). <https://doi.org/10.1016/j.jallcom.2008.04.039>
- [5] S. Jeetendra, H. Nagabhushana, K. Mrudula, C.S. Naveen, P. Raghu, and H.M. Mahesh, "Concentration Dependent Optical and Structural Properties of Mo doped ZnTe Thin Films Prepared by e-beam Evaporation Method," *Int. J. Electrochem. Sci.* **9**, 2944-2954 (2014). <http://www.electrochemsci.org/papers/vol9/90602944.pdf>
- [6] S.M. Ali, A.A.A. Shehab, and S.A. Maki, "Study of the Influence of Annealing Temperature on the Structural and Optical Properties of ZnTe Prepared by Vacuum Thermal Evaporation Technique," *Ibn Al-Haitham Journal for Pure and Applied sciences*, **31**(1), 50-57 (2018). <https://doi.org/10.30526/31.1.1851>
- [7] Y. Yu et al., "Ab initio study of structural, dielectric, and dynamical properties of zinc-blende ZnX (X= O, S, Se, Te)," *Journal of alloys and compounds*, **471**(1-2), 492-497 (2009). <https://doi.org/10.1016/j.jallcom.2008.04.039>
- [8] D. Bahri and L. Amirouche, "Ab initio study of the structural, electronic and optical properties of ZnTe compound," *AIP Conference Proceedings*, **1653**(1), (2015). <https://doi.org/10.1063/1.4914210>
- [9] J. Serrano, Y. Tech, A. H. Romero, and R. Lauck, "Pressure dependence of the lattice dynamics of ZnO: An ab initio approach," *Physical Review B*, **69**, 094306 (2004). <https://doi.org/10.1103/PhysRevB.69.094306>.
- [10] V.O.I. Ume, P. Walter, L. Cohen, and Y. Petroff, "Calculated and Measured Reflectivity of ZnTe and ZnSe," *Phys. Rev. B*, **1**, 2661 (1970). <https://doi.org/10.1103/PhysRevB.1.2661>
- [11] M. Caid et al., "Electronic structure of short-period ZnSe/ZnTe superlattices based on DFT calculations," *Condensed Matter Physics*, **25**(1), 1-10 (2022). <https://doi.org/10.5488/CMP.25.13701>
- [12] F. Parandin, J. Jalilian, and J. Jalilian, "Tuning of electronic and optical properties in ZnX (X = O, S, Se and Te) monolayer: Hybrid functional calculations," *Chemical Review & Letters*, **2**(2), 76-83 (2019). <https://doi.org/10.22034/crl.2019.195774.1019>
- [13] Z. Nourbakhsh, "Structural, electronic and optical properties of ZnX and CdX compounds (X = Se, Te and S) under hydrostatic pressure," *J. Alloys Compd.* **505**(2), 698-711 (2010). <https://doi.org/10.1016/j.jallcom.2010.06.120>.
- [14] F.D. Murnaghan, "The Compressibility of Media under Extreme Pressures," *Proceedings of the National Academy of Sciences of the United States of America*, **30**(9), 244-247 (1944). <https://www.jstor.org/stable/87468>
- [15] M. Safari, Z. Izadi, J. Jalilian, and I. Ahmad, "Metal mono-chalcogenides ZnX and CdX (X = S, Se and Te) monolayers: Chemical bond and optical interband transitions by first principles calculations," *Phys. Lett. A*, **381**(6), 663-670 (2017). <https://doi.org/10.1016/j.physleta.2016.11.040>.
- [16] S. K. Gupta, S. Kumar, and S. Auluck, "Structural, electronic and optical properties of high pressure stable phases of ZnTe," *Physica B: Condensed Matter*, **404**, 3789-3794 (2009). <https://doi.org/10.1016/j.physb.2009.06.149>
- [17] A.A. Audu, W.A. Yahya, and A.A. Abdulkareem, *Physics Memoir: Journal of Theoretical & Applied Physics*, "Ab initio Studies of the Structural, Electronic and Mechanical Properties of Zn<sub>1-x</sub>Crx e," **3**, 38-47 (2021).
- [18] M. Achehboune, M. Khenfouch, I. Boukhoubza, I. Derkaoui, B.M. Mothudi, I. Zorkani, A. Jorio, "Effect of Yb Concentration on the Structural, Magnetic and Optoelectronic Properties of Yb Doped ZnO: First Principles Calculation". <http://dx.doi.org/10.21203/rs.3.rs-877060/v1>
- [19] R. John, and S. Padmavathi, "Ab Initio Calculations on Structural, Electronic and Optical Properties of ZnO in Wurtzite Phase," *Cryst. Struct. Theory Appl.* **5**(2), 24-41 (2016). <https://doi.org/10.4236/csta.2016.52003>
- [20] R. Chowdhury, S. Adhikari, and P. Rees, "Optical properties of silicon doped ZnO," *Phys. B Condens. Matter*, **405**(23), 4763-4767 (2010). <https://doi.org/10.1016/j.physb.2010.08.072>

- [21] C. Feng *et al.*, “First-principle calculation of the electronic structures and optical properties of the metallic and nonmetallic elements-doped ZnO on the basis of photocatalysis,” *Phys. B Condens. Matter*, **555**, 53-60 (2019). <https://doi.org/10.1016/j.physb.2018.11.043>.
- [22] L. Chen, X. Zhou, and J. Yu, “First-principles study on the electronic and optical properties of the ZnTe/InP heterojunction,” *J. Comput. Electron.* **18**(3), 749-757 (2019). <https://doi.org/10.1007/s10825-019-01358-8>
- [23] A.M. Ghaleb, and A.Q. Ahmed, “Structural, electronic, and optical properties of sphalerite ZnS compounds calculated using density functional theory (DFT),” *Chalcogenide Lett.* **19**(5), 309-318 (2022). <https://doi.org/10.15251/CL.2022.195.309>
- [24] Q. Hou, and S. Sha, “Effect of biaxial strain on the p-type of conductive properties of (S, Se, Te) and 2 N co-doped ZnO,” *Mater. Today Commun.* **24**, 101063 (2020). <https://doi.org/10.1016/j.mtcomm.2020.101063>
- [25] Md.A. Momin, Md.A. Islam, A. Majumdar, “Influence on structural, electronic and optical properties of Fe doped ZnS quantum dot: A density functional theory based study,” *Quantum Chemistry*, **121**(1), 1-13 (2020). <https://doi.org/10.1002/qua.26786>
- [26] M. Dong, P. Zhou, C. Jiang, B. Cheng, and J. Yu, “First-principles investigation of Cu-doped ZnS with enhanced photocatalytic hydrogen production activity State Key Laboratory of Advanced Technology for Materials Synthesis and,” *Chem. Phys. Lett.* **668**, 1-6 (2016). <https://doi.org/10.1016/j.cplett.2016.12.008>
- [27] A. Pattnaik, M. Tomar, P.K. Jha, A.K. Bhoi, V. Gupta, and B. Prasad, “Theoretical Analysis of the Electrical and Optical Properties of ZnS,” In: A. Konkani, R. Bera, and S. Paul, editors, *Advances in Systems, Control and Automation. Lecture Notes in Electrical Engineering*, vol. 442. (Springer, Singapore, 2018). [https://doi.org/10.1007/978-981-10-4762-6\\_2](https://doi.org/10.1007/978-981-10-4762-6_2)
- [28] Y.L. Su, Q.Y. Zhang, N. Zhou, C.Y. Ma, X.Z. Liu, and J.J. Zhao, “Study on Co-doped ZnO comparatively by first-principles calculations and relevant experiments,” **250**, 123-128 (2017). <https://doi.org/10.1016/j.ssc.2016.12.002>
- [29] T. Kato, J. L. Wu, Y. Hirai, H. Sugimoto, and V. Bermudez, “Record Efficiency for Thin-Film Polycrystalline Solar Cells Up to 22.9% Achieved by Cs-Treated Cu(In,Ga)(Se,S)<sub>2</sub>,” *IEEE J. Photovoltaics*, **9**(1), 325-330 (2019). <https://doi.org/10.1109/JPHOTOV.2018.2882206>
- [30] A. Bouzidi, and I. Bouchama, “Numerical study of the buffer influence on the Cu(In,Ga)Se<sub>2</sub> solar cells performances by SCAPS-ID,” in: International Conference on Electronics and New Technologies (ICENT), 2017.
- [31] S.K. Gupta, S. Kumar, and S. Auluck, “Structural, electronic and optical properties of high pressure stable phases of ZnTe,” *Phys. B Condens. Matter*, **404**(20), 3789-3794 (2009). <https://doi.org/10.1016/j.physb.2009.06.149>
- [32] R. Tala-Ighil Zair, C. Oudjehani, and K. Tighilt, “SCAPS Simulation for Perovskite Solar Cell,” *J. Sol. Energy Res. Updat.* **8**, 21-26 (2021). <https://doi.org/10.31875/2410-2199.2021.08.3>
- [33] H.I. Abdalmageed, M. Fedawy, and M.H. Aly, “Effect of absorber layer bandgap of CIGS-based solar cell with (CdS/ZnS) buffer layer,” *J. Phys. Conf. Ser.* **2128**(1), (2021). <https://doi.org/10.1088/1742-6596/2128/1/012009>
- [34] C. Platzer-Björkman, J. Kessler, and L. Stolt, “Analysis of Zn(O,S) films for Cu(In,Ga)Se<sub>2</sub> solar cells,” *Proc. Estonian Acad. Sci. Phys. Math.* **52**(3), 299-307 (2003). <https://doi.org/10.3176/phys.math.2003.3.06>
- [35] Y.-K. Liao *et al.*, “A look into the origin of shunt leakage current of Cu(In, Ga)Se<sub>2</sub> solar cells via experimental and simulation methods,” *Sol. Energy Mater. Sol. Cells*, **117**, 145-151 (2013). <https://doi.org/10.1016/j.solmat.2013.05.031>
- [36] P. Srivastava *et al.*, “Theoretical study of perovskite solar cell for enhancement of device performance using SCAPS-1D,” *Phys. Scr.* **97**(2), 12 (2022). <https://doi.org/10.1088/1402-4896/ac9dc5>
- [37] M. Safari, Z. Izadi, J. Jalilian, I. Ahmad, and S. Jalali-Asadabadi, “Metal mono-chalcogenides ZnX and CdX (X = S, Se and Te) monolayers: Chemical bond and optical interband transitions by first principles calculations,” *Phys. Lett. Sect. A Gen. At. Solid State Phys.* **381**(6), 663-670 (2017). <https://doi.org/10.1016/j.physleta.2016.11.040>
- [38] H. T. Ganem, and A. N. Saleh, “The effect of band offsets of absorption layer on CNTS/ZnS/ZnO solar cell by SCAPS-1D,” *Tikrit Journal of Pure Science*, **25** (6), 79-87 (2020). <http://dx.doi.org/10.25130/tjps.25.2020.114>
- [39] N. Adim, M. Caid, D. Rached, and O. Cheref, “Computational study of structural, electronic, magnetic and optical properties of (ZnTe)<sub>m</sub>/(MnTe)<sub>n</sub> superlattices,” *Journal of Magnetism and Magnetic Materials*, **499**, 166314 (2020). <https://doi.org/10.1016/j.jmmm.2019.166314>

#### АВ-ІНІЦІО ДОСЛІДЖЕННЯ СТРУКТУРНИХ, ЕЛЕКТРОННИХ ТА ОПТИЧНИХ ВЛАСТИВОСТЕЙ ZnX (X = Te, S і O): ЗАСТОСУВАННЯ ДО СОНЯЧНИХ БАТАРЕЙ

Файза Бенлахдар<sup>a</sup>, Ідріс Бушама<sup>b,c</sup>, Тайєб Чіхі<sup>c,d</sup>, Ібрагім Гебулі<sup>c,d</sup>,

Мохамед Амін Гебулі<sup>c</sup>, Зохра Зерругі<sup>e</sup>, Кеттаб Хатір<sup>f</sup>, Мохамед Алам Сайєд<sup>g</sup>

<sup>a</sup>Кафедра електроніки, технологічний факультет, Університет Сетіфа 1, 19000, Алжир

<sup>b</sup>Кафедра електроніки, технологічний факультет, Університет Мсіла, Мсіла, 28000, Алжир

<sup>c</sup>Дослідницький відділ нових матеріалів (RUEM), Університет Ферхат Аббас із Сетіфа 1, Сетіф, 19000, Алжир

<sup>d</sup>Лабораторія розробки нових матеріалів і характеристик (LENMC), Університет Ферхата Аббаса, Сетіф 19000, Алжир

<sup>e</sup>Лабораторія досліджень поверхонь і розділу твердих матеріалів (LESIMS), Департамент технологій, Ферхат АББАС Сетіфський університет, Сетіф, Алжир

<sup>f</sup>Кафедра електротехніки, технологічний факультет, Університет Мсіла, Мсіла, 28000, Алжир

<sup>g</sup>Департамент фізики, Відділ науки та технологій, Педагогічний університет, Лахор, Пакистан

Метою роботи є дослідження структурних, електронних і оптичних властивостей сполук ZnX, зокрема тих, у яких X = Te, S і O, які мають пряму заборонену зону, що робить їх оптично активними. Щоб краще зрозуміти ці сполуки та їхні пов'язані властивості, ми провели детальні розрахунки за допомогою теорії функціоналу щільності (DFT) і програми CASTEP, яка використовує узагальнене градієнтне наближення (GGA) для оцінки функції крос-кореляції. Наші результати щодо модуля ґратки, ширини забороненої зони та оптичних параметрів узгоджуються як з експериментальними даними, так і з теоретичними прогнозами. Енергетична заборонена зона для всіх сполук є відносно великою через збільшення s-станів у валентній зоні. Наші результати показують, що оптичний перехід між (O - S - Te) - p-станами у найвищій валентній зоні та (Zn - S - O) - s-станами в нижчій зоні провідності зміщується до нижчої енергетичної зони. Таким чином, сполуки ZnX (X = Te, S і O) є перспективним варіантом для оптоелектронних пристроїв, таких як матеріали для сонячних елементів.

**Ключові слова:** ZnTe; ZnS; ZnO; CASTEP; DFT; щільність стану; оптичні властивості



## MEAN LIFETIMES OF ns, np, nd, & nf LEVELS OF N V<sup>†</sup>

Rizwana Siddique<sup>a</sup>, Roohi Zafar<sup>b</sup>,  Salman Raza<sup>a</sup>, S.M. Zeeshan Iqbal<sup>a</sup>,  Zaheer Uddin<sup>a,\*</sup>

<sup>a</sup>Department of Physics, University of Karachi, Karachi, Pakistan

<sup>b</sup>Department of Physics, NED University of Engineering and Technology, Karachi, Pakistan

\*Corresponding Author e-mail: [zuddin@uok.edu.pk](mailto:zuddin@uok.edu.pk)

Received June 22, 2023; revised July 9, 2023; accepted July 11, 2023

Nitrogen is one of the key elements in the evolution and formation of stellar objects. Earth's atmosphere contains 21% oxygen and 78% nitrogen; these two gases give rise to aurora when ions of the solar wind in the ionosphere collide with them. Some aerosols made of nitrogen and oxygen are also found in the atmosphere. Nitrogen, hydrogen, carbon, and oxygen are the main contributors to the origin of life on Earth. The spectrum of nitrogen ion (N V) has been studied using Quantum defect theory (QDT) and Numerical Coulombic approximation (NCA). N V has two electrons in the core, with the nucleus, and one electron outside the core. It makes it hydrogen or lithium-like. In the first part, the energies of the ns, np, nd, and nf up to  $n < 30$  were calculated with the help of QDT. In the second part, the wavelengths were calculated using the energies and line strength parameters using NCA. Very little experimental data on lifetime and transition probability are available; however, Biemont et al. have calculated the lifetime of the 48 levels of N V using coulomb approximation. In this study, we calculated the lifetime of 196 multiplets of N V. The results are compared with the available experimental and theoretical lifetimes; an excellent agreement was found between known lifetimes and calculated in this work. The lifetimes of 100 multiplets are presented for the first time. The lifetimes of each of the Rydberg series of N V were fitted, and a third-degree polynomial represents the lifetimes of each series.

**Keywords:** Nitrogen ion (N V); Lifetimes; Quantum defect theory; Numerical coulomb approximation; Lithium-like ions

**PACS:** 31.10.+z, 31.15.-p, 31.15.Ct, 31.90.+s, 32.30.-r

### INTRODUCTION

In the evolution of chemically peculiar stars, nitrogen plays an important role. For example, Pluto is believed to have a rocky core and layers of various ices in the surface crust; most of the ice is nitrogen. It indicates a high abundance of nitrogen on Pluto. Improved spectroscopic data is essential in determining reliable values of stellar abundances. Kancerecivius calculated transition probabilities and Oscillator Strengths using analytic wave functions of helium and lithium-like atoms from np to ms ( $m < 3$ ,  $n < 6$ ). They used three different expressions for the dipole moments [1]. Fischer et al. calculated transition data, including lifetimes using the multiconfiguration Breit-Pauli method of the Li sequence. They calculated the lifetimes of all configuration levels of principal quantum number  $< 4$ , including the configuration  $1s^2 4s$  [2]. Mohammed El-Mekki used a semi-empirical Coulomb Approximation to calculate 2p levels of isoelectronic Li-sequence lifetimes. With the help of Hartree Slater's core, he calculated lifetimes for  $Z = 3 - 92$  [3]. Chen and Crasemann used the Multiconfiguration Dirac-Fock approach to calculate the transition data of the highest spin metastable  $^4F_{9/2}$  of  $1s 2p 3d$  configuration of Li-like ions for  $Z = 6$  to 42. They calculated Auger energies, Auger rate, radiative energies, and radiative rate for the transition  $2s - 2p$ ,  $3p - 3d$ ,  $1s - 2p$ , and  $2s-3d$  [4]. Blanke et al. studied decay curves of the quartet system of Li-like ions for  $n = 6 - 9$ . The decay curve measured the lifetimes of  $n = 3$  states of the configuration  $1s 2p 3d$  [5]. Tunnell and Bhalla estimated the lifetimes of the  $^4P$  state of the configuration  $1s 2p^2$  of the lithium-like ions ( $Z = 7, 8, 10, \text{ and } 12$ ) [6]. Kernahan et al. measured the lifetimes of 11 levels belonging to N II – N V. They considered the transition below  $500\text{\AA}$  [7]. Baudinet-Robinet and P. D. Dumont used the beam foil technique to measure the lifetimes of N V levels in the ultraviolet spectrum range. Using Coulomb approximation, they found branching fractions and combined them with the lifetime to measure the transition probabilities [8]. Kernahan et al. also used the beam-foil technique to measure the lifetimes of 41 states of N I – N V. They studied transitions in the range  $374$  to  $2064\text{\AA}$ . They compared the results with existing known lifetimes and found that they agree well for levels near the ionization stage [9]. Dumont also used the beam-foil technique to measure the lifetime of nitrogen in the UV spectrum range. They studied nitrogen spectra and found lifetimes of 24 levels in the range  $650 - 2000\text{\AA}$  [10]. Desesquelles used the technique of beam of ions by a thin Carbon foil to prepare a nitrogen beam. This technique can make an ions beam between  $100$  keV and  $16$  MeV. Most of the lines of the spectra of neutral nitrogen to N VII can be observed. The lifetimes of upper levels and transition probabilities were found by the spatial decay of the light emitted by fast-moving atoms and ions [11]. Lewis et al. also used the foil excitation technique at high energy of  $2$  MeV of nitrogen through carbon foil and measured the lifetimes of upper levels of the transition in N II to N V. The transition lines they observed were in the range of  $2000$  to  $5000\text{\AA}$ . The measured lifetime by the spatial decay of the excited levels was  $0.4$  to  $10$  ns [12]. Heroux also used the same technique Desesquelles [10] and Lewis [12] used to measure the lifetime of multiplets in N II to N V. The beam energy of nitrogen ions was the same as used by Lewis [12], but the range of wavelengths was from  $1085$  to  $162\text{\AA}$  [13]. Berry et al. studied nitrogen transition in N I-VI using the beam foil technique; they used an energy range of  $0.25-2.0$  MeV in wavelength range  $1050-3000\text{\AA}$  and  $5.5$  MeV between  $2000-5000\text{\AA}$  [14].

<sup>†</sup> Cite as: R. Siddique, R. Zafar, S. Raza, S.M.Z. Iqbal, Z. Uddin, East Eur. J. Phys. 3, 424 (2023), <https://doi.org/10.26565/2312-4334-2023-2-46>

© R. Siddique, R. Zafar, S. Raza, S.M.Z. Iqbal, Z. Uddin, 2023

### THEORY

Quantum mechanical systems are complex systems; the exact analytical solutions of the systems are often unavailable or impossible to find. Numerical approaches are one of the best alternatives to reach an approximate solution. Schrödinger equation can be solved analytically for hydrogen atoms, with the approximation that variables are separable, but this equation is difficult to solve for helium and other elements. If the system is approximated as hydrogen, the solution is achievable and close to the exact solution in many cases, such as Li and lithium-like ions. Nitrogen ion (N V) is a lithium-like ion; its transition data can be obtained by numerically solving the Schrödinger equation.

$$\left(\frac{d^2}{dr^2} - 2V(r) - \frac{l^*(l^*+1)}{r^2} + 2E\right)P(r) = 0. \quad (1)$$

The equation (1) can be written as

$$\frac{d^2R}{dr^2} + \frac{2}{r} \frac{dR}{dr} + 2\left(E - \frac{A}{r_i} - \frac{B}{r_i^2} - \frac{l(l+1)}{r_i^2}\right) = 0. \quad (2)$$

Here  $R(r) = \frac{P(r)}{r}$ ,  $A/r_i - B/r_i^2 = V(r_i)$  is the potential observed by the electron outside the core formed by the nucleus and other electrons in the atom,  $A = -z^*$  is the effective nuclear charge where  $r_i$  is the distance between electron  $i$  and the nucleus.

The solution of equation (2) gives the radial wavefunction R as:

$$R = C \exp\left(-\frac{Z^*r}{n^*}\right) r^{l^*} L_{n^*-l^*-1}^{2l^*+1}\left(\frac{2Z^*r}{n^*}\right). \quad (3)$$

Where  $C = \left(\frac{2Z^*}{n^*}\right)^{l^*+\frac{3}{2}} \sqrt{\frac{(n^*-l^*-1)!}{2n^*\Gamma(n^*+l^*+1)}}$ ,  $n^*$  is the effective principal quantum number. The lifetime can be calculated using equation (4)

$$\tau_i = \left(\frac{\lambda(\text{\AA})}{1265.38}\right)^3 \frac{g_i}{S_{if}}, \quad (4)$$

where the line strength factor  $S_{if}$  is given by,

$$S_{if} = \sum_{n_i, n_f} |\langle f|r|i \rangle|^2. \quad (5)$$

The matrix element values in equation (5) can be obtained using the wavefunctions in equation (3).

### RESULT AND DISCUSSION

Quantum defect theory (QDT) and Numerical Coulombic approximation (NCA) were used to study the lifetimes of the nitrogen ion (N V). The energies and quantum defects were calculated with the help of QDT. These energies and quantum defects were used to calculate the lifetimes of the levels of N V. The lifetimes of any branch of the transition depend on the transition wavelength and line strength parameter. The wavelengths were calculated by the difference of energies of upper and lower levels calculated by QDT. The wavefunctions of upper and lower levels are required to calculate line strength parameters. Since nitrogen ion (N V) may be considered hydrogen-like, hydrogen wavefunction can be used to calculate the matrix element needed for the line strength parameters. The matrix elements are calculated using NCA.

The lifetimes of the Rydberg Series  $1s^2 ns$ ,  $1s^2 np$ ,  $1s^2 nd$ , and  $1s^2 nf$  levels of N V have been calculated and compared with the available experimental and theoretical values. Generally, a good agreement is found between calculated and available lifetime data. It was found that the available experimental data on lifetime is very little. The most detailed theoretical work on the lifetime of N V is by Biemont et al. However, they reported lifetimes of forty-eight levels of N V. In this work, the lifetimes of 196 multiplets are presented. Table 1 gives the lifetimes of N V levels; the first column gives the configuration, the second column gives the angular momentum third columns give the lifetimes calculated in this work, and the fourth and last column gives the corresponding lifetimes available in the literature. The lifetime calculated for  $1s^2 2p$  is slightly different from the experimental value. The reason could be its closeness to the core, which may affect the effective charge compared to the other levels that lie relatively far from the core. It was observed in the calculations of transition probability and lifetimes of the same configuration in Li I [16], Be II [17], and C IV [18] that the calculated and experimental values are slightly different. For the configuration  $1s^2 2p$  in Li-like atoms and ions, one should expect a slight difference in theoretical and experimental lifetimes. A study is needed to see if the problem is resolved by changing  $Z$  by its effective value.

**Table 1.** The lifetimes of multiplets of N V calculated in this work and compared with available data

Term 1s <sup>2</sup> .nl	J	This work	Other works	Term 1s <sup>2</sup> .nl	J	This work	Other works
3d	3/2	0.0228	0.02 <sup>g</sup>	29d	3/2	18.541	
3d	5/2	0.0228		29d	5/2	18.5608	
4d	3/2	0.0527	0.065 <sup>a</sup> , 0.05 <sup>g</sup>	30d	3/2	20.5184	
4d	5/2	0.0527	0.95 <sup>d</sup>	30d	5/2	20.538	
5d	3/2	0.1012	0.1 <sup>g</sup>	10f	5/2	1.7395	
5d	5/2	0.1012		11f	5/2	2.3098	
6d	3/2	0.1726	0.18 <sup>g</sup>	12f	5/2	2.9928	
6d	5/2	0.1728		13f	5/2	3.7989	
7d	3/2	0.2715	0.28 <sup>g</sup>	14f	5/2	4.738	
7d	5/2	0.2718		15f	5/2	5.8205	
8d	3/2	0.4024	0.41 <sup>g</sup>	16f	5/2	7.0566	
8d	5/2	0.4028		17f	5/2	8.4564	
9d	3/2	0.5698	0.59 <sup>g</sup>	18f	5/2	10.0302	
9d	5/2	0.5703		19f	5/2	11.7882	
10d	3/2	0.7781	0.8 <sup>g</sup>	20f	5/2	13.7405	
10d	5/2	0.7789		21f	5/2	15.8974	
11d	3/2	1.032	1.05 <sup>g</sup>	22f	5/2	18.2692	
11d	5/2	1.033		23f	5/2	20.8659	
12d	3/2	1.3359	1.37 <sup>g</sup>	24f	5/2	23.6978	
12d	5/2	1.3372		25f	5/2	26.7752	
13d	3/2	1.6943	1.77 <sup>g</sup>	26f	5/2	30.1082	
13d	5/2	1.6959		27f	5/2	33.7071	
14d	3/2	2.1118	2.12 <sup>g</sup>	28f	5/2	37.5821	
14d	5/2	2.1139		29f	5/2	41.7421	
15d	3/2	2.5929	2.53 <sup>g</sup>	30f	5/2	46.1474	
15d	5/2	2.5955		4f	5/2	0.1153	0.12 <sup>g</sup>
16d	3/2	3.1421	3.19 <sup>g</sup>	4f	7/2	0.1153	
16d	5/2	3.1453		5f	5/2	0.223	0.22 <sup>g</sup>
17d	3/2	3.7639	3.73 <sup>g</sup>	5f	7/2	0.2231	
17d	5/2	3.7678		6f	5/2	0.3823	0.61 <sup>d</sup> , 0.38 <sup>g</sup>
18d	3/2	4.463	4.75 <sup>g</sup>	6f	7/2	0.3824	
18d	5/2	4.4675		7f	5/2	0.6034	0.6 <sup>g</sup>
19d	3/2	5.2437		7f	7/2	0.6036	
19d	5/2	5.2491		8f	5/2	0.8965	0.89 <sup>g</sup>
20d	3/2	6.1106		8f	7/2	0.8968	
20d	5/2	6.117		9f	5/2	1.2718	1.26 <sup>g</sup>
21d	3/2	7.0684		9f	7/2	1.2723	
21d	5/2	7.0758		10f	7/2	1.7402	1.72 <sup>g</sup>
22d	3/2	8.1214		11f	7/2	2.3107	
22d	5/2	8.1299		12f	7/2	2.994	
23d	3/2	9.2742		13f	7/2	3.8004	
23d	5/2	9.284		14f	7/2	4.7399	
24d	3/2	10.5314		15f	7/2	5.8229	
24d	5/2	10.5425		16f	7/2	7.0596	
25d	3/2	11.8974		17f	7/2	8.46	
25d	5/2	11.91		18f	7/2	10.0345	
26d	3/2	13.3769		19f	7/2	11.7932	
26d	5/2	13.3911		20f	7/2	13.7465	
27d	3/2	14.9743		21f	7/2	15.9044	
27d	5/2	14.9903		22f	7/2	18.2771	
28d	3/2	16.6942		23f	7/2	20.8751	
28d	5/2	16.7118		24f	7/2	23.7083	

Term 1s <sup>2</sup> .nl	J	This work	Other works
25f	7/2	26.787	
26f	7/2	30.1216	
27f	7/2	33.7221	
28f	7/2	37.5987	
29f	7/2	41.762	
30f	7/2	46.2199	
2p	3/2	2.8423	2.9741 <sup>a</sup> , 3.12 <sup>b</sup> , 3.2 <sup>d</sup> , 3.3 <sup>f</sup> , 2.95 <sup>g</sup>
2p	1/2	2.871	2.9442 <sup>a</sup> , 3.08 <sup>b</sup> , 3.3 <sup>d</sup> , 3.3 <sup>f</sup>
3p	1/2	0.0821	0.081328 <sup>a</sup> , 0.084 <sup>c</sup> , 0.51 <sup>f</sup> 0.08 <sup>g</sup>
3p	3/2	0.0822	0.082058 <sup>a</sup>
4p	1/2	0.1333	0.14 <sup>g</sup> , 0.17 <sup>c</sup>
4p	3/2	0.1335	
5p	1/2	0.2224	0.22 <sup>g</sup>
5p	3/2	0.2227	
6p	1/2	0.353	0.51 <sup>f</sup> , 0.36 <sup>g</sup>
6p	3/2	0.3534	
7p	1/2	0.5321	0.54 <sup>g</sup>
7p	3/2	0.5327	
8p	1/2	0.7672	0.77 <sup>g</sup>
8p	3/2	0.7679	
9p	1/2	1.0659	1.08 <sup>g</sup>
9p	3/2	1.0669	
10p	1/2	1.436	1.46 <sup>g</sup>
10p	3/2	1.4373	
11p	1/2	1.8854	1.85 <sup>g</sup>
11p	3/2	1.887	
12p	1/2	2.4219	2.45 <sup>g</sup>
12p	3/2	2.4239	
13p	1/2	3.0532	2.96 <sup>g</sup>
13p	3/2	3.0557	
14p	1/2	3.7873	3.92 <sup>g</sup>
14p	3/2	3.7904	
15p	1/2	4.632	4.26 <sup>g</sup>
15p	3/2	4.6357	
16p	1/2	5.5951	4.3 <sup>g</sup>
16p	3/2	5.5996	
17p	1/2	6.6846	5.03 <sup>g</sup>
17p	3/2	6.6899	
18p	1/2	7.9083	
18p	3/2	7.9145	
19p	1/2	9.2741	
19p	3/2	9.2814	
20p	1/2	10.7899	
20p	3/2	10.7983	
21p	1/2	12.4635	
21p	3/2	12.4731	

Term 1s <sup>2</sup> .nl	J	This work	Other works
22p	1/2	14.3028	
22p	3/2	14.3138	
23p	1/2	16.3157	
23p	3/2	16.3282	
24p	1/2	18.5101	
24p	3/2	18.5242	
25p	1/2	20.8939	
25p	3/2	20.9098	
26p	1/2	23.4749	
26p	3/2	23.4927	
27p	1/2	26.2611	
27p	3/2	26.2809	
28p	1/2	29.26	
28p	3/2	29.2821	
29p	1/2	32.4742	
29p	3/2	32.5049	
30p	1/2	35.906	
30p	3/2	35.9494	
3s	1/2	0.11	0.10985 <sup>a</sup> , 0.121 <sup>c</sup> , 0.12 <sup>c</sup> , 0.11 <sup>g</sup>
4s	1/2	0.1733	0.5 <sup>a</sup> , 0.17212 <sup>c</sup> , 0.18 <sup>g</sup>
5s	1/2	0.2849	0.29 <sup>g</sup>
6s	1/2	0.4486	0.45 <sup>g</sup>
7s	1/2	0.6731	0.68 <sup>g</sup>
8s	1/2	0.9678	0.98 <sup>g</sup>
9s	1/2	1.3425	1.39 <sup>g</sup>
10s	1/2	1.8069	1.84 <sup>g</sup>
11s	1/2	2.3709	
12s	1/2	3.0444	
13s	1/2	3.8375	
14s	1/2	4.7599	
15s	1/2	5.8216	
16s	1/2	7.0327	
17s	1/2	8.403	
18s	1/2	9.9426	
19s	1/2	11.6614	
20s	1/2	13.5694	
21s	1/2	15.6766	
22s	1/2	17.993	
23s	1/2	20.5286	
24s	1/2	23.2933	
25s	1/2	26.2971	
26s	1/2	29.5501	
27s	1/2	33.0623	
28s	1/2	36.843	
29s	1/2	40.8972	
30s	1/2	45.1651	

<sup>a</sup>[2], <sup>b</sup>[7], <sup>c</sup>[9], <sup>d</sup>[10], <sup>e</sup>[13], <sup>f</sup>[14], <sup>g</sup>[15]

The plot of lifetimes is smoothly increasing; the different polynomials J were fitted on the calculated lifetime's data of N V. Third-degree polynomial ( $\tau = a_0 + a_1n + a_2n^2 + a_3n^3$ ) fitting gives closer values of calculated lifetimes. Figure 1(i)-1(vii) gives plots of calculated lifetimes with fitted values for 1s<sup>2</sup> ns, 1s<sup>2</sup> np, 1s<sup>2</sup> nd, and 1s<sup>2</sup> nf levels of N V. In fitting the np series, the level 1s<sup>2</sup> 2p was not included as its lifetime does not follow the trend.

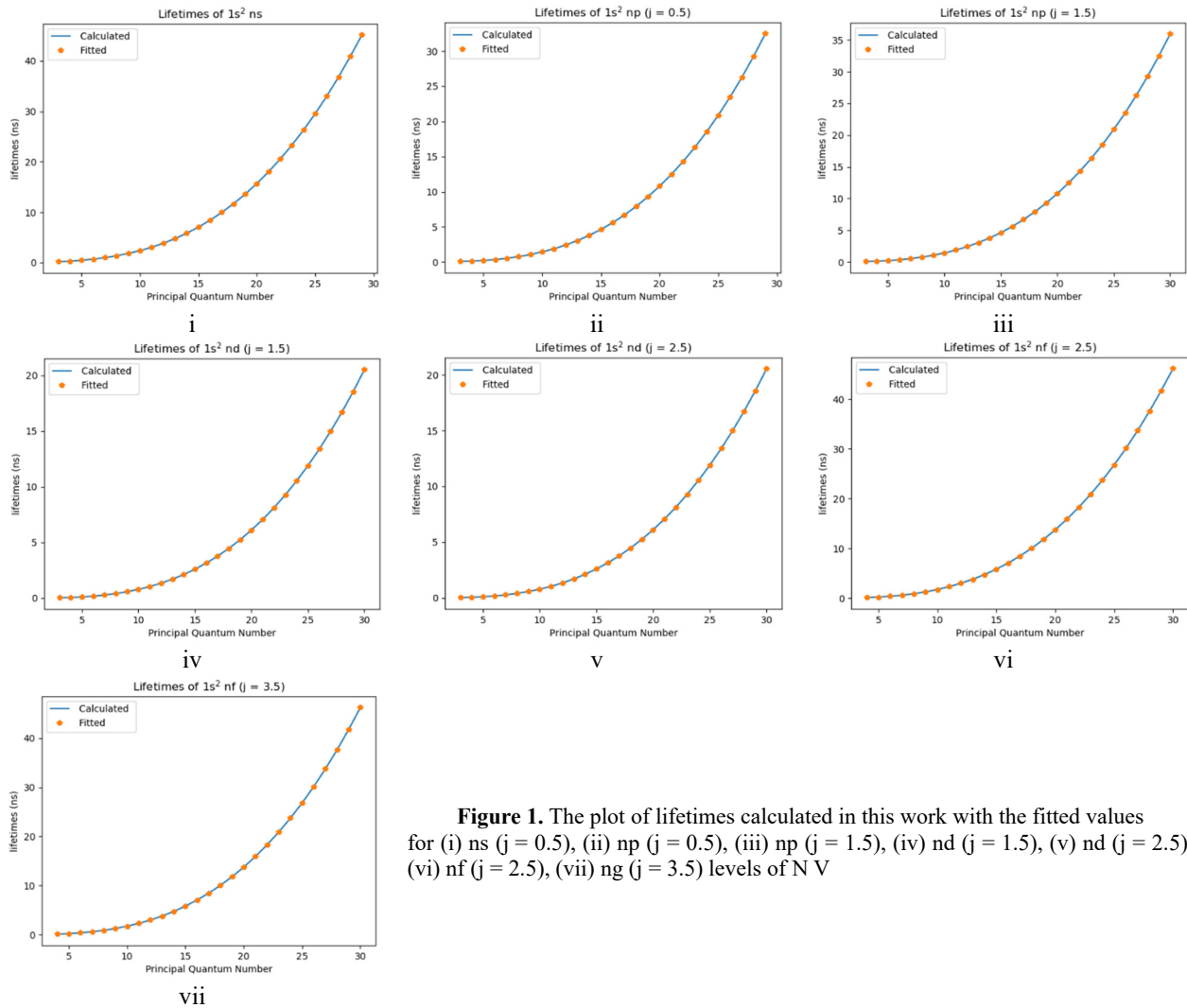


**Figure 1.** The plot of lifetimes calculated in this work with the fitted values for (i) ns ( $j = 0.5$ ), (ii) np ( $j = 0.5$ ), (iii) np ( $j = 1.5$ ), (iv) nd ( $j = 1.5$ ), (v) nd ( $j = 2.5$ ), (vi) nf ( $j = 2.5$ ), (vii) ng ( $j = 3.5$ ) levels of N V

Third-degree polynomial represents the lifetimes of various Rydberg series  $1s^2 ns$ ,  $1s^2 np$ ,  $1s^2 nd$ ,  $1s^2 nf$  of N V. The coefficients of the polynomials are given in Table 2. There are two polynomials for each of the series np, nd, and nf for two different possible values of angular momentum. nd series is the only series for which the coefficients for both angular momenta are approximately the same.

**Table 1.** Coefficients of the polynomial fitted for calculated lifetimes of N V for different series

Term and J value	Coefficients of the Polynomial			
	$a_0$	$a_1$	$a_2$	$a_3$
ns (1/2)	0.053562	0.009137	0.005815	0.00164
np (1/2)	0.019362	0.005954	0.000504	0.001306
np (3/2)	0.017367	0.006626	0.000449	0.001309
nd (3/2)	-0.0035	0.001466	0.000128	0.000754
nd (5/2)	-0.0034	0.001432	0.00013	0.000755
nf (5/2)	0.018192	-0.00479	0.000773	0.001689
nf (7/2)	-0.00463	0.001625	0.000275	0.001701

### CONCLUSIONS

The Rydberg levels series  $1s^2 ns$ ,  $1s^2 np$ ,  $1s^2 nd$ , and  $1s^2 nf$  of N V have been studied. The lifetimes of multiplets belonging to these levels have been calculated and compared with the available data. The agreement is excellent except for  $1s^2 2p$  levels, where a slight difference between calculated and experimental values of lifetimes was observed. The same can be observed in all Lithium like ions due to the cooper minimum. The cooper minimum was first observed for alkali atoms. It occurs due to overlapping the positive and negative amplitude of the wavefunctions of the levels taking part in the transition [16]. Due to this, the dipole matrix elements have zero or a minimum value for a particular set of principal quantum numbers of both levels. According to Fano and Cooper [19], the oscillator strength as a function of effective principal quantum number ( $n^*$ ) drops rapidly towards a minimum, where a reversal sign in the R integral occurs. QDT and NCA were used to calculate energy, quantum defects, and lifetimes of N V. The lifetimes of 196 multiplets were

calculated, but the available experimental data was insufficient. However, Biemont et al. theoretically determined the lifetimes of forty-eight levels; hence, 100 lifetimes presented in this paper are new. The plot of lifetimes against the principal quantum number follows a polynomial, so different polynomials were fitted, and in each series third-degree polynomial fits well on the calculated lifetimes of the N V Rydberg series.

#### ORCID

©Salman Raza, <https://orcid.org/0000-0002-1880-6796>; ©Zaheer Uddin, <https://orcid.org/0000-0002-8807-6186>

#### REFERENCES

- [1] A. Kancereivius, *Leituvos Fiz. Rinkinys*, **2**, (1962).
- [2] C.F. Fischer, M. Saporov, G. Gaigalas, and M. Godefroid, *Atomic data and nuclear data tables*, **70**(1), 119 (1998). <https://doi.org/10.1006/adnd.1998.0788>
- [3] C.E. Theodosiou, L.J. Curtis, and M. El-Mekki, *Physical Review A*, **44**(11), 7144 (1991). <https://doi.org/10.1103/PhysRevA.44.7144>
- [4] M.H. Chen, and B. Crasemann, *Physical Review A*, **35**(11), 4839 (1987). <https://doi.org/10.1103/PhysRevA.35.4839>
- [5] J.H. Blake, P.H. Heckmann, and E. Träbert, *Physica Scripta*, **32**(5), 509 (1985). <https://doi.org/10.1088/0031-8949/32/5/010>
- [6] T.W. Tunnell, and C.P. Bhalla, *Physics Letters A*, **67**(2), 119 (1978). [https://doi.org/10.1016/0375-9601\(78\)90038-5](https://doi.org/10.1016/0375-9601(78)90038-5)
- [7] J.A. Kernahan, E.H. Pinnington, and K.E. Donnelly, *Physics Letters A*, **57**(4), 323-324 (1976). [https://doi.org/10.1016/0375-9601\(76\)90595-8](https://doi.org/10.1016/0375-9601(76)90595-8)
- [8] Y. Baudinet-Robinet, P.D. Dumont, E. Biémont, and N. Grevesse, *Physica Scripta*, **11**(6), 371 (1975). <https://doi.org/10.1088/0031-8949/11/6/006>
- [9] J.A. Kernahan, A.E. Livingston, and E.H. Pinnington, *Canadian Journal of Physics*, **52**(19), 1895 (1974). <https://doi.org/10.1139/p74-250>
- [10] P.D. Dumont, *Physica*, **62**(1), 104 (1972). [https://doi.org/10.1016/0031-8914\(72\)90152-8](https://doi.org/10.1016/0031-8914(72)90152-8)
- [11] J. Desesquelles, *Annales de Physique*, **14**(6), 71 (1971). <https://doi.org/10.1051/anphys/197114060071>
- [12] M.R. Lewis, T. Marshall, E.H. Carnevale, F.S. Zimnoch, and G.W. Wares, *Radiative Physical Review*, **164**(1), 94 (1967). <https://doi.org/10.1103/PhysRev.164.94>
- [13] L. Heroux, *Physical Review*, **153**(1), 156 (1967). <https://doi.org/10.1103/PhysRev.153.156>
- [14] H.G. Berry, W.S. Bickel, S. Bashkin, J. Désesquelles, and R.M. Schectman, *JOSA*, **61**(7), 947 (1971). <https://doi.org/10.1364/JOSA.61.000947>
- [15] E. Biemont, and N. Grevesse, *Atomic Data and Nuclear Data Tables*, **12**(3), 217 (1973). [https://doi.org/10.1016/0092-640X\(73\)90011-9](https://doi.org/10.1016/0092-640X(73)90011-9)
- [16] R. Siddiq, M.N. Hameed, M.H. Zaheer, M.B. Khan, and Z. Uddin, *Beni-Suef University Journal of Basic and Applied Sciences*, **11**(1), 42 (2022). <https://doi.org/10.1186/s43088-022-00224-0>
- [17] M. Saeed, S. Raza, and Z. Uddin, *Jordan Journal of Physics*, **18**(5), (2023).
- [18] M. Saeed, S.U. Rehman, M.M. Khan, and Z. Uddin, *East European Journal of Physics*, **2**, 165 (2023). <https://periodicals.karazin.ua/eejp/article/view/21663/20144>
- [19] U. Fano, J.W. Cooper, *Rev. Mod. Phys.* **40**(3), 441 (1968). <https://doi.org/10.1103/RevModPhys.40.441>

#### СЕРЕДНИЙ ЧАС ЖИТТЯ РІВНІВ ns, np, nd та nf у N V

Рівзана Сіддік<sup>a</sup>, Рухі Зафар<sup>b</sup>, Салман Раза<sup>a</sup>, С.М. Зішан Ікбал<sup>a</sup>, Захір Уддін<sup>a</sup>

<sup>a</sup>Кафедра фізики, Університет Карачі, Карачі, Пакистан

<sup>b</sup>Кафедра фізики, Університет інженерії та технології NED, Карачі, Пакистан

Азот є одним із ключових елементів еволюції та формування зоряних об'єктів. Атмосфера Землі містить 21% кисню і 78% азоту; ці два гази викликають полярне сяйво, коли з ними стикаються іони сонячного вітру в іоносфері. Деякі аерозолі з азоту та кисню також знаходяться в атмосфері. Азот, водень, вуглець і кисень є головними причинами виникнення життя на Землі. Спектр іонів азоту (N V) досліджено за допомогою квантової теорії дефектів (КТД) і чисельного кулонівського наближення (НКА). N V має два електрони в ядрі з ядром і один електрон поза ядром. Це робить його подібним до водню або літію. У першій частині за допомогою QDT розраховано енергії ns, np, nd та nf до  $n < 30$ . У другій частині довжини хвиль були розраховані з використанням параметрів енергії та сили лінії за допомогою NCA. Доступно дуже мало експериментальних даних щодо тривалості життя та ймовірності переходу; однак Biemont et al. розрахували час життя 48 рівнів N V, використовуючи кулонівське наближення. У цьому дослідженні ми розрахували тривалість життя 196 мультиплетів N V. Результати порівнюються з доступними експериментальними та теоретичними тривалістю життя; У цій роботі було знайдено відмінну відповідність між відомими і розрахованими часами життя. Тривалість життя 100 мультиплетів представлена вперше. Часи життя кожного ряду Рідберга N V були підібрані поліномом третього ступеня яким представлено час життя кожного ряду.

**Ключові слова:** іон азоту (N V); терміни життя; квантова теорія дефектів; числова кулонівська апроксимація; літійоподібні іони

## INVESTIGATION OF DEFECT FORMATION IN SILICON DOPED WITH SILVER AND GADOLINIUM IMPURITIES BY RAMAN SCATTERING SPECTROSCOPY<sup>†</sup>

 Sharifa B. Utamuradova<sup>a†</sup>, Shakhrukh Kh. Daliev<sup>a‡</sup>,  Elmira M. Naurzalieva<sup>a\*</sup>,  
Xushnida Yu. Utemuratova<sup>b\*</sup>

<sup>a</sup>*Institute of Semiconductor Physics and Microelectronics of National University of Uzbekistan, Tashkent, Uzbekistan*

<sup>b</sup>*Karakalpak State University, Nukus, Karakalpakstan*

\*Corresponding Author e-mail: [n.elmira0504@gmail.com](mailto:n.elmira0504@gmail.com),

<sup>†</sup>E-mail: [sh-utamuradova@yandex.ru](mailto:sh-utamuradova@yandex.ru); <sup>‡</sup>E-mail: [shakhrukh@mail.ru](mailto:shakhrukh@mail.ru), \*E-mail: [utemuratova.kh@yandex.ru](mailto:utemuratova.kh@yandex.ru)

Received July 10, 2023; revised July 21, 2023; accepted July 23, 2023

Silicon doped with gadolinium and silver impurities were studied using a Renishaw InVia Raman spectrometer. Registration and identification of both crystalline and amorphous phase components in the samples was carried out. Some changes are observed in the Raman spectra of gadolinium-doped silicon samples compared to the initial sample. It has been experimentally found that an increase in the silver impurity concentration in gadolinium-doped silicon leads to a smoothing of the Raman spectrum, which indicates the formation of a more perfect crystal structure.

**Keywords:** Silicon, Gadolinium, Silver, Raman spectrum, Doping, Complex defects

**PACS:** 42.55.Ye, 61.72.Yx, 61.72.Tt

### INTRODUCTION

In recent years, silicon structures have been actively studied both theoretically and experimentally in order to realize their possible applications. Structured silicon is currently of great interest, since silicon itself is an extremely promising material not only for electronics, but also for optoelectronics and solar cells [1-3].

For many years, Raman scattering has become a standard tool for studying the structure of silicon crystal [4-7]. Raman scattering studies of materials give us information about energy dispersion, structure, bonds, and defects. The analysis of structures is usually based on the phonon confinement model, in which the finite size of crystallites is taken into account by estimating the efficiency of phonon scattering. Constraint effects in structures lead to modification of the electronic, optical, and vibrational properties. It should be noted that while the Raman spectrum of crystalline silicon has been sufficiently well studied, the Raman spectra of silicon doped with transition and rare earth metals have not yet been studied in full.

In this paper, we present the spectra of one- and two-phonon Raman scattering of light from single-crystal silicon doped with Ag and Gd atoms.

### EXPERIMENTAL PART

Samples of n-Si and p-Si with initial resistivity from 1 to 100 Ohm·cm were chosen for the study. Doping of the samples with Ag and Gd impurities was carried out sequentially by the thermal diffusion method. Before doping, the samples were subjected to chemical cleaning and etching, while the oxide layers were removed from the surface of the samples using an HF solution. After thermal degassing of the samples, films of high-purity gadolinium and silver impurities (99.999%) were deposited on clean Si surfaces using vacuum deposition. Vacuum conditions in the volume of the working chamber of the order of  $10^{-6}$ - $10^{-7}$  Torr were provided by an oil-free vacuum pumping system.

Before diffusion annealing, the samples were placed in evacuated quartz ampoules. The diffusion of Ag impurities into the Si volume was provided by heating the deposited samples in a diffusion furnace at a temperature of 1100°C, with a heating duration of 7-10 hours, followed by rapid cooling. To study the interaction of impurity atoms in silicon, it is necessary not only to uniformly dope the material, but also to maximize the concentration. In this regard, we not only took into account the mechanisms of diffusion and solubility in more detail, but also the optimal conditions for doping silicon with these impurity atoms.

Doped silicon samples were studied using a Renishaw InVia Raman spectrometer equipped with a confocal microscope. The Raman spectra were excited by a laser with a wavelength of 785 nm. The spectral resolution was  $\leq 0.5$  cm<sup>-1</sup> in the visible region. Brightness > 30% provided high resolution with maximum stability. Measurement reproducibility  $\leq 0.1$  cm<sup>-1</sup>. The measurements used a diffraction grating with 1200 lines/mm and a standard Renishaw CCD detector. The laser power was varied to provide optimal experimental conditions. The minimum power at which the signal could be measured was limited by the signal-to-noise resolution of the detector in the spectrometer. A×50 lens was used. The exposure time was 10 s, the diameter of the laser spot on the sample was 10 μm. All measurements were carried out at room temperature in ambient atmosphere.

<sup>†</sup> Cite as: S.B. Utamuradova, S.Kh. Daliev, E.M. Naurzalieva, X.Yu. Utemuratova, East Eur. J. Phys. 3, 430 (2023), <https://doi.org/10.26565/2312-4334-2023-3-47>

© S.B. Utamuradova, S.Kh. Daliev, E.M. Naurzalieva, X.Yu. Utemuratova, 2023

### RESULTS AND THEIR DISCUSSION

Under normal conditions (standard pressure and temperature), silicon crystallizes into the diamond lattice structure. The diamond structure of silicon allows the presence of only one Raman active phonon of the first order, located at the center of the Brillouin zone (BZ), which corresponds to a phonon wave vector of  $520.0 \pm 1.0 \text{ cm}^{-1}$  with a full width at half maximum (FWHM) of  $3.5 \text{ cm}^{-1}$ .

The Raman spectra of an n-type silicon sample doped with Gd and Ag impurity atoms are shown in Fig. 1a. The Raman spectrum of Si<Gd> samples show a high peak in the region of  $521\text{-}522 \text{ cm}^{-1}$ . Intensity of first-order scattering due to optical phonons (TO - transverse optical vibrations, LO - longitudinal optical vibrations) at the central point  $\Gamma$  of the Brillouin zone (BZ).

In the Raman spectrum of Si<Ag> samples, a gentle slope of the main Si peak on the left wing in the region at  $303\text{-}489 \text{ cm}^{-1}$  (Fig. 1b) is observed. It indicates the presence of an Ag-O type bond vibration [7]. The authors of [8] in this region observed modes at  $302, 379, 429, 467,$  and  $487 \text{ cm}^{-1}$  associated with Raman vibrations of Ag-O. The violation of the symmetry of the peak at  $521 \text{ cm}^{-1}$  of the Raman spectrum at  $1100 \text{ }^\circ\text{C}$  is associated with the formation of interstitial defects, since in the silicon lattice at this temperature an intense precipitation of free interstitial oxygen is observed [9]. As is known, the precipitates of the first phase of  $\text{SiO}_2$  have a strong bond, and the concentration of Ag-O complexes under such a diffusion regime was insufficient for detection in the Raman spectrum.

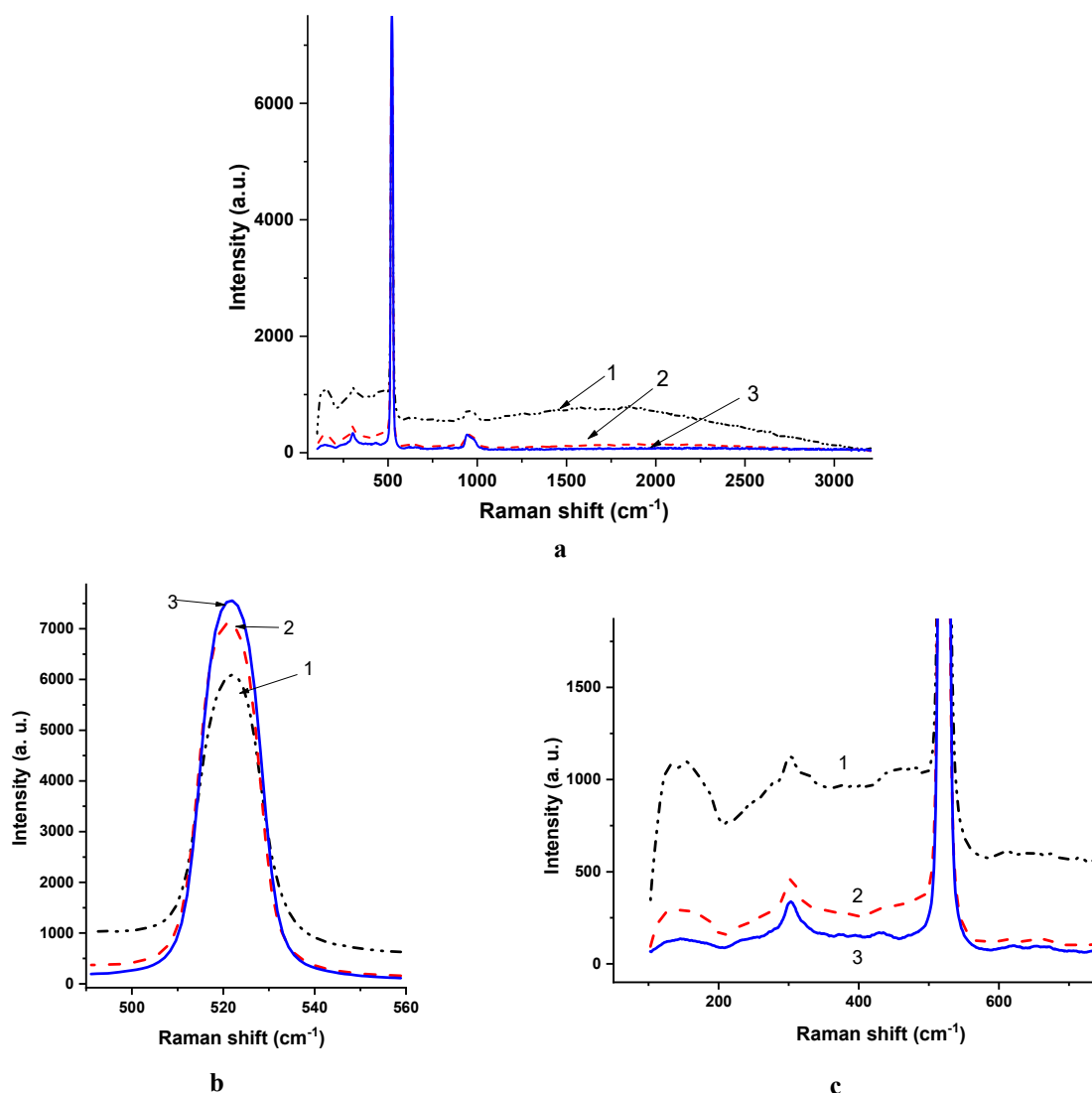


**Figure 1.** Raman spectrum of n-type silicon doped with Gd and Ag impurities: 1- Raman spectrum of Si<Gd> samples, 2- Raman spectrum of Si<Ag> samples, 3- Raman spectrum of Si<Gd, Ag> samples.

In contrast to the  $521 \text{ cm}^{-1}$  mode, in the Raman spectrum of the Si<Gd> samples one can observe a peak having several vibrational modes. Using the Gaussian distribution of this peak (Fig. 2a), it was found that the Raman scattering at  $123$  and  $186 \text{ cm}^{-1}$  belongs to the vibrational modes of the first and second order of Gd [8-10], and the  $150 \text{ cm}^{-1}$  mode belongs to the first-order scattering by acoustic phonons (TA), which characterizes the  $\text{SiO}_2$  bond. The last peak indicates the presence of silicon in the amorphous state [9-11]. A peak in the region  $420\text{-}500 \text{ cm}^{-1}$  with a weak intensity is the result of scattering by optical phonons (LO) at  $440 \text{ cm}^{-1}$  and vibrations of the Gd-O structure (Fig. 2b).



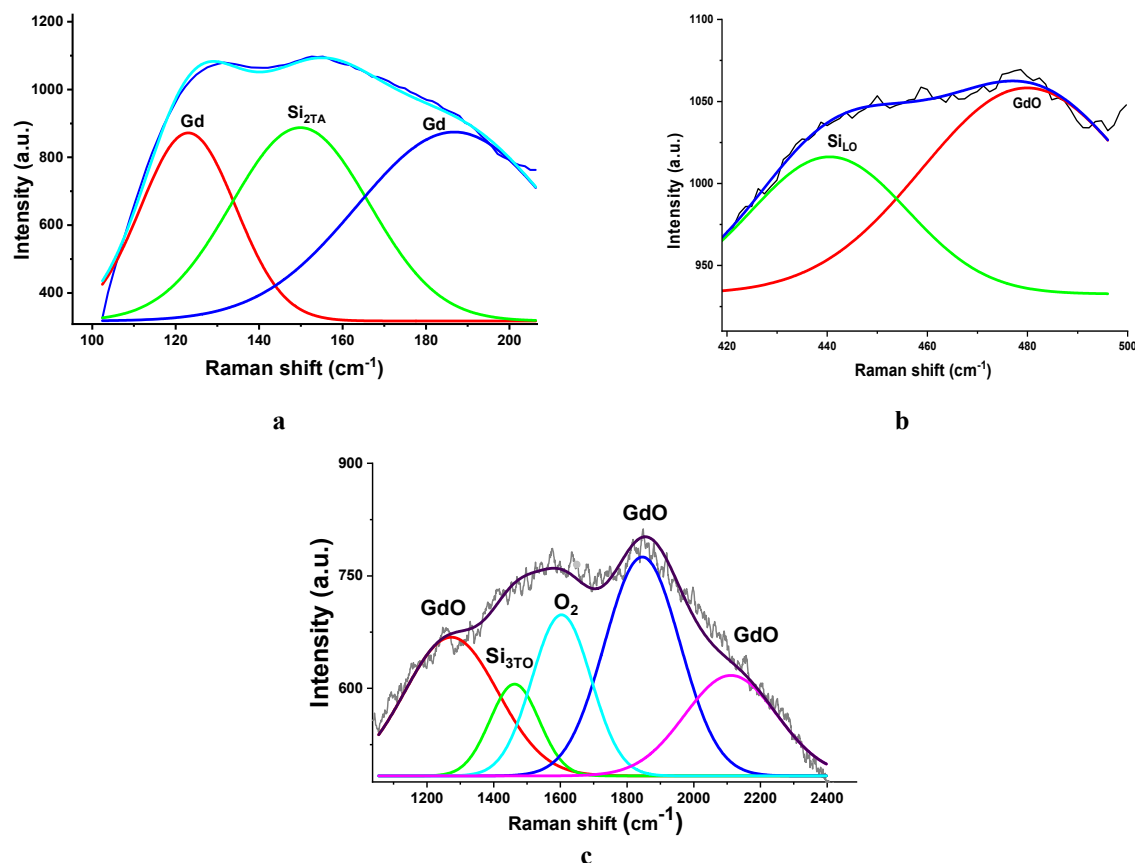


**Figure 2.** Gaussian distribution of peaks in the region (a) 102-206  $\text{cm}^{-1}$  and (b) 420-500  $\text{cm}^{-1}$  and (c) 1046-3176  $\text{cm}^{-1}$

The second order spectrum is much weaker than the first order LTO ( $\Gamma$ ) peak with characteristics in the range of 100-1100  $\text{cm}^{-1}$ . The second-order spectrum of transverse 2TA acoustic phonons is clearly observed near 303  $\text{cm}^{-1}$ . Some authors suggest that this peak corresponds to the LA modes [10-12], but there is no exact confirmation of this fact. We are probably observing a superposition of transverse and longitudinal acoustic modes. There is also a broad peak between 900–1000  $\text{cm}^{-1}$ , which is due to the scattering of several transverse optical phonons  $\sim$ 2TO phonons [11-13].

The broad peak in the region of 1100–2400  $\text{cm}^{-1}$  is associated with vibrations of Si, Gd, and O atoms, since such scattering was not observed in the original silicon. The broadening of the peak may be due to the high density of defects and local composition fluctuations [12-14]. The procedure for approximating the spectral bands of the Raman spectrum (Fig. 2c) performed using the standard software option of the spectrometer showed peaks with a Gaussian distribution located at 1273, 1462, 1600, 1845, and 2111  $\text{cm}^{-1}$ . Comparing literature data, it was found that the modes at 1273, 1845, and 2111  $\text{cm}^{-1}$  are associated with Raman vibrations of the Gd–O structure [13-15]. Whereas, the peaks at 1462 and 1600  $\text{cm}^{-1}$  refer to vibrations of Si scattering of the third order due to optical phonons (TO) [14-16] and vibrations of interstitial oxygen ( $\text{O}_2$ ), respectively [15-17].

As can be seen from Fig. 1a, the Raman spectrum of the Si<Gd> sample smoothes out after the introduction of the Ag impurity. The Raman spectrum of the main Si peak with a Gaussian distribution was also obtained and data on the peak position, peak intensity, and full width at half maximum (FWHM) were analyzed. As indicated in Table 1, the intensity and FWHM changed significantly in the Si<Gd, Ag> samples. At the same time, the position of the peak remained almost unchanged. A higher peak position at lower FWHM values corresponds to a higher crystallization quality [11-13]. This indicates that the presence of Ag atoms in doped Si, Gd impurities increases the degree of perfection of the crystal.

**Table 1.** Raman peak parameters of the samples.

Sample	Peak position, $\text{cm}^{-1}$	Intensity, a.u.	FWHM, $\text{cm}^{-1}$
Si<Gd>	521.62	6621	15
Si<Ag>	521.23	7098	13.38
Si<Gd, Ag>	521.68	7503	13.5

It was noted that the scattering in the range of 102-206  $\text{cm}^{-1}$  and 1100-2400  $\text{cm}^{-1}$  associated with Gd, Si and O atoms, after doping with Ag impurity atoms, is completely smoothed out as the concentration of silver atoms increases. It is likely that in the process of diffusion, silver atoms in silicon form neutral clusters and structural defects, such as Ag-Gd and Ag-O, due to which the intensity of this peak decreases. A change in the oxygen concentration in silicon upon

doping with silver was also observed by us earlier [16-18], when, based on the analysis of IR absorption spectra, it was shown that the concentration of optically active oxygen ( $N_0^{opt}$ ) in samples of silicon doped with silver was, on average, 10-25% less than in controls.

### CONCLUSION

The applied experimental procedure made it possible to obtain characteristic Raman spectra of silicon doped with Gd and Ag impurities. An analysis of the Raman spectra showed that, in contrast to the fundamental vibrations of silicon, the Raman spectrum of the Si<Gd> samples exhibit peaks characteristic of the first and second order scattering of the Gd impurity. It is shown that in the process of diffusion, silver atoms in silicon form neutral complex defects of the Ag-O type, which is typical for the case of a decrease in the oxygen concentration in silicon. It was also revealed that the presence of Gd atoms in the volume of Si, with the diffusion introduction of silver atoms, leads to the formation of aggregates of the Ag-Gd type, which, in turn, leads to a smoothing of the Raman spectrum and an improvement in the defect structure of the Si single crystal.

### ORCID

©Sharifa B. Utamuradova, <https://orcid.org/0000-0002-1718-1122>; ©Elmira M. Naurzalieva, <https://orcid.org/0000-0002-5110-1851>

### REFERENCES

- [1] Kh.S. Daliev, Sh.B. Utamuradova, O.A. Bozorova, and Sh.Kh. Daliev, *Geliotekhnika*. **41**(1), 80 (2005).
- [2] Kh.S. Daliev, Sh.B. Utamuradova, I.Kh. Khamidzhonov, A.Zh. Akbarov, I.K. Mirzairova, and Zh. Akimova, *Inorganic Materials*, **37**(5), 436 (2001). <https://doi.org/10.1023/A:1017556212569>
- [3] B.E. Egamberdiev, Sh.B. Utamurodova, S.A. Tachilin, M.A. Karimov, K.Yu. Rashidov, A.R. Kakhramonov, M.K. Kurbanov, et al., *Applied Solar Energy*, **58**(4), 490 (2022). <https://doi.org/10.3103/S0003701X22040065>
- [4] Sh.B. Utamuradova, A.V. Stanchik, K.M. Fayzullaev, and B.A. Bakirov, *Applied Physics*, (2), 33 (2022). [https://applphys.orion-ir.ru/appl-22/22-2/PF-22-2-33\\_RU.pdf](https://applphys.orion-ir.ru/appl-22/22-2/PF-22-2-33_RU.pdf) (in Russian)
- [5] M. Yang, D. Huang, P. Hao, F. Zhang, X. Hou, and X. Wang, *J. Appl. Phys.* **75** (1), 651 (1993). <https://doi.org/10.1063/1.355808>
- [6] H. Tanino, A. Kuprin, and H. Deai, *Phys. Rev. B*, **53** (4), 1937 (1996), <https://doi.org/10.1103/PhysRevB.53.1937>
- [7] Sh.B. Utamuradova, Sh.Kh. Daliyev, K.M. Fayzullayev, D.A. Rakhmanov, and J.Sh. Zarifbayev, *New Materials, Compounds and Applications*, **7**(1), 37 (2023). [http://jomardpublishing.com/UploadFiles/Files/journals/NMCA/V7N1/Utamuradova\\_et\\_al.pdf](http://jomardpublishing.com/UploadFiles/Files/journals/NMCA/V7N1/Utamuradova_et_al.pdf)
- [8] N.R.C. Raju, K.J. Kumar, and A. Subrahmanyam, *AIP Conference Proceedings*, **1267**(1), 1005 (2010). <https://doi.org/10.1063/1.3482261>
- [9] Sh.B. Utamuradova, Kh.S. Daliev, Sh.Kh. Daliev, and K.M. Fayzullaev, *Applied Physics*, (6), 90 (2019).
- [10] T. Grzyb, R.J. Wiglusz, V. Nagirnyi, A. Kotlov, and S. Lisa, *Dalton Trans.* **43**(18), 6925 (2014), <https://doi.org/10.1039/C4DT00338A>
- [11] M. Ivanda, O. Gamulin, and W. Kiefer, *Journal of Molecular Structure*. **480–481**, 651 (1999), [https://doi.org/10.1016/s0022-2860\(98\)00922-3](https://doi.org/10.1016/s0022-2860(98)00922-3)
- [12] W. Wei, *Vacuum*. **81**(7), 857 (2007). <https://doi.org/10.1016/j.vacuum.2006.10.005>
- [13] D. Abidi, B. Jusserand, and J.-L. Fave, *Phys. Rev. B*, **82**(7), 075210 (2010), <https://doi.org/10.1103/PhysRevB.82.075210>
- [14] C. Smit, R.A. C.M.M. van Swaaij, H. Donker, A.M.H.N. Petit, W.M.M. Kessels and M.C.M. van de Sanden, *Journal of Applied Physics* **94**(5), 3582 (2003), <https://doi.org/10.1063/1.1596364>
- [15] A.M. Grishin, A. Jalalian, and M.I. Tsindlekht, *AIP Advances* **5**(5), 057104 (2015), <https://doi.org/10.1063/1.4919810>
- [16] P. G. Spizzirri, J.-H. Fang, S. Rubanov, E. Gauja, S. Praver, *Materials Forum*. **34**, (2010).
- [17] S. Agnello, D. Di Francesca, A. Alessi, G. Iovino, M. Cannas, S. Girard, A. Boukenter, and Y. Ouerdane, *Journal of Applied Physics*. **114**(10), 104305 (2013), <https://doi.org/10.1063/1.4820940>
- [18] Sh.B. Utamuradova, and E.M. Naurzalieva, *Semiconductor Physics and Microelectronics*. **4**(1), 8 (2022) (in Russian)

### ДОСЛІДЖЕННЯ ДЕФЕКТОУТВОРЕННЯ КРЕМНІЮ, ЛЕГОВАНОГО ДОМІШКАМИ СРІБЛА ТА ГАДОЛІНІЮ, МЕТОДОМ СПЕКТРОСКОПІЇ КОМБІНАЦІЙНОГО РОЗСІЮВАННЯ

Шаріфа Б. Утамурадова<sup>а</sup>, Шахрух Х. Далієв<sup>а</sup>, Ельміра М. Наурузалієва<sup>а</sup>, Хушніда Ю. Утемуратова<sup>б</sup>

<sup>а</sup>Інститут фізики напівпровідників та мікроелектроніки Національного університету Узбекистану, Ташкент, Узбекистан  
<sup>б</sup>Каракалпакський державний університет, м. Нукус, Каракалпакстан

Кремній, легований домішками гадолінію та срібла, досліджували на раманівському спектрометрі Renishaw InVia. Проведено реєстрацію та ідентифікацію компонентів як кристалічної, так і аморфної фази у зразках. Спостерігаються деякі зміни спектрів комбінаційного розсіювання зразків кремнію, легованих гадолінієм, проти вихідним зразком. Експериментально встановлено, що збільшення концентрації домішки срібла в легованому кремнії гадолінієм призводить до згладжування спектра комбінаційного розсіювання, що свідчить про формування більш досконалої кристалічної структури.

**Ключові слова:** кремній; гадоліній; срібло; спектри комбінаційного розсіювання; легування; складні дефекти

## ISOLATION OF RESPONSIVE ELEMENTS OF PLANAR MULTI-ELEMENT PHOTODIODES<sup>†</sup>

Mykola S. Kukurudziak<sup>a,b</sup>

<sup>a</sup>*Rhythm Optoelectronics Shareholding Company, Holovna str. 244, 58032, Chernivtsi, Ukraine*

<sup>b</sup>*Yuriy Fedkovych Chernivtsi National University, Kotsyubyns'kogo str. 2, 58012, Chernivtsi, Ukraine*

*E-mail: mykola.kukurudzyak@gmail.com*

Received July 15, 2023; revised July 30, 2023; accepted August 10, 2023

In the mass production of multi-element silicon *p-i-n* photodiodes, the problem of systematic rejection of products due to a decrease in the insulation resistance between the active elements of photodetectors has been revealed. The purpose of this work is to study the causes of insulation resistance degradation and to establish optimal methods for avoiding this phenomenon. A comparative analysis of three insulation methods was carried out: classical insulation by the surface of a non-conductive substrate and a dielectric layer; insulation by means of mesaprofile grooves with a dielectric film; insulation by means of limitation of surface leakage channels isotopic with the substrate material (in this case, *p*<sup>+</sup>-type) formed in the gaps between active elements. The study found that the reason for the deterioration of the insulation resistance between the active elements of photodiodes is the presence of conductive inversion channels at the Si-SiO<sub>2</sub> interface due to the use of silicon with high resistivity. One mechanism for the formation of inversion channels is the redistribution of impurities in the masking oxide (in particular, phosphorus) and their diffusion to the interface during thermal operations. Another mechanism for the formation of inversion layers is the diffusion of boron from silicon into SiO<sub>2</sub> during heat treatment due to the fact that the boron segregation coefficient is less than one. In the manufacture of samples with insulation using non-conductive areas of the substrate, a decrease in insulation resistance was observed as the technological route was performed (after each subsequent operation, the resistance degraded). The degree of degradation can be reduced by reducing the duration of thermal operations. It has been shown that reducing the thickness of the masking oxide causes a decrease in insulation resistance. When using mesa-technology, it is possible to increase the insulation resistance by eliminating the high-temperature oxidation operation and, in fact, due to the absence of a masking coating during phosphorus deposition. Insulation by means of *p*<sup>+</sup>-type areas in the gaps between the active elements allows to obtain the highest insulation resistance values. The formation of these regions with a width of 100 μm in the gaps with a width of 200 μm allowed us to obtain an insulation resistance of 25-30 MΩ. To ensure the insulation of the active elements of photodiodes by this method, two thermal operations are added to the technological route. The number of thermal operations can be reduced by doping the entire silicon surface with a low boron concentration before forming a masking coating.

**Keywords:** *Silicon; Photodiode; Insulation resistance; Silicon oxide; Inversion layer*

**PACS:** 61.72.Ji, 61.72.Lk, 85.60.Dw

An important task of modern photoelectronics is to detect the coordinates of objects in space. Usually, multi-element coordinate photodiodes (PD) are used in coordinate determination systems. The coordinate PD is usually a two- or four-element photodiode on one semiconductor plate, in which the responsive elements (RE) are separated by gaps smaller than the size of the light probe [1]. To ensure the high responsivity of the used photodetectors, a high-resistance material is used. When we serially manufactured coordinate silicon PDs, we saw a slight decrease in the insulation resistance between the REs, and in the case of the production of the PDs with a guard ring (GR), a decrease in the insulation resistance between the REs and the GR was also observed. This contributed to the growth of the dark currents of the active elements and the photocoupling coefficient between the elements. When investigating the reasons for the deterioration of the insulation resistance, it was established that when using high-resistance silicon at the Si-SiO<sub>2</sub> interface, the formation of conductive *n*-type inversion channels is possible [2-4]. Accordingly, the presence of these channels contributes to the deterioration of PDs parameters. This problem required research to establish methods of its avoidance or minimization of the influence on the insulation resistance between the REs.

When reviewing the literature, it was seen that most of the works are devoted to the methods of isolation of integrated circuits (ICs). Thus, methods of isolation of IC elements allow to manufacture devices on conductive and non-conductive substrates. On the conductive substrate, the insulation of the IC elements is carried out by a *p-n*-junction and a thin dielectric film, and on the non-conductive one by insulation with air gaps and dielectric materials [5]. In particular, [6] describes the principle of isolation of active IC elements using the isoplanar method. The method is combined. In this technology, the insulation of the vertical walls of the components is carried out by a thick layer of silicon dioxide, which extends from the surface of the epitaxial layer to the *n*<sup>+</sup>-hidden layer; the isolation of the bottom part of the components is carried out by a reverse-biased *p-n*-junction. Another combined method of isolation of IC elements is epiplanar [7]. It was implemented after the development of local epitaxial growth of silicon on certain areas of the substrate surface. The method of selective epitaxial growth of silicon allows the formation of IC components, providing self-connection of isolated regions and the *n*<sup>+</sup>-hidden layer. One of the new "exotic" insulation methods is the IPOS technology - insulation with oxidized porous silicon. In this technological method, two main processes can be distinguished. The first is a selective

<sup>†</sup> *Cite as:* M.S. Kukurudziak, East Eur. J. Phys. 3, 434 (2023), <https://doi.org/10.26565/2312-4334-2023-3-48>

© M.S. Kukurudziak, 2023

anodic dissolution of silicon in hydrofluoric acid, in which porous silicon is formed in the treated area. The second is heat treatment in an oxidizing environment, in which porous silicon oxidizes at a high rate due to the presence of pores and strongly developed surface. As a result of such selective processing are formed silicon regions are isolated from the sides by silicon dioxide. At this, unlike isoplanar technology, is excluded in this case the need for long-term high-temperature oxidation [8]. There are also methods of isolating IC elements using etched grooves on the surface of the substrates. In particular, insulation using V-grooves, filled polycrystalline silicon (VIP-method, VIP-V-brave isolation polysilicon) is based on vertical anisotropic etching of silicon substrates with formation of V-shaped grooves filled with polycrystalline silicon [9, 10]. V-ATE - technology (V-ATE - vertical anisotropic etch) is available a variant of the method of combined isolation of components, in which the separation tracks are not filled with silicon dioxide or others insulating materials [10, 11].

However, no information was found about the optimal options for isolating the REs of multi-element photodiodes. But it is known that often photodiode matrices or actually multi-element photodetectors are made in the form of mesa-structures [12, 13]. Classical planar structures are usually insulated with silicon oxide films formed in a single technological process with diffusion of acceptors or donors or silicon nitride films [4, 14].

Ensuring proper insulation resistance of multicellular photodetectors is an urgent scientific and technical task, and, accordingly, the purpose of this work is to establish the causes of insulation resistance degradation between the active elements of photodiodes, to study insulation methods, and to establish optimal technological options that allow obtaining high insulation resistance of the active elements of the PDs among themselves.

### EXPERIMENTAL

It was decided to investigate the influence of the isolation methods of REs based on silicon four-element  $p$ - $i$ - $n$  PDs with a guard ring. Production was carried out using diffusion-planar technology according to the technological modes of diffusion processes given in [15]. The starting material was single-crystal dislocation-free  $p$ -type silicon with orientation [111],  $\rho \approx 17$ -20 k $\Omega$ ·cm.

We will consider the resistance between all REs and GR ( $R_{con}$ ) as a parameter that allows us to evaluate the degree of insulation of active elements. Determination of  $R_{con}$  was carried out according to the method given in [1] with  $U_{bias}=2$  V and load resistance  $R_l=10$  k $\Omega$ .

A comparative analysis of three methods of isolation was carried out: classical – isolation with the surface of a conditionally non-conductive substrate and a dielectric layer (PD<sub>1</sub>) (Fig. 1); insulation using mesa-profile grooves with a dielectric film (similar to the V-ATE method) (PD<sub>2</sub>); and isolation using surface leakage restriction channels isotopic with the substrate material (in this case  $p^+$ -type) formed in the gaps between the active elements (PD<sub>3</sub>). In this case,  $p^+$ -type regions will be formed by diffusion of boron into the front layer of the substrate.

The technological process of production of PD<sub>1</sub> consisted of a complex of thermal operations and photolithography: semiconductor substrates (Fig. 2-5) were oxidized to obtain a masking coating (Fig. 2-3); photolithography was carried out to create windows for phosphorus diffusion; diffusion of phosphorus (predeposition) to the front side to create  $n^+$ -type REs (Fig. 2-1) and GR (Fig. 2-2); driving-in of phosphorus in an oxygen atmosphere to redistribute the alloying impurity, increase the depth of the  $n^+$ - $p$ -junction and form an anti-reflective coating (Fig. 2-4); diffusion of boron to the reverse side of the substrate to create a  $p^+$ -type ohmic contact (Fig. 2-8); photolithography for creating contact windows; sputtering of Cr-Au on the front and back sides (Fig. 2-6 and 7).

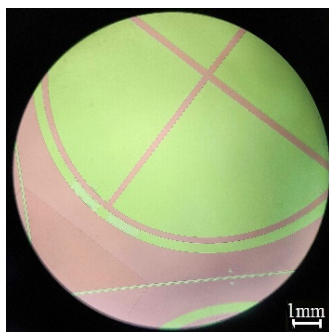


Figure 1. Image of a PD<sub>1</sub> crystal

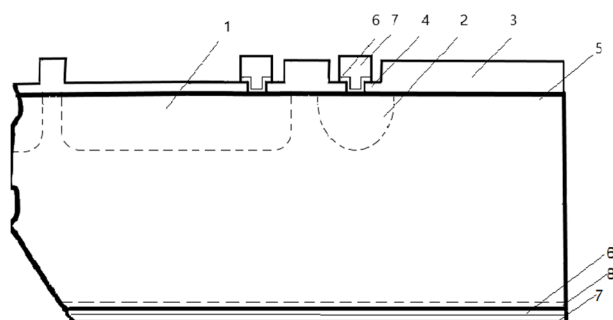


Figure 2. Schematic section of a part of the PD crystal: 1 –  $n^+$ -responsive element; 2 –  $n^+$ -guard ring; 3 – masking SiO<sub>2</sub>; 4 – anti-reflective SiO<sub>2</sub>; 5 –  $p$ -Si substrate; 6 – chrome sublayer; 7 – contact surface-Au; 8 – ohmic  $p^+$ -Si

Photodiodes with a mesa structure (Fig. 3) were manufactured according to the following technological route: predeposition of phosphorus to the front side to create  $n^+$ -type layer, etching the grooves of the mesa profile by the method of chemical dynamic polishing [16] to obtain REs (Fig. 4-1) and GR (Fig. 4-2), driving-in of phosphorus in an oxygen atmosphere to redistribute the alloying impurity, increase the depth of the  $n^+$ - $p$ -junction and form an anti-reflective coating (Fig. 4-3); diffusion of boron to the reverse side of the substrate to create a  $p^+$ -type ohmic contact (Fig. 4-4); sputtering of Cr-Au on the front and back sides (Fig. 4-5 and 6).

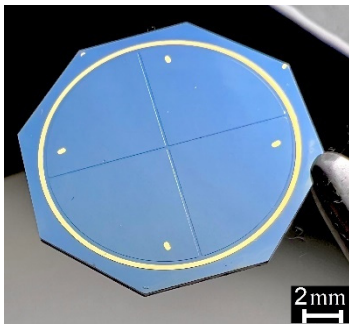


Figure 3. Image of a PD<sub>2</sub> crystal

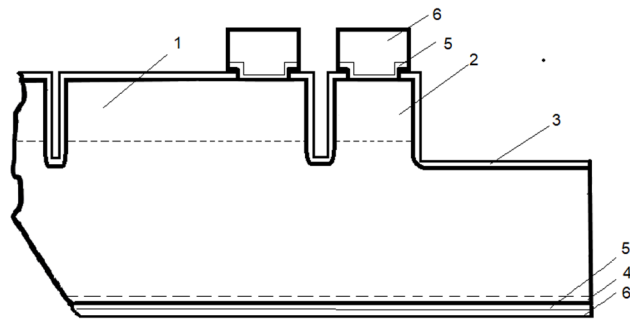


Figure 4. Schematic section of a part of the PD<sub>2</sub> crystal: 1 –  $n^+$ -responsive element; 2 –  $n^+$ -guard ring; 3 – anti-reflective SiO<sub>2</sub>; 4 – ohmic  $p^+$ -Si; 5 – chrome sublayer; 6 – contact surface-Au

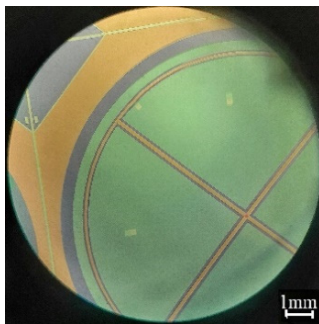


Figure 5. Image of fragment a PD<sub>2</sub> crystal

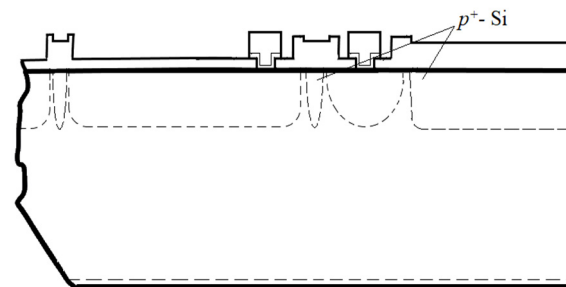


Figure 6. Image of a PD crystal with  $p^+$ -region between active elements

Photodiodes with surface leakage restriction channels isotypic with the substrate material (Fig. 5) were manufactured according to the following technological route: oxidation of silicon substrates to obtain a masking coating; photolithography for the formation of windows for boron diffusion; diffusion of boron to the front side of the crystal to obtain a  $p^+$ -region; oxidation / boron driving-in - to mask the  $p^+$ -layer and increase the depth of the  $p^+$ - $p$ -junction; photolithography for the formation of windows for phosphorus diffusion; diffusion/predeposition of phosphorus to obtain  $n^+$ -type REs and GR; phosphorus driving in - to increase the depth of the  $n^+$ - $p$ -junction and the formation of anti-reflective SiO<sub>2</sub>; diffusion of boron to the rear side of the substrate to create an ohmic  $p^+$ - layer and heterization of generation-recombination centers. A schematic cross-section of the PD<sub>3</sub> crystal can be seen in Fig. 6.

## RESULTS OF THE RESEARCH AND THEIR DISCUSSION

### A) Mechanisms of insulation resistance degradation.

It should be noted that one of the mechanisms for the formation of conductive inversion channels at the Si-SiO<sub>2</sub> interface and the reduction of insulation resistance between active elements is the redistribution of impurities in the masking oxide (including phosphorus) and their diffusion to the interface of the two phases during thermal operations, respectively, with an increase in the total duration of thermal operations, it is possible to doping of impurities in the silicon surface through the masking SiO<sub>2</sub> [17]. Therefore, in the formation of masking coatings, it is necessary to take into account not only the thickness of the oxide that masks the silicon from doping during the diffusion (predeposition) operation itself, but also the thickness that will mask during subsequent heat treatments. Thus, according to [18], a silicon oxide thickness of about 0.3  $\mu\text{m}$  completely masks silicon during phosphorus diffusion lasting 30 minutes at  $T = 1323 \text{ K}$ , but given that the predeposition operation is followed by a high-temperature phosphorus driving-in and boron diffusion operation, respectively, to take into account this duration of thermal operations, a masking coating thickness of 0.6 - 0.7  $\mu\text{m}$  should be used.

Another mechanism for the formation of inversion layers is the diffusion of boron from silicon into SiO<sub>2</sub> during heat treatment due to the fact that the boron segregation coefficient is below one [19]. Accordingly, with an increase in the duration of heat treatment, the degree of depletion of the silicon surface with boron increases and an inverted type of conductivity is observed.

### B) Investigation of the insulation resistance between the active elements of photodiodes isolated using sections of a non-conductive substrate and a dielectric layer.

In the manufacture of PD<sub>1</sub> samples, a decrease in insulation resistance was observed as the technological route was followed. Thus, in the trial batch of samples, the  $R_{con}$  after phosphorus diffusion, after boron diffusion, and after the metallization operation on the final crystals was monitored. After phosphorus diffusion, the  $R_{con}$  reached 10-25 M $\Omega$ . After boron diffusion  $R_{con} \approx 3$ -6.5 M $\Omega$ , and after the metallization operation  $R_{con} \approx 1.3$ -2 M $\Omega$ . The described phenomenon of

insulation resistance degradation between the REs and the GR is clearly explained by the above mechanisms of inversion layer formation. The degree of degradation can be reduced by reducing the duration of thermal operations (if possible). It should be noted that the decrease in  $R_{con}$  during Cr-Au sputtering operations is caused by heating the substrates to a temperature of 473-523 K.

It is worth noting that during the storage of unsealed PD crystals for a long time, a decrease in the insulation resistance between the REs and the GR is observed. Thus, storage of crystals for about 6 months leads to a 10-30-fold degradation of  $R_{con}$ . This is caused by the diffusion of impurities at room temperatures.

It was also decided to investigate the actual effect of the thickness of the masking  $\text{SiO}_2$  on the insulation resistance value. No change in  $R_{con}$  was observed when the thickness of the oxide was alternately reduced in the gaps between the REs and the GR of the final crystals. This confirms the fact that conductivity is formed at the interface between the two phases. Also, samples of PDs with different initial thicknesses of the masking coating were fabricated by changing the duration of thermal oxidation. The oxidation operation was carried out separately, and all other operations were carried out in a single technological cycle. Half of the batches had a masking coating thickness of 0.47  $\mu\text{m}$ , and the other half had a thickness of 0.61  $\mu\text{m}$ . By controlling the values of  $R_{con}$  after phosphorus diffusion, it was seen that samples with a smaller oxide film thickness had  $R_{con} \approx 5.4 - 5.8 \text{ M}\Omega$ , and samples with a larger oxide thickness had  $R_{con} \approx 8 - 10 \text{ M}\Omega$ . On the final crystals, samples with a smaller oxide thickness had  $R_{con} \approx 0.9 - 1.1 \text{ M}\Omega$ , and those with a larger one had  $R_{con} \approx 2 - 2.5 \text{ M}\Omega$ . It can be seen from this that a decrease in the thickness of the masking coating with a significant overall duration of thermal operations can lead to a decrease in the insulation resistance between the active elements of photodetectors according to the mechanisms described above. However, it should be noted that the values of dark currents of the PDs in the case of a shorter thermal oxidation operation are two times lower than in the case of a longer oxidation. This is probably due to a decrease in the amount of uncontrolled impurities introduced into the semiconductor volume during the high-temperature operation.

It should be noted that in the presence of inversion layers at the interface between the two phases, it is possible to increase the values of the dark currents of the guard rings ( $I_{GR}$ ) and responsive elements, but the latter react when the insulation resistance is reduced to tens of kilohms, and the GRs react even with a slight decrease in  $R_{con}$ . Thus, a graph of the dependence of the dark current of the guard rings on the voltage at different values of  $R_{con}$  was obtained (Fig. 7).

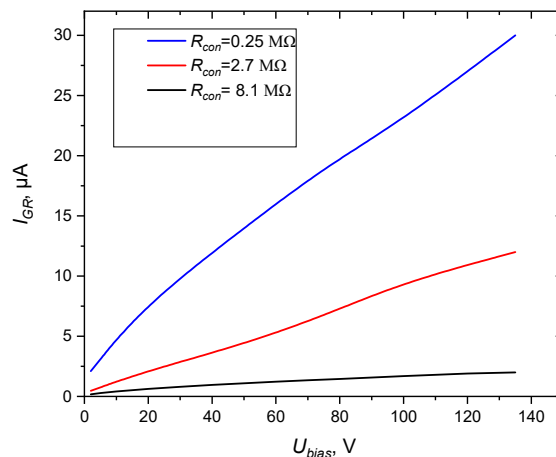


Figure 7.  $I$ - $V$  characteristic of  $\text{PD}_1$  at different values of  $R_{con}$

As can be seen from Fig. 7, when the insulation resistance between the active elements decreases, the degree of increase in the  $I_{GR}$  increases with an increase in the bias voltage. When testing the PDs at elevated temperatures, the increase in the dark currents of the guard rings is more pronounced and can manifest itself in the instability of the current values in time, i.e., an uncontrolled increase in  $I_{GR}$  is observed without an increase in bias voltage or temperature [20].

If reduced insulation resistance values are detected after the phosphorus diffusion stage, it is necessary to completely etch the masking and anti-reflective coating in hydrofluoric acid and repeat the phosphorus driving-in operation. This will remove the oxide with the inversion layers and form a new anti-reflective coating. However, we note that this manipulation allows us to correct only those samples in which the diffusion of impurities has occurred only to the interface between the two phases. In the case of doping the silicon surface through the masking oxide, it is worth etching the surface layers by chemical-dynamic polishing [16] or plasma chemical etching [21] method, but given that the  $p$ - $n$ -junctions have already been formed at this stage of manufacturing, these operations are complicated.

To assess the degree of undesirable doping of the silicon surface by measuring  $R_{con}$  before and after oxide etching. Thus, a study was conducted: the entire oxide film was removed from a PD crystal with  $R_{con} \approx 133 \text{ k}\Omega$  and a value of  $R_{con} \approx 157 \text{ k}\Omega$  was obtained. In this case, there was no significant increase in the insulation resistance after removing the oxide, indicating the presence of conductive channels on the silicon surface due to donor doping. Another case was also observed during the study: the entire oxide film was removed from the PD crystal with  $R_{con} \approx 3.3 \text{ k}\Omega$  and a value of  $R_{con} \approx 10 \text{ M}\Omega$  was obtained. This indicated that the conductive channels were formed at the Si- $\text{SiO}_2$  interface, but

the impurities did not diffuse into the silicon surface. Accordingly, in the second case, it is possible to repeat the phosphorus driving-in operation with positive results, and samples as in the first case can be restored only after a shallow etching of the plate surface. It is worth noting that the above study shows that the predominant mechanism of inversion channel formation is the redistribution of impurities in the oxide film. It should be added that the mechanism of formation of inversion layers due to the diffusion of boron into the SiO<sub>2</sub> is more effective at a significant duration of heat treatment.

Using the described method of isolation allows obtaining an isolation resistance of 1-10 MΩ, and it should be used in photodetectors with a relatively low bias voltage. When using silicon with  $\rho \geq 20$  kΩ, this method is ineffective.

### C) Investigation of the insulation resistance between the active elements of photodiodes isolated using mesa-profile grooves with a dielectric film

It is possible to increase the value of insulation resistance relative to PD<sub>1</sub> by using a crystal topology with a mesa profile. In the case of manufacturing samples using the PD<sub>2</sub> technology, it is possible to obtain  $R_{con} \approx 13-16$  MΩ. The reason for the increase in insulation resistance between the active elements is the absence of an oxidation operation (no masking SiO<sub>2</sub>) and a reduction in the total duration of thermal heating. In this case, the stage of formation of the anti-reflective oxide is followed by only one thermal operation - boron diffusion, which is low-temperature relative to the previous thermal operations. During boron diffusion, the probability of diffusion of uncontrolled impurities through the oxide is minimal. It is worth noting that an important factor in the increase in the  $R_{con}$  of PD<sub>2</sub> is the absence of phosphorus diffusion through the masking oxide windows, since the diffusion was carried out before the formation of anti-reflective SiO<sub>2</sub>, respectively, in this case there is no phenomenon of diffusion of phosphorus in the oxide to the surface of silicon during heat treatment.

Given that one of the factors of inversion channels formation is the diffusion of impurities from the masking oxide introduced during previous thermal operations, the question arises whether the masking coating cannot be removed after it has performed its functions, i.e. after the phosphorus predeposition operation. In this case, the anti-reflective oxide grown during the phosphorus driving-in will be a protective layer on the front side of the substrate during the diffusion of boron to the back side. To confirm or refute this statement, the experiment described above was carried out. Measuring the resistance of insulation between the REs and GR of final crystal, it was seen that serial samples had  $R_{con} \approx 4-5.7$  MΩ, and samples with masking oxide etched before phosphorus driving-in had  $R_{con} \approx 0.6-1$  MΩ. The experiment showed that the etching of the masking oxide after phosphorus predeposition is negative, but in the case of samples with mesostructures, the presence of only an anti-reflective coating contributes to an increase in  $R_{con}$ . Nevertheless, it should be borne in mind that PD<sub>2</sub> has one less high-temperature operation in the technological route than PD<sub>1</sub>. Although the described assumptions require additional research.

### D) Investigation of the insulation resistance between the active elements of photodiodes isolated using surface leakage restriction channels isotypic with the substrate material

Isolation of active photodiode elements by means of *p*-type regions in the gaps between the elements allows to obtain the highest values of insulation resistance. The formation of these regions with a width of 100 μm in the gaps with a width of 200 μm allowed us to obtain  $R_{con} \approx 25-30$  MΩ. It should be noted that the implementation of this method of isolation requires the introduction of two additional thermal operations - boron diffusion to the front side of the substrate and boron oxidation/driving-in of boron. This factor can contribute to an increase in dark currents and a decrease in responsivity due to the degradation of the lifetime of non-basic charge carriers and the resistivity of the material due to an increase in the total duration of thermal operations [1]. In order to avoid the above, it is worthwhile to carry out gettering of generation and recombination center operations with modes that allow restoring the above parameters [22].

It is worth noting that the PD<sub>3</sub> technological route can be shortened. For example, it is possible to diffuse boron simultaneously to the front side to form areas of leakage channel confinement and to the back side of the substrate to form an ohmic contact. However, in this case, there is a need to include additional operations to ensure masking of the *p*<sup>+</sup>-type areas on the front side, which will be without a masking coating after the boron diffusion operation.

By introducing the boron diffusion operation into the entire area of the substrate front side with a low concentration (the first thermal operation), it is possible to avoid the need for additional photolithography or operations to form masking coatings. The key aspect of this method is the low concentration of diffused boron, since with an increase in the impurity concentration, the PD may fail due to an avalanche-like increase in dark currents, since in this case the crystal structure will resemble an avalanche photodiode [23]. Low concentrations can be achieved by lowering the temperature or duration of the operation, and the most effective method is ion implantation. Thus, when the entire surface of the substrate was doped with boron with a surface resistance of  $R_S \approx 175-200$  Ω/□, it was possible to obtain  $R_{con} \approx 40$  MΩ on the final samples.

It should be noted that the introduction of a boron impurity into the substrate surface reduces the density of dislocations formed during phosphorus diffusion. Since dislocations are formed during phosphorus diffusion due to the mismatch of the radius of phosphorus and silicon atoms: phosphorus atoms are larger than silicon atoms, mechanical stresses arise due to this difference, which leads to the formation of structural defects [24]. And since the radius of boron atoms is smaller than that of silicon, this will compensate for mechanical stresses and reduce the probability of dislocation formation due to the described mechanism.

The method of isolation by *p*<sup>+</sup>-regions should be used at  $\rho \geq 20$  kΩ·cm, when using high bias voltages and when it is necessary to reduce the width of the gaps between the Res.

## CONCLUSIONS

A comparative analysis of three methods of isolation was carried out: classical – isolation with the surface of a conditionally non-conductive substrate and a dielectric layer (PD<sub>1</sub>); insulation using mesa-profile grooves with a dielectric film (PD<sub>2</sub>); and isolation using surface leakage restriction channels isotypic with the substrate material (in this case *p*<sup>+</sup>-type) formed in the gaps between the active element (PD<sub>3</sub>). The following conclusions were made during the research:

1. The reason for the degradation of the insulation resistance between the active elements of photodiodes is the presence of conductive inversion channels at the interface Si-SiO<sub>2</sub>.
2. One of the mechanisms for the formation of conductive inversion channels at the Si-SiO<sub>2</sub> interface and the reduction of insulation resistance between active elements is the redistribution of impurities in the masking oxide (including phosphorus) and their diffusion to the interface of the two phases during thermal operations. Another mechanism for the formation of inversion layers is the diffusion of boron from silicon into SiO<sub>2</sub> during heat treatment due to the fact that the boron segregation coefficient is below one.
3. In the manufacture of PD<sub>1</sub> samples, a decrease in insulation resistance was observed as the technological route was followed. The degree of degradation can be reduced by reducing the duration of thermal operations.
4. Reducing the thickness of the masking oxide causes a decrease in insulation resistance.
5. If reduced insulation resistance values are detected after the phosphorus diffusion stage, it is necessary to completely etch the masking and anti-reflective coating in hydrofluoric acid and repeat the phosphorus driving-in operation.
6. In the case of manufacturing samples using the PD<sub>2</sub> technology, it is possible to obtain  $R_{con} \approx 13\text{-}16 \text{ M}\Omega$ . The reason for the increase in insulation resistance between the active elements is the absence of an oxidation operation (no masking SiO<sub>2</sub>) and a reduction in the total duration of thermal heating.
7. Isolation of active photodiode elements by means of *p*<sup>+</sup>-type regions in the gaps between the elements allows to obtain the highest values of insulation resistance. The formation of these regions with a width of 100 μm in the gaps with a width of 200 μm allowed us to obtain  $R_{con} \approx 25\text{-}30 \text{ M}\Omega$ .
8. When the entire surface of the substrate was doped with boron with a surface resistance of  $R_s \approx 175\text{-}200 \text{ }\Omega/\square$ , it was possible to obtain  $R_{con} \approx 40 \text{ M}\Omega$  on the final samples. Introduction of a boron impurity into the substrate surface reduces the density of dislocations formed during phosphorus diffusion.

## ORCID

Mykola S. Kukurudziak, <https://orcid.org/0000-0002-0059-1387>

## REFERENCES

- [1] M. Kukurudziak, *Radioelectronic and Computer Systems*, **105**(1), 92 (2023). <https://doi.org/10.32620/reks.2023.1.07>
- [2] V.M. Lytvynenko, and I.M. Vikulin, *Bulletin of the Kherson National Technical University*, (**1**), 46 (2018). (in Ukrainian)
- [3] Yu.O. Kruglyak, and M.V. Strikha, *Sensor Electronics and Microsystem Technologies*, **16**(2), 5 (2019). <https://doi.org/10.18524/1815-7459.2019.2.171224> (in Ukrainian)
- [4] M.S. Kukurudziak, *East Eur. J. Phys.* **2**, 311 (2023), <https://doi.org/10.26565/2312-4334-2023-2-36>
- [5] M. Sartori, M. Arosio, and A. Baschiroto, in: *2023 IEEE 18th Conference on Ph. D Research in Microelectronics and Electronics (PRIME)*, 2023, <https://doi.org/10.1109/PRIME58259.2023.10161956>
- [6] A.N. Horban, and V.V. Kravchyna, *Tekhnol. Konstr. Elektron. Appar.* **3**, (2011). (in Ukrainian)
- [7] T. Piotrowski, M. Węgrzecki, M. Stolarski, and T. Krajewski, *Opto-Electronics Review*. **23**(4), 265 (2015), <https://doi.org/10.1515/oere-2015-0035>
- [8] G. Gautier, and P. Leduc, *Applied Physics Reviews*, **1**(1), (2014), <https://doi.org/10.1063/1.4833575>
- [9] M. Shan, C. Guo, Y. Zhao, Q. Chen, L. Deng, Z. Zheng, and C. Chen, *ACS Applied Nano Materials*, **5**(7), 10081 (2022). <https://doi.org/10.1021/acsnm.2c02689>
- [10] O.Yu. Nalivaiko, *Electronics NTB*, **6**, 134 (2022), <https://doi.org/10.22184/1992-4178.2022.217.6.134.140>, (in Russian)
- [11] H. Yagyu, T. Yamaji, M. Nishimura, and K. Sato, *Japanese journal of applied physics*, **49**(9R), 096503 (2010). <https://doi.org/10.1143/JJAP.49.096503>
- [12] K.O. Boltar, I.V. Chinareva, A.A. Lopukhin, and N.I. Yakovleva, *Appl. Phys.* **5**, 10 (2013).
- [13] M.S. Kukurudziak, and E.V. Maistruk, *Semicond. Sci. Technol.* **38**, 085007 (2023), <https://doi.org/10.1088/1361-6641/acdf14>
- [14] O.V. Dubikovskiy, *Bulletin of the National Academy of Sciences of Ukraine*, **2**, 79 (2023). <https://doi.org/10.15407/visn2023.02.079> (in Ukrainian)
- [15] M.S. Kukurudziak, *Semiconductor Physics, Quantum Electronics & Optoelectronics*, **25**(4), 385 (2022). <https://doi.org/10.15407/spqeo25.04.385>
- [16] M.S. Kukurudziak, *Surface Chemistry, Physics and Technology*, **14**(1), 42 (2023). <https://doi.org/10.15407/hftp14.01.042> (in Ukrainian)
- [17] M.M. Atalla, E. Tannenbaum, and E.J. Scheibner, *Bell System Tech. J.* **38**, 749 (1959). <http://bstj.bell-labs.com/BSTJ/images/Vol38/bstj38-3-749.pdf>
- [18] Sah S.T., Sello H., Sah C., and Tremere D.A., *J. Phys. Chem. Solids*, **11**, 288 (1959). [https://doi.org/10.1016/0022-3697\(59\)90229-X](https://doi.org/10.1016/0022-3697(59)90229-X)
- [19] H. Chen, K. Morita, X. Ma, Z. Chen, and Y. Wang, *Solar Energy Materials and Solar Cells*, **203**, 110169 (2019). <https://doi.org/10.1016/j.solmat.2019.110169>
- [20] M.S. Kukurudziak, *Journal of nano- and electronic physics*, **14**(1), 01023 (2022). [https://doi.org/10.21272/jnep.14\(1\).01023](https://doi.org/10.21272/jnep.14(1).01023)
- [21] K. Racka-Szmidt, B. Stonio, J. Żelazko, M. Filipiak, and M. Sochacki, *Materials*, **15**(1), 123 (2022). <https://doi.org/10.3390/ma15010123>



- [22] A.Y. Liu, D. Yan, and S.P. Phang, *Solar Energy Materials and Solar Cells*, **179**, 136 (2018). <https://doi.org/10.1016/j.solmat.2017.11.004>
- [23] B. Wang, and J. Mu, *PhotoniX*, **3**, 8 (2022). <https://doi.org/10.1186/s43074-022-00052-6>
- [24] K. Ravey, *Defects and impurities in semiconductor silicon*, (Trans.), G.N. Gorina (Ed.). (Mir, Moscow, 1984) (in Russian)

### ІЗОЛЯЦІЯ ЧУТЛИВИХ ЕЛЕМЕНТІВ ПЛАНАРНИХ БАГАТОЕЛЕМЕНТНИХ ФОТОДІОДІВ

Микола С. Кукурудзяк<sup>a,b</sup>



<sup>a</sup>АТ «Центральне конструкторське бюро Ритм», 58032, м. Чернівці, вул. Головна, 244, Україна

<sup>b</sup>Чернівецький національний університет імені Юрія Федьковича, 58002, м. Чернівці, вул. Коцюбинського, 2, Україна

При серійному виробництві багатоелементних кремнієвих *p-i-n* фотодіодів виявлено проблему систематичного браку виробів внаслідок зниження опору ізоляції між активними елементами фотоприймачів. Дослідження причин деградації опору ізоляції та встановлення оптимальних методів уникнення цього явища є метою даної роботи. Проведено порівняльний аналіз трьох методів ізоляції: класичного – ізоляція поверхнею непровідної підкладки та шару діелектрика; ізоляція за допомогою канавок мезапрофілю з діелектричною плівкою; ізоляція за допомогою областей обмеження поверхневих каналів витоку, ізотипних із матеріалом підкладки (в даному випадку *p*<sup>+</sup>-типу), утворених у зазорах між активними елементами. Під час досліджень встановлено, що причиною погіршення опору ізоляції між активними елементами фотодіодів є наявність провідних інверсійних каналів на межі розділу Si-SiO<sub>2</sub> внаслідок використання кремнію із високим питомим опором. Одним із механізмів утворення інверсійних каналів є перерозподіл домішок у маскуючому оксиді (зокрема фосфору) та їх дифузія до межі розділу двох фаз під час термічних операцій. Іншим механізмом утворення інверсійних шарів є дифузія бору з кремнію в SiO<sub>2</sub> під час термообробок через те, що коефіцієнт сегрегації бору менше одиниці. При виготовленні зразків з ізоляцією за допомогою непровідних ділянок підкладки спостерігалось зниження опору ізоляції по мірі виконання технологічного маршруту (після кожної наступної операції опір деградував). Ступінь деградації можна знизити за рахунок скорочення тривалості термічних операцій. Побачено, що зменшення товщини маскуючого оксиду викликає зниження опору ізоляції. При використанні меза-технології вдається підвищити опір ізоляції за рахунок виключення високотемпературної операції окислення та власне завдяки відсутності маскуючого покриття під час загонки фосфору. Ізоляція активних елементів фотодіодів за допомогою ділянок *p*<sup>+</sup>-типу в проміжках між елементами дозволяє отримати найвищі значення опору ізоляції. Формування цих областей шириною 100 мкм у зазорах шириною 200 мкм дозволило отримати опір ізоляції 25-30 МОм. Для забезпечення ізоляції активних елементів фотодіодів даним методом в технологічний маршрут вноситься дві додаткові термічні операції. Скоротити кількість термічних операцій можна легуванням всієї поверхні кремнію низькою концентрацією бору перед утворенням маскуючого покриття.

**Ключові слова:** *кремній; фотодіод; опір ізоляції; оксид кремнію; інверсійний шар*

# UNSTEADY FLOW PAST AN ACCELERATED VERTICAL PLATE WITH VARIABLE TEMPERATURE IN PRESENCE OF THERMAL STRATIFICATION AND CHEMICAL REACTION<sup>†</sup>

 Nitul Kalita<sup>\*</sup>,  Rudra Kanta Deka,  Rupam Shankar Nath

*Department of Mathematics, Gauhati University, Guwahati-781014, Assam, India*

*\*Corresponding Author e-mail: [nitulkalita9602@gmail.com](mailto:nitulkalita9602@gmail.com)*

Received July 11, 2023; revised July 24, 2023; accepted July 26, 2023

This work aims to investigate the effect of thermal stratification on fluid flow past an accelerated vertical plate in the presence of first order chemical reaction. The dimensionless unsteady coupled linear governing equations are solved by Laplace transform technique for the case when the Prandtl number is unity. The important conclusions made in this study the effect of thermal stratification is compared with the scenario in which there was no stratification. The results of numerical computations for different sets of physical parameters, such as velocity, temperature, concentration, skin-friction, Nusselt number and Sherwood number are displayed graphically. It is shown that the steady state is attained more quickly when the flow is stratified.

**Keywords:** *Thermal Stratification, Chemical Reaction, Heat and Mass Transfer, Vertical Plate, Accelerated*

**PACS:** 47.55.P-, 44.25.+f, 44.05.+e, 47.11.-j

## 1. INTRODUCTION

Thermal stratification is a natural phenomenon that may be seen in many natural systems, such as lakes and seas. The presence of chemical reactions might further complicate the flow's dynamics. In this paper, we investigate how flow dynamics and interactions with chemical processes are impacted by thermal stratification. The applications of this study are wide. It may be used to build more efficient chemical reactors and heat exchangers. It may also be used to look at how the performance of cooling systems in electrical equipment is affected by thermal stratification.

[1] investigated the influence of a chemical reaction on the behavior of an unsteady flow through an accelerating vertical plate, where the mass transfer was variable and without considering stratification. The purpose of this research is to determine how fluid flow past an accelerated vertical plate impacts the interaction between thermal stratification and chemical reaction. [2] and [3] investigated the unsteady flow of a thermally stratified fluid past a vertically accelerated plate under a variety of conditions. Researchers [4], [5], and [6] have investigated steady flows in a stable stratified fluid with a focus on infinite vertical plates. [7] and [8] both investigated buoyancy-driven flows in a stratified fluid. The interaction between thermal stratification and chemical reaction to change MHD flow for vertical stretching surfaces has been studied by researchers [9] and [10]. These two phenomena were also investigated by [11], who investigated the impact of non-Newtonian fluid flow in a porous medium. The unsteady MHD flow past an accelerating vertical plate with a constant heat flux and ramped plate temperature respectively was researched by [12] and [13].

In this paper, we derived the special solutions for  $Sc = 1$  and classical solutions for the case  $S = 0$  (without stratification). These solutions are compared with the primary solutions, and graphs are used to demonstrate the differences. The impacts of physical parameters on velocity, temperature, and concentration profiles, including the stratification parameter ( $S$ ), thermal Grashof number ( $Gr$ ), mass Grashof number ( $Gc$ ), Schmidt number ( $Sc$ ) and Chemical Reaction Parameter ( $K$ ), are explored and presented in graphs. The results of this research have a wide range of applications in a variety of industries and chemical factories.

## 2. MATHEMATICAL ANALYSIS

We consider a fluid that is stratified, viscous, and in-compressible, traveling along an accelerating vertical plate with first-order chemical reaction present. As can be seen in fig. 1, we use a coordinate system in which the  $y'$  axis is perpendicular to the plate and the  $x'$  axis is taken vertically upward along the plate to study the flow situation. The starting temperature  $T'_\infty$  and initial fluid concentration  $C'_\infty$  of the plate and fluid are the same. At time  $t' > 0$ , the plate is subjected to an impulsive constant acceleration  $u_0$ , and the concentration and temperature of the plate are increased to  $C'_w$  and  $T'_w$ , respectively. All flow variables are independent of  $x'$

<sup>†</sup> *Cite as:* N. Kalita, R.K. Deka, R.S. Nath, East Eur. J. Phys. 3, 441 (2023), <https://doi.org/10.26565/2312-4334-2023-3-49>  
© N. Kalita, R.K. Deka, R.S. Nath, 2023

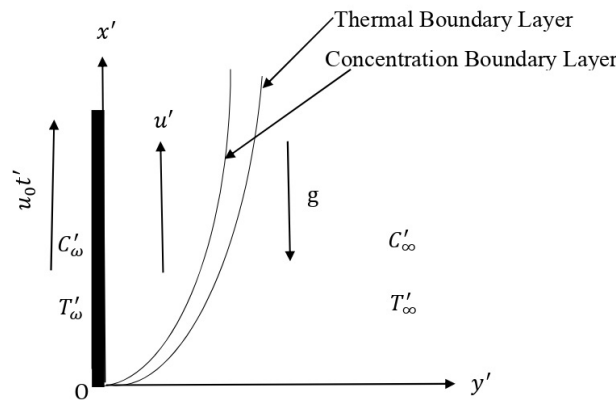


Figure 1. Physical Model and coordinate system

and only affected by  $y'$  and  $t'$  since the plate has an infinite length. As a result, we are left with a flow that is only one dimension and has one non-zero vertical velocity component,  $u'$ . The Boussinesq's approximation is then used to represent the equations for motion, energy, and concentration as follows:

$$\frac{\partial u'}{\partial t'} = g\beta(T' - T'_\infty) + g\beta^*(C' - C'_\infty) + \nu \frac{\partial^2 u'}{\partial y'^2} \tag{1}$$

$$\frac{\partial T'}{\partial t'} = \alpha \frac{\partial^2 T'}{\partial y'^2} - \gamma u' \tag{2}$$

$$\frac{\partial C'}{\partial t'} = D \frac{\partial^2 C'}{\partial y'^2} - K_1 C' \tag{3}$$

with the following initial and boundary Conditions:

$$\begin{array}{llll} u' = 0 & T' = T'_\infty & C' = C'_\infty & \forall y', t' \leq 0 \\ u' = u_0 t' & T' = T'_\infty + (T'_w - T'_\infty) A t' & C' = C'_w & \text{at } y' = 0, t' > 0 \\ u' = 0 & T' \rightarrow T'_\infty & C' \rightarrow C'_\infty & \text{as } y' \rightarrow \infty, t' > 0 \end{array}$$

where,  $\alpha$  is the thermal diffusivity,  $\beta$  is the volumetric coefficient of thermal expansion,  $\beta^*$  is the volumetric coefficient of expansion with concentration,  $\eta$  is the similarity parameter,  $\nu$  is the kinematic viscosity,  $g$  is the acceleration due to gravity,  $D$  is the mass diffusion coefficient. Also,  $\gamma = \frac{dT'_\infty}{dx'} + \frac{g}{C_p}$  denotes the thermal stratification parameter and  $\frac{dT'_\infty}{dx'}$  denotes the vertical temperature convection known as thermal stratification. In addition,  $\frac{g}{C_p}$  represents the rate of reversible work done on fluid particles by compression, often known as work of compression. The variable ( $\gamma$ ) will be referred to as the thermal stratification parameter in our research because the compression work is relatively minimal. For the purpose of testing computational methods, compression work is kept as an additive to thermal stratification.

and we provide non-dimensional quantities in the following:

$$U = \frac{u'}{(u_0 \nu)^{1/3}}, \quad t = \frac{t' u_0^{2/3}}{\nu^{1/3}}, \quad y = \frac{y' u_0^{1/3}}{\nu^{2/3}}, \quad \theta = \frac{T' - T'_\infty}{T'_w - T'_\infty}, \quad C = \frac{C' - C'_\infty}{C'_w - C'_\infty}, \quad Gr = \frac{g\beta(T'_w - T'_\infty)}{u_0}$$

$$Gc = \frac{g\beta^*(C'_w - C'_\infty)}{u_0}, \quad Pr = \frac{\nu}{\alpha}, \quad Sc = \frac{\nu}{D}, \quad K = \frac{K_1 \nu^{1/3}}{u_0^{2/3}}, \quad S = \frac{\gamma \nu^{2/3}}{u_0^{1/3} (T'_w - T'_\infty)}$$

where,  $A = \left(\frac{u_0^2}{\nu}\right)^{1/3}$  is the constant.

The non-dimensional forms of the equations (1)-(3) are given by

$$\frac{\partial U}{\partial t} = Gr\theta + GcC + \frac{\partial^2 U}{\partial y^2} \tag{4}$$

$$\frac{\partial \theta}{\partial t} = \frac{1}{Pr} \frac{\partial^2 \theta}{\partial y^2} - SU \tag{5}$$

$$\frac{\partial C}{\partial t} = \frac{1}{Sc} \frac{\partial^2 C}{\partial y^2} - KC \tag{6}$$

Non-dimensional form of initial and boundary Conditions are:

$$\begin{array}{llll} U = 0 & \theta = 0 & C = 0 & \forall y, t \leq 0 \\ U = t & \theta = t & C = 1 & \text{at } y = 0, t > 0 \\ U = 0 & \theta \rightarrow 0 & C \rightarrow 0 & \text{as } y \rightarrow \infty, t > 0 \end{array} \tag{7}$$

### 3. METHOD OF SOLUTION

The non-dimensional governing equations (4)- (6) with boundary conditions (7) are solved using Laplace’s transform method for  $Pr = 1$ . Hence, the expressions for concentration, velocity and temperature with the help of [14] and [15] are given by

$$C = \frac{1}{2} \left[ e^{-2\eta\sqrt{ScKt}} \operatorname{erfc} \left( \eta\sqrt{Sc} - \sqrt{Kt} \right) + e^{2\eta\sqrt{ScKt}} \operatorname{erfc} \left( \eta\sqrt{Sc} + \sqrt{Kt} \right) \right] \tag{8}$$

$$\begin{aligned} U = & \frac{1}{2} \{f_4(iA) + f_4(-iA)\} + \frac{iA}{2S} \{f_4(iA) - f_4(-iA)\} + \frac{Gc}{2(Sc - 1)} [C_1 \{f_1(iA) + f_1(-iA)\} \\ & + (C_2 - iC_3) \{f_2(iA, B + iB_1) + f_2(-iA, B + iB_1)\} + (C_2 + iC_3) \{f_2(iA, B - iB_1) \\ & + f_2(-iA, B - iB_1)\}] + \frac{Gc}{2iA} [(D_1 - 1) \{f_1(iA) - f_1(-iA)\} + (D_2 + iD_3) \{f_2(iA, B + iB_1) \\ & - f_2(-iA, B + iB_1)\} + (D_2 - iD_3) \{f_2(iA, B - iB_1) - f_2(-iA, B - iB_1)\}] \\ & - \frac{Gc}{(Sc - 1)} \left[ \frac{C_1}{2} \left\{ e^{-2\eta\sqrt{ScKt}} \operatorname{erfc} \left( \eta\sqrt{Sc} - \sqrt{Kt} \right) + e^{2\eta\sqrt{ScKt}} \operatorname{erfc} \left( \eta\sqrt{Sc} + \sqrt{Kt} \right) \right\} \right. \\ & \left. + (C_2 - iC_3) \{f_3(K, B + iB_1)\} + (C_2 + iC_3) \{f_3(K, B - iB_1)\} \right] \end{aligned} \tag{9}$$

$$\begin{aligned} \theta = & \frac{S}{2iA} \{f_4(iA) - f_4(-iA)\} + \frac{1}{2} \{f_4(iA) + f_4(-iA)\} + \frac{SGc}{2iA(Sc - 1)} [C_1 \{f_1(iA) - f_1(-iA)\} \\ & + (C_2 - iC_3) \{f_2(iA, B + iB_1) - f_2(-iA, B + iB_1)\} + (C_2 + iC_3) \{f_2(iA, B - iB_1) \\ & - f_2(-iA, B - iB_1)\}] + \frac{SGc}{2(Sc - 1)^2} [E_1 \{f_1(iA) + f_1(-iA)\} + (E_2 - iE_3) \{f_2(iA, B + iB_1) \\ & + f_2(-iA, B + iB_1)\} + (E_2 + iE_3) \{f_2(iA, B - iB_1) + f_2(-iA, B - iB_1)\}] \\ & - \frac{SGc}{(Sc - 1)^2} \left[ \frac{E_1}{2} \left\{ e^{-2\eta\sqrt{ScKt}} \operatorname{erfc} \left( \eta\sqrt{Sc} - \sqrt{Kt} \right) + e^{2\eta\sqrt{ScKt}} \operatorname{erfc} \left( \eta\sqrt{Sc} + \sqrt{Kt} \right) \right\} \right. \\ & \left. + (E_2 - iE_3) f_3(K, B + iB_1) + (E_2 + iE_3) f_3(K, B - iB_1) \right] \end{aligned} \tag{10}$$

where,

$$\begin{aligned} \eta = \frac{y}{2\sqrt{t}}, \quad A = \sqrt{SGr}, \quad B = \frac{ScK}{Sc - 1}, \quad B_1 = \frac{A}{Sc - 1} = \frac{\sqrt{SGr}}{Sc - 1}, \quad C_1 = \frac{B}{(B^2 + B_1^2)} \\ C_2 = \frac{-B}{2(B^2 + B_1^2)}, \quad C_3 = \frac{-B_1}{2(B^2 + B_1^2)}, \quad D_1 = \frac{B^2}{(B^2 + B_1^2)}, \quad D_2 = \frac{B_1^2}{2(B^2 + B_1^2)} \\ D_3 = \frac{BB_1}{2(B^2 + B_1^2)}, \quad E_1 = \frac{1}{(B^2 + B_1^2)}, \quad E_2 = \frac{-1}{2(B^2 + B_1^2)}, \quad E_3 = \frac{B}{2B_1(B^2 + B_1^2)} \end{aligned}$$

Also,  $f_i$ 's are inverse Laplace’s transforms given by

$$\begin{aligned} f_1(ip) = L^{-1} \left\{ \frac{e^{-y\sqrt{s+ip}}}{s} \right\}, \quad f_2(ip, q_1 + iq_2) = L^{-1} \left\{ \frac{e^{-y\sqrt{s+ip}}}{s + q_1 + iq_2} \right\} \\ f_3(p, q_1 + iq_2) = L^{-1} \left\{ \frac{e^{-y\sqrt{Sc(s+p)}}}{s + q_1 + iq_2} \right\}, \quad f_4(ip) = L^{-1} \left\{ \frac{e^{-y\sqrt{s+ip}}}{s^2} \right\} \end{aligned}$$

We separate the complex arguments of the error function contained in the previous expressions into real and imaginary parts using the formulas provided by [15].

**4. SPECIAL CASE [FOR SC=1]**

We came up with answers for the special case where  $Sc = 1$ . Hence, the solutions for the special case are as follows:

$$C^* = \frac{1}{2} \left[ e^{-2\eta\sqrt{Kt}} \operatorname{erfc}(\eta - \sqrt{Kt}) + e^{2\eta\sqrt{Kt}} \operatorname{erfc}(\eta + \sqrt{Kt}) \right] \tag{11}$$

$$U^* = \frac{1}{2} \{f_4(iA) + f_4(-iA)\} + \frac{KGc}{2(K^2 + A^2)} \{f_1(iA) + f_1(-iA)\} \\ + \frac{iAGc}{2(K^2 + A^2)} \{f_1(iA) - f_1(-iA)\} + \frac{iA}{2S} \{f_4(iA) - f_4(-iA)\} \\ - \frac{KGc}{2(K^2 + A^2)} \left[ e^{-2\eta\sqrt{Kt}} \operatorname{erfc}(\eta - \sqrt{Kt}) + e^{2\eta\sqrt{Kt}} \operatorname{erfc}(\eta + \sqrt{Kt}) \right] \tag{12}$$

$$\theta^* = \frac{1}{2} \{f_4(iA) + f_4(-iA)\} + \frac{SKGc}{2iA(K^2 + A^2)} \{f_1(iA) - f_1(-iA)\} \\ + \frac{SGc}{2(K^2 + A^2)} \{f_1(iA) + f_1(-iA)\} + \frac{S}{2iA} \{f_4(iA) - f_4(-iA)\} \\ - \frac{SGc}{2(K^2 + A^2)} \left\{ e^{-2\eta\sqrt{Kt}} \operatorname{erfc}(\eta - \sqrt{Kt}) + e^{2\eta\sqrt{Kt}} \operatorname{erfc}(\eta + \sqrt{Kt}) \right\} \tag{13}$$

**5. CLASSICAL CASE (S=0)**

We derived solutions for the classical case of no thermal stratification ( $S = 0$ ). We want to compare the results of the fluid with thermal stratification to the case with no stratification. Hence, the corresponding solutions for the classical case is given by :

$$\theta_c = t \left\{ (1 + 2\eta^2) \operatorname{erfc}(\eta) - \frac{2\eta}{\sqrt{\pi}} e^{-\eta^2} \right\} \tag{14}$$

$$U_c = \frac{Gc}{2KSc} \left[ 2\operatorname{erfc}(\eta) - e^{-Bt} \left\{ e^{-2\eta\sqrt{-Bt}} \operatorname{erfc}(\eta - \sqrt{-Bt}) + e^{2\eta\sqrt{-Bt}} \operatorname{erfc}(\eta + \sqrt{-Bt}) \right\} \right. \\ \left. - \left\{ e^{-2\eta\sqrt{ScKt}} \operatorname{erfc}(\eta\sqrt{Sc} - \sqrt{Kt}) + e^{2\eta\sqrt{ScKt}} \operatorname{erfc}(\eta\sqrt{Sc} + \sqrt{Kt}) \right\} \right. \\ \left. + e^{-Bt} \left\{ e^{-2\eta\sqrt{Sc(K-B)t}} \operatorname{erfc}(\eta\sqrt{Sc} - \sqrt{(K-B)t}) + e^{2\eta\sqrt{Sc(K-B)t}} \operatorname{erfc}(\eta\sqrt{Sc} + \sqrt{(K-B)t}) \right\} \right] \\ + \frac{\eta Grt^2}{3} \left\{ \frac{4}{\sqrt{\pi}} (1 + \eta^2) e^{-\eta^2} - \eta(6 + 4\eta^2) \operatorname{erfc}(\eta) \right\} + t \left\{ (1 + 2\eta^2) \operatorname{erfc}(\eta) - \frac{2\eta}{\sqrt{\pi}} e^{-\eta^2} \right\} \tag{15}$$

**5.1. Skin-Friction**

The non-dimensional Skin-Friction, which is determined as shear stress on the surface, is obtained by

$$\tau = - \frac{dU}{dy} \Big|_{y=0}$$

The solution for the Skin-Friction is calculated from the solution of Velocity profile  $U$ , represented by (9), as follows:

$$\tau = \sqrt{\frac{t}{\pi}} \cos At + t \sqrt{\frac{A}{2}} (r_1 - r_2) + \frac{(r_1 + r_2)}{2\sqrt{2A}} + \frac{A}{S} \left[ \sqrt{\frac{t}{\pi}} \sin At - t \sqrt{\frac{A}{2}} (r_1 + r_2) + \frac{(r_1 - r_2)}{2\sqrt{2A}} \right] \\ + \frac{Gc}{Sc - 1} \left[ C_1 \left\{ \frac{\cos At}{\sqrt{\pi t}} + \sqrt{\frac{A}{2}} (r_1 - r_2) - \sqrt{ScK} \operatorname{erf}(\sqrt{Kt}) - \sqrt{\frac{Sc}{\pi t}} e^{-Kt} \right\} \right. \\ \left. + 2C_2 \left\{ \frac{\cos At}{\sqrt{\pi t}} - \sqrt{\frac{Sc}{\pi t}} e^{-Kt} \right\} + e^{-Bt} \{(C_2P_1 + C_3Q_1)(r_3 \cos B_1t + r_4 \sin B_1t) \right. \\ \left. + (C_3P_1 - C_2Q_1)(r_4 \cos B_1t - r_3 \sin B_1t)\} + e^{-Bt} \{(C_2P_2 - C_3Q_2)(r_5 \cos B_1t - r_6 \sin B_1t) \right. \\ \left. - (C_3P_2 + C_2Q_2)(r_6 \cos B_1t + r_5 \sin B_1t)\} - 2e^{-Bt} \sqrt{Sc} \{(C_2P_3 - C_3Q_3) \right. \\ \left. (r_7 \cos B_1t - r_8 \sin B_1t) - (C_3P_3 + C_2Q_3)(r_8 \cos B_1t + r_7 \sin B_1t)\} \right]$$

$$\begin{aligned}
 & + \frac{Gc}{A} \left[ (D_1 - 1) \left\{ \frac{-\sin At}{\sqrt{\pi t}} + \sqrt{\frac{A}{2}} (r_1 + r_2) \right\} - \frac{2D_2 \sin At}{\sqrt{\pi t}} \right. \\
 & + e^{-Bt} \{ (D_2P_1 - D_3Q_1)(r_4 \cos B_1t - r_3 \sin B_1t) + (D_3P_1 + D_2Q_1)(r_3 \cos B_1t + r_4 \sin B_1t) \} \\
 & \left. + e^{-Bt} \{ (D_2P_2 + D_3Q_2)(r_6 \cos B_1t + r_5 \sin B_1t) - (D_3P_2 - D_2Q_2)(r_5 \cos B_1t - r_6 \sin B_1t) \} \right]
 \end{aligned}$$

The solution for the Skin-Friction for the special case is given from the expression (12), which is represented by

$$\begin{aligned}
 \tau^* = & \sqrt{\frac{t}{\pi}} \cos At + t\sqrt{\frac{A}{2}} (r_1 - r_2) + \frac{(r_1 + r_2)}{2\sqrt{2A}} + \frac{KGc}{K^2 + A^2} \left[ \frac{\cos At}{\sqrt{\pi t}} + \sqrt{\frac{A}{2}} (r_1 - r_2) \right. \\
 & \left. - \sqrt{K} \operatorname{erf}(\sqrt{Kt}) - \frac{e^{-Kt}}{\sqrt{\pi t}} \right] + \frac{A}{S} \left[ \sqrt{\frac{t}{\pi}} \sin At - t\sqrt{\frac{A}{2}} (r_1 + r_2) + \frac{(r_1 - r_2)}{2\sqrt{2A}} \right] \\
 & + \frac{AGc}{K^2 + A^2} \left\{ \frac{\sin At}{\sqrt{\pi t}} - \sqrt{\frac{A}{2}} (r_1 + r_2) \right\}
 \end{aligned}$$

The solution for the Skin-Friction for the classical case is given from the expression (15), which is represented by

$$\begin{aligned}
 \tau_c = & \frac{Gc}{KSc} \left[ e^{-Bt} \left\{ \sqrt{Sc(K - B)} \operatorname{erf}(\sqrt{(K - B)t}) - \sqrt{-B} \operatorname{erf}(\sqrt{-Bt}) \right\} - \sqrt{ScK} \operatorname{erf}(\sqrt{Kt}) \right] \\
 & + 2\sqrt{\frac{t}{\pi}} \left( 1 - \frac{tGr}{3} \right)
 \end{aligned}$$

### 5.2. Nusselt Number

The non-dimensional Nusselt number, which is determined as the rate of heat transfer, is obtained by

$$Nu = - \left. \frac{d\theta}{dy} \right|_{y=0}$$

The solution for the Nusselt number is calculated from the solution of Temperature profile  $\theta$ , represented by (10), as follows:

$$\begin{aligned}
 Nu = & \sqrt{\frac{t}{\pi}} \cos At + t\sqrt{\frac{A}{2}} (r_1 - r_2) + \frac{(r_1 + r_2)}{2\sqrt{2A}} - \frac{S}{A} \left[ \sqrt{\frac{t}{\pi}} \sin At - t\sqrt{\frac{A}{2}} (r_1 + r_2) + \frac{(r_1 - r_2)}{2\sqrt{2A}} \right] \\
 & + \frac{Gc}{A(Sc - 1)} \left[ C_1 \left\{ \frac{-\sin At}{\sqrt{\pi t}} + \sqrt{\frac{A}{2}} (r_1 + r_2) \right\} - \frac{2C_2 \sin At}{\sqrt{\pi t}} \right. \\
 & + e^{-Bt} \{ (C_2P_1 + C_3Q_1)(r_4 \cos B_1t - r_3 \sin B_1t) - (C_3P_1 - C_2Q_1)(r_3 \cos B_1t + r_4 \sin B_1t) \} \\
 & \left. + e^{-Bt} \{ (C_2P_2 - C_3Q_2)(r_6 \cos B_1t + r_5 \sin B_1t) + (C_3P_2 + C_2Q_2)(r_5 \cos B_1t - r_6 \sin B_1t) \} \right] \\
 & + \frac{SGc}{(Sc - 1)^2} \left[ E_1 \left\{ \frac{\cos At}{\sqrt{\pi t}} + \sqrt{\frac{A}{2}} (r_1 - r_2) - \sqrt{ScK} \operatorname{erf}(\sqrt{Kt}) - \sqrt{\frac{Sc}{\pi t}} e^{-Kt} \right\} \right. \\
 & + 2E_2 \left\{ \frac{\cos At}{\sqrt{\pi t}} - \sqrt{\frac{Sc}{\pi t}} e^{-Kt} \right\} + e^{-Bt} \{ (E_2P_1 + E_3Q_1)(r_3 \cos B_1t + r_4 \sin B_1t) \} \\
 & + (E_3P_1 - E_2Q_1)(r_4 \cos B_1t - r_3 \sin B_1t) + e^{-Bt} \{ (E_2P_2 - E_3Q_2)(r_5 \cos B_1t - r_6 \sin B_1t) \\
 & - (E_3P_2 + E_2Q_2)(r_6 \cos B_1t + r_5 \sin B_1t) \} - 2e^{-Bt} \sqrt{Sc} \{ (E_2P_3 - E_3Q_3)(r_7 \cos B_1t - r_8 \sin B_1t) \\
 & \left. - (E_3P_3 + E_2Q_3)(r_8 \cos B_1t + r_7 \sin B_1t) \} \right]
 \end{aligned}$$

The solution for the Nusselt number for the special case is given from the expression (13), which is represented by

$$\begin{aligned}
 Nu^* = & \frac{SKGc}{A(K^2 + A^2)} \left[ \frac{-\sin At}{\sqrt{\pi t}} + \sqrt{\frac{A}{2}} (r_1 + r_2) \right] + \left( 1 + \frac{SGc}{K^2 + A^2} \right) \left[ \frac{\cos At}{\sqrt{\pi t}} + \sqrt{\frac{A}{2}} (r_1 - r_2) \right] \\
 & - \frac{S}{A} \left[ \sqrt{\frac{t}{\pi}} \sin At - t\sqrt{\frac{A}{2}} (r_1 + r_2) + \frac{(r_1 - r_2)}{2\sqrt{2A}} \right] - \frac{SGc}{K^2 + A^2} \left\{ \sqrt{K} \operatorname{erf}(\sqrt{Kt}) + \frac{e^{-Kt}}{\sqrt{\pi t}} \right\}
 \end{aligned}$$

$$+\sqrt{\frac{t}{\pi}} \cos At + t\sqrt{\frac{A}{2}}(r_1 - r_2) + \frac{(r_1 + r_2)}{2\sqrt{2A}}$$

The solution for the Nusselt number for the classical case is given from the expression (14), which is represented by

$$Nu_c = \frac{1}{\sqrt{\pi t}}$$

### 5.3. Sherwood Number

The non-dimensional Sherwood number, which is determined as the rate of mass transfer, is obtained by

$$Sh = -\frac{dC}{dy} \Big|_{y=0}$$

The solution for the Sherwood number is calculated from the solution of Concentration profile  $C$ , represented by (8), as follows:

$$Sh = \sqrt{ScK} \operatorname{erf}(\sqrt{Kt}) + \sqrt{\frac{Sc}{\pi t}} e^{-Kt}$$

The solution for the Sherwood number for the special case is given from the expression (11), which is represented by

$$Sh^* = \sqrt{K} \operatorname{erf}(\sqrt{Kt}) + \frac{1}{\sqrt{\pi t}} e^{-Kt}$$

where,

$$B_2 = \sqrt{B^2 + (A - B_1)^2}, \quad B_3 = \sqrt{B^2 + (A + B_1)^2}, \quad B_4 = \sqrt{(K - B)^2 + B_1^2}, \quad P_1 = \sqrt{\frac{B_2 - B}{2}},$$

$$Q_1 = \sqrt{\frac{B_2 + B}{2}}, \quad P_2 = \sqrt{\frac{B_3 - B}{2}}, \quad Q_2 = \sqrt{\frac{B_3 + B}{2}}, \quad P_3 = \sqrt{\frac{B_4 - (K - B)}{2}}$$

$$Q_3 = \sqrt{\frac{B_4 + (K - B)}{2}}, \quad \sqrt{-B + i(A - B_1)} = P_1 + iQ_1, \quad \sqrt{-B + i(A + B_1)} = P_2 + iQ_2,$$

$$\sqrt{K - B + iB_1} = P_3 + iQ_3, \quad \operatorname{erf}(\sqrt{iAt}) = r_1 + ir_2, \quad \operatorname{erf}(P_1\sqrt{t} + iQ_1\sqrt{t}) = r_3 + ir_4,$$

$$\operatorname{erf}(P_2\sqrt{t} + iQ_2\sqrt{t}) = r_5 + ir_6, \quad \operatorname{erf}(P_3\sqrt{t} + iQ_3\sqrt{t}) = r_7 + ir_8$$

## 6. RESULT AND DISCUSSIONS

In order to better understand the physical significance of the problem, we calculated the velocity, temperature, concentration, Skin friction, Nusselt number, and Sherwood number using the solutions we found in the previous sections, for different values of the physical parameters  $S, Gr, Gc, Sc, K$  and time  $t$ . Additionally, we represented them graphically in Figures 2 to 13.

The effect of thermal stratification ( $S$ ) on the velocity profiles is seen in Figure 2. It can be seen that there is a decrease in velocity as a result of thermal stratification. An increase in the values of  $Gr$  and  $Gc$  leads to a rise in the value of the velocity, as seen in Figure 3. Figures 4 and 5 depicted the fluid's velocity at various values of  $Sc$  and  $K$ . The fluid velocity decreases as the values of  $Sc$  and  $K$  increase.

Figures 6 and 7 portray the effect of thermal stratification on fluid velocity and temperature against time. Without stratification, the velocity and temperature increase over time in an exponential manner; but, when stratification takes place, they finally stabilize. Due to the application of thermal stratification, which reduces velocity and temperature in comparison with the standard case ( $S = 0$ ). Hence, this research with stratification is more realistic than prior ones without stratification.

The combined effect of thermal stratification and chemical reaction on temperature can be seen in Figure 8. The temperature seems to decrease when the thermal stratification parameter is increased, yet chemical reactions enhance the temperature. The effects of  $Gr, Gc$  and  $Sc$  on the temperature profile are shown in Figures 9 and 10, respectively. For higher  $Gr, Sc$ , and lower  $Gc$  values, the temperature decreases.

Figure 11 illustrates how the parameters  $Sc$  and  $K$  influence the concentration of the fluid. The concentration decreases when the  $Sc$  and  $K$  parameters are increased. Figures 12 and 13 illustrate the skin friction and Nusselt number variations produced by thermal Stratification. They considerably rise in the presence of stratification compared to the absence of stratification. Additionally, stratification increases the frequency of oscillations for both skin friction and the Nusselt number.

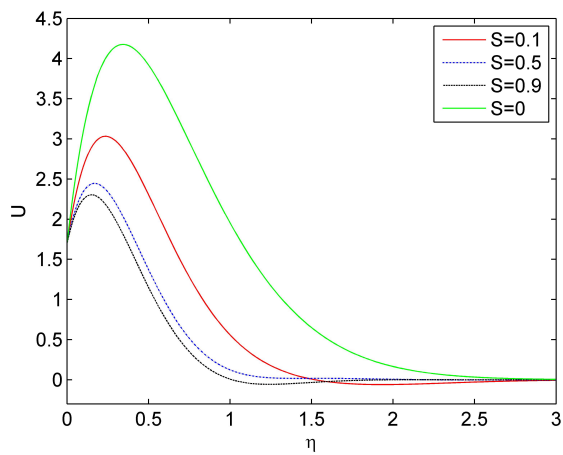


**Figure 2.** Effects of  $S$  on Velocity Profile for  $Gr = 5, Gc = 5, t = 1.7, Sc = 0.5, K = 0.2$

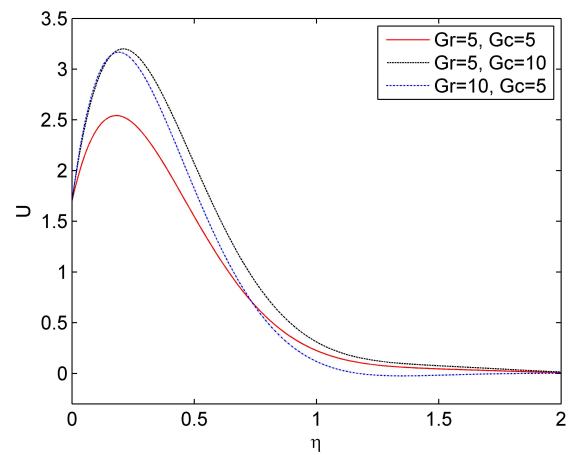


**Figure 3.** Effects of  $Gr$  and  $Gc$  on Velocity Profile for  $S = 0.4, Sc = 0.5, t = 1.7, K = 0.2$

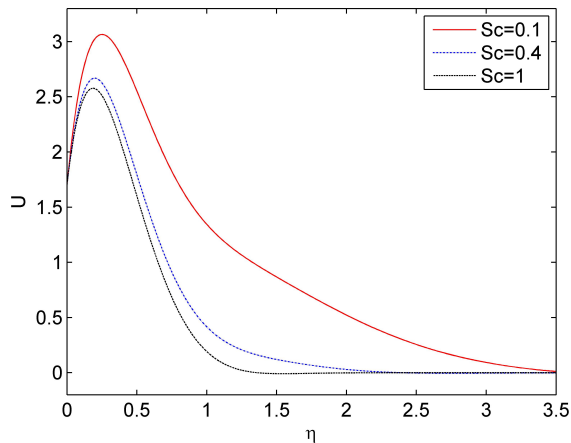


**Figure 4.** Effects of  $Sc$  on Velocity Profile for  $Gr = 5, Gc = 5, S = 0.4, t = 1.7, K = 0.2$

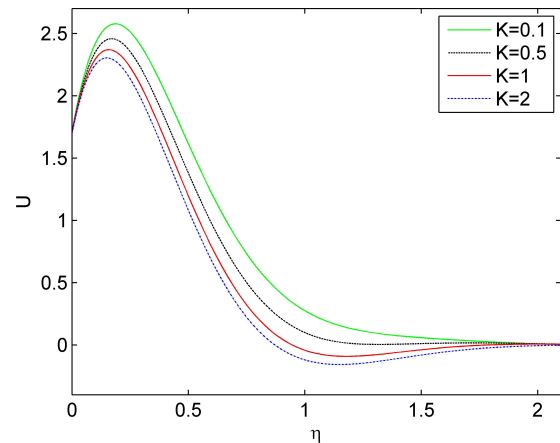


**Figure 5.** Effects of  $K$  on Velocity Profile for  $Gr = 5, Gc = 5, S = 0.4, Sc = 0.5, t = 1.7$

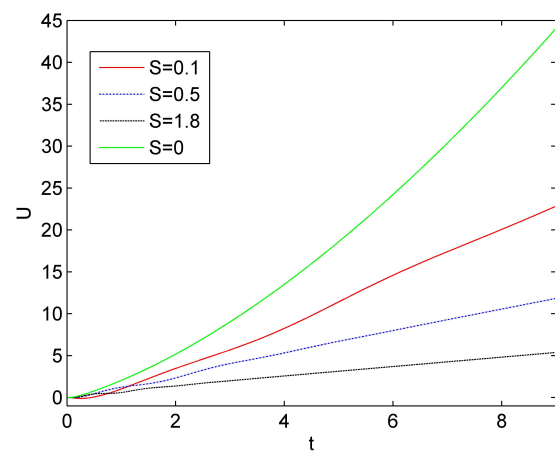


**Figure 6.** Effects of  $S$  on Velocity Profile against time for  $Gr = 5, Gc = 5, Sc = 0.5, y = 1, K = 0.2$

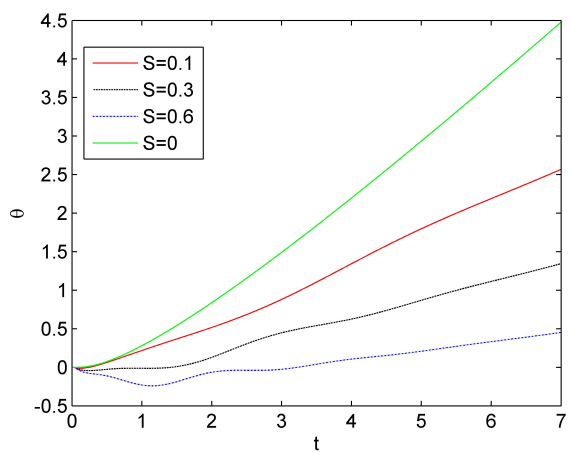


**Figure 7.** Effects of  $S$  on Temperature Profile against time for  $Gr = 5, Gc = 5, Sc = 0.5, y = 1, K = 0.2$



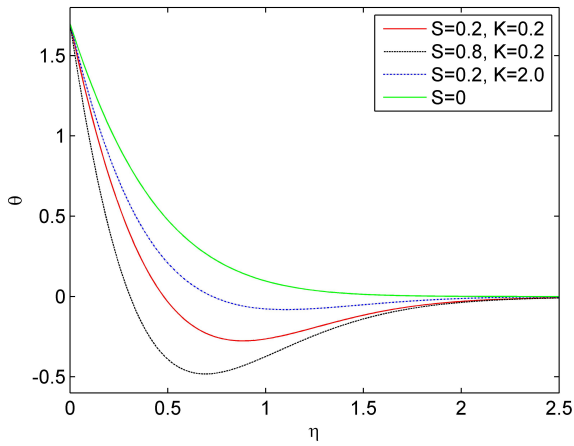


**Figure 8.** Effects of  $S$  and  $K$  on Temperature Profile for  $Gr = 5, Gc = 5, Sc = 0.5, t = 1.7$

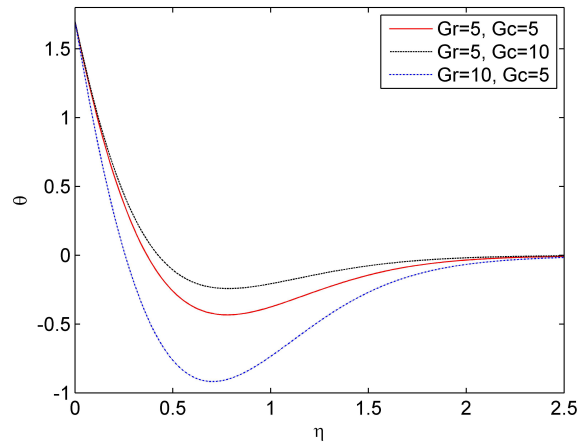


**Figure 9.** Effects of  $Gr$  and  $Gc$  on Temperature Profile for  $S = 0.4, Sc = 0.5, t = 1.7, K = 0.2$

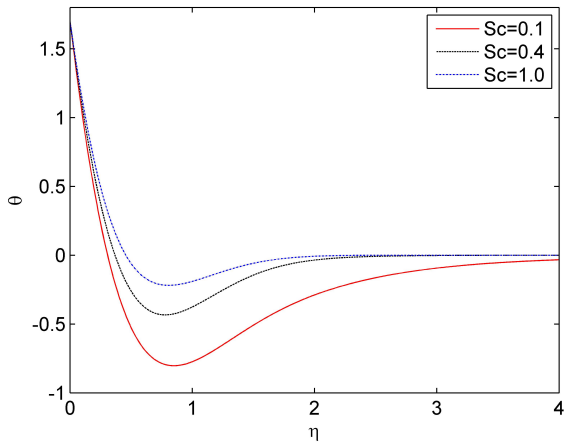


**Figure 10.** Effects of  $Sc$  on Temperature Profile for  $Gr = 5, Gc = 5, S = 0.4, t = 1.7, K = 0.2$

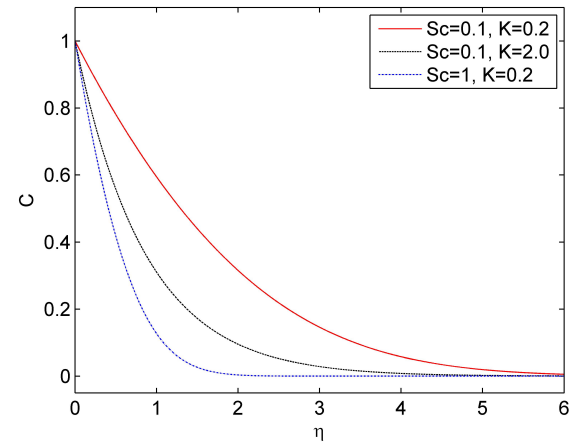


**Figure 11.** Effects of  $Sc$  and  $K$  on concentration Profile

**7. CONCLUSION**

We explored how chemical reactions impact the flow through an accelerated vertical plate in the presence of thermal stratification. The outcomes of the current study are compared with those of the classical situation

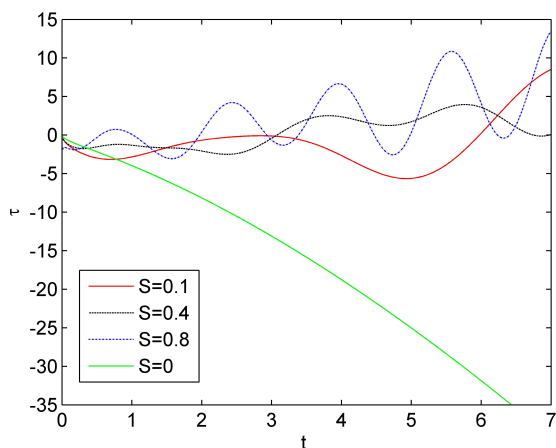


**Figure 12.** Effects of  $S$  on Skin friction for  $Gr = 5, Gc = 5, Sc = 0.5, K = 0.2$

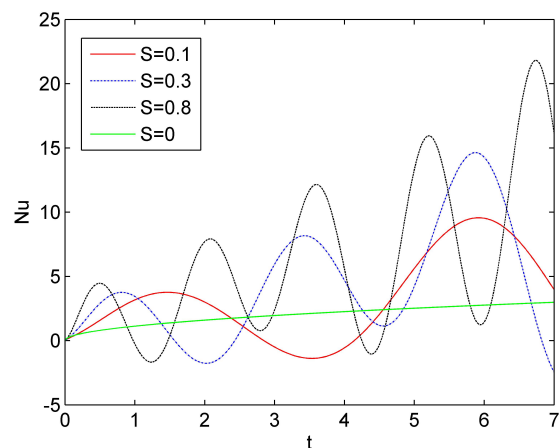





**Figure 13.** Effects of  $S$  on Nusselt Number for  $Gr = 5, Gc = 5, Sc = 0.5, K = 0.2$

in which stratification does not take place. As  $S, Sc$  and  $K$  grow, the fluid's velocity decreases, whereas an increase in  $Gr, Gc$  increases it. This research is more practical than earlier ones because it applies thermal stratification, which lowers velocity and temperature in comparison to the classical scenario ( $S = 0$ ). The temperature decreases when  $K$  and  $Gc$  decreases, and it increases when  $S, Gr$  increases. Thermal stratification increases the recurrence of oscillations in the skin friction and Nusselt number.

### Acknowledgments

One of the author (R.S. Nath) would like to thank University Grant Commission (UGC), New Delhi, India for their financial help in the form of Junior Research Fellowship (JRF) .

### ORCID

 Nitul Kalita, <https://orcid.org/0000-0001-8348-2225>;  Rudra Kanta Deka, <https://orcid.org/0009-0007-1573-4890>;  Rupam Shankar Nath, <https://orcid.org/0009-0002-2352-0538>

### REFERENCES

- [1] R. Muthucumaraswamy, N. Dhanasekar and G. E. Prasad, "Rotation effects on unsteady flow past an accelerated isothermal vertical plate with variable mass transfer in the presence of chemical reaction of first order," *Journal of Applied Fluid Mechanics*, **6**(4) , 485-490 (2013) <https://doi.org/10.36884/jafm.6.04.19561>
- [2] R. K.Deka and B. C. Neog,"Unsteady natural convection flow past an accelerated vertical plate in a thermally stratified fluid," *Theoretical and Applied Mechanics* **36**(4) 261-274 (2009) <https://doi.org/10.2298/TAM090426>
- [3] B. S. Goud, P. Srilatha, K. R. Babu and L. Indira, "Finite element approach on MHD flow through porous media past an accelerated vertical plate in a thermally stratified fluid," *Journal of Critical Reviews*, **7**(16), 69-74 (2020)
- [4] A. Bhattacharya, and R. K. Deka. "Theoretical Study of Chemical Reaction Effects on Vertical Oscillating Plate Immersed in a Stably Stratified Fluid," *Research Journal of Applied Sciences, Engineering and Technology*, **3**(9), 887-898 (2011). <https://maxwellsci.com/print/rjaset/v3-887-898.pdf>
- [5] E. Magyari, I. Pop, and B. Keller, "Unsteady Free Convection along an Infinite Vertical Flat Plate Embedded in a Stably Stratified Fluid-Saturated Porous Medium," *Transp. Porous. Med.* **62**, 233-249 (2006). <https://doi.org/10.1007/s11242-005-1292-6>
- [6] A. Shapiro, and E. Fedorovich, "Unsteady convectively driven flow along a vertical plate immersed in a stably stratified fluid," *Journal of Fluid Mechanics*, **498**, 333-352 (2004). <https://doi.org/10.1017/S0022112003006803>
- [7] J.S. Park, and J.M. Hyun, "Technical Note Transient behavior of vertical buoyancy layer in a stratified fluid," *International Journal of Heat and Mass Transfer*, **41**(24), 4393-4397 (1998), [https://doi.org/10.1016/S0017-9310\(98\)00175-6](https://doi.org/10.1016/S0017-9310(98)00175-6)
- [8] J.S. Park, "Transient buoyant flows of a stratified fluid in a vertical channel," *KSME International Journal*, **15**, 656-664 (2001). <https://doi.org/10.1007/BF03184382>
- [9] R. Kandasamy, K. Periasamy, and K.K.S. Prabhu, "Chemical reaction, heat and mass transfer on MHD flow over a vertical stretching surface with heat source and thermal stratification effects," *International Journal of Heat and Mass Transfer*, **48**(21-22), 4557-4561 (2005). <https://doi.org/10.1016/j.ijheatmasstransfer.2005.05.006>
- [10] M.A. Mansour, N.F. El-Anssary, and A.M. Aly, "Effects of chemical reaction and thermal stratification on MHD free convective heat and mass transfer over a vertical stretching surface embedded in a porous media considering Soret and Dufour numbers," *Chemical Engineering Journal*, **145**(2), 340-345 (2008). <https://doi.org/10.1016/j.cej.2008.08.016>
- [11] A.M. Megahed, and W. Abbas, "Non-Newtonian Cross fluid flow through a porous medium with regard to the effect of chemical reaction and thermal stratification phenomenon," *Case Studies in Thermal Engineering*, **29**, 101715 (2022). <https://doi.org/10.1016/j.csite.2021.101715>
- [12] M. Narahari and L. Debnath, "Unsteady magnetohydrodynamic free convection flow past an accelerated vertical plate with constant heat flux and heat generation or absorption," *ZAMM- Journal of Applied Mathematics and Mechanics/Zeitschrift für Angewandte Mathematik und Mechanik*, **93**(1), 38-49 (2013) <https://doi.org/10.1002/zamm.201200008>
- [13] Y. D. Reddy, B. Shankar Goud abd M. Anil Kumar,"Radiation and heat absorption effects on an unsteady MHD boundary layer flow along an accelerated infinite vertical plate with ramped plate temperature in the existence of slip condition," *Partial Differential Equations in Applied Mathematics*, **4**, 100166 (2021), <https://doi.org/10.1016/j.padiiff.2021.100166>
- [14] R.B. Hetnarski, "An algorithm for generating some inverse Laplace transforms of exponential form," *Journal of Applied Mathematics and Physics (ZAMP)*, **26**, 249-253 (1975). <https://doi.org/10.1007/BF01591514>.
- [15] Abramowitz, Milton, I.A. Stegun, and R.H. Romer. "Handbook of mathematical functions with formulas, graphs, and mathematical tables." *American Journal of Physics*, **56**(10), 958 (1988). <https://doi.org/10.1119/1.15378>

## НЕСТІЙКИЙ ПОТІК ПОВЗ ПРИСКОРЕНУ ВЕРТИКАЛЬНУ ПЛАСТИНУ ЗІ ЗМІННОЮ ТЕМПЕРАТУРОЮ ЗА НАЯВНОСТІ ТЕРМОСТРАТИФІКАЦІЇ ТА ХІМІЧНОЇ РЕАКЦІЇ

Нітул Каліта, Рудра Канта Дека, Рупам Шанкар Натх

*Факультет математики, Університет Гаухаті, Гувахаті-781014, Ассам, Індія*

Ця робота спрямована на дослідження впливу термічної стратифікації на потік рідини повз прискорену вертикальну пластину за наявності хімічної реакції першого порядку. Безрозмірні нестационарні пов'язані лінійні керуючі рівняння розв'язуються методом перетворення Лапласа для випадку, коли число Прандтля дорівнює одиниці. Важливі висновки, зроблені в цьому дослідженні, вплив термічної стратифікації порівнюють зі сценарієм, в якому стратифікації не було. Результати чисельних обчислень для різних наборів фізичних параметрів, таких як швидкість, температура, концентрація, тертя, число Нуссельта та число Шервуда, відображаються графічно. Показано, що стаціонарний стан досягається швидше, коли потік стратифікований.

**Ключові слова:** *термічна стратифікація; хімічна реакція; тепло- та масообмін; вертикальна пластина; прискорення*

## MULTIPARAMETER CONTROL OF ENERGY CHARACTERISTICS OF WAVEGUIDE-CAVITY RESONATOR-SLOT RADIATORS<sup>†</sup>

 Mikhail V. Nesterenko\*,  Victor A. Katrich,  Natalya K. Blinova

V.N. Karazin Kharkiv National University, 4, Svobody Sq., Kharkiv, Ukraine, 61022

\*Corresponding Author e-mail: [mikhail.v.nesterenko@gmail.com](mailto:mikhail.v.nesterenko@gmail.com)

Received June 9, 2023; revised June 20, 2023; accepted July 1, 2023

The problem of connecting three electrodynamic volumes with ideally conducting walls through electrically narrow rectilinear connecting slots and a radiating slot is solved by the generalized method of induced magnetomotive forces (MMF). The solution is obtained in an analytical form, taking into account the finite thickness of the walls of the connected volumes. The volumes are an infinite rectangular waveguide excited by a fundamental wave, a rectangular cavity resonator, and a half-space above an infinite plane. The energy characteristics of this system have been comprehensively studied depending on the geometric parameters of the constituent elements of the structure under consideration.

**Keywords:** Radiation slot; Connecting slots; Rectangular waveguide; Cavity resonator; Electromagnetic waves

**PACS:** 02.30.Rz;78.70Gq;84.40.-x;84.40Ba

Currently, in the antenna-waveguide technology of millimeter and centimeter wavelengths, slotted radiators in flat and spherical surfaces are widely used as feeds for highly directional mirror and lens antennas [1–5], elements of in-phase and scanning antenna arrays [6–19], as well as devices connections of electrodynamic volumes [20–22]. Single slotted radiators are characterized by a significant broadband, which in conditions, for example, of a complex electromagnetic environment, can lead to disruption of the operation of radio electronic systems (RES). In this regard, the problems of analysis, synthesis and control of the band characteristics of slot antennas are of undoubted interest for practice, in particular, from the point of view of ensuring the electromagnetic compatibility of various RES components.

The formation of the required frequency-energy characteristics of slot radiators and coupling holes can be ensured, for example, by using combined (with dipoles, dielectric inserts, etc.) radiators [21, 22 and references therein], or by placing in the supply waveguide channel through cavity resonators, which, in turn, are band-pass and band-stop filters [4, 16, 23]. There are also other constructive solutions to this problem, namely: placement between the radiating slot and the connection slot (slots) the cavity resonator [11, 18], and the presence of two closely spaced slots in the wall of the main waveguide makes it possible to significantly increase the value of the coupling coefficient in a narrow frequency band [14].

In this article, an electrodynamically rigorous mathematical model is constructed and the energy characteristics of the following radiating structure are studied: a system of two transverse slots in a wide wall of an infinite rectangular waveguide - a pass-through cavity resonator - a slot that radiates into a half-space above an infinite ideally conducting plane. On the basis of such structure, a linear or two-dimensional antenna array with new (compared to those known for similar structures) electrodynamic characteristics can be created.

### FORMULATION OF THE PROBLEM AND SOLUTION

The considered waveguide-resonator-slot structure and the designations adopted in the problem are shown in Fig. 1. Three electrodynamic volumes with ideally conducting walls, representing, respectively, an infinite rectangular waveguide with a cross section  $\{a \times b\}$  (index “Wg”), a rectangular resonator with dimensions  $\{a_R \times b_R \times H\}$  (index “R”), and a half-space above an unlimited screen (index “Hs”) are interconnected rectilinear slots  $S_1, S_2, S_3$  cut in infinitely thin common walls.

The geometric dimensions of all slots satisfy the following conditions

$$\frac{d_p}{2L_p} \ll 1, \quad \frac{d_p}{\lambda} \ll 1, \quad p=1,2,3, \quad (1)$$

where  $2L_p$  and  $d_p$  are the length and width of the slots, respectively, and  $\lambda$  is the wavelength in free space. In this case, the equivalent magnetic currents in the slots can be represented as ( $\vec{e}_{s_p}$  are the unit vectors,  $s_p$  and  $\xi_p$  are the local coordinates associated with slots,  $J_{0p}$  are the current amplitudes):

$$\vec{J}_p(s_p) = \vec{e}_{s_p} J_{0p} f_p(s_p) \chi_p(\xi_p). \quad (2)$$

<sup>†</sup> Cite as: M.V. Nesterenko, V.A. Katrich, N.K. Blinova, East. Eur. J. Phys. 3, 451 (2023), <https://doi.org/10.26565/2312-4334-2023-3-50>

© M.V. Nesterenko, V.A. Katrich, N.K. Blinova, 2023

In this case, the functions  $f_p(s_p)$  must satisfy the boundary conditions  $f_p(\pm L_p) = 0$ , and the functions  $\chi_p(\xi_p)$  must satisfy the conditions on the edges of the slots and the normalization conditions:  $\int_{\xi_p} \chi_p(\xi_p) d\xi_p = 1$ .

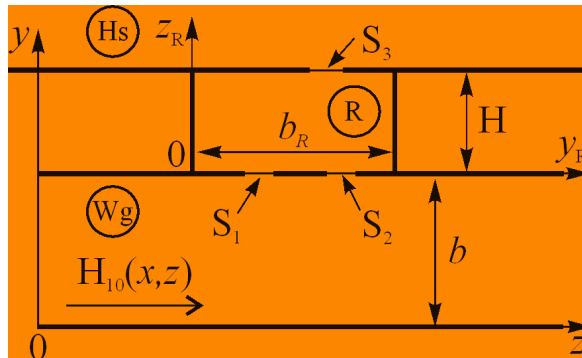


Figure 1. The structure geometry and notations

Let us choose as functional dependences  $f_p(s_p)$  on the longitudinal coordinates of the magnetic currents in the slots the functions obtained as a result of the approximate solution [15] of the integral equation for the current in a single transverse slot (symmetric with respect to the axis  $\{0x\}$ ), excited by a wave of the type  $H_{10}$  and connecting two rectangular waveguides ( $f_{1,2}(s_{1,2})$ ), and for the current in a slot in an infinite screen when a plane electromagnetic wave falls on it, the vector  $\vec{H}$  of which is parallel to the vector  $\vec{e}_{s_3}$  ( $f_3(s_3)$ ):

$$\begin{aligned} f_{1,2}(s_{1,2}) &= \left( \cos ks_{1,2} \cos \frac{\pi}{a} L_{1,2} - \cos kL_{1,2} \cos \frac{\pi}{a} s_{1,2} \right), \\ f_3(s_3) &= (\cos ks_3 - \cos kL_3). \end{aligned} \quad (3)$$

We note that such a choice of the function  $f_3(s_3)$  made it possible to obtain an expression for the external conductivity of the radiating slot in an analytical form.

Using the boundary conditions for the continuity of the tangential components of the magnetic field on the surfaces of slots and following the generalized method of induced MMF for a multi-slot structure [20], we obtain a system of algebraic equations for unknown current amplitudes  $J_{0p}$ :

$$\begin{cases} J_{01} (Y_{11}^{Wg} + Y_{11}^R) + J_{02} (Y_{12}^{Wg} + Y_{12}^R) + J_{03} Y_{13}^R = -\frac{i\omega}{2k} \int_{-L_1}^{L_1} f_1(s_1) H_{0s_1}(s_1) ds_1, \\ J_{02} (Y_{22}^{Wg} + Y_{22}^R) + J_{01} (Y_{21}^{Wg} + Y_{21}^R) + J_{03} Y_{23}^R = -\frac{i\omega}{2k} \int_{-L_2}^{L_2} f_2(s_2) H_{0s_2}(s_2) ds_2, \\ J_{03} (Y_{33}^R + Y_{33}^{Hs}) + J_{01} Y_{31}^R + J_{02} Y_{32}^R = 0. \end{cases} \quad (4)$$

Here

$$Y_{pp}^{Wg,R,Hs} = \frac{1}{2k} \int_{-L_p}^{L_p} f_p(s_p) \left[ \left( \frac{d^2}{ds_p^2} + k^2 \right) \int_{-L_p}^{L_p} f_p(s'_p) G_{s_p}^{Wg,R,Hs}(s_p, s'_p) ds'_p \right] ds_p \quad (5)$$

are the own conductivities of slots;

$$Y_{pq}^{Wg,R,Hs} = \frac{1}{2k} \int_{-L_{p,q}}^{L_{p,q}} f_{p,q}(s_{p,q}) \left[ \left( \frac{d^2}{ds_{p,q}^2} + k^2 \right) \int_{-L_{p,q}}^{L_{p,q}} f_{q,p}(s'_{q,p}) G_{s_{p,q}}^{Wg,R,Hs}(s_{p,q}, s'_{q,p}) ds'_{q,p} \right] ds_{p,q} \quad (6)$$

are the mutual conductivities of slots ( $q = 1,2,3$ );  $G_s^{Wg,R,Hs}$  are the  $s$  - components of quasi-one-dimensional ( $|\xi_p - \xi'_p| \approx d_p / 4$ ) Green's functions for the vector potential of the corresponding volumes [20];  $H_{0s_{1,2}}(s_{1,2})$  are the projections of the field of external sources on the axes of the first and second slots;  $\omega$  is the circular frequency;  $k = 2\pi / \lambda$ .

After substituting functions (3) and formulas for  $G_s^{Wg,R,Hs}$  [20] into relations (5), (6), we obtain the following expressions for the own and mutual conductivities of slots ( $p=1,2$ ):

$$Y_{pp}^{Wg} = \frac{2\pi}{ab} \sum_{m=1,3,\dots} \sum_{n=0}^{\infty} \frac{\varepsilon_n (k^2 - k_x^2)}{kk_z} e^{-k_z \frac{d_p}{4}} I_{Wg}^2(kL_p)$$

$$Y_{12(21)}^{Wg} = \frac{2\pi}{ab} \sum_{m=1,3,\dots} \sum_{n=0}^{\infty} \frac{\varepsilon_n (k^2 - k_x^2)}{kk_z} e^{-k_z z_0} I_{Wg}(kL_{1(2)}) I_{Wg}(kL_{2(1)})$$

$$Y_{pp}^R = \frac{4\pi}{a_R b_R} \sum_{m=1,3,\dots} \sum_{n=0}^{\infty} \frac{\varepsilon_n (k^2 - k_{xR}^2)}{kk_{zR}} \coth k_{zR} H \cos k_{yR} y_{0p} \cos k_{yR} \left( y_{0p} + \frac{d_p}{4} \right) I_{R}^2(kL_p)$$

$$Y_{12(21)}^R = \frac{4\pi}{a_R b_R} \sum_{m=1,3,\dots} \sum_{n=0}^{\infty} \frac{\varepsilon_n (k^2 - k_{xR}^2)}{kk_{zR}} \coth k_{zR} H \cos k_{yR} y_{01(02)} \cos k_{yR} \left( y_{02(01)} + \frac{d_{2(1)}}{4} \right) I_R(kL_{1(2)}) I_R(kL_{2(1)})$$

$$Y_{33}^R = \frac{4\pi}{a_R b_R} \sum_{m=1,3,\dots} \sum_{n=0}^{\infty} \frac{\varepsilon_n (k^2 - k_{xR}^2)}{kk_{zR}} \coth k_{zR} H \cos k_{yR} y_{03} \cos k_{yR} \left( y_{03} + \frac{d_3}{4} \right) I_{R3}^2(kL_3)$$

$$Y_{p3(3p)}^R = \frac{4\pi}{a_R b_R} \sum_{m=1,3,\dots} \sum_{n=0}^{\infty} \frac{\varepsilon_n}{k_{zR} \operatorname{sh} k_{zR} H} \cos k_{yR} y_{0p(3)} \cos k_{yR} \left( y_{03(p)} + \frac{d_{3(p)}}{4} \right) I_R(kL_p) I_{R3}(kL_3)$$

$$Y_{33}^{Hs} = (\operatorname{Si} 4kL_3 - i \operatorname{Cin} 4kL_3) - 2 \cos kL_3 \left[ \frac{2(\sin kL_3 - kL_3 \cos kL_3) \left( \ln \frac{16L_3}{2d_3} - \operatorname{Cin} 2kL_3 - i \operatorname{Si} 2kL_3 \right)}{+ \sin 2kL_3 e^{-ikL_3}} \right].$$

Here

$$I_{Wg(R)}(kL_p) = 2 \left\{ \frac{k \sin(kL_p) \cos(k_{x(xR)} L_p) - k_{x(xR)} \cos(kL_p) \sin(k_{x(xR)} L_p)}{k^2 - k_{x(xR)}^2} \cos(k_c L_p) - \frac{k_c \sin(k_c L_p) \cos(k_{x(xR)} L_p) - k_{x(xR)} \cos(k_c L_p) \sin(k_{x(xR)} L_p)}{k_c^2 - k_{x(xR)}^2} \cos(kL_p) \right\},$$

$$I_{R3}(kL_3) = 2 \frac{k_{xR} \sin(kL_3) \cos(k_{xR} L_3) - k \cos(kL_3) \sin(k_{xR} L_3)}{k_{xR}},$$

$k_{x(xR)} = \frac{m\pi}{a(a_R)}$ ,  $k_{y(yR)} = \frac{n\pi}{b(b_R)}$ ,  $k_{z(zR)} = \sqrt{k_{x(xR)}^2 + k_{y(yR)}^2 - k^2}$ ,  $k_c = \pi/a$ ,  $\varepsilon_n = 1$  at  $n=0$ ,  $\varepsilon_n = 2$  at  $n \neq 0$ ,  $z_0$  is the distance between the axes of the slots  $S_1$  and  $S_2$ ,  $y_{0p}$  is the position of the  $p$ -th slot axis in the coordinate system associated with the resonator (Fig. 1),  $\operatorname{Si}$  and  $\operatorname{Cin}$  are the integral sine and cosine [24].

Solving the system of equations (4), taking into account the fact that for a wave of the type  $H_{10}$  in a rectangular waveguide  $H_{0s_1} = H_0 \cos k_c s_1$ ,  $H_{0s_2} = H_0 \cos k_c s_2 e^{-ik_g z_0}$  ( $H_0$  is the amplitude,  $k_g = \sqrt{k^2 - k_c^2}$  is the propagation constant of the  $H_{10}$ -wave), we find the currents in each of the slots and the reflection and transmission field coefficients  $S_{11}$  and  $S_{12}$ , as well as the power radiating coefficient  $|S_{\Sigma}|^2$ :

$$S_{11} = \frac{2\pi i k_c k_g}{bk^3} \left[ \tilde{J}_{01} F(kL_1) + e^{-ik_g z_0} \tilde{J}_{02} F(kL_2) \right] e^{2ik_g z}, \quad (7)$$

$$S_{12} = 1 + \frac{2\pi i k_c k_g}{bk^3} \left[ \tilde{J}_{01} F(kL_1) + e^{ik_g z_0} \tilde{J}_{02} F(kL_2) \right], \quad (8)$$

$$|S_{\Sigma}|^2 = 1 - |S_{11}|^2 - |S_{12}|^2. \quad (9)$$

In formulas (7)–(9)  $\tilde{J}_{0p} = J_{0p} / \left( -\frac{i\omega}{2k^2} H_0 \right)$  are the normalized amplitudes of currents in slots,

$$F(kL_p) = 2 \cos k_c L_p \frac{\sin kL_p \cos k_c L_p - (k_c / k) \cos kL_p \sin k_c L_p}{1 - (k_c / k)^2} - \cos kL_p \frac{\sin 2k_c L_p + 2k_c L_p}{(2k_c / k)}.$$

The normalized radiation pattern in the vector  $\vec{H}$  plane for the structure under consideration has the form ( $\theta$  is the angle measured from the axis  $\{0x\}$ , Fig. 1):

$$\bar{F}_H(\theta) = \frac{\sin kL_3 \cos(kL_3 \cos \theta) - \cos kL_3 [\sin(kL_3 \cos \theta) / \cos \theta]}{\sin \theta (\sin kL_3 - kL_3 \cos kL_3)}. \tag{10}$$

Accounting for the thickness  $h_p$  of metal walls, in which slots are located, can be made according to [20] by the following substitutions  $d_p \rightarrow d_{ep}(h_p)$  under conditions  $(h_p / \lambda) \ll 1$ :

$$d_{ep}(h_p) \cong d_p e^{\frac{\pi h_p}{2d_p}}, \tag{11}$$

where  $d_{ep}(h_p)$  is the “equivalent” width of the  $p$ -th slot.

### NUMERICAL RESULTS

On Figs. 2-5 are plots of dependences of the radiation coefficient  $|S_\Sigma|^2(\lambda)$  on the wavelength for the following parameters:  $a=23.0$  mm,  $b=10.0$  mm,  $H=a_R/2$ ,  $2L_p=14.0$  mm,  $d_p=h_p=1.0$  mm. As can be seen from Fig. 2, the presence in the structure under study of a cavity resonator with one or two coupling slots makes it possible to form different frequency-energy characteristics of the entire system as a whole in comparison with a single transverse slot (1 slot) in the broad wall of the waveguide. With a certain mutual arrangement of slots relative to each other,  $|S_\Sigma|^2$  can reach a value of  $\sim 0.9$  in a narrow band of wavelengths or a value of  $\sim 0.5$  in a relatively large part of the range of the fundamental wave of the waveguide. A change in the transverse dimensions of the resonator ( $a_R, b_R$ ) has practically no effect on the position of the maximum  $|S_\Sigma|^2$  (Fig. 3). Moving the position of the radiating slot  $S_3$  within the resonator wall leads to a change in both the maximum (Fig. 4) and minimum (Fig. 5) values  $|S_\Sigma|^2$  at a certain wavelength, depending on the geometric dimensions of the slot and the thickness of the waveguide and resonator walls. Changing lengths of radiating and coupling slots at their fixed positions in the waveguide and resonator walls gives additional possibilities for the formation of characteristics required in the case of waveguide-resonator structures considered here (Fig. 6,  $a=23.0$  mm,  $b=10.0$  mm,  $a_R=20.0$  mm,  $b_R=10.0$  mm,  $H=a_R/2$ ,  $d_p=h_p=1.0$  mm,  $y_{01}=b_R/8$ ,  $y_{02,03}=b_R/4$ ).

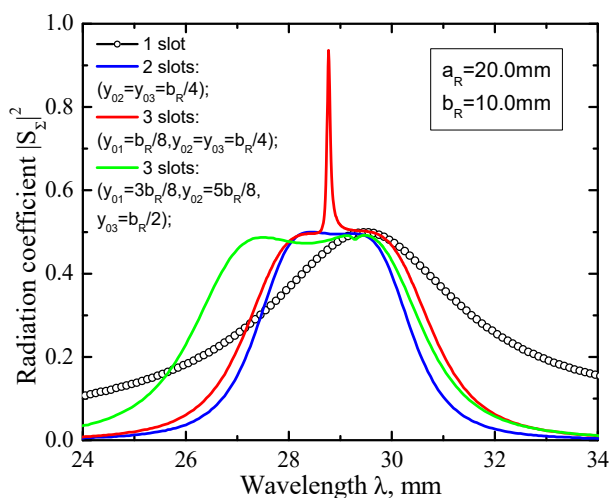


**Figure 2.** Wavelength dependence  $|S_\Sigma|^2(\lambda)$  for structures with one, two, and three slots

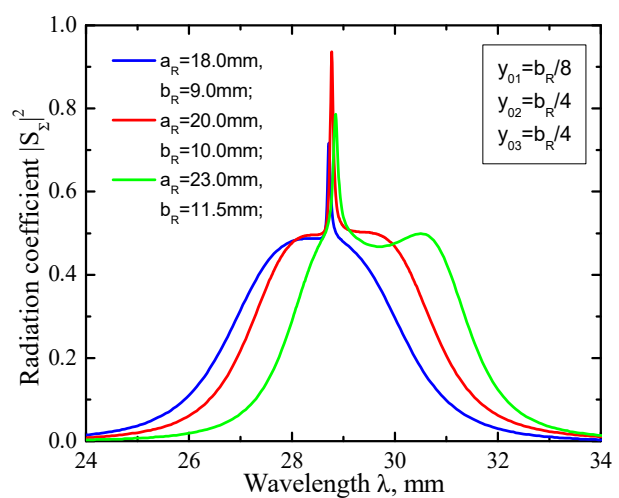


**Figure 3.** Wavelength dependence  $|S_\Sigma|^2(\lambda)$  for a structure with three slots for various resonator sizes

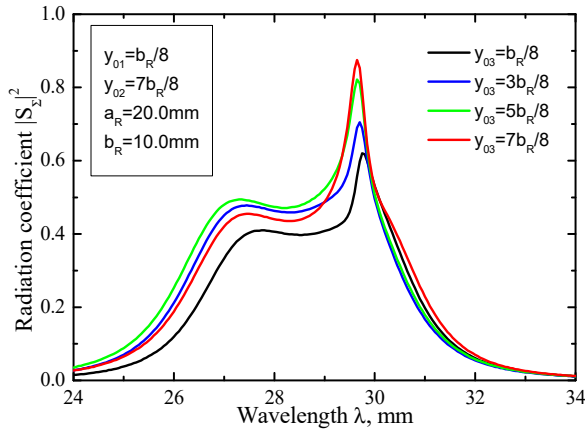


**Figure 4.** Wavelength dependence  $|S_z|^2(\lambda)$  for a structure with three slots at different positions of the radiating slot in the case of spaced coupling slots

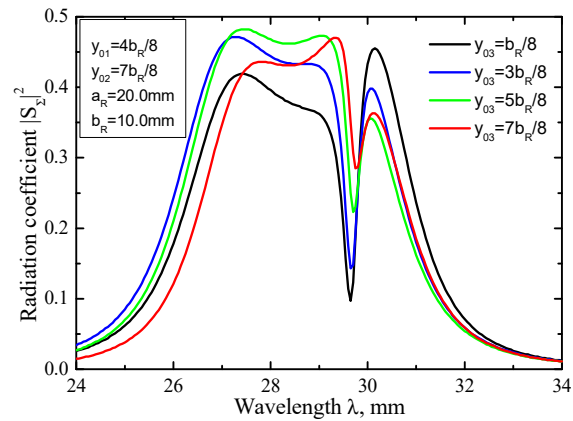
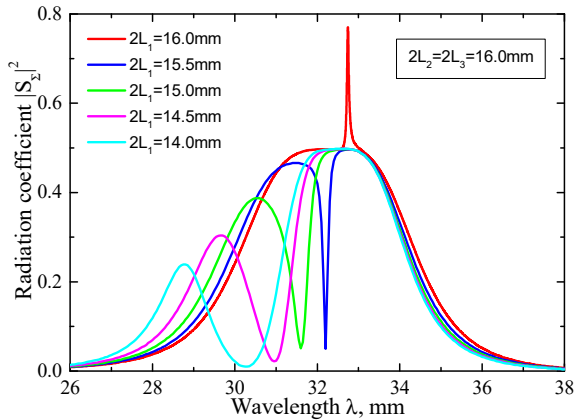
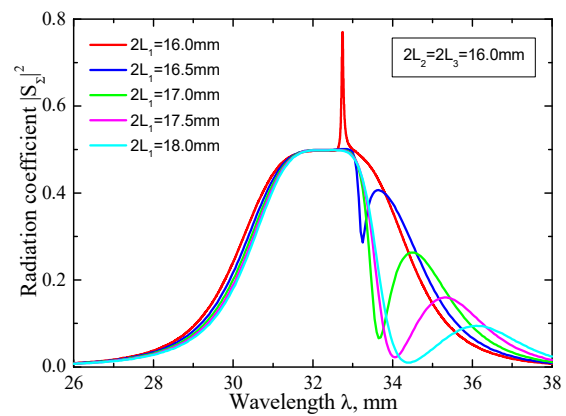


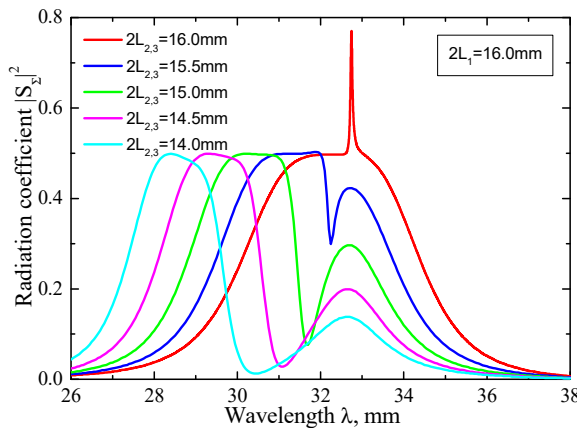
**Figure 5.** Wavelength dependence  $|S_z|^2(\lambda)$  for a structure with three slots at different positions of the radiating slot in the case of closely spaced coupling slots



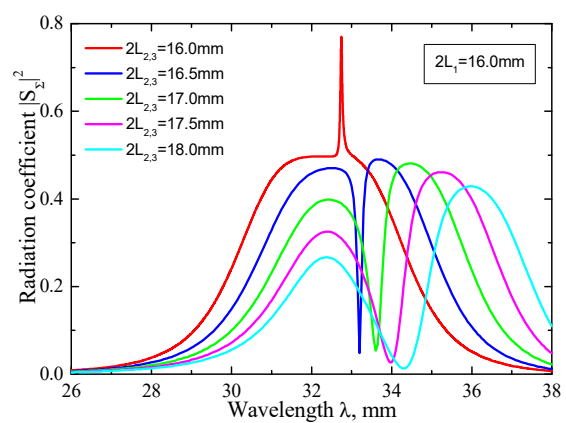
a)



b)



c)



d)

**Figure 6.** Wavelength dependence  $|S_z|^2(\lambda)$  for a structure with three slots at different lengths of the slots

### CONCLUSIONS

It is known from the classical theory of slot radiators and coupling holes [20] that a single slot in the side wall of a rectangular waveguide cannot radiate (transmit) more than half of the input power. An increase in the value of the radiation (transmission) coefficient can be carried out by placing other resonant elements in the waveguide, for example, vibrators (dipoles) [21] or dielectric inserts [22]. As shown by the calculations performed in the article, the placement of a rectangular resonator between the coupling slots and the radiating slot also leads to a significant increase the radiation coefficient value (up to  $\sim 0.9$ ) in a narrow wavelength (frequency) band. The multi-element waveguide-resonator-slot radiators studied in the article can be useful both in the development of new antenna transceiver systems of centimeter and millimeter wavelengths (including slotted antenna arrays), and for the modernization of existing ones based on the existing element base by means of insignificant design changes.



## ORCID

- ©Mikhail V. Nesterenko, <https://orcid.org/0000-0002-1297-9119>; ©Victor A. Katrich, <https://orcid.org/0000-0001-5429-6124>  
©Natalya K. Blinova, <https://orcid.org/0000-0001-9388-0008>

## REFERENCES

- [1] K. Yoshitomi, "Radiation from a slot in an impedance surface", IEEE Trans. Antennas Propag., **49**, 1370-1376 (2001). <https://doi.org/10.1109/8.954925>
- [2] M.V. Nesterenko, and Yu.M. Penkin, "Diffraction radiation from a slot in the impedance end of a semi-infinite rectangular waveguide", Radiophysics and Quantum Electronics, **47**, 489-499 (2004). <https://doi.org/10.1023/B:RAQE.0000047240.37895.ea>
- [3] S.L. Berdnik, Y.M. Penkin, V.A. Katrich, M.V. Nesterenko, and V.I. Kijko, "Electromagnetic waves radiation into the space over a sphere by a slot in the end-wall of a semi-infinite rectangular waveguide", Prog. Electromagn. Res. B, **46**, 139-158 (2013). <http://dx.doi.org/10.2528/PIERB12102203>
- [4] S.L. Berdnik, V.A. Katrich, V.I. Kijko, M.V. Nesterenko, and Y.M. Penkin, "Slotted spherical antenna with a multi-element diaphragm in the waveguide", Prog. Electromagn. Res. M, **95**, 1-12 (2020). <http://dx.doi.org/10.2528/PIERM20050806>
- [5] M.V. Nesterenko, V.A. Katrich, V.I. Kijko, and S.V. Pshenichnaya, "Radiation of electromagnetic waves by an arbitrarily oriented slot at the end wall of a rectangular waveguide", Prog. Electromagn. Res. C, **113**, 47-58 (2021). <http://dx.doi.org/10.2528/PIERC21042303>
- [6] R.F. Hyneman, "Closely-spaced transverse slots in rectangular waveguide", IRE Trans. Antennas Propag. **7**, 335-342 (1959). <https://doi.org/10.1109/TAP.1959.1144696>
- [7] E.M.T. Jones, and J.K. Shimizu, "A Wide-band transverse-slot flush-mounted array", IEEE Trans. Antennas Propag., **8**, 401-407 (1960). <https://doi.org/10.1109/TAP.1960.1144864>
- [8] H.J. Schaik, "The performance of an iris-loaded planar phased-array antenna of rectangular waveguides with an external dielectric sheet", IEEE Trans. Antennas Propag., **26**, 413-419 (1978). <https://doi.org/10.1109/TAP.1978.1141860>
- [9] R.F. Harrington, and J.R. Mautz, "Computational methods for transmission of waves", in: *Electromagnetic Scattering*, edited by P.L.E. Uslenghi, (Academic Press, NY, 1978). pp. 429.
- [10] A.J. Sangster, "Slotted waveguide linear array with polarization control", Electron. Lett., **14**, 616-618 (1978). <https://doi.org/10.1049/el:19780415>
- [11] F.J. Paoloni, "Cavity-backed resonant slot array – theory and measurement," IEEE Trans. Antennas Propag., **28**, 259-263 (1980). <https://doi.org/10.1109/TAP.1980.1142321>
- [12] R.S. Elliott, and W.R. O'Loughlin, "The design of slot arrays including internal mutual coupling", IEEE Trans. Antennas Propag., **34**, 1149-1154 (1986). <https://doi.org/10.1109/TAP.1986.1143947>
- [13] G. Montisci, M. Musa, and G. Mazzarella, "Waveguide slot antennas for circularly polarized radiated field", IEEE Trans. Antennas Propag., **52**, 619-623 (2004). <https://doi.org/10.1109/TAP.2004.823873>
- [14] S.L. Berdnik, V.A. Katrich, V.I. Kiiko, and M.V. Nesterenko, "Electrodynamic characteristics of the nonresonant system of transverse slots in the wide wall of rectangular waveguide", Radioelectronics Commun. Syst. **48**, 52, (2005).
- [15] M.V. Nesterenko, V.A. Katrich, Yu.M. Penkin, and S.L. Berdnik, "Analytical methods in theory of slot-hole coupling of electrodynamic volumes", Prog. Electromagn. Res., **70**, 79-174 (2007). <http://dx.doi.org/10.2528/PIER06121203>
- [16] Y. Hou, Z. Meng, L. Wang, and Y. Li, "Endfire antenna array using microstrip-fed cavity-backed slot elements", IEEE Trans. Antennas Propag. **68**, 24482433 (2020). <https://doi.org/10.1109/TAP.2019.2940493>
- [17] M. Chen, X.C. Fang, W. Wang, H.T. Zhang, and G.L. Huang, "Dual-band dual-polarized waveguide slot antenna for SAR applications", IEEE Antennas Wireless Propag. Lett., **19**, 17191723 (2020). <https://doi.org/10.1109/LAWP.2020.3014878>
- [18] Y. Kan, R. Yang, A. Zhang, Z. Lei, Y. Jiao, and J. Li, "Meta-surface cavity-based waveguide slot array for dual-circularly polarized dual beam", IEEE Trans. Antennas Propag., **70**, 3894-3898 (2022). <https://doi.org/10.1109/TAP.2021.3137211>
- [19] M.S. Masouleh, A.K. Behbahani, M. Sharafi, M. Sajedi, and M. Adjonadi, "Pattern synthesis of a resonant slot on a broad wall of the rectangular waveguide using amplitude and phase control", Prog. Electromagn. Res. C, **129**, 51-61 (2023). <http://dx.doi.org/10.2528/PIERC22101005>
- [20] M.V. Nesterenko, V.A. Katrich, Yu.M. Penkin, and S.L. Berdnik, *Analytical and Hybrid Methods in Theory of Slot-Hole Coupling of Electrodynamic Volumes*, (Springer Science+Business Media, NY, 2008).
- [21] M.V. Nesterenko, V.A. Katrich, Yu.M. Penkin, S.L. Berdnik, and O.M. Dumin, *Combined Vibrator-Slot Structures: Theory and Applications*. (Springer Nature Switzerland AG, Cham, Switzerland, 2020). <https://doi.org/10.1007/978-3-030-60177-5>
- [22] Yu.M. Penkin, V.A. Katrich, M.V. Nesterenko, S.L. Berdnik, and N.K. Blinova, "Analysis of resonant characteristics of E- and H-plane waveguide junctions with local dielectric inclusions", Prog. Electromagn. Res. L, **91**, 17-24 (2020). <http://dx.doi.org/10.2528/PIERL20020705>
- [23] M.V. Nesterenko, V.A. Katrich, S.V. Pshenichnaya, and V.I. Kijko, "Scattering of electromagnetic waves by a multi-element system of pass-through resonators in a rectangular waveguide", Prog. Electromagn. Res. C, **131**, 135-143 (2023). <http://dx.doi.org/10.2528/PIERC23020903>
- [24] M. Abramowitz, and I.A. Stegun, *Handbook of Mathematical Functions with Formulas, Graphs and Mathematical Tables*, (National Bureau of Standards, Applied Mathematics Series-55, 1964).

**БАГАТОПАРАМЕТРИЧНЕ КЕРУВАННЯ ЕНЕРГЕТИЧНИМИ ХАРАКТЕРИСТИКАМИ  
ХВИЛЕВОДНО-РЕЗОНАТОРНО-ЩІЛИННИХ ВИПРОМІНЮВАЧІВ**

**Михайло В. Нестеренко, Віктор О. Катрич, Наталя К. Блинова**

*Харківський національний університет імені В.Н. Каразіна, майдан Свободи, 4, Харків, Україна, 61022*

Задача з'єднання трьох електродинамічних об'ємів з ідеально провідними стінками через електрично вузькі прямолінійні сполучні щілини та випромінювальну щілину вирішується узагальненим методом наведених магніторухливих сил (МРС). Розв'язок отримано в аналітичній формі з урахуванням кінцевої товщини стінок зв'язаних об'ємів. Об'єми являють собою нескінченний прямокутний хвилевід, який збуджено основною хвилею, резонатор прямокутної порожнини та півпростір над нескінченною площиною. Всебічно вивчено енергетичні характеристики цієї системи в залежності від геометричних параметрів складових елементів конструкції, що розглядається.

**Ключові слова:** випромінювальна щілина; сполучні щілини; прямокутний хвилевід; об'ємний резонатор; електромагнітні хвилі

## DOSIMETRIC EVALUATION STUDY OF 10-MV FFF USED IN SBRT FOR LUNG TUMOURS<sup>†</sup>

✉ **Mohamed I. Soliman<sup>a\*</sup>, Wahib M. Attia<sup>b†</sup>, Khaled M. Elshahat<sup>c#</sup>**

<sup>a</sup>Zagazig armed forces oncology center, Zagazig, Egypt; <sup>b</sup>Suez Canal university, professor of physics, Egypt

<sup>c</sup>AL Azhar university, professor of physics, Egypt

<sup>#</sup>e-mail: [khelshahat@yahoo.com](mailto:khelshahat@yahoo.com); <sup>†</sup>e-mail: [wahibattia@hotmail.com](mailto:wahibattia@hotmail.com)

<sup>\*</sup>Corresponding Author e-mail: [al\\_zok@yahoo.com](mailto:al_zok@yahoo.com)

Received July 13, 2023; revised August 3, 2023; accepted August 4, 2023

**Purpose:** The objective of this research was to conduct a comparative and dosimetric analysis of three different radiotherapy techniques used in lung stereotactic body radiotherapy (SBRT), the three-dimensional conformal radiotherapy (3DCRT), intensity-modulated radiation therapy (IMRT), and volumetric modulated arc therapy (VMAT), using a 10 MV flattening filter-free (FFF) photon beam.

**Materials and methods:** The present study employed computed tomography (CT) images of a humanoid phantom for the purpose of treatment planning. The gross tumour volumes (GTVs) delineated in both the central and peripheral positions of the lungs. The determination of Planning Target Volumes (PTVs) involved the addition of a margin of 0.5 cm to the Gross Tumour Volume (GTV). Three-dimensional conformal radiotherapy (3DCRT), intensity-modulated radiation therapy (IMRT), and volumetric modulated arc therapy (VMAT) treatment plans produced employing a 10-megavolt (MV) flattening filter-free (FFF) photon beam. The calculation of dosage for all plans Performed using the anisotropic analytical algorithm (AAA). **Results:** IMRT and VMAT had better PTV dose conformation than 3DCRT for both central and peripheral targets. PTV conformity improved in VMAT compared to IMRT, and CI values were acceptable for VMAT, IMRT, and 3DCRT plans. VMAT plans had slightly better CI than IMRT, with better results in peripheral lung PTVs compared to central PTVs. VMAT and IMRT are superior for treating HDV and D2cm, with lower HDV for peripheral lung tumours. Both 3DCRT and IMRT improved outcomes for peripheral lung PTVs, while VMAT was better for central lung PTVs. The former proved better with less low lung doses and improved D2cm results. 3DCRT plans demonstrated higher precision in dose distribution than VMAT and IMRT plans, with superior average GI values. VMAT and IMRT had higher HI, Dmax, and D2% than 3DCRT. VMAT plans compared to IMRT plans, with similar HI values for central lung PTVs. VMAT better spares OARs than other techniques, but V20 and V30 lung doses were lower with 3DCRT. VMAT increases lung dose, but OAR stays below thresholds.

**Conclusion:** The investigation found that all three treatment techniques can deliver SBRT plans that meet RTOG dose constraints. However, VMAT is a better treatment strategy than IMRT and 3DCRT for both peripheral and central lung PTVs, based on dosimetric indices like CI, D2cm, HI, and HDV. The study found that 3DCRT improves dosimetric indices, especially gradient index (GI), more than VMAT. Despite the need for more monitor units (MUs) in VMAT plans, treatment time reduced due to faster gantry velocity and higher dose rates (2400cGy/min) via free flattening filter energy.

**Keywords:** 3DCRT; IMRT; VMAT; Lung cancer; Dosimetric comparison; SBRT

**PACS:** 29.20.-c, 29.20.Ej, 87.56.bd

### INTRODUCTION

Stereotactic body radiation therapy (SBRT) is a type of radiation therapy that delivers high doses of radiation to a small, well-defined target in the body while minimizing the radiation dose to surrounding healthy tissue. SBRT is often used to treat tumours in the lung, liver, spine, and other areas of the body. There are several types of radiation therapy techniques that can be used to deliver SBRT, including 3D conformal radiation therapy (3DCRT), intensity-modulated radiation therapy (IMRT), and volumetric modulated arc therapy (VMAT) [1].

SBRT is a commonly used treatment option for non-small cell lung cancer (NSCLC), particularly for patients who are not candidates for surgery or traditional radiation therapy. NSCLC is the most common type of lung cancer, accounting for about 85% of all lung cancer cases [2]. SBRT delivers high doses of radiation to the tumour in a highly targeted and precise manner, while minimizing the dose to surrounding healthy tissue. This can be particularly important for NSCLC, as the lungs and surrounding organs are highly sensitive to radiation.

Studies have shown that SBRT can be an effective treatment option for NSCLC, with high rates of local tumour control and good overall survival rates. In fact, SBRT has been shown to have similar outcomes to surgery for early-stage NSCLC, with lower rates of complications and shorter recovery times [3].

SBRT is typically delivered over a few treatment sessions. The number of treatment sessions and the radiation dose delivered will depend on the size and location of the tumour, as well as the patient's overall health and treatment goals [4].

Typically, flattening filter (FF) photon beams are employed in all of these therapeutic techniques. In recent times, an alternative choice for FF beams called flattening filter-free (FFF) beams has been made available. FFF beams offer a significant benefit over FF in terms of a dose rate that is between two to four times greater [5].

Overall, SBRT can be an important treatment option for patients with NSCLC, particularly those who are not candidates for surgery or traditional radiation therapy. However, as with any cancer treatment, the decision to use SBRT should be made in consultation with a multidisciplinary team of healthcare professionals, including radiation oncologists, medical oncologists, and pulmonologists.

<sup>†</sup> Cite as: M.I. Soliman, W.M. Attia, K.M. Elshahat, East Eur. J. Phys. 3, 457 (2023), <https://doi.org/10.26565/2312-4334-2023-3-51>

© M.I. Soliman, W.M. Attia, K.M. Elshahat, 2023

## MATERIALS AND METHODS

When developing and testing treatment plans for SBRT using 10FFF for NSCLC, a common approach is to use a humanoid phantom. A humanoid phantom is a human-shaped object made of materials that mimic human tissue, and it is used to simulate the effects of radiation on the body. Here are some general material and methods for SBRT using 10FFF for NSCLC with a humanoid phantom:

### 1. Humanoid phantom

A humanoid phantom made of tissue-equivalent materials is used to simulate the human body shown in Figure (1). The phantom should be of a similar size and shape to the patient being treated. Polyurethane material was used to create artificial muscles and soft tissue. A substance that is similar to soft tissue in terms of its atomic properties.

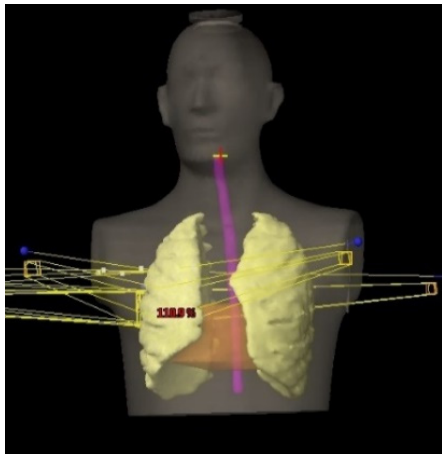


Figure 1. Humanoid phantom

healthy tissue. The use of 10FFF beams may require adjustments to the treatment plan to optimize dose delivery.

Polyurethane simulated muscle and soft tissue, while a lower density material with the same effective atomic number as soft tissue was used for lungs. The phantom is a 175 cm, 73.5 kg male body sliced at 2.5 cm intervals. [6,7]

Simulation: A CT scan of 25mm slices of the phantom is performed to create a 3D image of the phantom. This image is used to develop a treatment plan, similar to what would be done for a patient. The radiation oncologist and medical physicist work together to develop the treatment plan using specialized software.

### 2. Characteristics of Treatment Planning

The image registration and contouring tasks were carried out through utilization of the Eclipse 15.6 treatment planning system, which was developed by Varian Medical Systems, Palo Alto, California, United States. The treatment plan is developed using the CT scan image and other information about the tumour. The goal is to deliver a high dose of radiation to the tumour while minimizing exposure to surrounding

### 3. Delineation and characteristics of the tumor

The delineation of the gross tumour volumes (GTVs) took place in two locations within the lungs: central and peripheral regions. To mimic the impact of a lung tumour on the phantom, GTV was provided with a skeletal muscle substance possessing a mass density of  $1.05 \text{ g}\cdot\text{cm}^{-3}$  and a CT number of 48 HU. The volume for planning purposes, referred to as the PTV, was acquired by incorporating a margin of 0.5cm to the GTV. 30 PTVs were defined, with 15 being located in each of the lungs. A group of 15 distinct tumour sizes ranging from 1.7 cc to 99.6 cc and located at the same central point were known as PTVs. The volumes of these PTVs differed from one another. Both PTVs were used to contour both tumour locations. The volume of the 15 PTVs in each location (central or peripheral) of the lungs are shown in Table 1.

Table 1. Volumes of fifteen lesions at central and peripheral lung

Target No	Central target volume $\text{cm}^3$	Peripheral target volume $\text{cm}^3$
1	1.7	1.7
2	2.5	2.5
3	3.6	3.6
4	4.5	4.5
5	5.8	5.8
6	7.2	7.2
7	9.6	9.6
8	14.4	14.4
9	22.5	22.5
10	41	41
11	63.2	63.2
12	74.4	74.4
13	87.3	87.3
14	91.8	91.8
15	99.6	99.6

### 4. Treatment Planning Techniques

This study evaluates the techniques of 3DCRT, IMRT and VMAT planning when performing SBRT for lung tumours. The Eclipse TPS (version 15.6) was utilized to produce the treatment plans. For planning purposes, a 10-MV FFF photon beam was derived from a True Beam linear accelerator manufactured by Varian Medical Systems, Inc. located in Palo Alto, CA, USA. High-definition multi-leaf collimators comprised of 120 leaves were employed to establish field apertures. The

plans were subjected to radiation dose calculations using the AAA algorithm with dose rate 2400MU/min. The plans underwent normalization to ensure that the prescribed dose encompassed 95% of the planning target volume (PTV) [8].

Three-dimensional conformal radiation therapy (3DCRT), intensity-modulated radiation therapy (IMRT), and volumetric modulated arc therapy (VMAT) are all forms of radiation therapy used to treat cancer. Each treatment technique employs different methods to deliver radiation to the cancerous cells while sparing surrounding healthy tissue.

#### a. 3DCRT

Three-dimensional conformal radiation therapy (3DCRT) is a type of external beam radiation therapy that uses multiple beams of radiation to deliver high doses of radiation to the tumour while sparing surrounding healthy tissue. The beams are shaped using collimators to match the shape of the tumour and delivered from different angles [9,10].

3DCRT using 5- fields involves delivering radiation to the tumour using five different beams, which aimed at the tumour from different angles. The goal of using multiple beams is to maximize the dose of radiation delivered to the tumour while minimizing the dose to healthy surrounding tissue.

#### b. IMRT

Intensity-modulated radiation therapy (IMRT) is a type of external beam radiation therapy that uses multiple beams of radiation with varying intensities to deliver precise doses of radiation to the tumour while minimizing the dose to surrounding healthy tissue. This is achieved by using a collimator with movable leaves that can shape the radiation beam to conform to the shape of the tumour. [11,12]

IMRT using 7- fields involves delivering radiation to the tumour using seven different beams, which aimed at the tumour from different angles. The intensity of each beam modulated using specialized software to deliver different amounts of radiation to various parts of the tumour. This allows for precise dose delivery to the tumour while sparing surrounding healthy tissue. The treatment planned to use specialized software that calculates the optimal beam angles, beam intensities, and leaf positions for delivering the radiation.

#### c. VMAT

Volumetric modulated arc therapy (VMAT) is a type of external beam radiation therapy that uses a single or multiple arcs of radiation to deliver precise doses of radiation to the tumour while sparing surrounding healthy tissue. The beam shaped using a collimator with movable leaves, similar to IMRT.

VMAT using two full arcs involves delivering radiation to the tumour using two full arcs of radiation to central lung tumour and two half arcs for peripheral lung tumour, which aimed at the tumour from different angles. The collimator leaves move continuously during the delivery of the radiation to modulate the intensity of the beam and shape it to conform to the shape of the tumour. This allows for precise dose delivery to the tumour while sparing surrounding healthy tissue [13,14].

### 5. Dosimetric Plan Evaluation Indices

- i. The conformity index (CI): defined as the ratio of the prescribed dose volume (VPD) to the volume of the planning target receiving the prescribed dose or more (PTVPD). The planned ideal ratio was to be below 1.2 [15].

$$CI = \frac{VPD}{PTVPD} \quad (1)$$

- ii. High dose volume (HDV): refers to the volume of tissue that receives a radiation dose above a certain threshold. The threshold dose used to define HDV varies depending on the clinical situation, but it is typically higher than the prescribed dose and can range from 105% to 150% of the prescribed dose [16].
- iii. low-dose location (D2cm): is the maximum dose administered to healthy tissue situated at a distance of 2 cm from the planning target volume (PTV) in all directions [17,18].
- iv. The gradient index (GI): is the ratio between the volume which receives 50% of the prescribed dose (V50PD) to the volume of prescription isodose (PTV V100%) [19,20].

$$GI = \frac{Vol(50\%)}{PTV V100\%} \quad (2)$$

- v. Homogeneity Index (HI): is an objective tool used to analyse the uniformity of dose distribution in the target volume. HI basically indicates the ratio between the maximum and minimum dose in the target volume and the lower value indicates a more homogenous dose distribution within this volume.

$$HI = \frac{D2\% - D98\%}{D50\%} \quad (3)$$

- vi. Maximum dose (Dmax): is the maximum point dose located inside the PTV.
- vii. A monitor unit (MU): is a unit of measurement used in radiation therapy to quantify the amount of radiation delivered to a patient. One monitor unit is equal to the amount of charge that is required to produce one cGy of dose in a water phantom.

viii. Beam on time (BOT): the time when a radiation beam used to deliver a set number of monitor units [16,19].

$$BOT = \frac{\text{Total monitor unit}}{\text{Dose rate (2400cGy/min)}} \tag{4}$$

### 6. Organ at risk constrains

The dose tolerances for Lungs, Oesophagus, Heart, and spinal cord illustrated in Table 2.

**Table 2.** Organ at risk dose constrains

Structure	Metric	Tolerance (5 fractions)
Both lungs	V20%	10 Gy
	Dmean	8 Gy
Esophagus	D0.01cc	35 Gy
Heart	D0.01cc	29 Gy
Spinal cord	D0.035	25.3 Gy

### RESULTS

A set of clinically appropriate plans of volumetric-modulated arc therapy VMAT, IMRT, and 3DCRT were successfully developed for all 15 cases. The dosimetry data pertaining to all Stereotactic Body Radiation Therapy (SBRT) plans were derived through the process of Dose-Volume Histogram (DVH) analysis. Subsequently, a comparison was made between the plans for the three techniques through the utilization of these indices. Table 7 presents the dosimetry outcomes for the treatment plans utilizing 3DCRT, IMRT, and VMAT for the combined lung targets, encompassing all planning target volumes (PTVs) situated in both peripheral and central regions of the lungs. The results of the study were subjected to separate evaluations based on the location of the lung tumour, namely the central and peripheral lung planning target volumes, which are presented in Tables 3-5 respectively. Figure 1 illustrates the axial plane dose allocation in three distinct treatment approaches, 3DCRT, IMRT, and VMAT, for the Planning Target Volume (PTV) encompassing both central and peripheral regions.

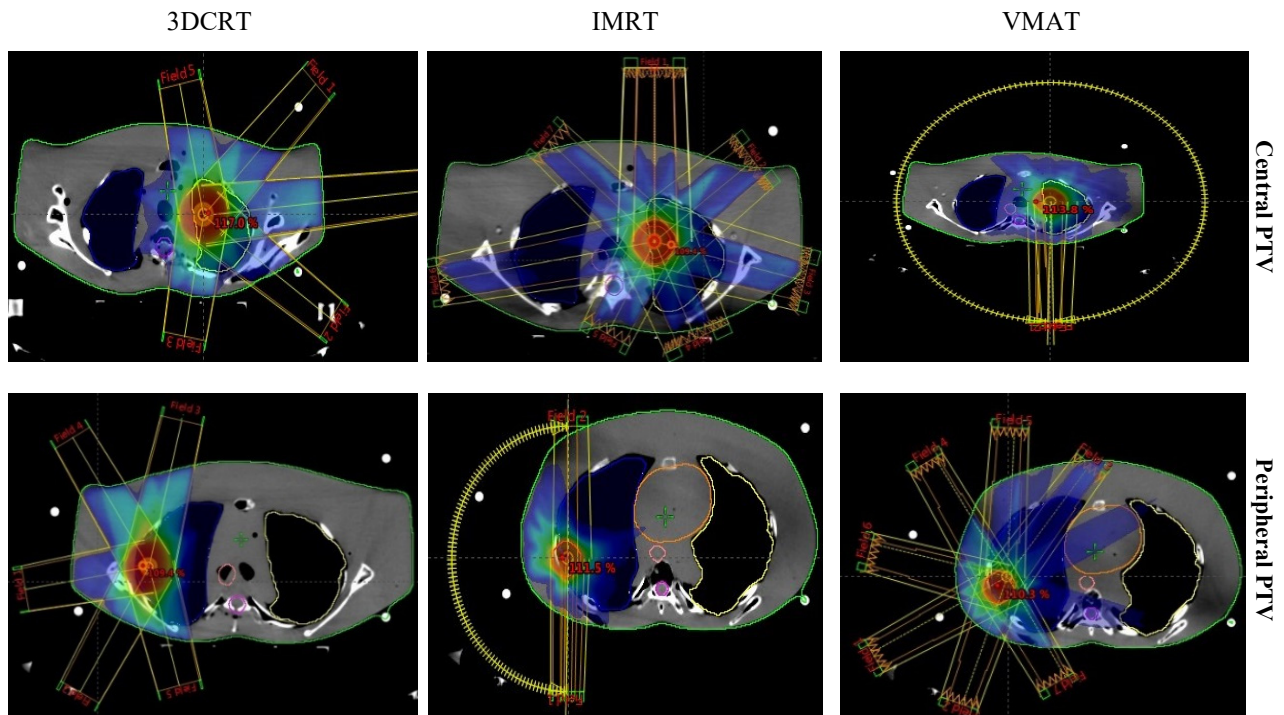


**Figure 1.** Dose distribution for the three planning techniques in the axial plane both peripheral and central

**Table 3.** Dosimetric differences in plan parameters between three treatment techniques for central lung PTV

Parameters	3-DCRT	IMRT	VMAT	P-VALUE		
				3DCRT/IMRT	3DCRT/VMAT	IMRT/VMAT
HI	0.18±0.03	0.21±0.02	0.21±0.023	0.17	0.13	0.48
CI	1.17±1.3	1.07±0.08	1.04±0.06	0.032	0.029	0.034
GI	3.2±0.65	3.42±0.84	4.1±0.47	0.42	0.004	0.003
DMAX%	115±5	117±4	118±5	0.003	0.003	0.009

Parameters	3-DCRT	IMRT	VMAT	P-VALUE		
				3DCRT/ IMRT	3DCRT/ VMAT	IMRT/VM AT
D2%	112±4	113±2	115±3	0.004	0.002	0.003
D2CM%	57±8.3	43.6±5	38±6	0.004	0.003	0.002
HDV%	1.7±0.46	0.44±0.53	0.37±.26	0.003	0.003	0.006
BOT(MIN)	1.54±0.9	1.98±1.2	1.82±0.7	0.005	.008	0.003
MUs	3703±322	4747±534	4367±253	0.003	0.003	0.002

1. Maximum dose (Dmax) and Minimum dose (D2%)  
The results from the statistical analysis for Maximum dose (Dmax) and Minimum dose (D2%) indicated a remarkable variation ( $p < 0.05$ ) among the various techniques, except for the p-value associated with maximum dose (Dmax) when comparing the IMRT and VMAT techniques in relation to central lung PTVs. Notably, the calculated p-value for this comparison was found to be 0.09 Table 3.
2. Homogeneity Index (HI)  
Homogeneity index (HI) comparison for central lung PTVs, revealed a significant difference could not be established between three different techniques ( $p > 0.05$ ) Table.3, while yielded significant differences ( $p < 0.05$ ) between three different techniques for peripheral and combined lung PTVs Table.5,7.

**Table (4).** Comparison of doses to organs at risk for central lung PTV

organs	parameters	3-DCRT	IMRT	VMAT	P-VALUE		
					3DCRT/ IMRT	3DCRT/ VMAT	IMRT/ VMAT
Both lungs	V20%	4.3±2.3	5.2±3.1	4.01±1.9	0.05	0.162	0.045
	Dmean	3.1±1.8	2.28±2.1	2.7±2.3	0.022	0.033	0.134
Esophagus	D 0.1cc, (Gy)	16.33±2.6	17.8±4.4	13.4±2.8	0.43	0.003	0.002
Heart	D 0.1cc, (Gy)	17.6±1.13	5.4±1.9	3.7±1.8	0.003	0.002	0.003
Spinal cord	D0.035	14.3±2.5	11.7±1.8	10.3±1.6	0.03	0.003	0.002

3. Conformity Index (CI)  
The present study observed a significant improvement in the mean conformity index (CI) values for IMRT and volumetric arc therapy (VMAT) in the combined lung planning target volume (PTV) as compared to (3DCRT). Furthermore, the peripheral lung PTV demonstrated superior CI values as compared to the central lung PTV. All PTV apparatuses fulfilled the corresponding Radiotherapy Oncology Group (RTOG) standards via the utilization of three different techniques. Four smaller planning target volumes (PTVs) were initially scheduled to be delineated within the central lung region using (3DCRT) techniques. However, these PTVs obtain minor deviations. The statistical test conducted for individual comparisons indicated statistically significant differences ( $P < 0.05$ ) among the various techniques Tables 3,5,7.

**Table 5.** Dosimetric differences in plan parameters between three treatment techniques for peripheral lung PTV

parameters	3-DCRT	IMRT	VMAT	P-VALUE		
				3DCRT/ IMRT	3DCRT/ VMAT	IMRT/ VMAT
HI	0.17±0.06	0.23±0.02	0.22±0.03	0.003	0.003	0.002
CI	1.09±0.08	1.07±0.08	1.04 ±0.06	0.003	0.002	0.003
GI	3.06±0.45	3.3±0.76	3.8±0.39	0.003	0.004	0.174
DMAX%	113±4	116±5	116±7	0.003	0.003	0.005
D2%	110±7	111±5	114±4	0.003	0.003	0.002
D2CM%	52±9	40.6±7	38±5	0.088	0.014	0.19
HDV%	1.1±0.87	0.4±0.77	0.32±.66	0.006	0.003	0.002
BOT(MIN)	1.35±1.04	1.79±0.8	1.65±0.95	0.006	0.003	0.003
MUs	3238±243	4287±435	3956±383	0.003	0.003	0.002

4. High dose volume (HDV) and Low dose location (D2cm)  
The mean values of high-dose volume (HDV) and 2cm dose distance (D2cm) were optimized via VMAT and IMRT techniques for the combined lung planning target volume (PTV). Except for IMRT, which exhibited superior D2cm in comparison to VMAT and (3DCRT) for peripheral lung planning target volumes (PTVs), both central and peripheral lung PTVs illustrated a comparable objective towards the incorporation of the entire lung PTVs. The statistical analysis performed to compare the HDV and D2cm techniques revealed a significant difference with a p-value of less than 0.05, similar to the Conformity Index (CI) procedure. However, it is observed that the p-values obtained for the D2cm technique in the evaluation of peripheral lung Planning Target Volumes (PTVs) did not yield statistically significant differences between the various techniques investigated ( $p > 0.05$ ) Tables 5.

**Table 6.** Comparison of doses to organs at risk for peripheral lung PTV

organs	parameters	3-DCRT	IMRT	VMAT	P-VALUE		
					3DCRT/I MRT	3DCRT/V MAT	IMRT/V MAT
Both lungs	V20%	4.7±2.8	5.6±3.5	5.91±2.2	0.003	0.003	0.007
	Dmean	3.7±2.3	3.2±1.8	3.7±2.6	0.005	0.003	0.005
Esophagus	(Gy) D0.1cc	4.6±1.6	5.4±1.2	3.8±1.6	0.006	0.003	0.003
Heart	(Gy) D0.1cc	2.2±2.6	2.8±2.2	3.3±1.5	0.003	0.003	0.003
Spinal cord	Dmax (Gy)	7.3±2.6	6.7±3.1	5.6±2.34	0.08	0.003	0.003

5. Gradient Index (GI):

The statistical analysis indicated significant differences ( $p < 0.05$ ) among the gradient index (GI) outcomes observed in the three investigated techniques. However, it should be noted that the p-values for GI outcomes in central lung planning target volumes (PTVs) between (3DCRT) and IMRT plans, as well as in peripheral lung PTVs between IMRT and VMAT plans, were found to be non-significant ( $p = 0.427$  and  $0.134$ , respectively) Tables 3,5.

**Table 7.** Dosimetric differences in plan parameters between three treatment techniques for combined lung PTV

parameters	3-DCRT	IMRT	VMAT	P-VALUE		
				3DCRT/I MRT	3DCRT/ VMAT	IMRT/ VMAT
HI	0.025±0.05	0.28±0.04	0.27±0.02	0.003	0.002	0.002
CI	1.08±0.08	1.06±0.08	1.03 ±0.06	0.002	0.002	0.002
GI	3.16±0.75	3.34±0.66	3.7±0.45	0.002	0.003	0.003
DMAX%	115±4.6	118±3.3	118±4.4	0.003	0.003	0.003
D2%	113±5.4	116±4.6	115±3.6	0.001	0.001	0.002
D2CM%	49.3±5.3	43.6±6.6	40.6±4.5	0.001	0.001	0.007
HDV%	1.2±0.24	0.49±0.44	0.42±.75	0.001	0.001	0.001
BOT(MIN)	1.5±0.84	1.9±1.02	1.75±0.9	0.001	0.001	0.002
MUs	3603±356	4544±544	4188±311	0.002	0.003	0.003

6. Monitor Unit (MU)and Beam on Time (BOT)

When compared to 3DCRT, the mean MU values for central lung tumours increased by 28.2% with IMRT and 17.9% with VMAT; and 32.39% with IMRT and 22.17% with VMAT for peripheral lung tumours and MU values for combined lung tumours increased by 26.11% with IMRT and 16.23% with VMAT. Similar to monitor unit (MU) Compared with 3DCRT, mean beam on time (BOT) values for central lung tumours increased by 32.5% with IMRT and 18.18% with VMAT; 32.5% with IMRT and 22.2% with VMAT for peripheral lung tumours and combined lung tumours with BOT values increased by 26.7% for IMRT and 16.7% for VMAT Tables 3,5,7.

**Table 8.** Comparison of doses to organs at risk for combined lung PTV

organs	parameters	3-DCRT	IMRT	VMAT	P-VALUE		
					3DCRT/ IMRT	3DCRT/ VMAT	IMRT/ VMAT
Both lungs	V20%	4.5±2.8	5.6±2.4	4.41±2.6	0.001	0.001	0.273
	Dmean	3.7±2.4	3.3±2.8	2.9±3.3	0.002	0.030	0.223
esophagus	Dmax (Gy)	14.5±5.6	15.8±5.9	11.4±4.6	0.09	0.001	0.001
Heart	Dmax (Gy)	11.6±6.8	4.2±4.2	3.05±1.8	0.05	0.04	0.001
Spinal cord	Dmax (Gy)	11.3±3.5	10.2±3.8	8.6±2.8	0.03	0.003	0.002

7. Organ at Risk Dose limits

All three treatment techniques satisfactorily followed to the dose limits of the organs-at-risk (OAR). The statistical test was conducted for V20 and Dmax in various organs including the spinal cord, oesophagus, and heart, and revealed significant differences amongst different techniques ( $p < 0.05$ ), except for specific instances where p-values for Dmax (spinal cord and oesophagus) between 3DCRT and IMRT for peripheral lung PTVs Table 6 and Dmax (oesophagus) between 3DCRT and IMRT for combined and central lung PTVs ( $p > 0.05$ ) Tables 4,8. Additionally, V20 (lung) between IMRT and VMAT for combined lung PTVs, Dmean (lung) between IMRT and VMAT for combined lung and central lung PTVs, and V20 (lung) between 3DCRT and VMAT for central lung PTVs also exhibited p-values greater than 0.05 Tables 4,8.

## DISCUSSION

The aim of the current investigation was to conduct a comparative evaluation of the 3D conformal radiotherapy (3DCRT), intensity-modulated radiotherapy (IMRT), and volumetric arc therapy (VMAT) planning methodologies regarding their suitability for SBRT treatment of lung tumours using 10-MV FFF. Both the VMAT and intensity modulated radiation therapy IMRT techniques have demonstrated superior conformal delivery of prescribed doses to the planning target volume (PTV) for both central and peripheral lung targets in comparison to the traditional (3DCRT) approach. The conformity of the planned target volume (PTV) dose in VMAT plans demonstrated a minor enhancement in comparison to that of modulated radiation therapy (MRT). The conformity index (CI) values of VMAT, IMRT, and 3DCRT plans were found to be within the clinically acceptable limit ( $CI < 1.2$ ) which specified in the Radiation Therapy Oncology Group (RTOG) protocols. However, minor deviations in the CI values ( $CI > 1.5$ ) were observed for the 3DCRT plans designed for the smallest planning target volumes (PTVs) - PTV 1 {1.7cc}, PTV 2 {2.5cc}, PTV 3 {3.6cc}, and PTV 4 {4.5cc} - located in the central and peripheral lung PTVs, respectively. The IMRT and VMAT plans demonstrated superior conformity index (CI) outcomes in comparison to the (3DCRT) plans. A marginal enhancement in the conformity index (CI) was noted in the VMAT plans when compared with those of the IMRT plans. The peripheral lung planning target volumes (PTVs) exhibited a superior conformity index (CI) in comparison to the central lung PTVs.

For the treatment of HDV and D2cm, both VMAT and IMRT have revealed superior outcomes compared to 3DCRT. The results of the volumetric analysis indicated a lower high dose volume (HDV) for peripheral lung tumours in comparison to central lung tumours across all three techniques employed in the SBRT treatment plans. The study revealed a linear increase in D2cm with a rise in PTV volumes for both 3DCRT and VMAT techniques. On the other hand, IMRT obtained a notable elevation in D2cm especially for smaller PTV volumes, whereas a was observed for larger PTV volumes. The present study yielded that both 3DCRT and IMRT demonstrated enhanced D2cm outcomes for peripheral lung planning target volumes (PTVs), whereas VMAT showed superior enhancements in D2cm outcomes for central lung PTVs. The present study employed VMAT to administer radiotherapy to patients with centrally and peripherally located primary lung tumours. Specifically, the treatment plan for central lung planning target volumes (PTVs) involved the use of two full coplanar arcs, whereas two half arcs were employed for peripheral lung PTVs. The superior performance of the former approach was attributed to the reduction of low lung doses, thereby improving the D2cm outcomes for central PTVs. When compared to (3DCRT), IMRT and VMAT demonstrated enhanced D2cm outcomes for peripheral and central lung planning target volumes (PTVs). The optimal D2cm was attained through the utilization of VMAT for centrally located lung planning target volumes (PTVs).

The Gradient Index (GI) values of the three-dimensional conformal radiotherapy (3DCRT) plans demonstrated a comparatively higher precision in dose distribution, as opposed to the VMAT and IMRT plans. Moreover, the average GI values of the 3DCRT plans were found to be significantly superior.

The results indicated that the IMRT plans exhibited a superior dose fall-off in the normal tissue compared to the VMAT plans, as evidenced by lower dose values. This outcome was anticipated due to the utilization of non-coplanar (3DCRT) and non-coplanar IMRT, as they attenuate beam overlap from the targeted tumour region. This contrasted with the coplanar VMAT techniques [13, 17].

The present study identifies that the measures of homogeneity index (HI), maximum dose (Dmax), and dose to 2% volume (D2%) attained greater values in both VMAT and intensity modulated radiation therapy IMRT plans compared to those obtained through (3DCRT). A marginal enhancement in the homogeneity index was noted through our observation.

The maximum dose (Dmax) and Dose received by 2% of the volume (D2%) in association with the VMAT plans were compared with those of the Intensity Modulated Radiation Therapy IMRT plans. Notably, the central lung Planning Target Volumes (PTVs) exhibited similar Homogeneity Index (HI) values in both the IMRT and VMAT plans. A heightened level of dosage heterogeneity within the planning target volume (PTV) has the potential to result in a subsequent decline in dosage within healthy tissues [15]. Prior academic research has indicated that an elevated Homogeneity Index (HI) exhibits a negative correlation with the Gastrointestinal Index (GI) (referencing studies 22 and 23). The utilization of the HI parameter as an indicator of plan quality appears promising, however, the existing literature on SBRT has yet to offer any guidance on the optimal HI value for the PTV dose [17, 19]. At present, it appears that the HI parameter demonstrates restricted utility in the optimization of a lung SBRT plan. However, the analysis of dose-volume histograms (DVHs) and dose distribution within axial CT sections remains an important part of the plan review.

VMAT has been found to offer substantial advantages in terms of dose-sparing to the organs at risk (OARs) in comparison to other treatment planning techniques. It should be noted, though, that the V20 and Dmean of the lung dose were significantly lower for the plans conducted using three-dimensional conformal radiotherapy (3DCRT). The disparity in outcomes could be attributed to the non-coplanar beam arrangement utilized in the 3DCRT plans. The increased pulmonary dose observed with VMAT can be attributed to the volumetric distribution of the dose within the planning target volume (PTV) by the rotational arcs. Nevertheless, the administered doses of organ-at-risk (OAR) in each treatment modality were deemed to be substantially lower than the accepted clinical thresholds. IMRT yielded superior outcomes in comparison to (3DCRT) in general. To comprehensively assess the functionality of Organs-At-Risk (OARs), their individual performance analysed with respect to both central and peripheral regions.

The target volumes of the lungs, known as lung Planning Target Volumes (PTVs), are a significant aspect of radiation therapy planning for various thoracic malignancies. Upon analysis, it was found that the VMAT technique outperformed



all other techniques. It was noted that in the context of peripheral tumours, 3-Dimensional Conformal Radiation Therapy (3DCRT) demonstrated certain enhancements in contrast to Intensity Modulated Radiation Therapy (IMRT). Nonetheless, none of the examined locations proved to be universally optimal for all organs at risk (OARs) with the usage of (3DCRT).

When comparing with the 3DCRT, both IMRT and VMAT demonstrated a higher value in terms of the monitor units (MUs) required for treatment delivery. However, VMAT exhibited a superior improvement over IMRT. Our investigation revealed that even though a greater number of Monitor Units (MUs) were necessary for VMAT techniques, the duration of treatment was less than that for (3DCRT). The present study indicates that the dose rate of flattening filter free energy (FFF) beams may be between two to four times greater when compared to conventional FF beams. Consequently, the implementation of FFF-based free flattening filter (FFF) 3D conformal radiotherapy (3DCRT) has resulted in a slightly shorter treatment duration than that observed for FFF-based intensity modulated radiotherapy IMRT in clinical trials. In the case of (FFF) VMAT plans, the treatment delivery time is primarily constrained by the rotational speed of the gantry, rather than the dose rate. Accelerated delivery may potentially decrease the likelihood of intra-fractional setup inaccuracies, which have been reported to occur in treatment procedures lasting over 15 minutes [7, 12].

### CONCLUSIONS

The results of this investigation indicate that the three treatment techniques could deliver conformal stereotactic body radiation therapy (SBRT) plans while satisfying the dose constraints specified by the Radiation Therapy Oncology Group (RTOG). Conversely, by assessing dosimetric indices, including conformity index (CI), 2 cm away from the planning target volume (D2cm), homogeneity index (HI), and high dose volume (HDV), VMAT demonstrates a more favourable treatment strategy compared to IMRT and (3DCRT) for treating both peripheral and central lung planning target volumes (PTVs). The present study observed a significant enhancement in dosimetric indices, particularly the gradient index (GI), with the implementation of three-dimensional conformal radiotherapy (3DCRT) over volumetric modulated arc therapy (VMAT). The present observation evidently indicates that, despite the increased demand for higher monitor units (MUs) involved within VMAT plans compared to Three-Dimensional Conformal Radiotherapy (3DCRT), the administration time for treatment is significantly reduced due to the superior gantry velocity employed in the VMAT technique and using free flattening filter energy that increase dose rate to 2400cGy/min.

### ORCID

©Mohamed I. Soliman, <https://orcid.org/0000-0001-5136-6449>; ©Khaled M. Elshahat, <https://orcid.org/0000-0003-0658-5735>

### REFERENCES

- [1] A. Tajaldeem, P. Ramachandran, S. Alghamdi, and M. Geso, "On the use of AAA and AcurosXB algorithms for three different stereotactic ablative body radiotherapy (SABR) techniques: Volumetric modulated arc therapy (VMAT), intensity modulated radiation therapy (IMRT) and 3D conformal radiotherapy (3D-CRT)," *Reports of Practical Oncology and Radiotherapy*, **24**(4), 399-408 (2019). <https://doi.org/10.1016/j.rpor.2019.02.008>
- [2] K.M. Prezzano, S.J. Ma, G.M. Hermann, C.I. Rivers, J.A. Gomez-Suescun, and A.K. Singh, "Stereotactic body radiation therapy for non-small cell lung cancer: A review," *World journal of clinical oncology*, **10**(1), 14 (2019). <https://doi.org/10.5306%2Fwjco.v10.i1.14>
- [3] H. Onishi, H. Shirato, Y. Nagata, M. Hiraoka, M. Fujino, K. Gomi, K. Karasawa, et al., "Stereotactic body radiotherapy (SBRT) for operable stage I non-small-cell lung cancer: can SBRT be comparable to surgery?" *International Journal of Radiation Oncology\* Biology\* Physics*, **81**(5) 1352-1358 (2011). <https://doi.org/10.1016/j.ijrobp.2009.07.1751>
- [4] M.R. Folkert, and R.D. Timmerman, "Stereotactic ablative body radiosurgery (SABR) or Stereotactic body radiation therapy (SBRT)," *Advanced drug delivery reviews*, **109**, 3-14 (2017). <https://doi.org/10.1016/j.addr.2016.11.005>
- [5] S.D. Sharma, "Unflattened photon beams from the standard flattening filter free accelerators for radiotherapy: Advantages, limitations and challenges," *Journal of Medical Physics/Association of Medical Physicists of India* **36**(3), 123-125 (2011). [https://journals.scholarsportal.info/details/09716203/v36i0003/123\\_upbftsfralac.html](https://journals.scholarsportal.info/details/09716203/v36i0003/123_upbftsfralac.html)
- [6] . Paul, B. Krauss, R. Banckwitz, W. Maentele, R.W. Bauer, and T.J. Vogl, "Relationships of clinical protocols and reconstruction kernels with image quality and radiation dose in a 128-slice CT scanner: study with an anthropomorphic and water phantom," *European journal of radiology*, **81**(5), e699-e703 (2012). <https://doi.org/10.1016/j.ejrad.2011.01.078>
- [7] S. Dwivedi, S. Kansal, J. Shukla, A. Bharati, and V.K. Dangwal, "Dosimetric evaluation of different planning techniques based on flattening filter-free beams for central and peripheral lung stereotactic body radiotherapy," *Biomedical Physics & Engineering Express*, **7**(6), 065037 (2021). <https://doi.org/10.1088/2057-1976/ac2f0d>
- [8] H. Mabhouti, M.Sc. thesis, "The comparison of peripheral dose in stereotactic brain irradiation with the use of different treatment techniques," İstanbul Medipol Üniversitesi Sağlık Bilimleri Enstitüsü, 2017.
- [9] W. Zia, M.Sc. thesis, "Dosimetric Comparison of Three-Dimensional Conformal Radiation Therapy (3d-Crt), Intensity Modulated Radiation Therapy (IMRT) and Volumetric Modulated Arc Therapy (Vmat) for Distal Esophageal Cancer Treated with External Radiation," McMaster University, Ontario, Canada, 2022.
- [10] G.A. Ezzell, J.M. Galvin, D. Low, J.R. Palta, I. Rosen, M.B. Sharpe, P. Xia, et al., "Guidance document on delivery, treatment planning, and clinical implementation of IMRT: report of the IMRT Subcommittee of the AAPM Radiation Therapy Committee," *Medical physics*, **30**(8), 2089-2115 (2003). <https://doi.org/10.1118/1.1591194>
- [11] S. Webb, *Intensity-modulated radiation therapy*, (CRC Press, 2015).
- [12] B.S. Laughlin, M. Golafshar, M. Prince, W. Liu, C.J. Kuttyreff, S.K. Ahmed, T.Z. Vern Gross, et al., "Dosimetric comparison between proton beam therapy, intensity modulated radiation therapy, and 3D conformal therapy for soft tissue extremity sarcoma," *Acta Oncologica*, **62**(5), 473-479 (2023). <https://doi.org/10.1080/0284186X.2023.2209267>

- [13] S. Bi, R. Zhu, and Z. Dai, "Dosimetric and radiobiological comparison of simultaneous integrated boost radiotherapy for early-stage right side breast cancer between three techniques: IMRT, hybrid IMRT and hybrid VMAT," *Radiation Oncology*, **17**(1), 60 (2022). <https://doi.org/10.1186/s13014-022-02009-2>
- [14] S.O. Hunte, C.H. Clark, N. Zyuzikov, and A. Nisbet, "Volumetric modulated arc therapy (VMAT): a review of clinical outcomes—what is the clinical evidence for the most effective implementation?" *The British Journal of Radiology*, **95**(1136), 20201289 (2022). <https://doi.org/10.1259/bjr.20201289>
- [15] T.-N. Wei, H.-L. Yeh, J.-F. Lin, and C.-C. Hung, "The clinical outcome of postoperative radiotherapy using hybrid planning technique in left breast cancer after breast-conserving surgery," *Cancer Medicine*, **12**(5), 5364-5371 (2023). <https://doi.org/10.1002/cam4.5358>
- [16] I. I. Olaciregui-Ruiz, B. Vivas-Maiques, S. van der Velden, M.E. Nowee, B. Mijnheer, and A. Mans, "Automatic dosimetric verification of online adapted plans on the Unity MR-Linac using 3D EPID dosimetry," *Radiotherapy and Oncology*, **157**, 241-246 (2021). <https://doi.org/10.1016/j.radonc.2021.01.037>
- [17] D. Desai, G. Narayanan, M. Bimali, I. Cordrey, H. Elasmr, S. Srinivasan, and E.L. Johnson, "Cleaning the dose falloff in lung SBRT plan," *Journal of Applied Clinical Medical Physics*, **22**(1), 100-108 (2021). <https://doi.org/10.1002/acm2.13113>
- [18] G.M.M. Videtic, C. Hu, A.K. Singh, J.Y. Chang, W. Parker, K.R. Olivier, and S.E. Schild, "A randomized phase 2 study comparing 2 stereotactic body radiation therapy schedules for medically inoperable patients with stage I peripheral non-small cell lung cancer: NRG Oncology RTOG 0915 (NCCTG N0927)," *International Journal of Radiation Oncology\*Biophysics\**, **93**(4), 757-764 (2015). <https://doi.org/10.1016/j.ijrobp.2015.07.2260>
- [19] "The International Commission on Radiation Units and Measurements," *Journal of the International Commission on Radiation Units and Measurements*, **10**(2), 5-6 (2010). <https://doi.org/10.1093/jicru/ndq025>
- [20] I. Paddick, and B. Lippitz, "A simple dose gradient measurement tool to complement the conformity index," *Journal of neurosurgery*, **105**(Issue Supplement), 194-201 (2006). <https://doi.org/10.3171/sup.2006.105.7.194>

#### ДОЗИМЕТРИЧНЕ ОЦІНЮВАННЯ 10-MV FFF, ВИКОРИСТАНОГО У SBRT ДЛЯ ПУХЛИН ЛЕГЕНЬ

Мохамед І. Соліман<sup>а</sup>, Вахіб М. Агтя<sup>б</sup>, Халед М. Ельшахат<sup>с</sup>

<sup>а</sup>Онкологічний центр збройних сил Загазіга, Загазіга, Єгипет; <sup>б</sup>Університет Суецького каналу, Єгипет

<sup>с</sup>Університет аль-Азхар, медичний факультет, Єгипет

**Мета:** Метою цього дослідження було проведення порівняльного та дозиметричного аналізу трьох різних методів променевої терапії, які використовуються в стереотаксичній променевої терапії легень (SBRT), тривимірній конформній променевої терапії (3DCRT), променевої терапії з модуляцією інтенсивності (IMRT) та об'ємно-модульованій дугової терапії (VMAT) з використанням пучка фотонів 10 МВ без фільтра (FFF). **Матеріали та методи.** У цьому дослідженні з метою планування лікування використовували зображення гуманної фантома за допомогою комп'ютерної томографії (КТ). Великі об'єми пухлини (GTVs), окреслені як у центральному, так і в периферичному положеннях легень. Визначення планових цільових об'ємів (PTV) передбачало додавання запасу в 0,5 см до загального об'єму пухлини (GTV). Тривимірні конформні променева терапія (3DCRT), інтенсивно-модульована променева терапія (IMRT) і об'ємно-модульована дугова терапія (VMAT), створені з використанням 10-мегавольтного (MV) вирівнюючого пучка фотонів без фільтра (FFF). Розрахунок дозування для всіх планів виконується за допомогою анізотропного аналітичного алгоритму (AAA). Результати: IMRT і VMAT мали кращу конформацію дози PTV, ніж 3DCRT як для центральних, так і для периферичних мішеней. Відповідність PTV покращилася у VMAT порівняно з IMRT, а значення CI були прийнятними для планів VMAT, IMRT і 3DCRT. Плани VMAT мали дещо кращий ДІ, ніж IMRT, з кращими результатами в PTV периферичних легень порівняно з центральними PTV. VMAT та IMRT кращі для лікування HDV та D2cm, з нижчим HDV для периферичних пухлин легень. Як 3DCRT, так і IMRT покращили результати для PTV периферичних легень, тоді як VMAT був кращим для центральних PTV легень. Перший виявився кращим з менш низькими дозами в легенях і покращив результати D2cm. Плани 3DCRT продемонстрували вищу точність розподілу дози, ніж плани VMAT та IMRT, з вищими середніми значеннями ГІ. VMAT і IMRT мали вищі HI, Dmax і D2%, ніж 3DCRT. Плани VMAT порівняно з планами IMRT, з подібними значеннями HI для центральних легневих PTV. VMAT краще заощаджує OAR, ніж інші методи, але дози V20 і V30 у легенях були нижчими з 3DCRT. VMAT збільшує легневу дозу, але OAR залишається нижче порогових значень. **Висновок:** дослідження виявило, що всі три методики лікування можуть забезпечити плани SBRT, які відповідають обмеженням дози RTOG. Однак VMAT є кращою стратегією лікування, ніж IMRT і 3DCRT, як для периферичних, так і для центральних легневих PTV, заснованих на дозиметричних показниках, таких як CI, D2cm, HI і HDV. Дослідження показало, що 3DCRT покращує дозиметричні показники, особливо градієнтний індекс (GI), більше, ніж VMAT. Незважаючи на потребу в більшій кількості моніторів (MU) у планах VMAT, час лікування скоротився завдяки вищій швидкості генератора та вищим потужностям дози (2400 сГр/хв) через вільну енергію фільтра.

**Ключові слова:** 3DCRT; IMRT; VMAT; Рак легень; дозиметричне порівняння; SBRT

## EXPLORING THE IMPACT OF LIPID DOMAIN SIZE ON THE LIFETIME: A DISSIPATIVE PARTICLE DYNAMICS STUDY<sup>†</sup>

 **Kan Sornbundit**

*Ratchaburi Learning Park, King Mongkut's University of Technology Thonburi (Ratchaburi), Ratchaburi, Thailand, 70150*

*E-mail: kan.sor@kmutt.ac.th*

Received June 19, 2023; revised July 3, 2023; accepted July 4, 2023

In this research, we have used the dissipative particle dynamics (DPD), a mesoscopic simulation technique, in order to investigate the dynamics of lipid domains in near critical temperature. Our specific focus has been on exploring the influence of lipid domain size on its lifetime, which mimics the behavior of lipid rafts within cellular membranes. The lipid membranes used in this study were composed of saturated and unsaturated lipids, which have been immersed in water. Through the simulation of these membranes close to their critical temperature, we have successfully generated fluctuating domains that mimic the lipid rafts observed in cellular systems. We have proposed a method to obtain the lifetime of the fluctuating domains by analyzing the sizes of the lipid domains at specific intervals of time. Our investigations have revealed a linear correlation between the initial size of the lipid domain and its lifetime. Our research finding give an insight into the underlying mechanisms that govern lipid rafts and their vital role in various cellular processes.

**Keywords:** *Lipid bilayer; Dissipative particle dynamics; Domain fluctuation lifetime*

**PACS number:** 87.16.dt, 87.16.dj

### INTRODUCTION

There is a small component (10-200 nm) known as lipid rafts that float on the surface of lipid membranes [1-3]. Lipid rafts primarily consist of saturated lipids and cholesterol, which results in a higher density compared to their surroundings. Certain proteins, such as GPI-anchor proteins, can attach to lipid rafts and carry out their functions [4]. It is believed that lipid rafts serve as platforms for specific biological activities within the cell membrane, such as signal transduction [5]. Very recently lipid rafts were thought to involve in COVID 19 entry [6] and cancer cell [7].

To study lipid rafts, researchers often employ giant unilamellar vesicles (GUVs) instead of real cell membranes due to their simplicity in lipid composition [8]. Lipid domains in GUVs are larger compared to lipid rafts in real cell membranes, making them detectable using standard optical instruments. In 2008, experiments on giant plasma membrane vesicles extracted from real cell membranes suggested that lipid domains that mimic the behavior of lipid rafts can be found by tuning the vesicles to their critical temperature [9]. For signal transduction to occur, a raft should persist for minutes [10].

Lipids with a structure consisting of both saturated and unsaturated lipids are referred to as hybrid lipids [11]. Hybrid lipids tend to accumulate at the boundary between saturated and unsaturated lipids in order to reduce line tension [12]. Interestingly, hybrid lipids have been proposed to prolong the lifetime of lipid rafts. In 2013, a theoretical work by Palmieri and Safran demonstrated that the inclusion of hybrid lipids can increase the domain lifetime by three orders of magnitude compared to cases without hybrid lipids [13]. Subsequent computational studies using dissipative particle dynamics (DPD) simulations for the similar system can be found in Ref. [14].

However, it is necessary to explore the lifetime of lipid domains at different sizes, as lipid rafts in real cell membranes exhibit varying sizes [22]. It is possible that the lifetime of large lipid rafts may be sufficient for cellular processes. Currently, computer simulations on lipid bilayers have been employed to obtain data that is challenging to acquire experimentally. Mesoscopic simulation methods, such as dissipative particle dynamics (DPD), have been widely used to simulate lipid membrane systems [12, 14-17]. DPD is preferred in lipid membrane simulations due to its reduced computational resource requirements and time compared to classical molecular dynamics (MD) methods. Moreover, DPD is more suitable for studying the physical properties of lipid membranes. In this study, we aim to investigate the effect of lipid domain size on the duration of lifetime using dissipative particle dynamics. Additionally, we propose a method to measure the lifetime by examining lipid domain sizes.

### MODEL AND SIMULATION

The lipid bilayer is constructed by arranging two layers of lipid molecules. Each lipid molecule consists of a head group with two DPD particles and tails with three DPD particles each. There are two types of lipids, namely lipid A and lipid B, which have the same structure but exhibit unfavorable repulsion in their tail groups, as indicated by the interaction parameter provided below. Three water molecules are represented by a single DPD particle. In our computational experiment, the bilayer is positioned at the center of the simulation box, which has dimensions of  $(60 \times 60 \times 40)r^3$ , as shown in Figure 1. The areas above and below the bilayer are filled with DPD water particles. Each DPD particle experiences three forces: a conservative force  $\vec{F}_{ij}^C = a_{vij} \omega(r_{ij}) \hat{r}_{ij}$ , a dissipative force  $\vec{F}_{ij}^D = \gamma_{ij} \omega^2(r_{ij}) (\hat{r}_{ij} \cdot \mathbf{v}_{ij}) \hat{r}_{ij}$ , and a random force

<sup>†</sup> **Cite as:** K. Sornbundit, East Eur. J. Phys. 3, 466 (2023), <https://doi.org/10.26565/2312-4334-2023-3-52>

© K. Sornbundit, 2023

$\vec{F}_{ij}^R = \frac{\sigma_{ij}}{(\delta t)^{1/2}} \omega(r_{ij}) \theta_{ij} \hat{r}_{ij}$ . The notion in the force equations are explained as follows:  $\vec{r}_{ij} = \vec{r}_j - \vec{r}_i$ ,  $\hat{r}_{ij} = \vec{r}_{ij} / |\vec{r}_{ij}|$ ,  $\vec{v}_{ij} = \vec{v}_j - \vec{v}_i$  and  $\delta t$  represents the computational steps, and the coefficients of the dissipative and random forces are related by  $\gamma_{ij} = \sigma_{ij} / k_B T$  [18] where  $T$  is temperature,  $k_B$  is the Boltzmann constant, type of particle  $i(j)$  are denoted by  $v_i (\mu_j)$ . The symmetric random variable  $\theta_{ij}$  obeys  $\langle \theta_{ij}(t) \rangle = 0$ , and  $\langle \theta_{ij}(t) \theta_{kl}(t') \rangle = (\delta_{ik} \delta_{jl} + \delta_{il} \delta_{jk}) \delta(t-t')$ , where  $i \neq j$  and  $k \neq l$ . The weight function in  $\omega(r)$  is given by  $\omega(r) = 1 - r/r_c$  for  $r \leq r_c$  and is zero elsewhere. The length scale of the system is  $r_c$ . The equations of motions for DPD particle  $i$  are given by  $\frac{d\vec{r}_i(t)}{dt} = \vec{v}_i(t)$  and  $\frac{d\vec{v}_i(t)}{dt} = \frac{1}{m} \sum_j (\vec{F}_{ij}^C + \vec{F}_{ij}^D + \vec{F}_{ij}^R + \vec{F}_{ij}^S)$ . The mass of every bead is assumed to be equal  $m_i = m$ . The interaction strength  $a_{v_i \mu_j}$  in  $\vec{F}_{ij}^C$  are given by the following table

**Table 1.** the interaction strength in the  $\varepsilon/r_c$  unit

$h_A$	$h_B$	$t_A$	$t_B$	$w$	
25	25	200	200	25	$h_A$
25	25	200	200	25	$h_B$
200	200	25	X	200	$t_A$
200	200	X	25	200	$t_B$
25	25	200	200	25	$w$

Where  $\varepsilon$  is the energy scale,  $h_A$  ( $h_B$ ) represents head group of saturated lipids (unsaturated lipid),  $t_A$  ( $t_B$ ) represents the tail group of saturated lipids (unsaturated lipid) and  $w$  represent a group of water. The notion X is 100(26) for two(one) phase regime.

For the lipid molecules, consecutive particles are subjected to a harmonic force described by the following equation  $\vec{F}_{i,i+1}^S = -C(1 - r_{i,i+1}/b)\hat{r}_{i,i+1}$ , where  $C=100\varepsilon$  is the positive constant and  $b=0.45r_c$  is the desired bond length.

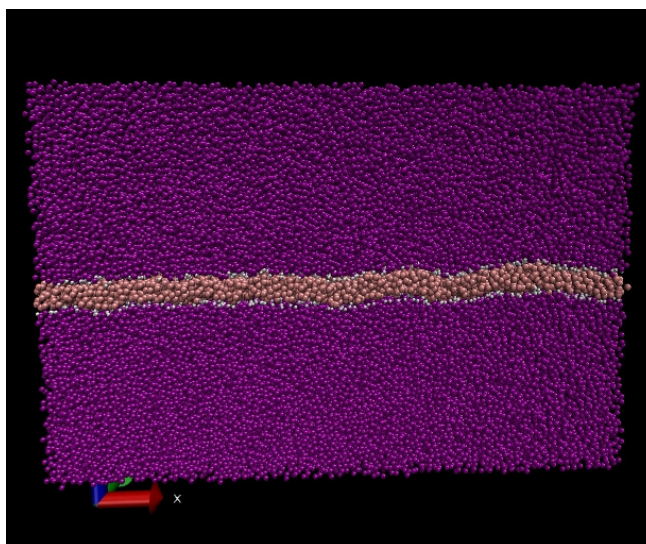


**Figure. 1** Lipid bilayer position in the simulation box. White particles represent the lipid head group, and pink particles represent the lipid tail group. Purple particles denote water

Simulations were conducted at  $k_B T = \varepsilon$  with the fluid density  $\rho = 3.0r_c^{-3}$ . The amplitude of the noise is  $\sigma_{ij} = \sigma = (\varepsilon m / r_c^2)^{1/4}$ . The velocity-Verlet algorithm [19, 20] was used to integrate the equation of motion. The time unit used all simulations are denoted by  $\delta t = 0.05\tau$ , where the time scale  $\tau = (m r_c^2 / \varepsilon)^{1/2}$ .

To conduct the simulation, we initially create a bilayer consisting of a single type of lipid. The system is allowed to evolve for 1000 steps. Subsequently, two opposing circular domains, one on each layer, with a specific diameter are generated, and the systems are allowed to equilibrate for 5000 steps. It is important to note that the circular shape of the domains is maintained due to the unfavorable interaction between the two lipid types, resulting in the lowest free energy state for the system.

Next, the domains are allowed to decay by adjusting the interaction parameter between unlike tails from 100 to 26, which is slightly larger than the interaction parameter between tails of the same type. This adjustment promotes a mixing situation between the two types of lipids, as referenced in [14]. In order to determine the lifetime of the domains, the size of the domains ( $D$ ) is calculated every 100-time steps using the relation  $D = \pi / k^*$ , where  $k^*$  represents the dominant wave vector [21]. The methodology for domain size calculation is explained in Ref. [12].

The lifetime of a domain is defined as the time at which the domain size is half of its initial value. Since the shape of the domain becomes irregular after decay, we use the term “domain size” instead of “domain diameter”. The lifetime is calculated using the equation

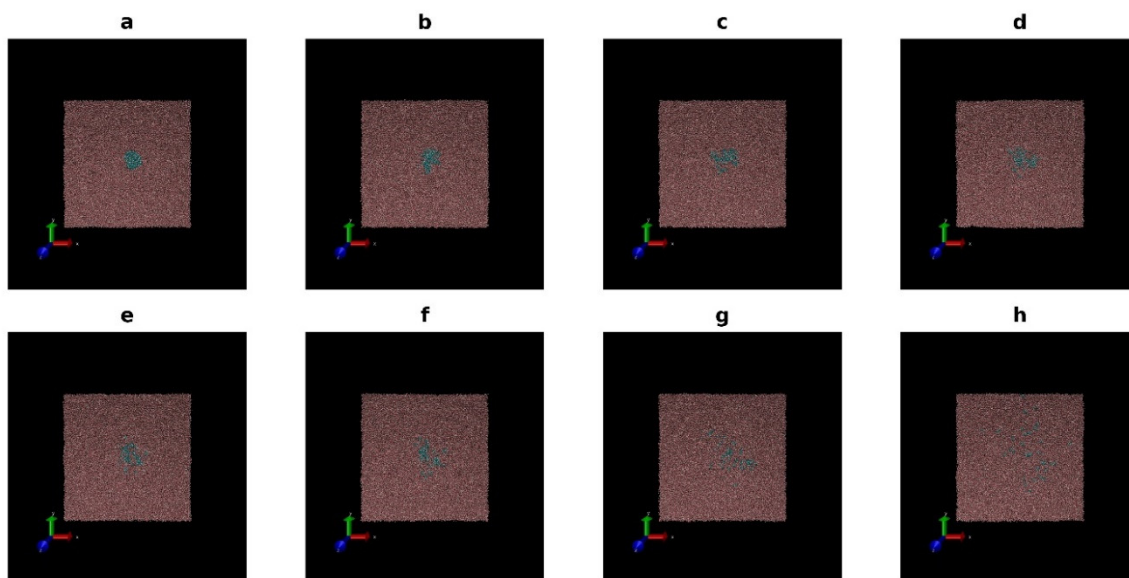
$$\text{Life time} = \frac{D(0) + \bar{D}}{2},$$

Where  $D(0)$  represents the size at the beginning of the decay process,  $\bar{D}$  denotes the averaged size calculated from the equilibrium region (the region where the size reaches saturation).

It should be noted that the chosen definition for calculating the lifetime of fluctuating domains does not have a universally accepted consensus. However, we have adopted this definition because a domain at half its initial size should not be functioning properly. Please note that the lifetime calculation method described here differs from the one presented in Ref. [14], which is suitable for much smaller domain fluctuations.

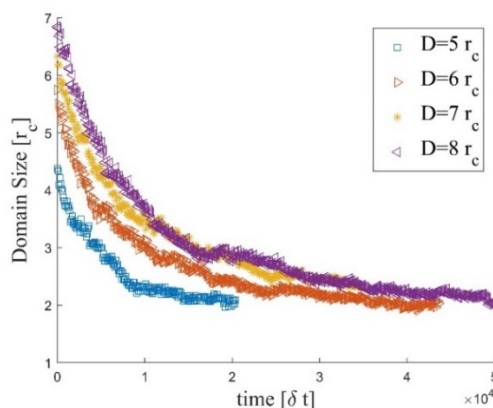
### RESULTS AND DISCUSSION

The results are presented and discussed in this section. Figure 2 reveals a snapshot of the upper domain with an initial diameter ( $D$ ) of  $8 r_c$  at various time points since the decay process began. In this figure, time  $t = 0 \delta t$  corresponds to a simulation time of  $t = 6 \times 10^3 \delta t$ , as we are solely considering the decay process. It is customary to designate this time as  $t = 0 \delta t$ . Initially, the domain exhibits a circular shape, as shown in Fig. 2a. Subsequently, the domain starts to decay, and Fig. 2f represents the snapshot at which the size of the domain is half of its initial value, which we define as the lifetime. It is evident that the domain fractures into smaller domains. At  $t = 1 \times 10^4 \delta t$ , the domain is completely decomposed into numerous small domains. By  $t = 3 \times 10^4 \delta t$ , these small domains disperse further from each other, indicating a mixing scenario.



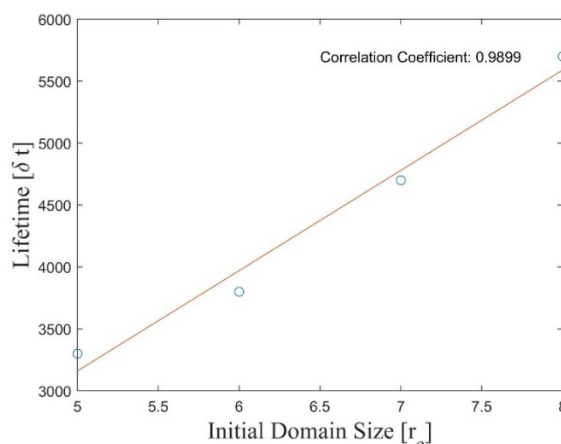
**Figure 2.** Snapshot (a-h) representing the upper layer of lipid bilayer at  $t=0, 1 \times 10^3, 2 \times 10^3, 3 \times 10^3, 4 \times 10^3, 4.7 \times 10^3, 1 \times 10^4, 3 \times 10^4 \delta t$ , respectively

Figure 3 illustrates the average domain size over time for initial diameters ranging from  $D = 3.0$  to  $8.0 r_c$ . It is noticeable that the domains decay rapidly from the beginning. When the system reaches a mixing state, the domain size stabilizes around  $4 r_c$ .



**Figure 3.** Characteristic domain sizes versus time for domains of initial diameter  $D = 3.0$  to  $8.0 r_c$ .

As depicted in Fig. 3, larger domains require more time to reach saturation. Hence, it is worthwhile to investigate the relationship between the initial domain size and the lifetime. Fig. 4 demonstrates a linear relationship between the initial domain size and lifetime. Consequently, cell membrane's activities that take a certain amount of time may occur on large domains.



**Figure 4.** The linear relationship between initial domain sizes and their lifetime

### CONCLUSION

This study has revealed that the initial size of a domain plays a crucial role in its lifetime. Larger domains exhibit a longer lifetime compared to smaller domains. Furthermore, a linear relationship between the initial domain size and its lifetime has been established. These findings contribute to our understanding of domain dynamics and have implications for cell membrane activities on large domains.

### Acknowledgement

I would like to express my sincere gratitude to the Ratchaburi Learning Park, King Mongkut's University of Technology Thonburi (Ratchaburi), for providing me with the opportunity to conduct this research.

### ORCID

© Kan Sornbundit, <https://orcid.org/0000-0003-0787-8580>

### REFERENCES

- [1] L.J. Pike, *Journal of lipid research* **47**(7), 1597 (2006). <https://doi.org/10.1194/jlr.E600002-JLR200>
- [2] D. Lingwood, and K. Simons, *Science*, **327**(5961), 46 (2010). <https://doi.org/10.1126/science.1174621>
- [3] I. Levental, K.R. Levental, and F.A. Heberle, *Trends in cell biology*, **30**(5), 341 (2020). <https://doi.org/10.1016/j.tcb.2020.01.009>
- [4] K. Simons, and E. Ikonen, *Nature*, **387**(6633), 569 (1997). <https://doi.org/10.1038/42408>
- [5] K. Simons, and D. Toomre, *Nature reviews Molecular cell biology*, **1**(1), 31 (2000). <http://dx.doi.org/10.1038/35036052>
- [6] M. Sorice, R. Misasi, G. Riitano, V. Manganelli, S. Martellucci, A. Longo, T. Garofalo, and V. Mattei, *Frontiers in Cell and Developmental Biology*, **8**, 618296 (2021). <https://doi.org/10.3389/fcell.2020.618296>
- [7] F. Mollinedo, and C. Gajate, *Journal of lipid research*, **61**(5), 611 (2020). <https://doi.org/10.1194/jlr.tr119000439>
- [8] S.L. Veatch, and S.L. Keller, *Biophysical journal*, **85**(5), 3074 (2003). [https://doi.org/10.1016%2FS0006-3495\(03\)74726-2](https://doi.org/10.1016%2FS0006-3495(03)74726-2)
- [9] S.L. Veatch, P. Cicuta, P. Sengupta, A. Honerkamp-Smith, D. Holowka and B. Baird, *ACS chemical biology*, **3**(5), 287 (2008). <https://doi.org/10.1021/cb800012x>
- [10] W. K. Subczynski, and A. Kusumi, *Biochimica et Biophysica Acta (BBA)-Biomembranes* **1610**(2), 231 (2003). [https://doi.org/10.1016/S0005-2736\(03\)00021-X](https://doi.org/10.1016/S0005-2736(03)00021-X)
- [11] R. Brewster, P.A. Pincus, and S.A. Safran, *Biophysical journal*, **97**(4), 1087 (2009). <https://doi.org/10.1016%2Fj.bpj.2009.05.051>
- [12] K. Sornbundit, *Journal of the Korean Physical Society*, **73**, 1899 (2018). <https://doi.org/10.3938/jkps.73.1899>
- [13] B. Palmieri, and S. A. Safran, *Physical Review E*, **88**(3), 032708 (2013). <https://doi.org/10.1103/PhysRevE.88.032708>
- [14] K. Sornbundit, *Journal of the Korean Physical Society*, **76**, 860 (2020). <https://doi.org/10.3938/jkps.76.860>
- [15] S. Yamamoto, Y. Maruyama, and S.-A. Hyodo, *The Journal of chemical physics*, **116**(13), 5842 (2002). <https://doi.org/10.1063/1.1456031>
- [16] M. Laradji, and P.S. Kumar, *The Journal of chemical physics*, **123**(22), 224902 (2005). <https://doi.org/10.1063/1.2102894>
- [17] M. Laradji, and P.S. Kumar, *Physical review letters*, **93**(19), 198105 (2004). <https://doi.org/10.1103/PhysRevLett.93.198105>
- [18] P. Espanol, and P. Warren, *Europhysics letters*, **30**(4), 191 (1995). <https://doi.org/10.1209/0295-5075/30/4/001>
- [19] P. Nikunen, M. Karttunen, and I. Vattulainen, *Computer physics communications*, **153**(3), 407 (2003). [https://doi.org/10.1016/S0010-4655\(03\)00202-9](https://doi.org/10.1016/S0010-4655(03)00202-9)
- [20] G. Besold, I. Vattulainen, M. Karttunen, and J.M. Polson, *Physical Review E*, **62**(6), R7611 (2000). <https://doi.org/10.1103/PhysRevE.62.R7611>
- [21] J.G. Amar, F.E. Sullivan, and R.D. Mountain, *Physical Review B*, **37**(1), 196 (1988). <https://doi.org/10.1103/PhysRevB.37.196>
- [22] R.F. de Almeida, L.M. Loura, A. Fedorov and M. Prieto, *Journal of molecular biology*, **346**(4), 1109 (2005). <https://doi.org/10.1016/j.jmb.2004.12.026>

**ВИВЧЕННЯ ВПЛИВУ РОЗМІРУ ЛІПІДНОГО ДОМЕНУ НА ТРИВАЛІСТЬ ЙОГО ЖИТТЯ:  
ДОСЛІДЖЕННЯ ДИНАМІКИ ДИСИПАТИВНОЇ ЧАСТИНКИ**

**Кан Сорнбундіт**

*Навчальний парк Ратчабури, Технологічний університет короля Монгкута Тонбури (Ратчабури), Ратчабури, Таїланд, 70150*

У цьому дослідженні використана дисипативна динаміка частинок (DPD), мезоскопічна техніка моделювання, для дослідження динаміки ліпідних доменів при температурі, близькій до критичної. Наша спеціальна увага була зосереджена на дослідженні впливу розміру ліпідного домену на його тривалість життя, що імітує поведінку ліпідних плотів у клітинних мембранах. Ліпідні мембрани, використані в цьому дослідженні, склалися з насичених і ненасичених ліпідів, які були занурені у воду. Завдяки моделюванню цих мембран, близьких до їх критичної температури, ми успішно створили флуктуаційні домени, які імітують ліпідні плоти, що спостерігаються в клітинних системах. Ми запропонували метод визначення тривалості життя флуктуючих доменів шляхом аналізу розмірів ліпідних доменів через певні проміжки часу. Дослідження виявили лінійну кореляцію між початковим розміром ліпідного домену та часом його життя. Результати дослідження дають зрозуміти основні механізми, які керують ліпідними плотами, і їх життєво важливу роль у різних клітинних процесах.

**Ключові слова:** ліпідний бішар; дисипативна динаміка частинок; час життя домену флуктуації

## EFFECT OF RADIATION AND HEAT DISSIPATION ON MHD CONVECTIVE FLOW IN PRESENCE OF HEAT SINK<sup>†</sup>

✉ **Salma Akhtar**<sup>a\*</sup>, ✉ **Keshab Borah**<sup>a†</sup>, ✉ **Shyamanta Chakraborty**<sup>b§</sup>

<sup>a</sup>*Department of Mathematics, Gauhati University, Guwahati-781014, Assam, India*

<sup>b</sup>*UGC-HRDC, Gauhati University, Guwahati-781014, Assam, India*

<sup>\*</sup>*Corresponding Author e-mail: [salmaakhtar96903@gmail.com](mailto:salmaakhtar96903@gmail.com)*

<sup>†</sup>*E-mail: [keshabborah388@gmail.com](mailto:keshabborah388@gmail.com); <sup>§</sup>E-mail: [schakrabortyhrdc@gauhati.ac.in](mailto:schakrabortyhrdc@gauhati.ac.in)*

Received July 15, 2023; revised August 19, 2023; accepted August 23, 2023

The paper examines heat and mass transfer in MHD convective flow across a vertical porous plate in presence of radiation, heat sink, and dissipation of heat. A strong magnetic field is applied perpendicular to the plate and directed into the fluid area. The governing non-dimensional equations are solved using MATLAB built-in `bvp4c` solver technique. With the use of mathematical software, the findings are computed, and the effect of the various non-dimensional parameters entering into the problem on the velocity, temperature and concentration profiles are displayed in graphical formats. It has been noted that the application of the magnetic field slows down fluid velocity. Additionally, both the thermal radiation effect and the Prandtl number are fully applicable to the fluid temperature. It is significant to notice that the heat sink dramatically reduces fluid temperature and fluid velocity. The current work is utilized in many real life applications, such as chemical engineering, industrial processes, a system may contain multiple components, each of whose concentrations varies from one point to the next in a number of different circumstances.

**Keywords:** *Heat and mass transfer; MHD; Heat dissipation; Porous medium; bvp4c*

**PACS:** 44.25.+g; 44.05.+e; 44.30.+v; 44.40.+a

### INTRODUCTION

Buoyancy force is the outcome of the variation in density brought on by a change in concentration or temperature in a flowing fluid. The flow induced by buoyancy forces is called free convective or natural flow. Natural convection also, known as free convection, is a mechanism, or type of mass and heat transport. In chemical engineering and industrial processes, there are several where a system contains more than one component whose concentrations differ from one point to the next. Mass transfer operations are concerned with the transfer of matter from one stream to another. As a result, a mass transfer occurs, which is the movement of one ingredient from a high-concentration zone to a low-concentration zone. That is to say, mass transfer is the mass in transient due to the concentration gradient. Furthermore, heat transfer is defined as the movement of heat across the border of system due to difference in temperature between the system and its surroundings. Studies pertaining to coupled heat and mass transfer due to free convection has got wide applications in different realms, such as, mechanical, geothermal, chemical sciences, etc. and many industrial and technological, physical set up such as nuclear reactors, food processing, polymer production, etc. MHD refers to the study of the magnetic properties and behavior of electrically conducting fluids. As a result, it is a mix of electromagnetic and fluid dynamics fields. Magnetohydrodynamics (MHD) attracts the attention of many authors due to its applications in geophysics, in the study of stellar and solar structures, inter stellar matter, radio propagation through the ionosphere etc.

Despite all these important investigations, there are few investigations in porous medium taking dissipation into account. It is worth mentioning that heat dissipation through a porous medium has been conventionally considered as combined that heat flows, such as thermal conduction along its solid matrix, thermal radiation across internal pores, and either thermal convection by or conduction through gases filling the pores. Heat and mass transfer in wet porous media are coupled in a very complicated way. Alfven [1], Cowling [2], Shercliff [3] and many other authors have studied and presented in the form MHD, and various problems of MHD. Raptis and Massals [4] and Hossain and Alim [5] studied the radiation effect on free and forced convection flows passed a vertical plate including various physical aspects. MHD free convection flows has been studied by Ferraro and Plumpton [6]. Chen [7] studied the problem of combined heat and mass transfer of an electrically conducting fluid in MHD natural convection, adjacent to vertical surface with Ohmic heating. Based on the significance of heat and mass transfer problems, several authors geometrical and physical situations. Ahmed and Choudhury [8], Raptis and Perdikis [9], and others are among them.

Kim [10] discussed unsteady MHD free convective heat transfer past a semi-infinite vertical porous moving plate with variable suction. Senapati *et.al* [11] have studied magnetic effect on mass and heat transfer of a hydromagnetic flow past a vertical oscillating plate in presence of chemical reaction. Shekhawat *et.al* [12], have been discussed the Dissipation heat and mass transfer in porous medium due to continuously moving pate. Rajesh [13] used the Crank-Nicolson type finite difference method to investigate the chemical reaction and radiation effects of a transient MHD natural convective dissipation flow through a porous plate in the presence of ramped wall temperature. Ahmed and Dutta [14] extended the work Rajesh [13]. The heat and mass transfer dissipative flow in the presence of porous medium have been studied Ahmed and Chamuah [15] very recently.

<sup>†</sup> **Cite as:** S. Akhtar, K. Borah, S. Chakraborty, East Eur. J. Phys. 3, 471 (2023), <https://doi.org/10.26565/2312-4334-2023-3-53>

© S. Akhtar, K. Borah, S. Chakraborty, 2023



Reddy et al. [16] investigated the magneto-hydrodynamic boundary layer flow with the influence of thermal radiation, ramped plate temperature, and heat absorption. Sedki [17] studied the combined impact of chemical reaction, thermal radiation, thermophoresis, and Brownian motion on mixed convective heat and mass transfer within the boundary layer of a moving magnetonano fluid adjacent to a permeable stretching surface, considering heat generation through a porous medium. Basant et al. [18] investigated the effects of heat source/sink on magnetohydrodynamic free convective flow in a channel filled with nanofluid. Matta et al. [19] analyzed the effects of viscous dissipation on magnetohydrodynamic (MHD) free convection flow past a semi-infinite moving vertical porous plate with heat sink and chemical reaction. Manvi et al. [20] investigated the influence of radiation on magnetohydrodynamic (MHD) Eyring-Powell fluid flow past a stretching sheet with non-uniform heat source/sink. Bhaskar et al. [21] examined the impact of heat generation and thermal radiation on steady hydromagnetic fully developed natural convection flow in a vertical micro-porous channel in the presence of viscous dissipation. Andreeva et al. [22] conducted a theoretical investigation into the stability of a rotating and heated-from-below horizontal cylindrical layer of a viscous, incompressible liquid with free boundaries. Andrieieva et al. [23] carried out a theoretical investigation of convective mass transfer in a cylindrical viscous incompressible conductive fluid layer. The study focused on the presence of an inhomogeneous temperature field and an external magnetic field resulting from the vacuum arc current passing through the fluid layer.

This paper deals with the study of heat dissipation in presence of porous medium due to continuously moving plate in presence of magnetic field and heat and mass flux. Governing equation is retained in vector form as readers will be able to generalize the problem without much difficulty. In the existing literature, there are few papers dealing with the above-mentioned aspects. However, in the current work, a comparison with an already published paper has been shown to ensure the accuracy of our current problem.

### BASIC EQUATIONS

The following vector equations describe how a viscous, electrically conducting, stable, incompressible, radiating fluid moves in the presence of a uniform magnetic field:

Equation of continuity:

$$\vec{\nabla} \cdot \vec{q} = 0 \tag{1}$$

Gauss's law of magnetism:

$$\vec{\nabla} \cdot \vec{B} = 0 \tag{2}$$

Ohm's law:

$$\vec{j} = \sigma (\vec{E} + \vec{q} \times \vec{B}) \tag{3}$$

Momentum equation:

$$\rho(\vec{q} \cdot \vec{\nabla})\vec{q} = \rho\vec{g} - \vec{\nabla}p + \vec{j} \times \vec{B} + \mu\nabla^2\vec{q} - \frac{\mu\vec{q}}{K} \tag{4}$$

Energy equation:

$$\rho C_p(\vec{q} \cdot \vec{\nabla})T = k\nabla^2T + \phi + \frac{j^2}{\sigma} + Q'(T - T_\infty) - \vec{\nabla} \cdot \vec{q}_r \tag{5}$$

Species continuity equation:

$$(\vec{q} \cdot \vec{\nabla})C = D_M\nabla^2C + \bar{K}c(C_\infty - C) \tag{6}$$

Equation of state:

$$\rho_\infty = \rho[1 + \beta(T - T_\infty) + \bar{\beta}(C_\infty - C)] \tag{7}$$

Those equations are identified by nomenclature.

### MATHEMATICAL ANALYSIS

We introduced the electrically conducting two-dimensional natural convective flow of a viscous, steady, incompressible, and radiating fluid through a porous vertical plate with uniform suction in the presence of a uniform strong magnetic field. The current theoretical inquiry is carried out to idealize the mathematical model, the investigation is based on the following basic assumptions.

1. All of the fluid's properties are constant, with the exception of density.
2. The plate has a surface that is electrically insulated.
3. The system is not subjected to any external electrical field.
4. The plate is parallel to the flow of fluid.

Presenting a Cartesian coordinate systems  $(x', y', z')$  with  $x'$ -axis upward vertical direction along the plate,  $y'$ -axis normal to the plate and directed into the fluid region, and  $z'$ -axis along the plate's width, and the induced magnetic field is insignificant. The physical model of the problem is shown in Figure 1.

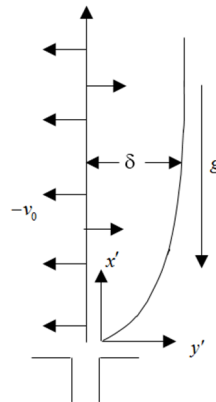


Figure 1. Physical Configuration of the problem.

Cogley *et al.* [24] demonstrated that the following form represents the radiative heat flux for a Gray gas near equilibrium in the optically thin limit:

$$\frac{\partial q_r}{\partial y'} = 4(T - T_\infty)I. \tag{8}$$

Where  $I = \int K_{\lambda w} \frac{\partial e_{b\lambda}}{\partial T^*} d\lambda$ , is the wall absorption coefficient, and  $e_{b\lambda}$  is the Planck's function.

Given by Equation (7), the preceding principles, and the normal boundary layer approximations, the basic equations take the following forms:

$$\frac{\partial v'}{\partial y'} = 0 \tag{9}$$

$$v' \frac{\partial u'}{\partial y'} = g\beta(T - T_\infty) + g\bar{\beta}(C - C_\infty) + \vartheta \frac{\partial^2 u'}{\partial^2 y'} - \frac{\sigma B_o^2 u'}{\rho} - \frac{\vartheta u'}{k'}, \tag{10}$$

$$\rho C'_p \frac{\partial T}{\partial y'} = k \frac{\partial^2 T}{\partial^2 y'^2} + \mu \left( \frac{\partial u'}{\partial y'} \right) + \sigma B_o^2 u'^2 - \frac{\partial q_r}{\partial y'} - Q'(T - T_\infty) - \frac{\mu}{k'} u'^2, \tag{11}$$

$$v' \frac{\partial C}{\partial y'} = D'_M \frac{\partial^2 C}{\partial^2 y'} + \bar{k}C(C_\infty - C). \tag{12}$$

The boundary conditions that are relevant are

$$y' = 0: u' = U, \frac{\partial T}{\partial y'} = -\frac{q^*}{k}, C = C_w, \tag{13}$$

$$y' \rightarrow \infty: u' \rightarrow 0, T \rightarrow T_\infty, C \rightarrow C_\infty. \tag{14}$$

Equation (9) gives,

$$v' = \text{a constant} = -V_o (V_o > 0). \tag{15}$$

The following non-dimensional parameters are introduced

$$y = \frac{v_o y'}{v}, u = \frac{u'}{U}, \theta = \frac{T - T_\infty}{\frac{q^* v}{k v_o}}, \varphi = \frac{(C - C_\infty)}{C_w - C_\infty}, G_r = \frac{v^2 g \beta q^*}{k U v_o^3}, E = \frac{\rho U^2 v_o}{q^*}, P_r = \frac{\mu C_p}{k},$$

$$K_c = \frac{\bar{k} c \vartheta}{v_o^2}, G_m = \frac{g \bar{\beta} \vartheta}{U v_o^2} (C_w - C_\infty), S_c = \frac{\vartheta}{D_M}, M = \frac{\sigma B_o^2 \vartheta}{\rho v_o^2}, R = \frac{4 \vartheta I}{\rho C_p v_o^2 q^{*2}}, Q = \frac{Q' \vartheta}{\rho v_o^2 C_p}.$$

The governing equations in dimensionless form are as follows:

$$\frac{d^2 u}{dy^2} + \frac{du}{dy} - \lambda u = -G_r \theta - G_m \varphi, \tag{16}$$

$$\frac{d^2 \theta}{dy^2} - P_r \frac{d\theta}{dy} - \lambda_1 \theta = -E \left( \frac{du}{dy} \right)^2 - E M u^2 - \frac{E}{K} u^2, \tag{17}$$

$$\frac{d^2 \varphi}{dy^2} + S_c \frac{d\varphi}{dy} - \lambda_2 \varphi = 0. \tag{18}$$

Where,  $\lambda = M + \frac{1}{K}$ ,  $\lambda_1 = Pr (R+Q)$ , and  $\lambda_2 = ScK_c$ , with boundary conditions

$$y = 0 : u = 1, \frac{\partial \theta}{\partial y} = -1, \varphi = 1, \tag{19}$$

$$y \rightarrow \infty : u \rightarrow 0, \theta \rightarrow 0, \varphi \rightarrow 0. \tag{20}$$

**METHOD OF SOLUTION**

In this paper, the numerical method ‘‘MATLAB built-in bvp4c solver technique’’ is used to solve the ordinary differential equations [(16)-(18)] along with the boundary conditions [(19), (20)].

The set of boundary ordinary differential equations are converted into a set of first order differential equations as follows:

Let,

$$u = y(1), u' = y(2), \theta = y(3), \theta' = y(4), \varphi = y(5), \varphi' = y(6).$$

Next, we have the set of first order differential equations shown below:

$$\begin{aligned} y'(2) &= -y(2) + \left( M + \frac{1}{K} \right) - Gr y(3) - Gm y(5) \\ y'(4) &= Pr y(4) + Pr (R + Q) y(3) - E y(2) y(2) - M E y(1) y(1) - \left( \frac{E}{K} \right) y(1) y(1) \\ y'(6) &= -Sc y(6) + Sc K_c y(5) \end{aligned} \tag{5}$$

The resulting ordinary differential equations' boundary conditions can be reduced to the following forms

$$y_0(1) - 1, y_0(4) + 1, y_0(5) - 1, y_1(1) - 1, y_1(3) - 0, y_1(5) - 0.$$

**RESULT AND DISCUSSION**

In this paper, the effect of the parameters as magnetic parameter M, thermal radiation R, heat sink Q thermal Grashof number  $G_r$ , solutal Grashof number  $G_m$ , Prandtl number  $P_r$ , chemical reaction parameter  $K_c$ , Schmidt number  $S_c$  on the velocity u, temperature field  $\theta$  and concentration field  $\varphi$  have been studied and shown by means of graphs. The graphs of velocity, temperature and concentration are taken with respect to y. The Prandtl number  $P_r$  is set to 0.71, which corresponds to air at 290K and 1 atm. Moreover, we have taken Eckert number  $E = 0.001$ ,  $S_c = 0.90$ ,  $P_r = 0.71$ ,  $K_c = 2$ ,  $K=1$ ,  $M = 10$ ,  $R = 5$ ,  $Q = 5$ ,  $G_r = 10$ ,  $G_m = 10$ .

**Velocity profiles:** The velocity profiles are depicted in Figures 2-8. Figure-2 shows that the fluid velocity decreases with the increase of magnetic parameter M. Figure 2 illustrates that as the magnetic parameter increases, the velocity profile decreases. This phenomenon occurs because the magnetic field generates a Lorentz force that opposes the fluid motion, leading to a reduction in fluid velocity. Therefore, the velocity decreases with an increase in the magnetic field strength. Figure 3 demonstrates the influence of the thermal radiation parameter on the velocity profile. It is evident that as the radiation parameter increases, the velocity of fluid particles decreases. This behavior can be attributed to the fact that increased radiation leads to enhanced heat transfer, causing a reduction in fluid velocity.

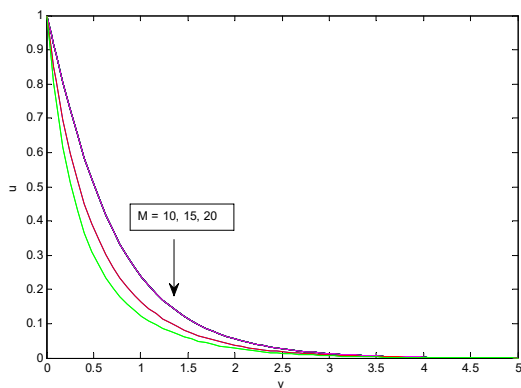


Figure 2. Velocity u versus y for the variation M

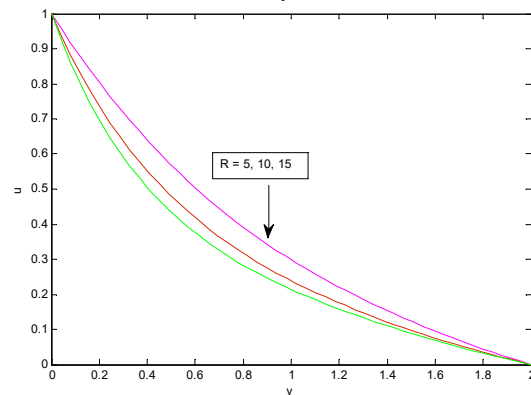


Figure 3. Velocity u versus y for the variation R

Figure-4 shows the impact of heat sink on velocity profile. It is observed that the fluid velocity decreases with the increase of heat sink Q. Figure-5 shows how fluid velocity changes with thermal Grashof number  $G_r$ . It is observed that as the thermal Grashof number increases, the velocity profile also increases. This can be explained by the fact that an increase in Grashof number corresponds to an increase in temperature gradients, which in turn leads to an augmentation in the velocity distribution within the flow.

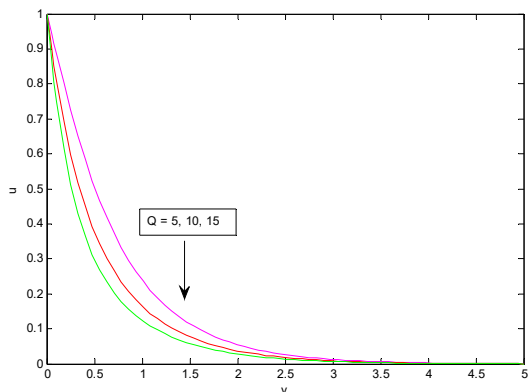


Figure 4. Velocity  $u$  versus  $y$  for the variation  $Q$

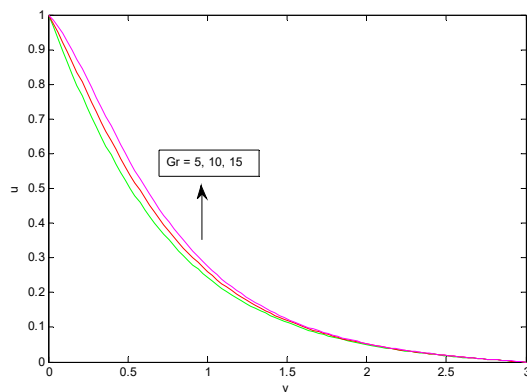


Figure 5. Velocity  $u$  versus  $y$  for the variation  $G_r$

Figure-6 shows the impact of solutal Grashof number  $G_m$  on the fluid velocity. It is observed that the fluid velocity increases with  $G_m$ . The velocity field increases significantly due to the thermal and solutal buoyancy forces. This is caused by the direct correlation between buoyant force and Grashof numbers. Figure-7 depicts the effect of Prandtl number  $P_r$  on velocity profile. It is seen that an elevation in the Prandtl number  $P_r$  is directly associated with a decrease in the fluid velocity. This can be attributed to the nature of higher Prandtl numbers leading to weakened convection currents, thereby qualitatively diminishing the temperature gradients and ultimately resulting in a decreased fluid velocity. In Figure 8, it can be observed that the fluid velocity increases as the porosity parameter rises. This phenomenon occurs because higher porosity values, provide the fluid with more space to flow. As a result, the fluid velocity experiences an increase.

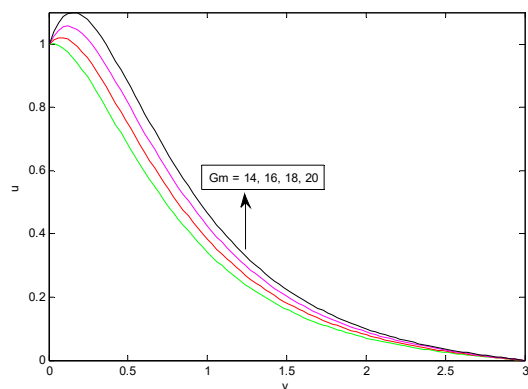


Figure 6. Velocity  $u$  versus  $y$  for the variation  $G_m$

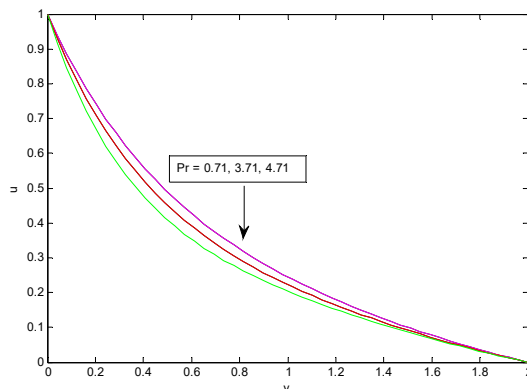


Figure 7. Velocity  $u$  versus  $y$  for the variation  $P_r$

**Temperature Profile:** The temperature profiles are depicted in Figures 9-11. Figure-9 demonstrates how temperature profile changes with heat sink  $Q$ . It is observed that the temperature decreases with the increase in  $Q$ . Figure 10 demonstrates that the temperature decreases as the Prandtl number increases. This behavior is attributed to the reduction in the thermal diffusivity of the fluid with higher Prandtl numbers. As a consequence, the thermal boundary layer thickness is diminished, leading to the observed decrease in temperature. The impact of the radiation parameter on the temperature profile is depicted in Figures 11. The trend observed indicates that as the radiation parameter increases, the temperature of the fluid decreases.

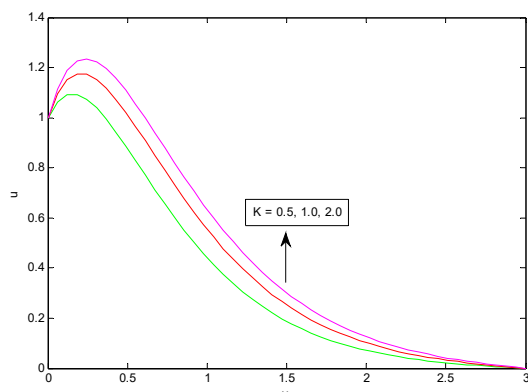


Figure 8. Velocity  $u$  versus  $y$  for the variation  $K$

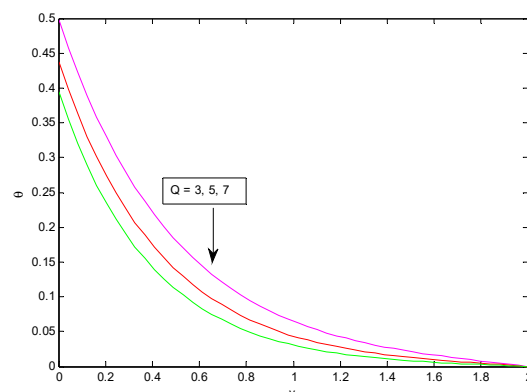


Figure 9. Temperature  $\theta$  versus  $y$  for the variation  $Q$

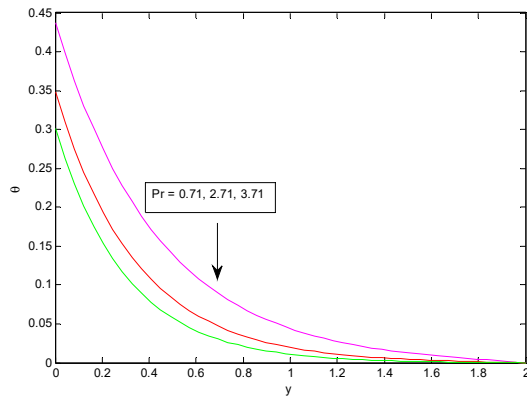


Figure 10. Temperature  $\theta$  versus  $y$  for the variation  $Pr$ .

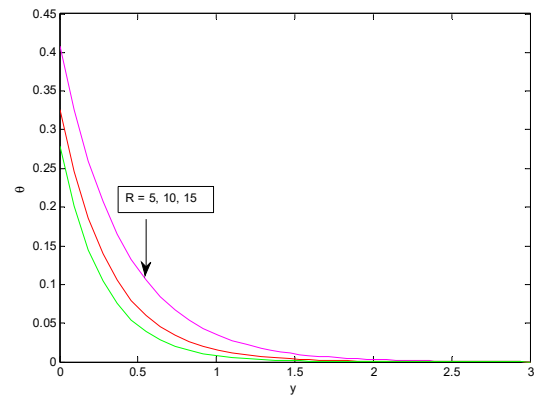


Figure 11. Temperature  $\theta$  versus  $y$  for the variation  $R$ .

**Concentration Profile:** The concentration profiles are depicted in Figures 12-13. Figure-12 depicts how concentration profile changes with Schmidt number  $Sc$ . It can be inferred that an increase in the Schmidt number corresponds to a decrease in solute diffusivity, leading to a shallower penetration of solutal effects. Consequently, the concentration decreases with an increase in the Schmidt number. Figure-11 shows how fluid concentration changes with chemical reaction parameter  $K_c$ . The concentration profile slows down with an increase in  $K_c$ . This effect is logical as higher values of the chemical reaction parameter lead to a decrease in the molecular diffusivity of the chemical species.

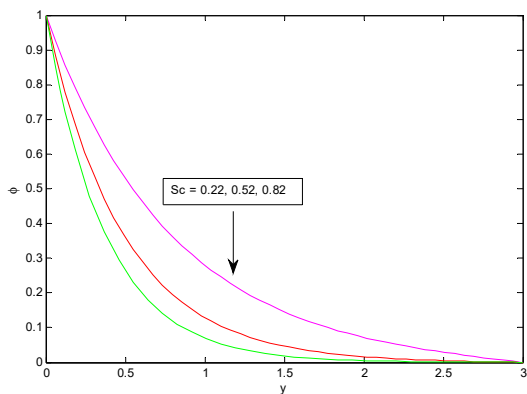


Figure 12. Concentration  $\phi$  versus  $y$  for different  $Sc$

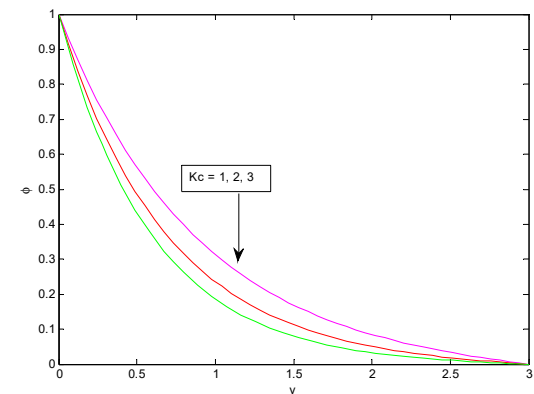


Figure 13. Concentration  $\phi$  versus  $y$  for different  $K_c$

## CONCLUSIONS

In this study, the impact of radiation and heat dissipation on magnetohydrodynamic (MHD) convective flow in the presence of a heat sink has been examined. The governing equations were numerically solved to obtain velocity, temperature, and concentration profiles, utilizing the MATLAB built-in bvp4c solver technique. The key findings of this investigation can be summarized as follows:

1. The transverse magnetic field's imposition causes fluid velocity to be delayed.
2. Thermal radiation consistently shows a propensity to reduce the atmosphere's temperature.
3. The plate's fluid concentration decreases as a result of decreased mass diffusivity.
4. The concentration of species decreases as a result of species eating.
5. With the use of a strong magnetic field in operation, the frictional resistance can be successfully inhibited.
6. As the porosity parameter increases, there is a corresponding increase in the fluid velocity.

## Nomenclature

$\vec{q}$	Fluid velocity	$U$	Velocity of free stream
$\rho$	Fluid density	$K$	Porosity parameter
$\theta$	Kinematic viscosity	$q^*$	Heat flux
$\vec{J}$	Current density	$\vec{q}_r$	Radiation heat flux
$\vec{g}$	Acceleration vector due to gravity	$T$	Fluid temperature
$\vec{B}$	Magnetic flux density vector	$C$	Concentration
$k$	Thermal conductivity	$C_w$	Plate species concentration
$k^*$	Mean absorption coefficient	$E$	Eckert number
$\varphi$	Energy viscous dissipation per unit volume	$C_\infty$	Free stream concentration
$p$	Fluid pressure	$\sigma$	Electrical conductivity

$\vec{E}$	Electrical field	$\Phi$	Non-dimensional concentration
B	Thermal expansion coefficient	$P_r$	Prandtl number
$\beta$	Solutal expansion coefficient	Q	Heat sink
$T_\infty$	Free stream concentration	$S_c$	Schmidt number
$C_\infty$	Free stream concentration	$G_r$	Thermal Grashof number
$B_0$	Applied magnetic field strength	M	Magnetic parameter
M	Viscosity coefficient	$G_m$	Solutal Grashof number
$\theta$	Non-dimensional temperature	R	Radiation

## ORCID

Salma Akhtar, <https://orcid.org/0009-0003-1793-001X>; Keshab Borah, <https://orcid.org/0009-0005-5486-5784>  
 Shyamanta Chakraborty, <https://orcid.org/0000-0001-5839-4856>

## REFERENCES

- [1] H. Alfvén, “Existence of Electromagnetic-Hydrodynamic Waves”, *Nature* **150**, 405–406 (1942), <https://doi.org/10.1038/150405d0>
- [2] T.G. Cowling, *Magnetohydrodynamics*, (Interscience Publishers, New York, 1957).
- [3] J.A. Shercliff, *A Textbook of Magnetohydrodynamics*, (Pergamon, Oxford, 1965).
- [4] A. Raptis, and C.V. Massals, “Flow past a plate by the presence of radiation”, *Heat and Mass Transfer*, **34**, 107-109 (1998). <https://doi.org/10.1007/s002310050237>
- [5] M.A. Hossain, M.A. Alim, and D.A.S. Rees, “The effect of radiation on free convection from a porous vertical plate,” *International Journal of Heat and Mass Transfer*, **42**(1), 181-191 (1999), [https://doi.org/10.1016/S0017-9310\(98\)00097-0](https://doi.org/10.1016/S0017-9310(98)00097-0)
- [6] V.C.A. Ferraro, and C. Plumpton, *An Introduction to Magneto Fluid Mechanics*, (Clarendon Press, Oxford, 1966).
- [7] C.-H. Chen, “Combined Heat and Mass Transfer in MHD Free Convection from a Vertical Surface with Ohmic Heating and Viscous Dissipation”, *International Journal of Engineering Science*, **42**(7), 699-713 (2004), <http://dx.doi.org/10.1016/j.ijengsci.2003.09.002>
- [8] N. Ahmed, and K. Choudhury, “Heat and mass transfer in three-dimensional flow through a porous medium with periodic permeability”, *Heat Transfer-Asian Research*, **48** (2), 644-662 (2018). <https://doi.org/10.1002/htj.21399>
- [9] A. Raptis, and C. Perdikis, “Radiation and Free Convection Flow past a Moving Plate”, *Applied Mechanics and Engineering*, **14**, 817-821 (1999).
- [10] J.Y. Kim, “Unsteady MHD convective heat transfer past a semi-infinite vertical porous moving plate with variable suction” *International Journal of Engineering Sciences*, **38**(8), 833-845 (2000), [https://doi.org/10.1016/S0020-7225\(99\)00063-4](https://doi.org/10.1016/S0020-7225(99)00063-4)
- [11] N. Senapati, and R.K. Dhal, “Magnetic effect on mass and heat transfer of a hydrodynamic flow past a vertical oscillating plate in presence of chemical reaction,” *Modelling, Measurement and Control B*, **79**, 60-75 (2010).
- [12] P. Vyas, A. Rai, and K. Shekhawat, “Dissipative heat and mass transfer in porous medium due to continuously moving plate,” *Applied Mathematical Science*, **6**(87), 4319–4330 (2012). <https://www.m-hikari.com/ams/ams-2012/ams-85-88-2012/raiAMS85-88-2012-2.pdf>
- [13] R. Vemula, “Chemical reaction and radiation effects on the transient MHD free convection flow of dissipative fluid past an Infinite vertical porous plate with ramped wall temperature,” *Chemical Industry and Chemical Engineering Quarterly*, **17**(2), (2011). <http://dx.doi.org/10.2298/CICEQ100829003R>
- [14] N. Ahmed, and M. Dutta, “Natural convection in transient MHD dissipative flow past a suddenly started infinite vertical porous plate: A finite-difference approach,” *Heat Transfer Research*, **49**(6), 491-508 (2018), <http://dx.doi.org/10.1615/HeatTransRes.2018016823>
- [15] K. Chamuah, and N. Ahmed, “MHD free convective dissipative flow past a porous plate in a porous medium in presence of radiation and thermal diffusion effects,” *Heat Transfer*, **51**(2), 1964-1981 (2022). <https://doi.org/10.1002/htj.22383>
- [16] Y.D. Reddy, B.S. Goud, & M.A. Kumar, “Radiation and heat absorption effects on an unsteady MHD boundary layer flow along an accelerated infinite vertical plate with ramped plate temperature in the existence of slip condition,” *Partial Differ. Equ. Appl. Math.* **4**, 100166 (2021). <https://doi.org/10.1016/j.padiff.2021.100166>
- [17] A. M. Sedki, “Effect of thermal radiation and chemical reaction on MHD mixed convective heat and mass transfer in nanofluid flow due to nonlinear stretching surface through porous medium”. *Results in Materials*, **16**, 100334 (2022) <https://doi.org/10.1016/j.rinma.2022.100334>
- [18] B.K. Jha, and G. Samaila, “Effect of heat source/sink on MHD free convection flow in a channel filled with nanofluid in the existence of induced magnetic field: an analytic approach,” *SN Appl. Sci.* **2**, 1321 (2020). <https://doi.org/10.1007/s42452-020-3139-8>
- [19] S. Matta, B.S. Malga, G.R. Goud, L. Appidi, and P.P. Kumar, “Effects of viscous dissipation on MHD free convection flow past a semi-infinite moving vertical porous plate with heat sink and chemical reaction,” *Materials Today: Proceedings*, (2023). <https://doi.org/10.1016/j.matpr.2023.06.108>
- [20] B. Manvi, J. Tawade, M. Biradar, S. Noeiaghdam, U. Fernandez-Gamiz, and V. Govindan, “The effects of MHD radiating and non-uniform heat source/sink with heating on the momentum and heat transfer of Eyring-Powell fluid over a stretching,” *Results in Engineering*, **14**, 100435 (2022). <https://doi.org/10.1016/j.rineng.2022.100435>
- [21] P. Bhaskar, and M. Venkateswarlu, “Influence of Heat Generation and Thermal Radiation on MHD Flow in a Vertical Micro-Porous-Channel in the Presence of Viscous Dissipation,” *Mapana Journal of Sciences*, **21**, 1-22 (2021).
- [22] O.L. Andreeva, L.A. Bulavin, and V.I. Tkachenko, “The Stability of a Rotating and Heated from Below Horizontal Cylindrical Layer of a Viscous, Incompressible Liquid with Free Boundaries,” *East European Journal of Physics*, **4**, 18–33 (2019). <https://doi.org/10.26565/2312-4334-2019-4-02>
- [23] O.L. Andrieieva, B.V. Borts, A.F. Vanzha, I.M. Korotkova, and V.I. Tkachenko, “Stability of a Viscous Incompressible Conducting Liquid Layer of a Cylindrical Shape in an Inhomogeneous Temperature Field and a Magnetic Field of a Vacuum Arc Current Through it,” *Problems of Atomic Science and Technology*, **133**(3), 91-97 (2021). <https://doi.org/10.46813/2021-133-091>

- [24] A.C. Cogley, W.G. Vincent, S.E. Gilles, "Differential approximation for radiative heat transfer in a Gray gas near equilibrium", AIAA Journal, 6(3), 551-553 (1968), <https://doi.org/10.2514/3.4538>

**ВПЛИВ ВИПРОМІНЮВАННЯ ТА РОЗСІЮВАННЯ ТЕПЛА НА МГД КОНВЕКТИВНИЙ ПОТІК ЗА НАЯВНОСТІ ТЕПЛОВІДВОДУ**

**Сальма Ахтар<sup>а</sup>, Кешаб Борах<sup>а</sup>, Шьяманта Чакраборти<sup>б</sup>**

<sup>а</sup>Департамент математики, Університет Гаухаті, Гувахаті-781014, Ассам, Індія

<sup>б</sup>UGC-HRDC, Університет Гаухаті, Гувахаті-781014, Ассам, Індія

У статті розглядається тепломасообмін у МГД-конвективному потоці через вертикальну пористу пластину за наявності випромінювання, тепловідводу та розсіювання тепла. Сильне магнітне поле прикладене перпендикулярно до пластини і спрямоване в область рідини. Керівні безвимірні рівняння розв'язуються за допомогою вбудованого в MATLAB методу вирішувача *bvp4c*. Результати обчислюються за допомогою математичного програмного забезпечення, а вплив різних безрозмірних параметрів, що входять у задачу, на профілі швидкості, температури та концентрації відображається в графічних форматах. Було відзначено, що застосування магнітного поля сповільнює швидкість рідини. Крім того, як ефект теплового випромінювання, так і число Прандтля повністю застосовні до температури рідини. Важливо зауважити, що радіатор різко знижує температуру та швидкість рідини. Поточна робота використовується в багатьох реальних програмах, таких як хімічна інженерія, промислові процеси, система може містити кілька компонентів, кожна з яких концентрація змінюється від однієї точки до іншої в ряді різних обставин.

**Ключові слова:** *тепломасообмін; МГД; розсіювання тепла; пористе середовище; bvp4c*

## PREDICTION OF VISCOSITY OF COBALT FERRITE/SAE50 ENGINE OIL BASED NANOFUIDS USING WELL TRAINED ARTIFICIAL NEURAL NETWORK (ANN) AND RESPONSE SURFACE METHODOLOGY (RSM)<sup>†</sup>

Malik Muhammad Hafeezullah<sup>a,c</sup>, Abdul Rafay<sup>b</sup>, Ghulam Mustafa<sup>d</sup>, Muhammad Khalid<sup>b\*</sup>, Zubair Ahmed Kalhoro<sup>c</sup>, Abdul Wasim Shaikh<sup>a</sup>, Ahmed Ali Rajput<sup>b</sup>

<sup>a</sup>Institute of Computer Science and Mathematics, University of Sindh, Jamshoro, Pakistan

<sup>b</sup>Department of Physics, University of Karachi, 75270, Karachi, Pakistan

<sup>c</sup>Department of Mathematics, Balochistan University of Information Technology, Engineering and Management Sciences, Quetta, Pakistan

<sup>d</sup>Department of Physics, NED University of Engineering and Technology, 75270, Karachi, Pakistan

\*Corresponding Author e-mail: [mkhalid@uok.edu.pk](mailto:mkhalid@uok.edu.pk)

Received May 16, 2023; revised July 1, 2023; accepted July 6, 2023

Heat transmission by ordinary fluids such as pure water, oil, and ethylene glycol is inefficient due to their low viscosity. To boost the efficiency of conventional fluids, very small percent of nanoparticles are added to the base fluids to prepare nanofluid. The impact of changing in viscosity can be used to investigate the rheological properties of nanofluids. In this paper, (CoFe<sub>2</sub>O<sub>4</sub>)/engine oil based nanofluids were prepared using two steps standard methodology. In first step, CoFe<sub>2</sub>O<sub>4</sub> (CF) were synthesized using the sol-gel wet chemical process. The crystalline structure and morphology were confirmed using X-Ray diffraction analysis (XRD) and scanning electron microscopy (SEM), respectively. In second step, the standard procedure was adapted by taking several solid volume fractions of CF as  $\phi = 0, 0.25, 0.50, 0.75, \text{ and } 1.0\%$ . Such percent of concentrations were dispersed in appropriate volume of engine oil using the ultrasonication for 5 h. After date, the viscosity of prepared five different nanofluids were determined at temperatures ranging from 40 to 80 °C. According to the findings, the viscosity of nanofluids ( $\mu_{nf}$ ) decreased as temperature increased while increased when the volume percentage of nanofluids  $\phi$  raised. Furthermore, total 25 experimental observations were considered to predict viscosity using an artificial neural network (ANN) and response surface methodology (RSM). The algorithm for building the ideal ANN architecture has been recommended in order to predict the fluid velocity of the CF/SAE-50 oil based nanofluid using MATLAB software. In order to determine the validation of the predicted model, the mean square error (MSE) was calculated as 0.0136 which corresponds to the predicted data is well correlated with experimental data.

**Keywords:** Cobalt Ferrite; Nanofluids; Viscosity; Solid volume fraction; ANN; RSM

**PACS:** 47.63.-b, 61.46.+w, 07.05.Mh, 05.40.Jc, 66.20.Ej

### 1. INTRODUCTION

Nanofluid is a form of fluid formed by dispersing nano-sized particles in a base fluid [1]. These nanofluids have gotten a lot of interest in the last few decades for their applications in microelectronics, transportation, solar, nuclear, and space technology [2]. Base fluids such as motor oil, water, and ethylene glycol were commonly employed as heat transporting fluids in a variety of industries [3]. By distributing nanoparticles in a normal fluid such as water, motor oil, and ethylene glycol, high heat conductive nanofluids can be formed, according to Choi [4]. The most important attribute of a nanofluid is its viscosity, which is related with heat transfer. It is obvious that when the volume percentage of nanoparticles increases, convective heat transmission increases [5]. As a result, accurate numbers for nanofluid viscosity are critical for industrial nanofluid demand [6].

Einstein created analytical methods for forecasting a mixture's viscosity in 1906, Brinkman in 1952, and Batchelor in 1977, but those models, which are based on the colloidal theory and contain particles on the order of micrometre, failed to predict the viscosity of the mixture numerous times. As a result, a new model based on nanofluid viscosity has been proposed. The majority of them were based on nanoparticle interfacial layers [7] and Brownian nanofluids nanoparticles in ordinary liquids [8]. Brownian motion has been discovered to be the cause of additional energy transmission of nano particles. Convection explains the relative mobility between nanoparticles and based fluids, according to Jang and Choi's first model, which is based on Brownian motion. Ravi Prasher, on the other hand, demonstrated that Choi and Jang's correlation is inaccurate, and he produced a new viscosity of nanofluid correlation [9]. Masoumi et al. construct an enhanced correlation [10] for nanofluid viscosity using the Ravi Prasher Correlation [11]. Yang et al. found a temperature influence on the viscosity of nanofluids. They experimented using graphene as a nanomaterial. They discovered that when temperature rises, viscosity decreases [12]. Chen et al. investigated the similar impact of MWCNT-distilled water nanofluid at temperatures ranging from 278 K to 338 K and discovered that beyond 338 K, the viscosity ratio increases dramatically [13].

He and colleagues observed that the viscosity of nanofluid increased with particle size. However, Lu and Fan observed that as particle radius grows, so does the viscosity of the nanofluid decreases [14, 15]. Chevalier et al. evaluated

<sup>†</sup> Cite as: M.M. Hafeezullah, A. Rafay, G. Mustafa, M. Khalid, Z.A. Kalhoro, A.W. Shaikh, A.A. Rajput, East Eur. J. Phys. 3, 479 (2023), <https://doi.org/10.26565/2312-4334-2023-3-54>

© M.M. Hafeezullah, A. Rafay, G. Mustafa, M. Khalid, Z.A. Kalhoro, A.W. Shaikh, A.A. Rajput, 2023



the viscosity of SiO<sub>2</sub>-Ethanol nanofluid for particle sizes and discovered that the viscosity increases as the diameter of the nanoparticles decreases [16]. According to [17] Chevalier et al. experimentally investigated that viscosity increases abnormally with increasing volume concentrations. The viscosity of nanofluid grows as the volume concentration increases, after the volume concentration of 0.4%, according to Lu and Fan. Chen et al. discovered that viscosity increases as the volume concentration increases [18]. According to Mahbulul et al. no correlation can estimate viscosity values across a wide range of particle volume concentrations [19].

Using various modelling tools, some researchers anticipated the rheological behavior of nanofluid [20]

To synthesize and assess nanofluid thermophysical characteristics such as viscosity [21] (Fig.1), special equipment and experiments, as well as a significant amount of time and money, are required [22].

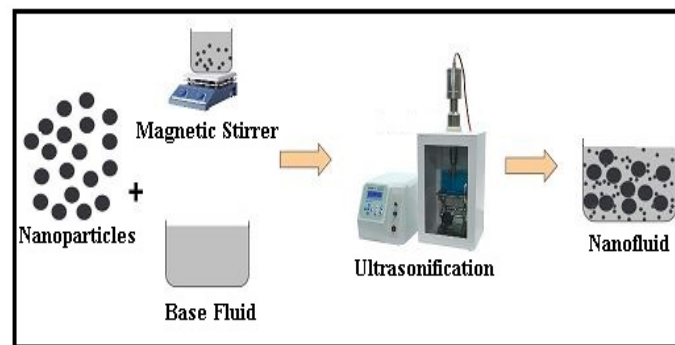


**Figure 1.** Special apparatus for the preparation of nanofluids

There are numerous research studies that may be utilized to determine the viscosity of nanofluids. Hajir-Karimi et al. investigated the viscosities of several nanoparticles in the temperature range 238.15–343.15 K, using a total number of eight nanoparticles, with a nanoparticle volume fraction of up to 9.4%. An effective and precise artificial neural network based on genetic algorithm (GA) is modelled for forecasting nanofluid viscosity using computational intelligence approaches. To optimize the neural network variables, the genetic algorithm (GA) is applied. As input data for computational intelligence models, they employed nanofluid temperature, nanoparticle size, nanoparticle percentage and nanofluid density. The nanofluid viscosity was the resulting data. The findings demonstrate that the GA-NN model matches the actual data effectively, with an absolute deviation of 2.48 % and a high degree of correlation value ( $R = 0.98$ ). [23]. Majid Gholizadeh et al. properly calculated the viscosity of thermodynamic nanofluids using a robust artificial intelligence technique known as random forest (RF). Temperature, solid volume percentage, base fluid viscosity, nanoparticle size, and nanoparticle density were used to build the model. In addition, 2890 data points were gathered. They utilised ( $R = 0.989$ ,  $RMSE = 0.139$ ,  $MAPE = 4.758$  %) rather than the MLP ( $R = 0.915$ ,  $RMSE = 0.377$ ,  $MPE = 16.194$  %) and the SVR ( $R = 0.941$ ,  $RMSE = 0.315$ ,  $MAPE = 7.895$  %) for model accuracy. They produced an effective model based on comparative findings with other approaches [24]. Praveen Kanti et al. used a modern computational intelligence strategy, ANN and MGGP, to enhance experimentally recorded dynamic viscosity data of nanofluids. This study looked at the dynamic viscosity of a water-based stable fly-ash nanofluid and a fly ash–Cu (80–20 % by volume) hybrid nanofluid at temperatures ranging from 30 to 60°C. The viscosity of flue-ash nanofluid is determined utilizing MGGP modeling ( $R = 0.99988$ ,  $RMSE = 0.0019$ , and  $MAPE = 0.25$  %). Furthermore, experiment also showed that the MGGP approach excels at predicting flue ash-Cu/Water hybrid nanofluid viscosity ( $R = 0.9975$ ,  $RMSE = 0.0063$ , and  $MAPE = 0.664$  %) [25]. Abdullah et al. examined the viscosity of MWCNT-COOH nanoparticles in water at temperatures ranging from 20 to 50° C and solid volume fractions ranging from 0 to 0.2%. As a result of the experimental results, the unique connection that predicts the relative thermophysical properties of the nanofluids was established. An adaptive neuro-fuzzy inference system (ANFIS) and the finest artificial neural network (ANN) were built in addition to nonlinear regression for the least prediction error. 120 experimental measurements were submitted to the model. Several theoretical models, predicted outcomes, and experimental findings were all compared. ANN has an RMSE of 0.46618, but ANFIS has an RMSE of 0.49062, and the mean absolute percentage error (MAPE) of ANN and ANFIS is 0.00023 and 0.00047, respectively [26]. To predict the viscosity of nanoparticles, Ahmedi et. al. used optimization techniques to simulate the fluid viscosity of silver (Ag)-water nanofluid: multivariable polynomial regression (MPR), artificial neural network–multilayer perceptron (ANN-MLP), and multivariate adaptive regression splines (MARS). Size of the particles, temperature, and silver nanoparticle concentration are the most essential input elements examined in the modelling approach. The ANN-MLP, MARS, and MPR techniques have  $R^2$  values of 0.9998, 0.9997, and 0.9996, respectively. [27]

By forecasting thermophysical qualities, scholars utilized artificial neural network simulation to perform their researches by the least amount of money and time feasible. A summary regarding the various authors have done the work using the nanofluids with different mathematical model are shown in Table 1.

In their investigation the artificial neural network model employed by Baranitharan et al. is presented schematically in (Fig. 2). An artificial neural network (ANN) is a computing approach that understands the relationship between input and

output by using neurons and their connections. Input neurons send data to buried layer neurons for processing. The data is then sent from the hidden neurons to the output neurons for processing. The letters "w" and "b" in this image reflect the amount of weight and bias, respectively (Fig. 2).

**Table 1.** Summary of the researches conducting by ANN, MLP and RSM using various nanofluids

Scholar	Nanofluid	Technique	Objective
Bahirai et al. [30]	Several Nanofluids (analysis)	ANN and hybrid AI algorithm	Nanofluids thermal characteristics.
Zhao et al. [31]	Several Nanofluids (analysis)	ANN	Predicting the viscosity of a substance in order to use it in a radiator.
Vakili et al. [32]	Water based grapheme.	MLP-genetic algorithm	Viscosity
Vakili et al. [33]	Water based CNT.	Levenberg–Marquardt algorithm	Thermal properties
Heideri et al.[34]	Al <sub>2</sub> O <sub>3</sub> and CuO nanoparticles dispersed in water.	ANN	Viscosity
Alirezai et al. [35]	Multiwall carbon nanotube.	MLP	Dynamic Viscosity
Esfe et.al. [36]	Oil based hybrid nanofluid.	RSM	Viscosity of nanoparticles-based oil.
Esfe et.al [37]	MgO-MWCNT (75–25%)/10W40	RSM	Thermophysical properties
Esfe et.al. [38]	Co <sub>3</sub> O <sub>4</sub> /EG (40/60) aqueous nanofluid.	RSM	Optimization of Viscosity.
Esfe et.al.[39]	CNT nanofluids.	RSM	
Maqsood et.al.[40]			
Esfe et al.[41]	Multi-walled CNT nanofluids.	ANN and RSM	Thermophysical properties.
	Water based nanofluids.	ANN and RSM	Thermophysical properties.

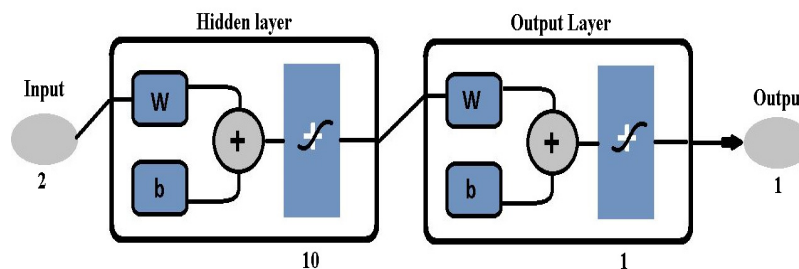


**Figure 2.** A schematic diagram of an artificial neural network

Many models for determining effective viscosity values have been established in the past. Some researchers, such as Einstein [42] provided a theoretical model for forecasting nanofluid relative viscosity. When SVF is less than 0.20 percent, the Einstein model (Eq.1) yields more accurate findings, and it is based on the notion that solid suspended particles in the base fluid are spherical:

$$\mu_{nf} = (1 + 2.5\phi)\mu_{bf} \tag{1}$$

Where 'μ' stands for viscosity, 'φ' for SVF, and the abbreviations "nf" and "bf" stand for nanofluid and base fluid, respectively. Wang et al. [21] also gave the model for estimating relative viscosity shown below

$$\mu_{nf} = (1 + 7.3\phi + 123\phi^2)\mu_{bf} \tag{2}$$

Also, H. De Bruijn[43] proposed a model to predict the relative viscosity of nanofluids containing spherical nanoparticles:

$$\mu_{nf} = (1 - 2.5\phi + 1.552\phi^2)\mu_{bf} \tag{3}$$

On the other hand, current theoretical models fail to detect the viscosity of nanoparticles. Nanofluids were predicted by Wang et al (1999) as a function of nanoparticle kind, particle size, volume percent, and temperature. A laboratory-based study is presented in this paper to analyze the viscosity of a Cobalt Ferrite (40-80°C)/SAE 50 Engine oil based nanofluid. Temperature and solid volume fraction (SVF) were employed as inputs in an ANN with two related hidden layers, and viscosity was used as an output. The ANN findings and the experimental results are likewise at variance. After this, the trial outcomes were compared to the RSM model and the ANN approach.

## 2. METHODOLOGY

### 2.1. X-Ray diffraction and Scanning electron Microscopy

To do this, the sol-gel method [44] was used to create cobalt ferrite nanoparticles (CoFe<sub>2</sub>O<sub>4</sub>). The structure was confirmed using X-Ray diffraction analysis (Fig.3) [45]. The composition of prepared Cobalt spinel ferrite is confirmed by the EDX [46]. Using the Scherer formula (eq.4), the particle size was measured to be 15 nm. The form and size of the particles were determined using scanning electron microscopy and the grain size of the particles is analyzed by histogram (Fig.4) [47].

$$D = \frac{0.94 \lambda}{\beta \cos \theta} \tag{4}$$

where “β” is the full width and half maximum, “λ” is the X-ray wavelength, and “θ” is the angle suspended.

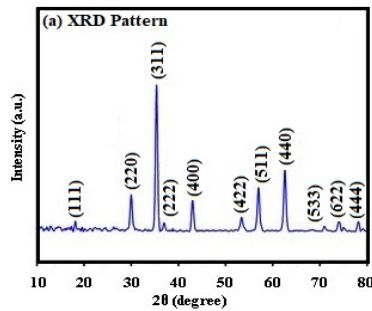


Figure 3. XRD pattern of cobalt spinel ferrite nanoparticles

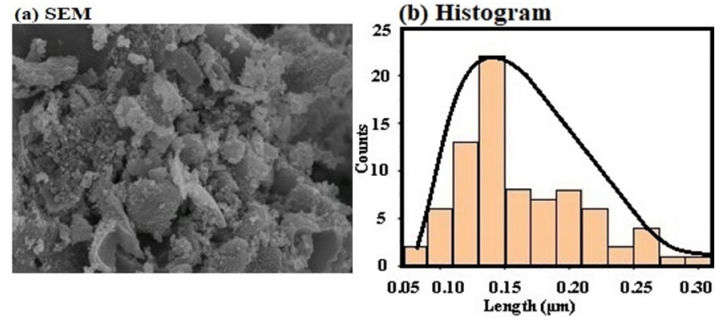


Figure 4. (a) SEM image and (b) grain size distribution of cobalt spinel ferrite nanoparticles

### 2.2. Surface Modification

To begin, mill the cobalt ferric oxide nanoparticles and then make an 80 ml orthoxylyene in a 20 ml oleic acid solution volume by volume ratio. The Stirring was done of the prepared solution for a few hours to achieve a homogeneous condition. On the other hand, 2 gm of milled particles, were added to 98 gm of orthoxylyene, stirred continuously for surface modification, and placed on a heated plate. The modified particles are filtered away, and then particles are added to the oleic acid solution.

### 2.3. Preparation of Nanofluids

The dried powder is then mixed with SAE 50 engine oil in predetermined proportions to make different samples with varied solid volume fractions, such as 0, 0.25, 0.50, 0.75, and 1.0% solid volume fraction. To make the concentrated solutions that are necessary, the weight of solid Cobalt nanoparticles and the oil SAE 50 is specified in (Table 2), which were calculated by using the relation given in (Eq. 5). Stir all the solution samples to obtain the stability of cobalt-based nanoparticles in engine oil. The experimental work was summarized in a flow chart that was supplied in order to acquire the greatest understanding of it (Fig.5).

$$\phi = \frac{m_{NP}}{m_{NP} + m_{oil}} \times 100. \tag{5}$$

Table 2. The composition weights for the preparation of different volume fractions of sample

Number of samples	Solid volume fraction (%)	Mass of cobalt nanoparticles (g)	Mass of oil (g)
1	0.00	0.000	49.83
2	0.25	0.137	49.69
3	0.50	0.275	49.55
4	0.75	0.4125	49.005
5	1.00	0.550	49.77

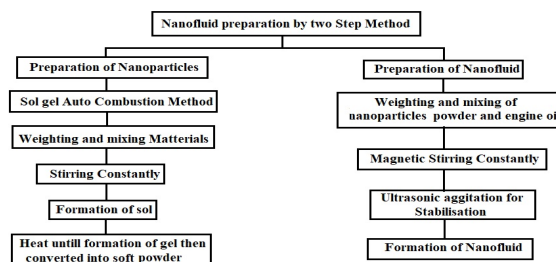
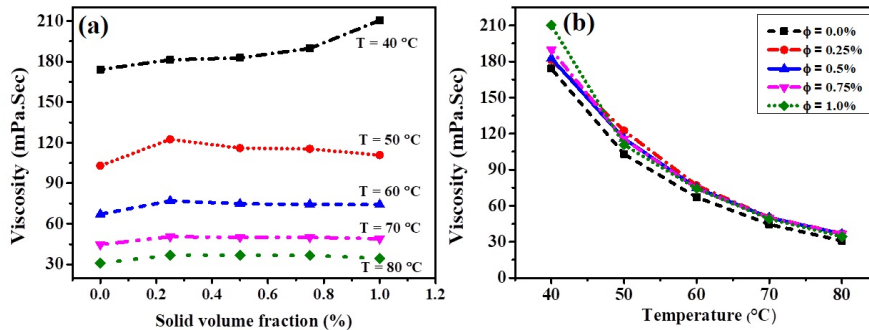


Figure 5. Flow chart to represents the preparation of cobalt spinel ferrite-based engine oil based nanofluids in two steps methods

Finally, using the free-falling technique, the viscosity of the prepared samples is determined experimentally by using relation given in (Eq.6).

$$\eta = KT(\rho_1 - \rho_2). \tag{6}$$

where “k” is the proportionality constant, “T” is the average time taken by the free fall body through the fluid between two fixed points, and “ρ<sub>1</sub>”, “ρ<sub>2</sub>” are the densities of ball and sample fluid respectively. The experimental viscosity is found to be correlated with the input parameters temperature and solid volume percent in (Fig. 6).



**Figure 6.** Experimental values of viscosity using various volume fractions of cobalt ferrites based nanofluids with effect of (a) temperature and (b) solid volume fraction

### 2.4 Artificial Neural Network (ANN)

One of the technologies used to study human brain activity is artificial neural networks. Many numerical methods inspired by the human brain have been presented in the subject of Artificial Neural Networks. Many industries have used the models provided to tackle a wide range of scientific and practical issues. There are many other ANN architectures, such as the well-known multilayer perceptron (MLP). This strategy was used to develop the present neural network. Many training approaches may be employed to train the ANN, and one of the most prevalent (the Levenberg-Marquardt approach) is used in this work.

In systems with various input parameters, neural networks are also utilized to anticipate output data. The viscosity of Cobalt Ferrite/SAE 50 Engine oil based nanofluids was investigated in this research using two input parameters which are SVF and Temperature. The ANN approach predicts output data by obtaining the problem's input parameters and training neurons based on a number of inputs and calculating their weight and bias; errors are gathered during the testing and validation stages. The most optimal ANN structure is shown in (Fig. 7). The ideal structure contains two inputs, nine neurons in the first hidden layer, five neurons in the second hidden layer, and one output.

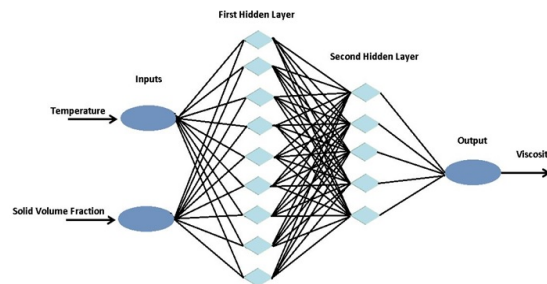


**Figure 7.** The design of the most ideal ANN network

The formulas in Eq. 7, 8 and 9 may be used to compute the most efficient number of hidden layers, neuron counts in each layer, neuron weighting, and the optimal combination of transfer functions.

$$MSE = \frac{1}{N} \sum_{i=1}^n (T_{ij} - P_{ij})^2, \tag{7}$$

$$MAE = \frac{1}{N} \sum_{i=1}^n (T_{ij} - P_{ij}), \tag{8}$$

$$R^2 = \frac{\sum_{i=1}^N (T_{ij}-T)^2 - (P_{ij}-P)^2}{\sum_{i=1}^N (T_{ij}-T)^2}. \tag{9}$$

where T<sub>ij</sub> and P<sub>ij</sub> are the expected and estimated values, and the total number of observations is N.

### 2.5. Mathematical Correlation Model

The exact viscosity of nanofluid cannot be predicted using theoretical models. As a result of analyzing the experimental data and applying the RSM method, a new quadratic equation for predicting viscosity has been constructed (Eq. 10). Experimental data was used to predict viscosity changes when SVF and temperature varied, as well as curve

fitting rates. The correlation coefficient  $R^2$  of this equation is 0.9663, indicating that the prediction is correct based on the experimental results.

$$\mu = 8.62 - 3.95T + 0.3412\phi - 0.2504T\phi + 1.25T^2 - 0.1313\phi^2 + 1.25T^2 - 0.1313\phi^2 \quad (10)$$

The results acquired by analysis variance indicate the correctness of the expected model using response surface technique. In the recommended equation (Eq. 7), the relevance of each variable is shown in (Tables 4 and 5). The parameter's relevance in the equation is high if the p-value is less than 0.05; if the p-value is more than 0.05, the parameter's importance in the equation is low, and the parameter's effect can be removed from the equation.

Table 4. ANOVA for nanofluid viscosity

Source	Square sum	Df	Square Mean	F-value	p-value
<b>Design</b>	99.500	5	9.90	576.52	<0.0001 Significant
A-TEMP	93.840	1	93.84	2718.71	< 0.0001
B-SVF	0.6983	1	0.6983	20.23	0.0028
AB	0.2508	1	0.2508	7.27	0.0308
A <sup>2</sup>	4.320	1	4.32	125.24	< 0.0001
B <sup>2</sup>	0.0476	1	0.0476	125.24	0.2785
<b>Residual</b>	0.2416	7	0.0345	1.38	
<b>Cor Total</b>	99.740	12			

Table 5. The present numerical model's evaluation of variance

<b>Std. Dev.</b>	0.1858	<b>R<sup>2</sup></b>	0.9976
<b>Mean</b>	9.14	<b>Adjusted R<sup>2</sup></b>	0.9958
<b>C.V. %</b>	2.03	<b>Predicted R<sup>2</sup></b>	0.9767
		<b>Adeq Precision</b>	68.0720

Fig. 8 (a) shows the excellent agreement between the experimental and predicted data using the RSM developed model which reveal the accuracy of the developed model.

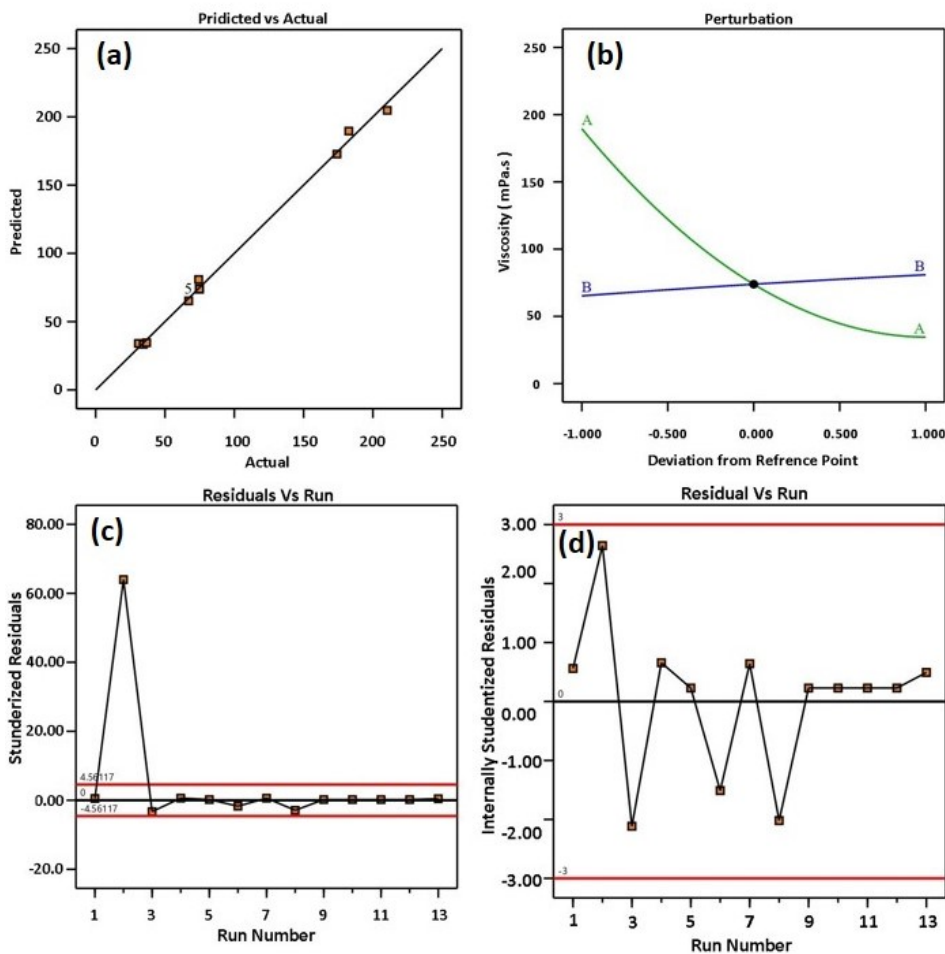


Figure 8. Experimental validation with RSM results

Fig. 8 (b) represent the graph between the deviation between the reference point and viscosity. This graph provides the central point (O) of the deviation which ultimately gives the overall influence of all process factors on the response function. The contrast effect of two factors such as solid volume fraction and temperature at the reference point provides the operating range of the perturbation presented graph. The residual graph based on run number and projected data can be seen in Fig. 8 (c). Only one data point at runs 2 is out from the other data points in between the red lines which is clear evidence the developed theoretical model has a significant and well adapted to predict the viscosity of the nanofluids. No abnormality in the random distribution of residuals can be seen in Fig. 8 (d)

### 3. RESULTS AND DISCUSSION

#### 3.1. ANN Accuracy Evaluation

The coefficients were obtained using the Levenberg-Marquardt learning procedures, which were utilized to train the network. In this case, the neural network repeats the prediction cycle, altering the weight and bias as well as the training stage to achieve the desired error rates. In this study, the error value is fully provided in (Table 3), which shows the relationship between eq. 7 and 9. The fact that  $R^2$  is so near to 1 (0.9999) demonstrates the constructed neural network's exceptional accuracy (Fig. 9).

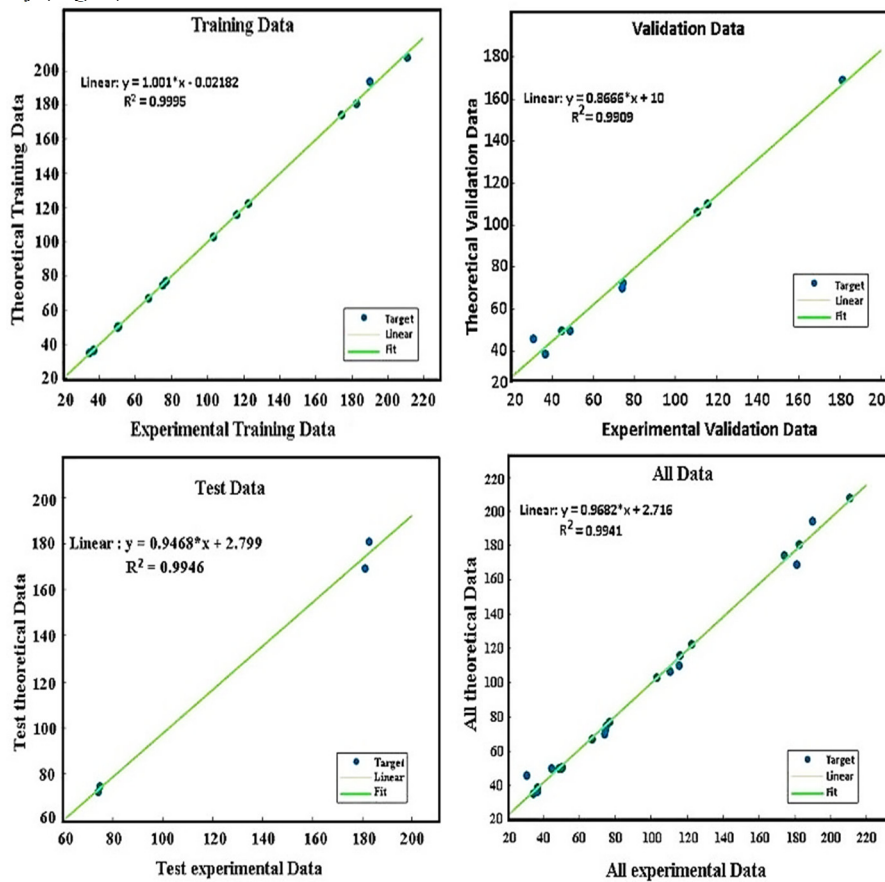


Figure 9. Confirmation of ANN results with experimental results

Table 3. The results of an ANN model to measure viscosity of cobalt ferrite / SAE 50 Engine Oil

Train Step accuracy analysis	
3.896 x 10 <sup>-6</sup>	MSE
0.037611	MAE
0.9995	R <sup>2</sup>
Test step accuracy	
0.3122	MSE
4.028138	MAE
0.9946	R <sup>2</sup>
Total accuracy analysis by ANN predicted topology	
0.9941	R <sup>2</sup>

The experimental data is compared to the ANN's predicted data in the Fig. 10. In this comparison, the trial, train, and total network data were compared. The ANN's projected values are well-trained, resulting in appropriate test data, validation, and total data correctness, as shown in this diagram.

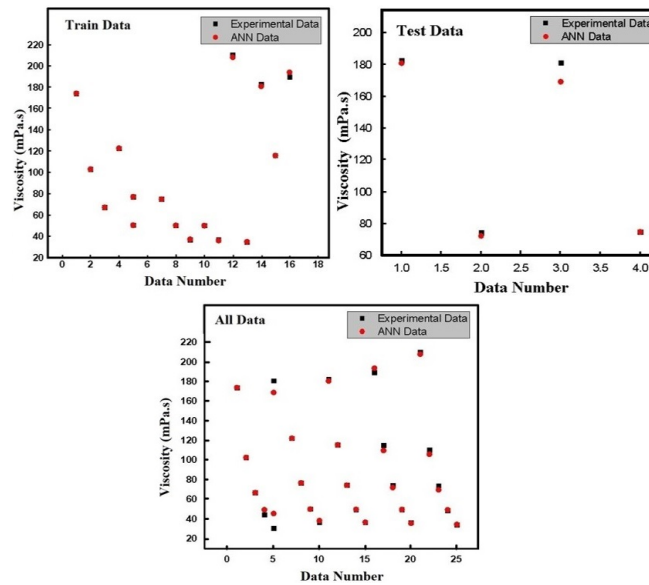


Figure 10. The correlation of intended ANN outputs with the experimental set of data during training, testing, and all data phases

### 3.2 Prediction Accuracy of Artificial Neural network against Mathematical Model

The validation of the ANN and RSM techniques in estimating viscosity at different temperature and solid volume fractions is compared in this section. The ANN forecast, on the other side, closely matches the patterns of experimental results. It can be concluded that the prediction of ANN method is better than the RSM prediction with experimental results. The outcomes of the ANN and RSM are compared in (Fig.11)

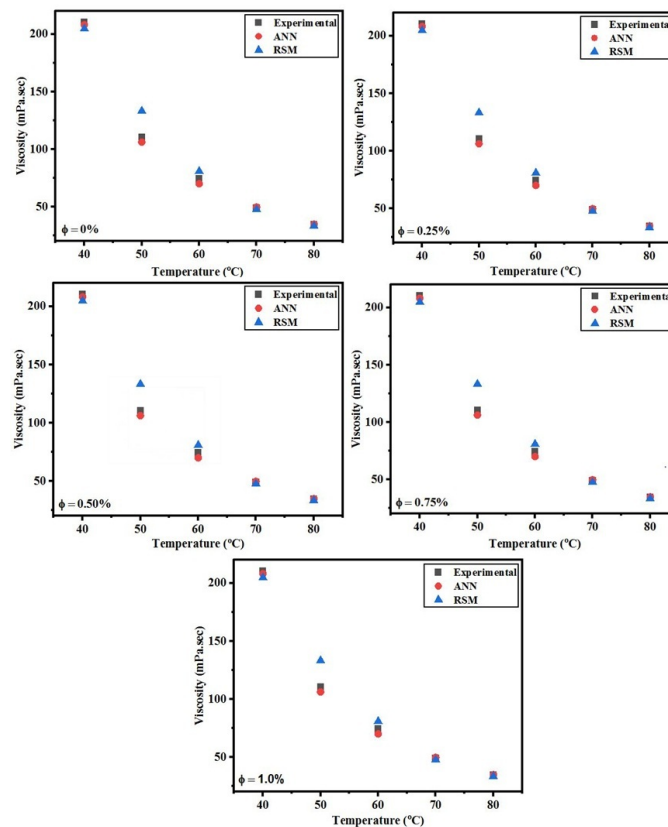


Figure 11. RSM and ANN predictions of viscosity compared with experimental values

The relationship average absolute percent deviation (AAD) is used to compare expected and observed data in (Eq.11).

$$AAD\% = \frac{1}{N} \sum_{i=1}^n \frac{|\mu_{exp} - \mu_{pre}|}{\mu_{exp}} \times 100. \quad (11)$$

Eq. 11 specifies the number of experiments (N), experimental calculated viscosity (exp), and expected viscosity (pre). Calculations revealed that the AAD% is 1.7112%, indicating that the results are accurate. Fig. 12 (a) depicts the experimental data that back up ANN predictions. Maximum margin of deviation (MOD) percent reported (-7% and 9%). The symbol placement on the bisector line also indicates whether the experimental data matches the neural network's predicted outcomes. Fig.12 (b) depicts the experimental data that back up RSM predictions, that's confirmed the RSM prediction is correlated with the experimental values. Maximum margin of deviation (MOD) percent reported (-8% and 10%) for RSM. The comparison of MOD% for ANN was observed less than the MOD% observed in RSM, indicates that the ANN model much better than RSM.

Another method for comparing experimental data with data produced from the suggested correlation is to use Eq.12 to calculate the percentage of data deviation from experimental data.

$$MOD\% = 1 - \frac{\mu_{Pred}}{\mu_{Exp}} \tag{12}$$

Another comparison chart for nf versus temperature and Solid volume fraction is shown in 3D space to evaluate the trained ANN method for estimating the viscosity  $\mu_{nf}$ . (Fig. 13a). Fig. 13b depicts another 3D space for estimating viscosity using the RSM model. We may deduce from the diagram that a well-trained ANN can be utilized to simulate viscosity. Furthermore, solid volume fraction has a larger impact on viscosity than temperature, which has a smaller impact on the output values.

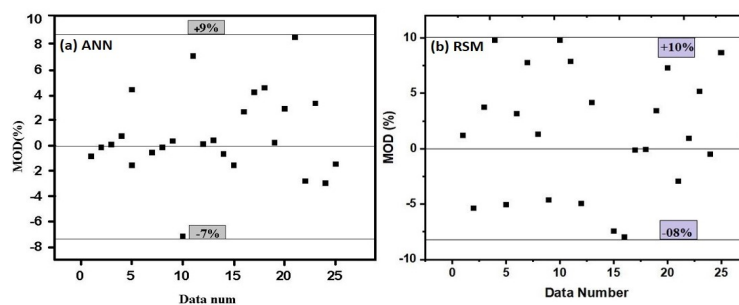


Figure 12. Margin of deviation for RSM and ANN projected data compared with experimental data

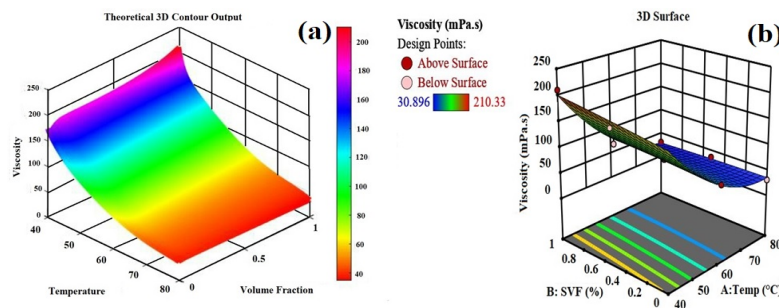


Figure 13. 3D graph of viscosity against temperature and SVF using the (a) ANN and (b) RSM methodology

#### 4. CONCLUSION

Under this research, 25 experimental results for the viscosity of cobalt ferrite/SAE 50 engine oil based nanofluids in all temperature ranges from 40, 50, 60, 70, and 80°C, at SVFs of 0, 0.25, 0.50, 0.75, and 1.0%, were tried to compare with the simulated values by the neural network, with their insignificant difference (-7%, +9%) representing a precise model for forecasting nanofluid viscosity. The sample's viscosity is significantly influenced by the parameters of the nanoparticle's temperature and solid volume fraction (SVF), therefore an increase in SVF across the range results in a notable increase in viscosity. For all SVF ranges, rising temperature will result in a decrease in dynamic viscosity. From a collection of 25 ANN data, the best optimum structure was chosen after analysis by two hidden layers that each had 9 and 5 neurons. For the first and second hidden layers, respectively, logsig and tansig are the ideal transfer functions. Another appropriate technique to use the RSM method was to build a mathematical relationship between the input parameters temperature and solid volume percentage. The correlation model's accuracy ( $R^2 = 0.9663$ ) was lower than the neural network model's ( $R^2 = 0.9941$ ). Furthermore, the experimental findings were compared to the data collected from the RSM and neural network data. The gap between experimental and anticipated model data is quite small, with the greatest difference occurring at temperature 50°C and SVF of 1.0. The MOD% for ANN was observed to be lower than the MOD% for RSM suggests that ANN is a much better model than RSM for predicting the viscosity.

#### Acknowledgments

The authors extend their appreciation to the Researchers Supporting grant number (DRG-2021-22/190), University of Karachi, Karachi, Pakistan



### Data Availability Statement

The datasets generated or analyzed during the current study are available from the corresponding author on reasonable request.

### Conflict of interest

The authors declare that they have no conflict of interest

### REFERENCES

- [1] A. Kasaeian, A.T. Eshghi, and M. Sameti, "A review on the applications of nanofluids in solar energy systems," *Renewable and Sustainable Energy Reviews*, **43**, 584-598 (2015). <https://doi.org/10.1016/j.rser.2014.11.020>
- [2] I. Nkurikiyimfura, Y. Wang, and Z. Pan, "Heat transfer enhancement by magnetic nanofluids - a review," *Renewable and Sustainable Energy Reviews*, **21**, 548-561 (2013). <https://doi.org/10.1016/j.rser.2012.12.039>
- [3] S. Angayarkanni, and J. Philip, "Review on thermal properties of nanofluids: Recent developments," *Advances in Colloid and Interface Science*, **225**: 146-176. 2015. <https://doi.org/10.1016/j.cis.2015.08.014>
- [4] M. Raja, R. Vijayan, P. Dineshkumar, and M. Venkatesan, "Review on nanofluids characterization, heat transfer characteristics and applications," *Renewable and Sustainable Energy Reviews*, **64**, 163-173 (2016). <https://doi.org/10.1016/j.rser.2016.05.079>
- [5] S.K. Das, S.U. Choi, and H.E. Patel, "Heat transfer in nanofluids—a review," *Heat transfer engineering*, **27**(10), 3-19 (2006). <https://doi.org/10.1080/01457630600904593>
- [6] T. Maré, S. Halelfadl, S. Van Vaerenbergh, and P. Estellé, "Unexpected sharp peak in thermal conductivity of carbon nanotubes water-based nanofluids," *International Communications in Heat and Mass Transfer*, **66**, 80-83 (2015). <https://doi.org/10.1016/j.icheatmasstransfer.2015.05.013>
- [7] Y.L. Zhai, G.D. Xia, X.F. Liu, and Y.F. Li, "Heat transfer enhancement of Al<sub>2</sub>O<sub>3</sub>-H<sub>2</sub>O nanofluids flowing through a micro heat sink with complex structure," **66**, 158-166 (2015). <http://dx.doi.org/10.1016%2Fj.icheatmasstransfer.2015.05.025>
- [8] M.A. Sheremet, I. Pop, and M.M. Rahman, "Three-dimensional natural convection in a porous enclosure filled with a nanofluid using Buongiorno's mathematical model," *International Journal of Heat and Mass Transfer*, **82**, 396-405 (2015). <https://doi.org/10.1016/j.ijheatmasstransfer.2014.11.066>
- [9] Jang, S.P. and S.U.S. Choi, "Role of Brownian motion in the enhanced thermal conductivity of nanofluids," *Appl. Phys. Lett.* **84**(21), 4316-4318. (2004). <https://doi.org/10.1063/1.1756684>
- [10] S.K. Das, and S.U.S. Choi, "A review of heat transfer in nanofluids," *Advances in Heat transfer*, **41**, 81-197 (2009). [https://doi.org/10.1016/S0065-2717\(08\)41002-X](https://doi.org/10.1016/S0065-2717(08)41002-X)
- [11] D.S. Udawattha, M. Narayana, and U.P.L. Wijayarathne, "Predicting the effective viscosity of nanofluids based on the rheology of suspensions of solid particles," **31**(3), 412-426 (2019). <https://doi.org/10.1016/j.jksus.2017.09.016>
- [12] Y. Yang, Z.G.Z., E.A. Grulke, W.B. Anderson, and G. Wu, "Heat transfer properties of nanoparticle-in-fluid dispersions (nanofluids) in laminar flow," **48**(6), 1107-1116 (2005). <https://doi.org/10.1016/j.ijheatmasstransfer.2004.09.038>
- [13] M. Gupta, R. Kumar, N. Arora, S. Kumar, and N. Dilbagi, "Forced convective heat transfer of MWCNT/water nanofluid under constant heat flux: an experimental investigation," *Arabian Journal for Science and Engineering*, **41**(2), 599-609 (2016). <https://doi.org/10.1007/s13369-015-1699-5>
- [14] W.-Q. Lu, and Q.-M. Fan, "Study for the particle's scale effect on some thermophysical properties of nanofluids by a simplified molecular dynamics method," **32**(4), 282-289 (2008). <https://doi.org/10.1016/j.enganabound.2007.10.006>
- [15] K.V. Wong, and O. De Leon, "Applications of nanofluids: current and future," *Advances in mechanical engineering*, **2**, 519659 (2010). <https://doi.org/10.1155/2010/519659>
- [16] A. Patra, M.K. Nayak, and A. Misra, "Viscosity of nanofluids-A Review," *International Journal of Thermofluid Science and Technology*, **7**(2), 070202 (2020). <https://doi.org/10.36963/IJTST.2020070202>
- [17] M.J. Pastoriza-Gallego, C. Casanova, J.L. Legido, and M.M. Piñeiro, "CuO in water nanofluid: influence of particle size and polydispersity on volumetric behaviour and viscosity," **300**(1-2), 188-196 (2011). <https://doi.org/10.1016/j.fluid.2010.10.015>
- [18] T.X. Phuoc, M. Massoudi, and R.-H. Chen, "Viscosity and thermal conductivity of nanofluids containing multi-walled carbon nanotubes stabilized by chitosan," *International Journal of Thermal Sciences*, **50**(1), 12-18 (2011). <https://doi.org/10.1016/j.ijthermalsci.2010.09.008>
- [19] P.K. Namburu, D.K. Das, K.M. Tanguturi, and R.S. Vajjha, "Numerical study of turbulent flow and heat transfer characteristics of nanofluids considering variable properties," **48**(2), 290-302 (2009). <https://doi.org/10.1016/j.ijthermalsci.2008.01.001>
- [20] J. Li, C. Zhou, G. Wang, and D. Zhao, "Study on rheological behavior of polypropylene/clay nanocomposites," *Journal of applied polymer science*, **89**(13), 3609-3617 (2003). <https://doi.org/10.1002/app.12643>
- [21] M. Gupta, V. Singh, R. Kumar, and Z. Said, "A review on thermophysical properties of nanofluids and heat transfer applications," *Renewable and Sustainable Energy Reviews*, **74**, 638-670 (2017). <https://doi.org/10.1016/j.rser.2017.02.073>
- [22] R. Saidur, K. Leong, and H.A. Mohammed, "A review on applications and challenges of nanofluids," *Renewable and sustainable energy reviews*, **15**(3), 1646-1668 (2011). <https://doi.org/10.1016/j.rser.2010.11.035>
- [23] H. Karimi, F. Yousefi, and M.R. Rahimi, "Correlation of viscosity in nanofluids using genetic algorithm-neural network (GA-NN)," *Heat and mass transfer*, **47**(11), 1417-1425 (2011). <http://dx.doi.org/10.1007%2F978-3-642-111-080-2-z>
- [24] M. Gholizadeh, M. Jamei, I. Ahmadianfar, and R. Pourrajab, "Prediction of nanofluids viscosity using random forest (RF) approach," *Chemometrics and Intelligent Laboratory Systems*, **201**, 104010 (2020). <https://doi.org/10.1016/j.chemolab.2020.104010>
- [25] P.K. Kanti, K.V. Sharma, K.M. Yashwantha, and S. Dmk, "Experimental determination for viscosity of fly ash nanofluid and fly ash-Cu hybrid nanofluid: Prediction and optimization using artificial intelligent techniques," *Energy Sources, Part A: Recovery, Utilization, and Environmental Effects*, 1-20 (2021). <https://doi.org/10.1080/15567036.2021.1877374>
- [26] A.A.A.A. Alrashed, M.S. Gharibdousti, M. Goodarzi, L.R. de Oliveira, M.R. Safaei, and E.P.B. Filho, "Effects on thermophysical properties of carbon based nanofluids: experimental data, modelling using regression, ANFIS and ANN," *International Journal of Heat and Mass Transfer*, **125**, 920-932 (2018). <https://doi.org/10.1016/j.ijheatmasstransfer.2018.04.142>
- [27] M.H. Ahmadi, B. Mohseni-Gharyehsafa, M. Farzaneh-Gord, R.D. Jilte, and R. Kumar, "Applicability of connectionist methods to predict dynamic viscosity of silver/water nanofluid by using ANN-MLP, MARS and MPR algorithms," *Engineering Applications of Computational Fluid Mechanics*, **13**(1), 220-228 (2019). <https://doi.org/10.1080/19942060.2019.1571442>
- [28] M.H. Esfe, S. Saedodin, M. Bahiraei, D. Toghraie, O. Mahian, and S. Wongwises, "Thermal conductivity modeling of MgO/EG nanofluids using experimental data and artificial neural network," *Journal of Thermal Analysis and Calorimetry*, **118**(1), 287-294 (2014). <https://doi.org/10.1007/s10973-014-4002-1>

- [29] N. Zhao, and Z. Li, "Experiment and artificial neural network prediction of thermal conductivity and viscosity for alumina-water nanofluids," *Materials*, **10**(5), 552 (2017). <https://doi.org/10.3390/ma10050552>
- [30] M. Vakili, S. Khosrojerdi, P. Aghajannezhad, and M. Yahyaee, "A hybrid artificial neural network-genetic algorithm modeling approach for viscosity estimation of graphene nanoplatelets nanofluid using experimental data," *International Communications in Heat and Mass Transfer*, **82**, 40-48 (2017). <https://doi.org/10.1016/j.icheatmasstransfer.2017.02.003>
- [31] M. Vakili, M. Karami, S. Delfani, and S. Khosrojerdi, "Experimental investigation and modeling of thermal radiative properties of f-CNTs nanofluid by artificial neural network with Levenberg–Marquardt algorithm," *International Communications in Heat and Mass Transfer*, **78**, 224-230 (2016). <https://doi.org/10.1016/j.icheatmasstransfer.2016.09.011>
- [32] A.M. Ghanadi, A.H. Nasab, D. Bastani, and A.A.S. Kordi, "The effect of nanoparticles on the mass transfer in liquid–liquid extraction," *Chemical Engineering Communications*, **202**(5), 600-605 (2015). <https://doi.org/10.1080/00986445.2013.858037>
- [33] M. Abdollahi-Moghaddam, K. Motahari, and A. Rezaei, "Performance characteristics of low concentrations of CuO/water nanofluids flowing through horizontal tube for energy efficiency purposes; an experimental study and ANN modeling," *Journal of Molecular Liquids*, **271**, 342-352 (2018). <https://doi.org/10.1016/j.molliq.2018.08.149>
- [34] M.H. Esfe, and S.M.S. Tilebon, "Statistical and artificial based optimization on thermo-physical properties of an oil-based hybrid nanofluid using NSGA-II and RSM," *Physica A: Statistical Mechanics and its Applications*, **537**, 122126 (2020). <https://doi.org/10.1016/j.physa.2019.122126>
- [35] M.H. Esfe, M. Goodarzi, and S. Esfandeh, "Experimental investigation of c(75–25%)/10W40 as a new nano-lubricant," *The European Physical Journal Plus*, **136**(5), 605 (2021). <https://doi.org/10.1140/epjp/s13360-021-01414-y>
- [36] M.H. Esfe, and M.H. Hajmohammad, "Thermal conductivity and viscosity optimization of nanodiamond-Co<sub>3</sub>O<sub>4</sub>/EG (40: 60) aqueous nanofluid using NSGA-II coupled with RSM," *Journal of Molecular Liquids*, **238**, 545-552 (2017). <https://doi.org/10.1016/j.molliq.2017.04.056>
- [37] M.H. Esfe, and S. Alidoust, "Modeling and precise prediction of thermophysical attributes of water/EG blend-based CNT nanofluids by NSGA-II using ANN and RSM," *Arabian Journal for Science and Engineering*, **46**(7), 6423-6437 (2021).
- [38] Maqsood, K., et al., Multi-objective optimization of thermophysical properties of multiwalled carbon nanotubes based nanofluids. *Chemosphere*, **286**, 131690 (2022). <https://doi.org/10.1007/s13369-020-05086-1>
- [39] M.H. Esfe, M.H. Kamyab, "Mathematical monitoring of agglomeration effects on thermophysical properties of water-based nanofluids using MLP and RSM," *Journal of Thermal Analysis and Calorimetry*, **146**(2), 739-756 (2021). <https://doi.org/10.1007/s10973-020-09996-y>
- [40] N. Zhao, and Z. Li, "Modeling and prediction of viscosity of water-based nanofluids by radial basis function neural networks," **281**, 173-183 (2015). <https://doi.org/10.3390/app7040409>
- [41] O.A. Alawi, N.A.C. Sidik, H.W. Xian, T.H. Kean, and S.N. Kazi, "Thermal conductivity and viscosity models of metallic oxides nanofluids," **116**, 1314-1325 (2018). <https://doi.org/10.1016/j.ijheatmasstransfer.2017.09.133>
- [42] D.-H. Chen, and X.-R. He, "Synthesis of nickel ferrite nanoparticles by sol-gel method," *Materials Research Bulletin*, **36**(7-8), 1369-1377 (2001). [https://doi.org/10.1016/S0025-5408\(01\)00620-1](https://doi.org/10.1016/S0025-5408(01)00620-1)
- [43] M. Salavati-Niasari, F. Davar, M. Mazaheri, and M. Shaterian, "Preparation of cobalt nanoparticles from [bis (salicylidene) cobalt (II)]–oleylamine complex by thermal decomposition," *Journal of Magnetism and Magnetic Materials*, **320**(3-4), 575-578 (2008). <https://doi.org/10.1016/j.jmmm.2007.07.020>
- [44] M. Scimeca, S. Bischetti, H.K. Lamsira, R. Bonfiglio, and E. Bonanno, "Energy Dispersive X-ray (EDX) microanalysis: A powerful tool in biomedical research and diagnosis," *European journal of histochemistry*, **62**(1), (2018). <https://doi.org/10.4081/ejh.2018.2841>
- [45] W. Zhou, R. Apkarian, Z.L. Wang, and D. Joy, "Fundamentals of scanning electron microscopy (SEM)," in: *Scanning microscopy for nanotechnology*, edited by D. Joy, and Z.L. Wang, (Springer, NY, 2006), pp. 1-40.

## ПРОГНОЗ В'ЯЗКОСТІ НАНОРІДИН НА ОСНОВІ КОБАЛЬТОВОГО ФЕРИТУ/SAE50 ТА МОТОРНОЇ ОЛИВИ ЗА ДОПОМОГОЮ НАВЧЕНОЇ ШТУЧНОЇ НЕЙТРАЛЬНОЇ МЕРЕЖІ (ANN) ТА МЕТОДОЛОГІЇ ВІДГУКУ ПОВЕРХНІ (RSM)

Малік Мухаммад Хафізуллах<sup>a,c</sup>, Абдул Рафай<sup>b</sup>, Гулам Мустафа<sup>d</sup>, Мухаммад Халід<sup>b</sup>,  
Зубайр Ахмед Калхоро<sup>c</sup>, Абдул Васім Шайх<sup>a</sup>, Ахмед Алі Раджпут<sup>b</sup>

<sup>a</sup>Інститут інформатики та математики, Університет Сінда, Джамшиоро, Пакистан

<sup>b</sup>Кафедра фізики, Університет Карачі, 75270, Карачі, Пакистан

<sup>c</sup>Департамент математики, Белуджистанський університет інформаційних технологій, інженерії та менеджменту, Кветта, Пакистан

<sup>d</sup>Кафедра фізики, Університет інженерії та технології NED, 75270, Карачі, Пакистан

Передача тепла звичайними рідинами, такими як чиста вода, масло та етиленгліколь, є неефективною через їх низьку в'язкість. Щоб підвищити ефективність звичайних рідин, дуже малий відсоток наночастинок додається до базових рідин для приготування нанорідини. Вплив зміни в'язкості можна використовувати для дослідження реологічних властивостей нанофлюїдів. У цьому дослідженні нанорідини на основі (CoFe<sub>2</sub>O<sub>4</sub>)/моторна олива були виготовлені за стандартною методологією у два етапи. На першому етапі CoFe<sub>2</sub>O<sub>4</sub> (CF) синтезували за допомогою золь-гель вологого хімічного процесу. Кристалічна структура та морфологія були підтвержені за допомогою рентгенівського дифракційного аналізу (XRD) та скануючої електронної мікроскопії (SEM), відповідно. На другому етапі стандартна процедура була адаптована, взявши кілька твердих об'ємних часток CF як  $\varnothing = 0, 0,25, 0,50, 0,75$  і  $1,0$  %. Такі відсотки концентрацій диспергували у відповідному об'ємі моторного масла за допомогою ультразвукової обробки протягом 5 годин. Після цього в'язкість підготовлених п'яти різних нанофлюїдів визначали при температурах від 40 до 80 °C. Відповідно до отриманих даних, в'язкість нанофлюїдів ( $\mu\text{нф}$ ) зменшувалася в міру підвищення температури, але збільшувалася, коли об'ємний відсоток нанофлюїдів  $\varnothing$  підвищувався. Крім того, було враховано 25 експериментальних спостережень для прогнозування в'язкості за допомогою штучної нейронної мережі (ANN) і методології відгуку поверхні (RSM). Алгоритм побудови ідеальної архітектури штучної нейронної мережі був рекомендований для прогнозування швидкості рідини нанофлюїду на основі нафти CF/SAE-50 за допомогою програмного забезпечення MATLAB. Щоб визначити правильність прогнозованої моделі, було розраховано середню квадратичну помилку (MSE) 0,0136.

**Ключові слова:** ферит кобальту; нанофлюїди; в'язкість; тверда об'ємна частка; ANN; RSM

## SPECTRA OF MULTIPLY CHARGED IONS IN LASER PLASMA FORMED FROM GAS-CONTAINING TARGETS<sup>†</sup>

✉ Azamat I. Japakov<sup>a\*</sup>, ✉ Murod E. Vapaev<sup>a</sup>, Ravshan M. Bedilov<sup>b</sup>, ✉ Zakir T. Azamatov<sup>b</sup>,  
Ikram Y. Davletov<sup>a</sup>

<sup>a</sup>Urgench State University, 220100, Urgench, st. Kh. Alimjan, 14, Uzbekistan

<sup>b</sup>Research Institute of Physics of Semiconductors and Microelectronics at the National University of Uzbekistan  
Uzbekistan, 100057, Tashkent

Corresponding Author e-mail: [azamat@urdu.uz](mailto:azamat@urdu.uz)

Received May 1, 2023; revised August 16, 2023; accepted August 17, 2023

The paper presents the results of a study of the charge and energy characteristics of multiply charged ions excited on the surface of a single-element and hydrogen-containing multi-component element targets under the influence of laser radiation with a power density ( $q=10^8-10^{12}$  W/cm<sup>2</sup>). It has been experimentally shown that, for all used values of  $q$  laser radiation, laser-induced plasma from gas-containing targets is characterized by a lower relative yield (dN/dE) of multi-charged ions with a charge number of  $Z>+3$ , compared to the plasma produced on the surface of the single element target. Moreover, the tendency to reduce dN/dE of multi-charged ions of the multi-element target, in comparison with the relative yield of ions from the plasma of the single-element target, is more significant and it depends on the charge of the excited ions. The increase in the charge and energy state, duration, and yield of ions of the heavy component, which occurs with an increase in the content of the light component in the target, has been established. This is explained by a decrease in the efficiency of recombination processes caused by an increase in the expansion velocity of a plasma plume due to a decrease in its average mass.

**Keywords:** Laser-induced plasma, Multiply charged ions, Mass spectrometer, Energy spectrum, Hydrogen-containing two-element plasma, Recombination processes

**PACS:** 52.38. r, 52.38.Mf

### 1. INTRODUCTION

The need for a highly efficient source of multiply charged ions has increased significantly due to the emergence of a new direction in the controlled thermonuclear fusion - inertial fusion on heavy ions. Heavy ions are attractive because of the charge features of their interaction with the target material. First of all, this is a strong deceleration of ions in a substance, which makes it possible to provide a high level of heating. In addition, the ion's high energy makes it possible to get by with relatively small currents. The laser ion source is considered one of the leading contenders for participation in the international program on controlled thermonuclear fusion [1–3].

At present, three types of ion sources are considered contenders for participation in the controlled inertial thermonuclear fusion (ITS) program: electron-beam, electron-cyclotron-resonance, and laser. An analysis of their comparative characteristics allows us to conclude that the most promising is the laser source of ions.

A laser-plasma generator (LPG) is a system of a high-power frequency laser, a chamber for interaction with a target, and a device for extracting a high-current ion beam. The system makes it possible to generate intense streams of highly ionized atoms and nuclei of various elements, including radioactive isotopes, and to inject them into electrophysical devices. The experiments showed that to match the ion source with various accelerators fully. It is necessary to reduce the current of low-charged ions and increase the current of highly-charged ions. Controlling the laser power density and selecting various single-element targets to increase the yield and charge of ions did not give the expected outcome [4]. In order to increase the efficiency of ionization processes in a plasma plume and reduce the efficiency of recombination processes, intensive studies are being carried out on the charge and energy state of mono- and multi-element laser plasma. As well as the release of ions from them, depending on the incident angle [5] and the laser wavelength, the conditions for its focusing on the target surface [6,7], the composition of a multi-component target [8,9] and the percentage (or weight) ratio of its constituent components of the target [10], its density, the state of the structure after various types of treatments [11], the presence of certain impurities, the frequency mode of exposure [12].

The formation of multiply charged ions is associated with the absorption of most of the laser radiation energy in the plasma and gradual ionization due to a decrease in the ablation rate with an increase in the laser radiation power density [13]. Creating multiply charged high-order ions is possible using ultrashort fs-pulsed laser radiation, which has a low light flux compared to short ns-pulsed laser radiation [14, 15]. The time evolution of the formation of multiply charged ions under the action of ns and fs pulsed laser radiation on carbon was studied [16, 17].

The term "monoelement target" can be used conditionally since, in real conditions, arbitrary solid material contains light adsorbed gases, such as H and N, which, at a certain content, can not only change the physical properties

<sup>†</sup> Cite as: A.I. Japakov, M.E. Vapaev, R.M. Bedilov, Z.T. Azamatov, I.Y. Davletov, East Eur. J. Phys. 3, 490 (2023), <https://doi.org/10.26565/2312-4334-2023-3-55>

© A.I. Japakov, M.E. Vapaev, R.M. Bedilov, Z.T. Azamatov, I.Y. Davletov, 2023

of the object under consideration but, in a certain degree, also affect the efficiency of the processes of its interaction with intense laser radiation, the formation and expansion of the resulting plasma plume.

Detailed and systematic studies are required to obtain a complete physical picture of the formation processes and multi-component plasma expansion depending on the composition of the target in the presence of various impurities. Here, attention must be paid to the factors like charge impurities, energy, angular and dynamic distributions, and the yield of multiply charged ions. Eventually, one can estimate the effectiveness of the kinetic processes of ionization, acceleration and recombination, the prevalence, under certain conditions, of one or another process, and the presence of other processes that affect the characteristics of multiply charged ions.

This work is a step forward to establishing the physical processes of formation and expansion of a two-component laser plasma, which determines the yield, charge, energy and spatial distribution of multiply charged ions. The relevance of this study lies in the fact that the experimental results will complement the physical picture of the formation and expansion of multiply charged ions in a multi-component laser plasma, and, in practice, they will allow not only increase the efficiency of sources of multiply charged ions but also to create a new method for analyzing solids for light injected gas.

This paper presents the results of a study of the charge and energy characteristics of multiply charged ions of a hydrogen-containing two-element plasma formed under the influence of laser radiation with a power density ( $q=10^8-10^{12} \text{ W/cm}^2$ ) depending on the atomic mass, the main component of the target. An essential advantage of the proposed work is obtaining complete information about the processes occurring in a two-element laser plasma formed under various initial conditions.

## 2. EXPERIMENTAL PART

The experiments were carried out on an electrostatic mass spectrometer with a mass resolution of  $dm/m=100$  and a TOF distance of  $100 \text{ cm}$  [6]. The Nd:YAG laser beam was directed perpendicular to the target surface. The laser operated at a wavelength of  $1.06 \mu\text{m}$ , a pulse duration of  $50 \text{ ns}$ , an energy per pulse of  $5 \text{ J}$ , and in a single-pulse mode. The laser beam was focused through a converging lens onto a target (with focal length  $f = 10-30 \text{ cm}$ ) placed inside a vacuum chamber evacuated to  $133.3 \cdot 10^{-6} \text{ Pa}$ . Creation and maintenance of vacuum at the level of  $10^{-3}-5 \cdot 10^{-6} \text{ Pa}$  both in the ion source chamber and throughout the entire drift space of ions (with the help of NORD-250 magneto discharge pumps). The spot size of the focused beam was  $10^{-4} \text{ cm}^2$ . The intensity of the neodymium glass laser operating in the single pulse mode was calibrated in the range  $q=10^8-10^{11} \text{ W/cm}^2$  using light filters. Note that the considered laser intensity exceeds the laser plasma formation threshold ( $\sim 10^8 \text{ W/cm}^2$ ). The parameters (energy and duration, laser pulse shape) of the laser are controlled separately by calorimeters and photoelectric methods [Fig. 1].

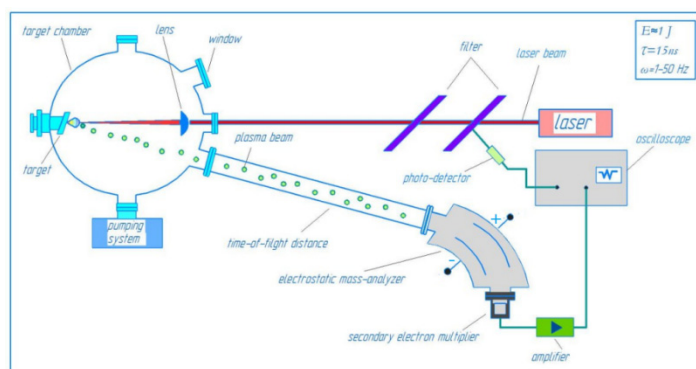


Figure 1. Experimental setup

The potential was applied to the plates of the electrostatic analyzer from a stabilized universal power supply (UPS-1). The ions inside the analyzer move all the time perpendicular to the direction of the electric field, there is no need for additional suggestions about the smallness of the deflection angle. It should be noted that a cylindrical electrostatic energy analyzer ensures the selection of a group of ions with the same ratio of kinetic energy to charge ( $E/Z$ ). Therefore, simple estimates show that the achieved sensitivity ( $\Sigma_c \approx 10^{-3} \text{ wt } \%$  and  $\Sigma_a \approx 10^{-12} \text{ G}$ ) and resolution ( $R_m=100$ ) of the laser mass spectrometer, consisting of a time-of-flight mass analyzer and an electrostatic energy analyzer, close to the limit for this class of devices.

The recording equipment of the mass spectrometer consists of the following elements. A block of laser plasma ion detectors was made, which is connected to the output of an electrostatic analyzer. This block consists of a Secondary electron multiplier (SEM-1A) type detector. The wind turbine gain is  $\sim 10^5$ .

The targets were made from pure C (i.e. graphite), Cu, polyethylene ( $\text{CH}_2$ )<sub>n</sub> (consisting of bound hydrogen (H) atoms), Cu[H] (with H atoms embedded) and Ti[H,N], Zr[H,N] (consisting of hydrogen atoms (H) and (N)) in the form of a thick cylinder with a thickness of  $d=2 \text{ mm}$  and a radius of  $R=0.5 \text{ cm}$ . The target could be moved vertically using a vacuum feed, so that each laser shot could hit a fresh surface to avoid the cratering effect. The target surface was cleaned with the first laser pulse, and the results presented here were averaged over the next four pulses. The error in measuring the mass-charge spectrum of ions is 10%.

### 3. RESULT AND DISCUSSION

In most experiments on laser-induced plasma ions, little attention is paid to the influence of light gas atoms (for example, H, N, Ar), which are present in most solid targets in either specially introduced bound atoms or uncontrolled impurities. However, the presence of such impurities not only changes the physical properties of the target, but also affects the formation of plasma ions under the action of laser radiation. Therefore, the main purpose of this work is to study the effect of such bound or embedded gas atoms on the charge and energy states, duration, and yield of ions in a multi-component plasma.

The time-of-flight spectra of plasma ions generated from the surface of polyethylene, copper, titanium, and zirconium with embedded hydrogen atoms with a concentration of  $10^{-4}$  wt % are experimentally obtained for a mono- and multi-element target depending on different laser radiation intensity  $q$ .

Investigating the charge spectra of Ti, Cu, and Zr ions obtained by exposure to intense laser radiation and a scanning electron microscope on Cu[H] containing  $10^{-4}$  wt.% H, Ti[H,N] and Zr[H,N], in which the concentration of intercalated H and N atoms was  $10^{-3}$ - $10^{-1}$  wt.%, their comparison with similar characteristics of ions of these elements in plasma of a mono-element composition showed:

1) Cu ions registered in laser plasma, formed from the copper rod, at  $q = 3 \cdot 10^{10}$  W/cm<sup>2</sup> and  $q = 10^{11}$  W/cm<sup>2</sup>, have  $Z_{\max} = +4$  and  $Z_{\max} = +6$ , respectively. Recall that in the plasma formed at the specified  $q$  laser radiation from C, not containing H, Cu ions with  $Z_{\max} = +5$  and  $+7$ , respectively, were registered;

2) for Ti and Zr ions formed from Ti[H,N] and Zr[H,N],  $Z_{\max}$  of ions of these elements at the above values of  $q$  of laser radiation was  $+4$  and  $+5$ , respectively. In plasma produced by the interaction of laser radiation with  $q = 3 \cdot 10^{10}$  and  $10^{11}$  W/cm<sup>2</sup> with mono-element Ti,  $Z_{\max}$  of ions of these elements was  $+7$  and  $+10$ , respectively, and  $Z_{\max}$  of Zr ions was  $+5$  and  $+7$ , respectively;

3) it should be especially noted that for all used values of  $q$  laser radiation for plasma obtained from gas-containing samples, a lower relative yield ( $dN/dE$ ) of ions of the heavy component with  $Z > +3$  is characteristic, in comparison with the plasma of a mono-element composition (see Fig.2). Moreover, the tendency to reduce  $dN/dE$  of ions of the heavy component, in comparison with the relative yield of ions from the plasma of a mono-element composition, is the more significant, the greater the charge of the ion. However, the total yield of ions with a given  $Z$  in the case of a multi-component plasma is always greater. This regularity is also characteristic of H ions formed from copper rods. However, in this case, it is less pronounced. Undoubtedly, this is due to a lower concentration of intercalated H in it and, secondly, to the presence of two light interstitial gases (H,N) in gas-containing Ti and Zr.

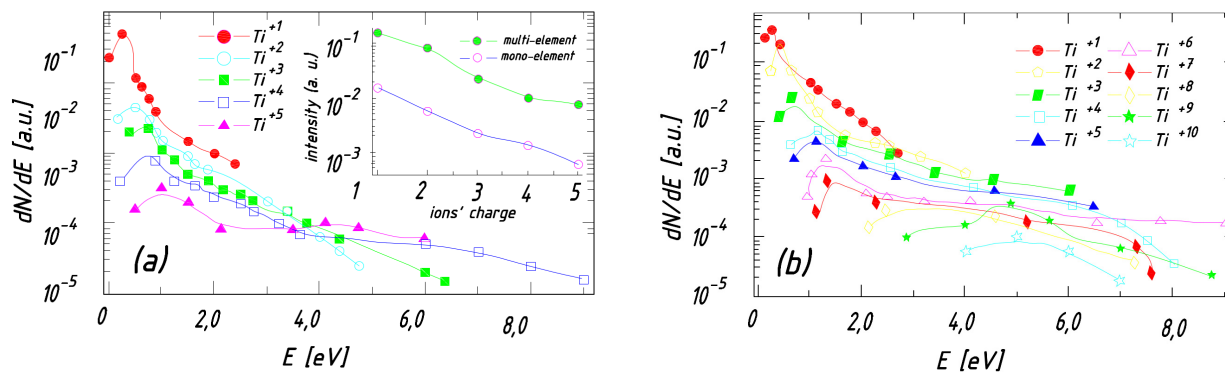


Figure 2. Energy spectrum of TiNH ions formed from multi-element (a) and mono (b) Ti targets at  $q \sim 10^{11}$  W/cm<sup>2</sup>

As an example, consider the energy spectra of titanium, which consists of hydrogen atoms (H and N) in a bound state. On fig. Figure 2 shows the energy spectrum of Ti ions formed from mono (b) and multi-element (a) TiNH targets at  $q \sim 10^{11}$  W/cm<sup>2</sup>. It can be seen from this figure that the charge and intensity of multiply charged ions in plasma (Ti) are greater than in plasma (TiNH) for all values of laser radiation intensity  $q$ . This is due to the higher concentration of H and N atoms in the target (TiNH). Another interesting result we found is that the intensity of H<sup>+</sup> and N<sup>+</sup> ions in plasma (TiNH) decreases with increasing laser intensity  $q$ , starting from a certain critical intensity.

The study of the energy spectra of Ti and Zr ions expanding in plasma together with H and N ions and comparing the results obtained with the identical characteristics of these ions in a single-element plasma showed that in a plasma obtained from Ti and Zr containing embedded light gases, the range of energy distributions of Ti and Zr ions with  $Z = 1-5$  for all values of  $q$  laser radiation is greater than the width of the energy spectra of Ti and Zr ions given  $Z$  in mono-element plasma.

As shown above, a similar regularity in the charge and energy spectra change is also characteristic of (CH<sub>2</sub>)<sub>n</sub> and Cu ions flying apart in a two-component laser plasma formed from a copper rod. Based on the analysis of the results of studies of the charge and energy distributions of ions of the heavy component of the plasma formed under the action of laser radiation on a solid body containing embedded light gases, and comparing them with similar characteristics, in the case of single-element targets, it can be argued that the absence of ions in this multi-component plasma with  $Z_{\max} > +5$  is due to

the fact that ions with  $Z > +6$ , for some reason, have lowered their initial charge. The absence of ions with a high charge multiplicity ( $Z > 4$ ) in  $(\text{CH}_2)_n$  plasma is associated not with an increase in the efficiency of the recombination process but with a decrease in the lifetime of such a dense plasma in the ionization zone. As a consequence, C ions leave the plasma with a lower charge. The similar energy spectra of C and H ions generated from the  $(\text{CH}_2)_n$  plasma and the similar spatial distribution of these ions also indicate that ionization processes play an important role in plasma formation and outflow.

A joint analysis of the patterns of change in the charge and energy spectra of the ions of the heavy component of the laser plasma formed from  $(\text{CH}_2)_n$ , Ti[H,N] and Zr[H,N] and Cu[H] shows that, if for all the studied samples identical in nature to the pattern of change in charge states, then the opposite picture is observed for the energy spectra (Table 1). Taking into account that the gases under consideration are in different states in the studied complex targets, it can be argued that the mechanism for reducing the maximum charge multiplicity of heavy ions obtained from  $(\text{CH}_2)_n$  is not adequate to the mechanism for reducing  $Z_{\text{max}}$  of these ions formed from gas-containing samples.

**Table 1.** Patterns of changes in the charge and energy spectra of ions of the heavy component of laser plasma

Element	Target	$Z_{\text{max}}$ at $q=3 \cdot 10^{10} \text{ W/cm}^2$ (a)	$Z_{\text{max}}$ at $q=10^{11} \text{ W/cm}^2$ (b)	$E_{\text{max}}$ , keV (a)	$E_{\text{max}}$ , keV (b)
C	$(\text{CH}_2)_n$	4	4	2,0	3,0
C	Monoelement	4	6	2,5	3,5
Ti	Ti [H,N]	4	5	6,8	8,0
Ti	Monoelement	7	10	7,0	9,0
Cu	Cu [H]	4	6	5,0	6,0
Cu	Monoelement	5	7	5,0	5,5
Zr	Monoelement	5	7	5,0	7,0
Zr	Zr[H,N]	4	5	4,0	5,5

It is known that at low laser radiation intensities ( $q < 10^8 \text{ W/cm}^2$ ) only evaporation of the target material occurs, and plasma is formed only at high laser radiation intensities [18]. Although the intensity of laser radiation in our experiments is high enough to form a plasma, evaporation of the target material occurs due to the long duration of the laser beam (50 ns). Neutral atoms and ions with low charge and energy receive additional energy from highly charged ions.

Thus, an analysis of the experimental results shows that the mechanisms of formation of light gas ions in a multi-component plasma and the charge and energy distribution of these ions strongly depend on the conditions for the entry of these gas atoms into the target. When they are introduced into a target in implanted forms, the formation of gas ions in a multi-component plasma occurs mainly due to energy transfer from heavy plasma components to light atoms, while ionization processes dominate.

#### 4. CONCLUSIONS

The effect of the presence of light gas atoms in a target on the formation of the charge and energy spectra of multiply charged plasma ions formed under the action of laser radiation has been studied by mass spectrometry. It has been experimentally shown that the mechanisms of formation of light gas ions in a multi-component plasma and the charge and energy distribution of these ions strongly depend on the conditions for the entry of these gas atoms into the target. When they are introduced into a target in implanted forms, the formation of gas ions in a multi-component plasma occurs mainly due to energy transfer from heavy plasma components to light atoms, while ionization processes dominate. An increase in the charge and energy state, duration and yield of ions of the heavy component, which occurs with an increase in the content of the light component in the target, has been established. This is explained by a decrease in the efficiency of recombination processes caused by an increase in the expansion velocity of a plasma bunch due to a decrease in its average mass.

#### ORCID

©Azamat I. Japakov, <https://orcid.org/0009-0001-8296-0931>; ©Zakir T. Azamatov, <https://orcid.org/0000-0001-7074-9437>

©Murod E. Vapaev, <https://orcid.org/0009-0007-5194-131X>

#### REFERENCES

- [1] M. Tulej, R. Wiesendanger, A. Riedo, G. Knopp, and P. Wurz, "Mass spectrometric analysis of the Mg plasma produced by double-pulse femtosecond laser irradiation," *J. Anal. At. Spectrom.* **33**, 1292-1303 (2018). <https://doi.org/10.1039/c8ja00036k>
- [2] B. Ilyas, A.H. Dogar, S. Ullah, N. Mahmood, and A. Qayyum, "Multiply charged ion emission from laser produced tungsten plasma," *Laser Part. Beams*, **30**(4), 651-657 (2012). <https://doi.org/10.1017/S0263034612000687>
- [3] Yu.A. Bykovskii, Yu.P. Kozyrev, S.M. Sil'nov, and B.Yu. Sharkov, "Spatial structure of an expanding laser plasma consisting of aluminum ions and nuclei," *Sov. J. Quantum Electron.* **4**(3), 405-406 (1974). <https://doi.org/10.1070/QE1974v004n03ABEH006762>
- [4] R.T. Khaydarov, H.B. Beisinbaeva, M.M. Sabitov, M. Kalal, and G.R. Berdiyrov, "Conditions defining the mechanisms of the formation of light gas ions in multi-component laser-produced plasmas," *Nucl. Fusion*, **50**(10), 105007 (2010). <https://doi.org/10.1088/0029-5515/50/10/105007>
- [5] M.R. Bedilov, I.Y. Davletov, M.S. Sabitov, G.R. Berdiyrov, and T.G. Tsoi, "Multiply charged ion spectra of a laser plasma produced on both sides of the target," *Quantum Electron.* **31**(5), 453-455 (2001). <https://doi.org/10.1070/QE2001v031n05ABEH001977>

- [6] A. Matnazarov, I. Davletov, and A. Japakov, "Upgraded Experimental Apparatus for the Detection and Investigation of Multiply Charged Ions of a Laser Plasma," *Bull. Sci. Pract.* **6**(9), 198-203 (2020). <https://doi.org/10.33619/2414-2948/58/19>
- [7] M.R. Bedilov, E.N. Tozhikhonov, I.Yu. Davletov, et al. "Emission of multicharged ions in the dependence of the focusing condition of laser radiation on W target surface," *Poverkhnost. Renthenovskyye, synkhrotronnyye i neitronnyye issledovaniya*, **8**, 35-39 (2003). (in Russian)
- [8] M.R. Bedilov, R.T. Khaidarov, and I.Yu. Davletov, "Spectra of ions in a four-element laser plasma," *Quantum Electronics*, **25**(6), 567 (1995). <https://doi.org/10.1070/QE1995v025n06ABEH000415>
- [9] M.R. Bedilov, R.T. Khaidarov, B.Kh. Yakubov, and U.S. Kunishev, "Charge and energy spectra of multiply charged ions of a two-element laser plasma formed from targets of different densities," *Quantum Electronics*, **26**(9), 814 (1996). <https://doi.org/10.1070/QE1996v026n09ABEH000788>
- [10] I.Y. Davletov, R.M. Bedilov, M.S. Sabitov, "An Installation for Obtaining Intense Flows of Multiply Charged Laser-Plasma Ions Using a Second Laser Beam," *Instruments Exp. Tech.* **45**(5), 708-710 (2002). <https://doi.org/10.1023/A:1020478723480>
- [11] M.R. Bedilov, K.B. Beisembaeva, and I.Y. Davletov, "Effect of  $\gamma$ -radiation-induced defects in glass on laser destruction," *Phys. Solid State*, **44**(6), 1093-1097 (2002). <https://doi.org/10.1134/1.1485013>
- [12] A. Matnazarov, M. Latipova, and A. Kodirov, "Formation and Heating of Plasma by Laser Radiation," *Bull. Sci. Pract.* **8**(5), 32-40 (2022). <https://doi.org/10.33619/2414-2948/78/03>
- [13] D. Wu, X. Mao, G.C.-Y. Chan, R.E. Russo, V. Zorba, and H. Ding, "Dynamic characteristics of multi-charged ions emitted from nanosecond laser produced molybdenum plasmas," *J. Anal. At. Spectrom.* **35**(4), 767-775 (2020). <https://doi.org/10.1039/C9JA00411D>
- [14] M.H.A. Shaim, F.G. Wilson, and H.E. Elsayed-Ali, "Aluminum multicharged ion generation from femtosecond laser plasma," *J. Appl. Phys.* **121**(18), 185901 (2017). <https://doi.org/10.1063/1.4983008>
- [15] G.S. Boltaev, M. Iqbal, S.R. Kamalov, M. Vapaev, I.Y. Davletov, and A.S. Alnaser, "Impact of plasma conditions on the shape of femtosecond laser-induced surface structures of Ti and Ni," *Appl. Phys. A*, **128**(6), 488 (2022). <https://doi.org/10.1007/s00339-022-05614-w>
- [16] O. Balki, M.M. Rahman, M.H. Abdel-Fattah, and H.E. Elsayed-Ali, "Carbon multicharged ions emission from femtosecond laser plume," *Opt. Laser Technol.* **120**, 105694 (2019). <https://doi.org/10.1016/j.optlastec.2019.105694>
- [17] M.M. Rahman, O. Balki, and H.E. Elsayed-Ali, "Carbon multicharged ion generation from laser-spark ion source," *Rev. Sci. Instrum.* **90**(9), 093303 (2019). <https://doi.org/10.1063/1.5110402>
- [18] J. Krása, L. Lásková, V. Nassisi, and L. Velardi, "Fe and Fe+2%Si targets as ion sources via UV laser ablation plasma," *Eur. Phys. J. D*, **54**, 473-476 (2009). <https://doi.org/10.1140/epjd/e2009-00023-y>

#### СПЕКТРИ БАГАТОЗАРЯДНИХ ІОНІВ У ЛАЗЕРНІЙ ПЛАЗМІ, СФОРМОВАНИЙ ІЗ ГАЗОВІСНИХ МІШЕНЕЙ

Азамат І. Джапаков<sup>а</sup>, Мурод С. Вапаєв<sup>а</sup>, Равшан М. Беділов<sup>б</sup>, Закір Т. Азаматов<sup>б</sup>, Ікрам Ю. Давлетов<sup>а</sup>




<sup>а</sup>Ургенчський державний університет, 220100, м. Ургенч, вул. х. Алімджан, 14в, Узбекистан

<sup>б</sup>Науково-дослідний інститут фізики напівпровідників і мікроелектроніки Національного університету Узбекистану, Узбекистан, 100057, м. Ташкент

У статті наведено результати дослідження зарядово-енергетичних характеристик багатозарядних іонів, що збуджуються на поверхні одноелементних і водневмісних багатоконпонентних елементних мішеней під дією лазерного випромінювання з густиною потужності ( $q = 10^8$ - $10^{12}$  Вт/см<sup>2</sup>). Експериментально показано, що для всіх використовуваних значень  $q$  лазерного випромінювання лазероіндукована плазма газовмісних мішеней характеризується меншим відносним виходом ( $dN/dE$ ) багатозарядних іонів із зарядовим числом  $Z > +3$ , порівняно з плазмою, утвореною на поверхні одноелементної мішені. Більше того, тенденція до зменшення  $dN/dE$  багатозарядних іонів багатоелементної мішені, порівняно з відносним виходом іонів із плазми одноелементної мішені, більш значна і залежить від заряду збуджених іонів. Встановлено збільшення зарядового та енергетичного стану, тривалості та виходу іонів важкої компоненти, яке відбувається із збільшенням вмісту легкої компоненти в мішені. Це пояснюється зниженням ефективності процесів рекомбінації, викликаним збільшенням швидкості розширення плазмового факелу внаслідок зменшення його середньої маси.

**Ключові слова:** лазерно-індукована плазма; багатозарядні іони; мас-спектрометр; енергетичний спектр; водневмісна двоелементна плазма; процеси рекомбінації

## EFFECTIVENESS OF WAVELET DENOISING ON SECONDARY ION MASS SPECTROMETRY SIGNALS<sup>†</sup>

 **Nadia Dahraoui**<sup>a,b,#</sup>,  **M'hamed Boulakroune**<sup>b</sup>, **S. Khelfaoui**<sup>a</sup>, **S. Kherroubi**<sup>a</sup>,  **Yamina Benkrima**<sup>c,\*</sup>

<sup>a</sup>*Electronics and Communication Department, Faculty of New Technologies of Information and Communication, University Kasdi Merbah of Ouargla, Ouargla 30000, Algeria*

<sup>b</sup>*Laboratory of Electrical Engineering Polytechnic Constantine, Electrical and Automatic Department, National Polytechnic School of Constantine, 25000 Constantine, Algeria*

<sup>c</sup>*Ecole Normale Supérieure de Ouargla, 30000 Ouargla, Algeria*

<sup>#</sup>*e-mail: [dahraoui.nadia@univ-ouargla.dz](mailto:dahraoui.nadia@univ-ouargla.dz)*

<sup>\*</sup>*Correspondence Author e-mail: [b-amina1@hotmail.fr](mailto:b-amina1@hotmail.fr)*

Received June 16, 2023; revised July 14, 2023; accepted July 16, 2023

Our objective is “Use of Digital Signal Processing to cross Physical and Instrumental Limits in the field of Microelectronics”. We interest of SIMS (Secondary Ions Mass Spectrometry) signals, denoising the secondary signal, which is altered by the measurement, is considered that an essential step prior to applying another signal processing technique, that aims enhance the SIMS signals, such as deconvolution (which is a technique for restoration the original signal). Wavelet theory has already achieved huge success. The most efficient and widely used wavelet denoising method is based on wavelet coefficient thresholding. Indeed, we choose the wavelet transform to denoise the SIMS signals. In this paper, we aim to achieve a better result for the denoised signal. To achieve this, we manipulate the parameters of the DWT (Discrete Wavelet Transform) such as the decomposition level and the type of wavelet. The choice of wavelet type and the level of resolution can have a significant influence; it is important to note that the choice of resolution level depends on the type of signal we are dealing with, the nature of the present noise, and our specific goals for the denoised signal. It is generally recommended to test different resolution levels and evaluate their impact on the quality of the denoised signal before making a final decision. Moreover, the results obtained in wavelet denoising can be significantly influenced by the selection of wavelet types. The chosen wavelet type plays a crucial role in the extraction of signal details. Indeed, the effectiveness of denoising the MD6 sample has been demonstrated by the results obtained with sym4, db8, Haar and coif5 wavelets. These wavelets have effectively reduced noise while preserving crucial signal information, leading to an enhancement in the quality of the denoised signal.

**Keywords:** SIMS Analysis; Discrete Wavelet Transform; Multiresolution Decomposition; Wavelet shrinkage; Denoising; Noise Reduction

**PACS:** 25.40.Ep, 25.40.Lw, 43.30.Re

### 1. INTRODUCTION

Secondary Ions Mass Spectrometry (SIMS) is an analytical technique used to analyze the elemental and molecular composition of solid surfaces. SIMS analysis has a wide range of applications in materials science semiconductor manufacturing, geology, and biology, among others. It is particularly valuable for its high sensitivity and the ability to provide detailed information about the elemental and molecular composition of surfaces at high special resolution [1-3]. Any measurement, regardless of its nature or the object being measured, is susceptible to being affected by various unwanted signals commonly referred to as noise. In other words, when conducting a measurement, it is common for disruptive or parasitic elements to mix with the desired signal, which can impact the quality or precision of the obtained measurement. Noise can originate from various sources, such as electromagnetic interference, environmental variations, instrumental errors, or even inherent limitations of the measurement method used. It is important to consider these parasitic signals during result analysis and implement appropriate techniques to attenuate or eliminate them in order to achieve the most accurate and reliable measurement possible. Wavelet denoising techniques provide a high quality and flexible solution for mitigating noise in signals and images. The wavelet transforms (WT), a powerful tool in signal and image processing, has been successfully applied in various scientific domains, including signal processing, image processing computer graphics, and pattern recognition [4-6]. The denoising of the secondary signal in SIMS is widely recognized as an effective pre-treatment technique for enhancing the signal quality and even depth resolution. In particular, deconvolution, a signal restoration technique, plays a crucial role as an important tool in improving depth resolution.

### 2. EXPERIMENTAL

#### 2.1. Data and acquiring techniques

In this work, we will use two types of signals, one is a simulated profile, and the other is a real profile that was measured using the Cameca Ims-6f at oblique incidence. The simulated profile is obtained by convolving a square wave signal with the DRF (Depth Resolution Function), which is the impulse response of the SIMS system. The addition of noise with a signal-to-ratio ultimately leads to a signal heavily distributed by noise. The experimental profile (real

<sup>†</sup> *Cite as:* N. Dahraoui, M. Boulakroune, S. Khelfaoui, S. Kherroubi, Y. Benkrima, East Eur. J. Phys. 3, 495 (2023), <https://doi.org/10.26565/2312-4334-2023-3-56>

© N. Dahraoui, M. Boulakroune, S. Khelfaoui, S. Kherroubi, Y. Benkrima, 2023



profile) is obtained by analysis of the delta of boron doped silicon in a silicon matrix, analyzed using Cameca Imf-6f at oblique incidence. MD4 is a profile that contains four multi-Delta-layer. Utilizing a threshold technique and discrete wavelet transform (DWT), the SIMS signals were denoised and implemented using the MATLAB wavelet toolbox.

## 2.2. Noise Removal

### Wavelet denoising with thresholding

The most efficient and widely used wavelet denoising is based on thresholding wavelet coefficients. This process follows three important steps: (i) Wavelet decomposition: the input signals are decomposed into wavelet coefficients; (ii) Thresholding: the wavelet coefficients are modified according to a threshold; and (iii) Reconstruction: modified coefficients are used in inverse transform to obtain the noise-free signal (Fig. 1). Several researchers have used thresholding wavelet denoising techniques [6-10].

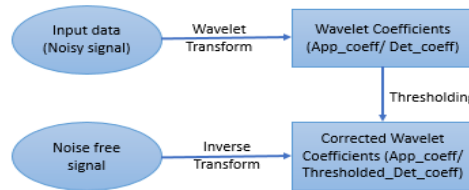


Figure 1. Basic flow chart of wavelet-based signal denoising.

## 3. RESULTS AND DISCUSSION

### 3.1. Denoising of simulated and experimental profiles. Influence of decomposition level

In this section, we discuss the influence of the decomposition level of the wavelet used for denoising. In this case, we use a simulated signal. The result is shown in Figure 2 (all the figures are illustrated on a logarithmic scale). A real profile is also used, and figure3 displays the result.

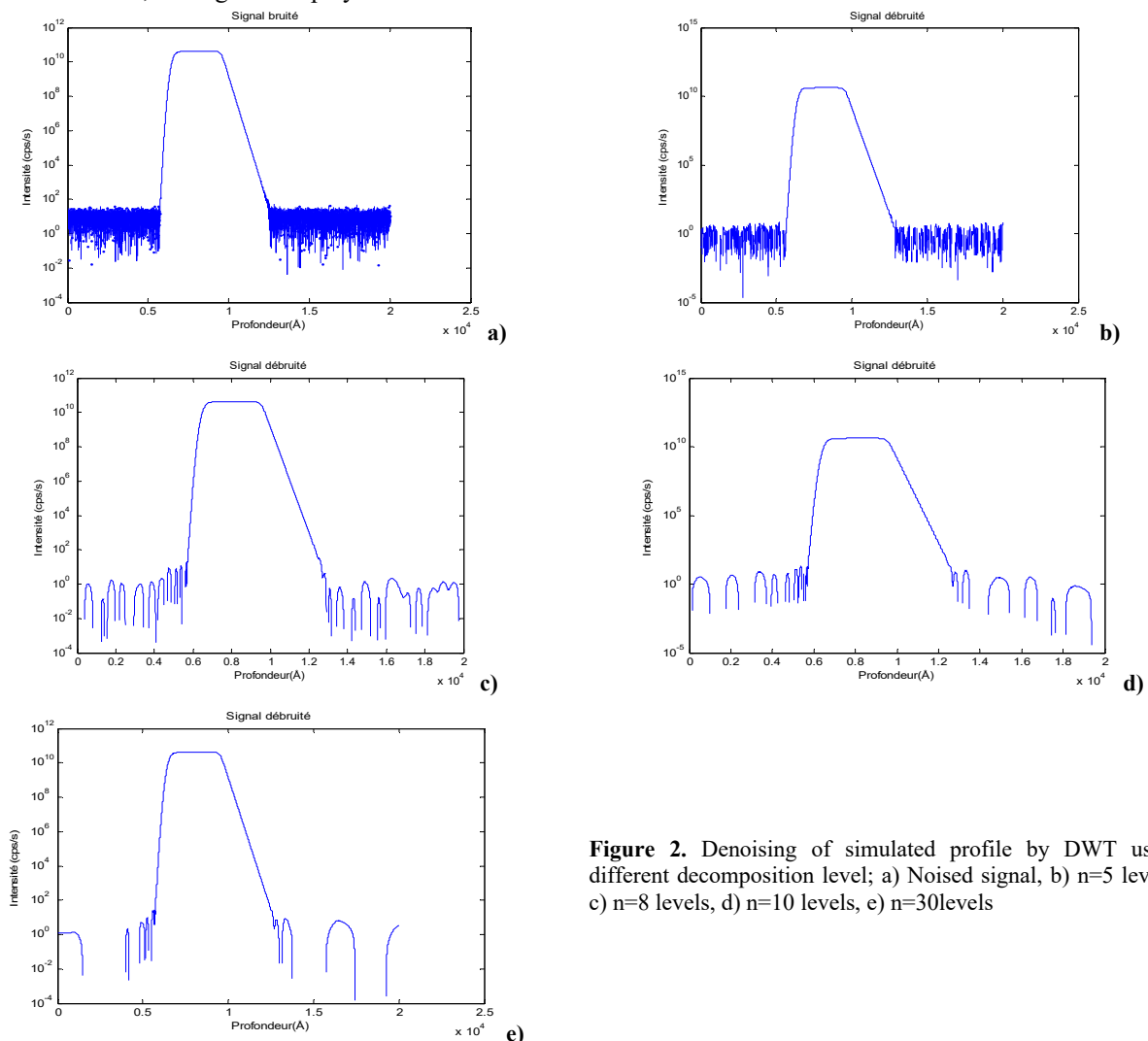
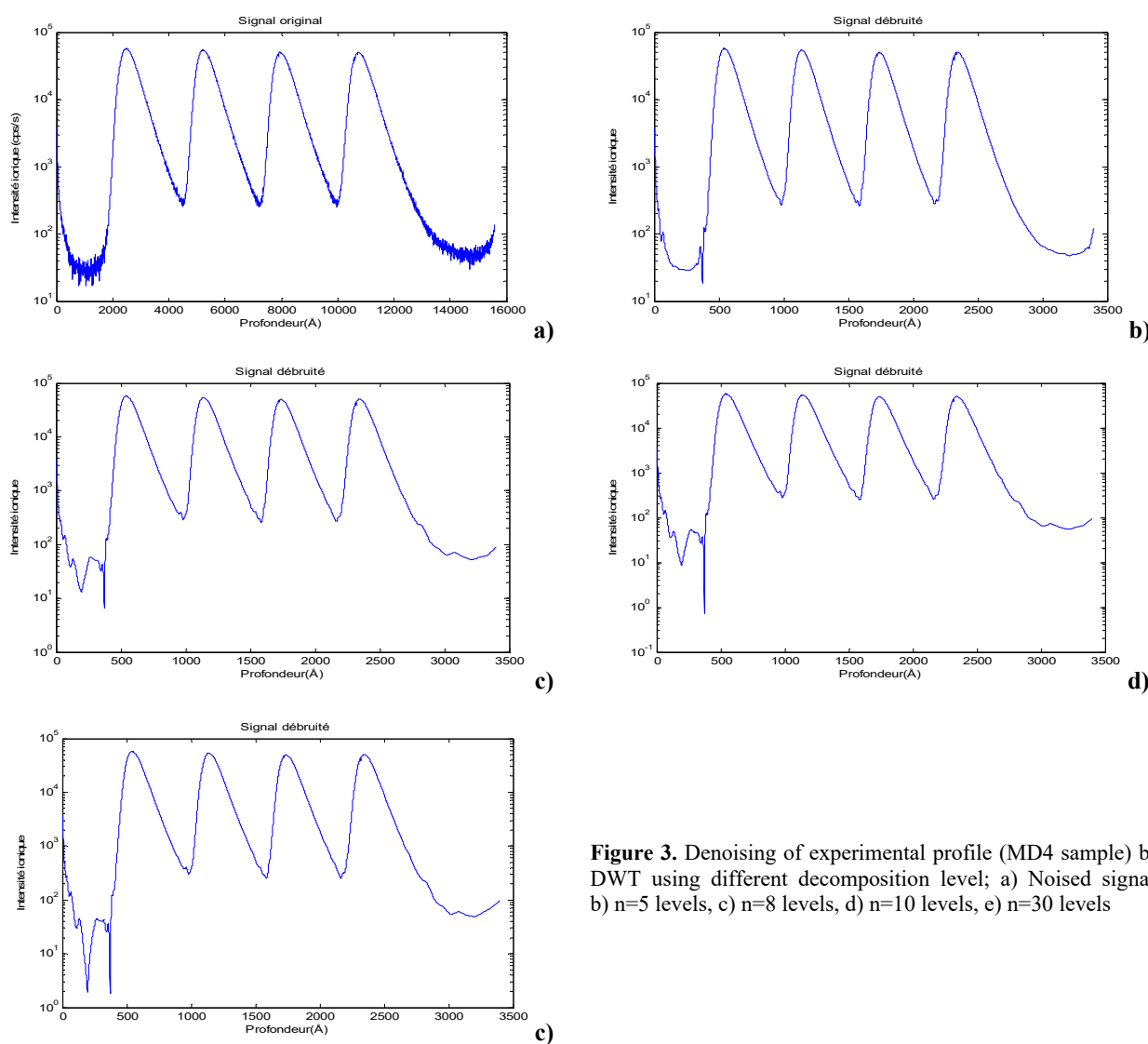


Figure 2. Denoising of simulated profile by DWT using different decomposition level; a) Noised signal, b) n=5 levels, c) n=8 levels, d) n=10 levels, e) n=30levels

During wavelet denoising of a signal, the level of decomposition is directly related to the level of resolution. In general, a higher number of decomposition levels allows for a finer resolution, while a lower number of decomposition levels leads to a coarser resolution.

If we choose a higher resolution level, it means that we will retain more fine details of the signal, but there is also a higher chance of preserving some of the noise. This can be useful if we want to analyze subtle details of the signal, but it can also make the final signal noisier.

On other hand, if we opt for a lower resolution level, we will achieve better noise suppression because higher-frequency components (which are often associated with noise) will be removed. However, this can result in a loss of important signal details, which may be undesirable in certain applications.



**Figure 3.** Denoising of experimental profile (MD4 sample) by DWT using different decomposition level; a) Noised signal, b)  $n=5$  levels, c)  $n=8$  levels, d)  $n=10$  levels, e)  $n=30$  levels

In summary, the influence of resolution level when using wavelet techniques to denoise the signal varies depending on the specific preferences and requirements of each application. It is essential to experiment with different resolution levels to find the right balance between noise suppression and preservation of signal details.

### 3.2. Denoising of sample MD6. Influence of wavelet types

In this section, we address the denoising of the MD6 sample (experimental profile which contains six Multi-Delta layers) using wavelet transform, with a focus on the influence of different types of wavelets used. The choice of wavelet type can have a significant impact on the denoising results (see Fig.4).

For signal decomposition, it is important to make a good choice of the mother wavelet or analysis wavelet. This wavelet must possess the following properties: symmetry, orthogonality, and suitability for discrete wavelet transform (DWT), [11-14]. A group of mother wavelets has been tested, including the Haar wavelet, Daubechies wavelet, Symlet wavelet, and Coiflet wavelet. The results obtained with the sym4, db8, Haar, and coif5 wavelets have demonstrated their effectiveness in denoising of the MD6 sample. These wavelets have successfully reduced noise while preserving important signal information, resulting in an improvement in the quality of the denoised signal.

In conclusion, the choice of wavelet type significantly influences the denoising process of the MD6 sample using wavelet transform. A thoughtful selection of the appropriate wavelet can result in a noticeable enhancement of signal quality by effectively eliminating noise while preserving essential information.

Regarding the SNR (signal-to-noise ratio), it is an evaluation criterion (quantitative criterion) that we use in this work. The result improves as the SNR increases, but with caution. Additionally, we use visually inspect the denoised signals, which serves as a qualitative evaluation criterion.

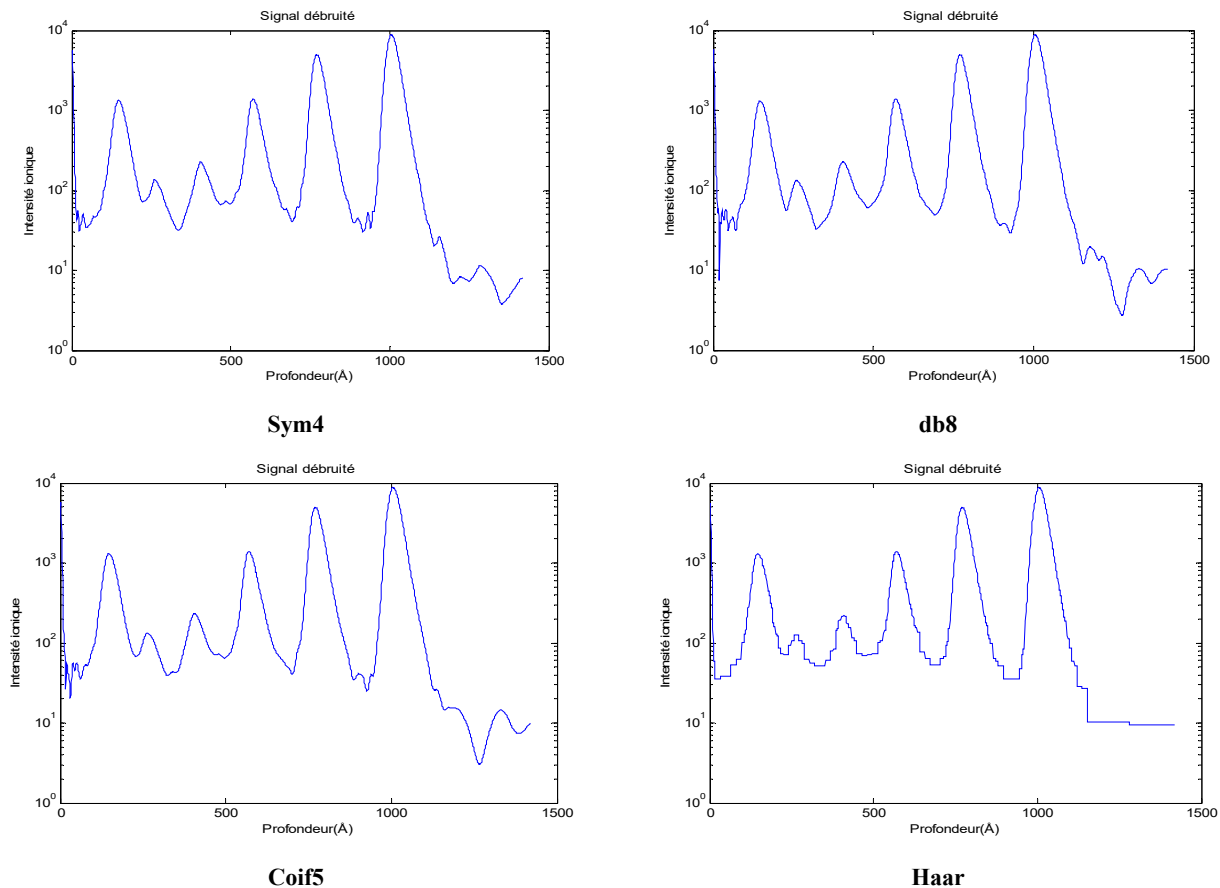


**Figure 4.** Denoising of experimental profile (MD6 sample) by DWT using different wavelet types (sym4, db8, Haar and coif5)

### 3.3. Evaluation by SNR

In the context of wavelet denoising, evaluation using Signal-to-Noise Ratio (SNR) is often employed to measure the effectiveness of noise reduction methods. However, it is important to note that SNR alone does not provide a comprehensive assessment of signal quality. Other factors such as preservation of signal details, introduced distortion, and subjective perception should also be considered for a more comprehensive evaluation. There is no strict rule to determine the exact number of appropriate decomposition levels in wavelet denoising procedures. The choice of the number of decomposition levels generally depends on the nature of signal and the level of noise present.

In some cases, using a larger number of decomposition levels may be preferable to capture finer details of the signal. However, this can also lead to the amplification of unwanted noise. On the other hand, using too few decomposition levels may not sufficiently represent the signal details and reduce the effectiveness of denoising.

**Table 1.** Signal-to-noise-ratio of SIMS signal after denoising using various levels of decomposition

Signals Levels	Simulated Profile	Experimental profile	
		MD 4	MD 6
5	171.8791	58.2853	46.9578
8	180.5946	64.5308	58.0944
10	185.6339	64.6143	65.3376
30	207.4209	114.2810	123.6753

Different wavelet types have distinct properties in terms of temporal resolution, frequency resolution, and filtering characteristics. The selected wavelet type can affect the ability to effectiveness extract signal details and suppress unwanted noise. Certain wavelet types, like the Haar wavelet transform, are well-suited for detecting abrupt discontinuities in a signal but may not be as effective in preserving continuous signals. On the other hand, other wavelet

types, such as the Daubechies wavelets, can provide better frequency resolution and are often employed for processing smoother signals.

**Table 2.** Signal-to-noise-ratio of SIMS signal after denoising using various wavelet types

SignalsWavelet	Simulated Profile	Experimental profile	
		MD 4	MD 6
Sym 4	171.8879	58.2853	46.9578
db 8	172.3121	56.9330	44.9978
Coif 5	172.3118	57.1596	44.5535
Haar	77.3432	53.7140	42.3112

#### 4. CONCLUSION

Wavelet theory has already a powerful tool in the field of signal processing. For SIMS signals, denoising the secondary signal, which is altered by the measurement, is considered that an essential step prior to applying such a signal processing technique that aims enhance the SIMS signals.

In the fields of signal processing and image processing, there are many types of criteria to evaluate such work. In our case, we choose a quantitative criterion, such as the signal-to-noise ratio (SNR), which does not require comparison with SNR values calculated prior to applying the DWT. Instead, the SNRs of the denoised signals are compared among themselves. And the other hand, we choose a qualitative criterion, which is based on the direct visualization of the denoised signals.

In this work, the choice of wavelet type and the level of resolution can have a significant influence; in practice, it is common to experiment with different numbers of decomposition levels and evaluate the results obtained. Criteria such as noise reduction, preservation of important signal features, and overall improvement in signal quality can be used to guide the selection of the appropriate number of decomposition levels.

In addition, it is a common practice to conduct experiments using various wavelet types and choose the one that delivers optimal outcomes in terms of noise reduction while preserving crucial signals features.

#### ORCID

©Nadia Dahraoui, <https://orcid.org/0000-0003-4481-392X>; ©M'hamed Boulakroune, <https://orcid.org/0000-0002-9614-3115>

©Yamina Benkrima, <https://orcid.org/0000-0001-8005-4065>

#### REFERENCES

- [1] J.C. Vickerman, Book Review "Secondary ion mass spectrometry-basic concept, instrumental aspects, applications and trends," A. Benninghoven, F.G. Rudenauer, and H.W. Werner, (Wiley-Interscience, 1987). <https://doi.org/10.1002/sia.740100811>
- [2] R. Shishido, M. Fujii, T. Seki, T. Aoki, J. Matsuo, and S. Suzuki, "Yields and images of secondary ions from organic materials by different primary Bi ions in time-of-flight secondary ion mass spectrometry", *Rapid Commun. Mass Spectrometry*, **30**(4), 476-482, (2016). <https://doi.org/10.1002/rcm.7455>
- [3] J.D. Holmes, J. O'Connell, R. Duffy, and B. Long, "Surface Functionalization Strategies for Monolayer Doping: Secondary ion mass spectrometry", *Encyclopedia of Interfacial Chemistry*, 829-834 (2018). <https://doi.org/10.1016/B978-0-12-409547-2.14125-3>
- [4] M. Boulakroune, and D. Benatia, "Multi-scale Deconvolution of Mass Spectrometry Signals", in: *Advanced in Wavelet Theory and Their Applications in Engineering, Physics and Technology*, edited by D. Baleanu, Chap. 7, (IntechOpen, 2012). pp. 125-152. <https://doi.org/10.5772/37772>
- [5] M.R.Md. Yusof, A.K. Ariffin, and M. Ismail, "Wavelet denoising as signal feature dependent kernel convolution," *The 2018 International Conference on Research and Learning of Physics, Journal of Physics: Conf. Series*, **1185**(1), 012026 (2019). <https://doi.org/10.1088/1742-6596/1185/1/012026>
- [6] S. Gaci, "The use of wavelet-based denoising techniques to enhance the first-arrival picking on seismic traces", *IEEE transactions on geoscience and remote sensing*, **52**(8), 4558-4563 (2014). <https://doi.org/10.1109/TGRS.2013.2282422>
- [7] M. Boulakroune, "Reliability of multiresolution deconvolution for improving depth resolution in SIMS analysis," *Applied Surface Science*, **386**, 24-32 (2016). <https://doi.org/10.1016/j.apsusc.2016.05.164>
- [8] L. Chiung-Chou, Y. Hong-Tzer, and C. Hsueh-Hsien, "Denoising Techniques with a Spatial Noise-Suppression Method for Wavelet-Based Power Quality Monitoring," *IEEE Transactions on Instrumentation and Measurement*, **60**(6), 1986-1996 (2011). <https://doi.org/10.1109/TIM.2011.2115610>
- [9] G. Maximilian, P. Souvik, G. Ebrahim, F.S. Aaron, S. Nidul, G. Rajdeep, and M.D.Z.I. Ahmed, "A Survey on Denoising Techniques of Electroencephalogram Signals using Wavelet Transform", *Signals*, **3**(3), 577-586 (2022). <https://doi.org/10.3390/signals3030035>
- [10] T. Zikov, S. Bibian, G.A. Dumont, M. Huzmezan, and C.R. Ries, "A wavelet based de-noising technique for ocular artifact correction of the electroencephalogram," in: *Proceedings of the Second Joint 24<sup>th</sup> Annual Conference and the annual Fall Meeting of the Biomedical Engineering Society Engineering in Medicine and Biology*, (Houston, TX, USA, 2002). <https://doi.org/10.1109/IEMS.2002.1134407>
- [11] X. Bo, X. Zhangqiang, W. Zhijian, Z. Lijiao, Z. Dazhou, and L. Fusheng, "Gamma spectrum denoising method based on improved wavelet threshold," *Nucleat Engineering and Technology*, **52**(8), 1771-1776 (2020). <https://doi.org/10.1016/j.net.2020.01.025>
- [12] Md. Mamun, M. Al-Kadi, and M. Marufuzzaman, "Effectiveness of wavelet denoising on electroencephalogram signals," *Journal of Applied Research and Technology*, **11**(1), 156-160 (2013). [https://doi.org/10.1016/S1665-6423\(13\)71524-4](https://doi.org/10.1016/S1665-6423(13)71524-4)

- [13] D. Vilimek, J. Kubicek, M. Golian, R. Jaros, R. Kahankova, P. Hanzlikova, D. Barvik, *et al.*, “Comparative analysis of wavelet transform filtering systems for noise reduction in ultrasound images,” *Plos. Global Public Health*, **17**(7), e0270745 (2022). <https://doi.org/10.1371/journal.pone.0270745>
- [14] A. Yahyaoui, B. Necib, A. Nour, and S. Rechak, “Analyse par la transformée d’ondelettes de delamination et porosité dans les composites stratifiés,” *Sciences & Technologie B, Sciences de l’ingénieur*, **0**(30), 17-24 (2009).

### ЕФЕКТИВНІСТЬ ВЕЙВЛЕТ-ПРИДУШЕННЯ ШУМУ В СИГНАЛАХ ВТОРИННОЇ ІОННОЇ МАСС-СПЕКТРОМЕТРІЇ

Надія Дахрауї<sup>a,b</sup>, Мхамед Булакрун<sup>b</sup>, С. Хелфауї<sup>a</sup>, С. Херрубі<sup>a</sup>, Яміна Бенкріма<sup>c</sup>

<sup>a</sup>Кафедра електроніки та зв'язку, факультет нових технологій інформації та зв'язку, Університет Касді Мербах, Уаргла, Алжир

<sup>b</sup>Лабораторія електротехніки Костянтинівського політехнічного інституту, Факультет електротехніки та автоматичної, Національна політехнічна школа Костянтина, 25000 Костянтин, Алжир

<sup>c</sup>Вища звичайна школа Уаргла, 30000 Уаргла, Алжир

Нашою метою є «Використання цифрової обробки сигналів для перетину фізичних та інструментальних обмежень у галузі мікроелектроніки». Нас цікавлять сигнали SIMS (мас-спектрометрія вторинних іонів), придушення шуму вторинного сигналу, який змінюється в результаті вимірювання, вважається важливим кроком перед застосуванням іншої техніки обробки сигналів, яка спрямована на посилення сигналів SIMS, наприклад деконволюція (яка є технікою відновлення вихідного сигналу). Теорія вейвлетів вже досягла величезного успіху. Найефективніший і широко використовуваний метод вейвлет-знищення шуму базується на пороговому визначенні вейвлет-коефіцієнта. Дійсно, ми вибираємо вейвлет-перетворення для придушення сигналів SIMS. У цій статті ми прагнемо досягти кращого результату для сигналу з шумом. Щоб досягти цього, ми керуємо параметрами DWT (дискретне вейвлет-перетворення), такими як рівень розкладання та тип вейвлета. Вибір типу вейвлета та рівня роздільної здатності може мати значний вплив; Важливо відзначити, що вибір рівня роздільної здатності залежить від типу сигналу, з яким ми маємо справу, характеру поточного шуму та наших конкретних цілей щодо знешумленого сигналу. Зазвичай рекомендується протестувати різні рівні роздільної здатності та оцінити їхній вплив на якість знешумленого сигналу перед прийняттям остаточного рішення. Крім того, вибір типів вейвлетів може суттєво вплинути на результати, отримані при вейвлет-знищенні. Вибраний тип вейвлета відіграє вирішальну роль у вилученні деталей сигналу. Дійсно, результати, отримані з вейвлетами *sum4*, *db8*, *Haar* і *coif5*, продемонстрували ефективність усунення шумів у зразку MD6. Ці вейвлети ефективно зменшили шум, зберігаючи важливу інформацію про сигнал, що призвело до покращення якості знешумленого сигналу.

**Ключові слова:** аналіз SIMS; дискретне вейвлет-перетворення; декомпозиція з різною роздільною здатністю; вейвлет-обрізання; знешумлення; зменшення шуму